DISSERTATION

PRECIPITATION DOWNSCALING AND ITS USE IN THE ASSESSMENT OF HYDROLOGIC EFFECTS OF CLIMATE VARIABILITY AND CHANGE

Submitted by

Boo-Sik Kang

Department of Civil Engineering

In partial fulfillment of the requirements

For the Degree of Doctor of Philosophy

Colorado State University

Fort Collins, Colorado

Summer 2003

UMI Number: 3107086

COLORADO STATE UNIVERSITY

July 1, 2003

WE HEREBY RECOMMEND THAT THE DISSERTATION PREPARED UNDER OUR SUPERVISION BY BOO-SIK KANG ENTITLED "PRECIPITATION DOWNSCALING AND ITS USE IN THE ASSESSMENT OF HYDROLOGIC EFFECTS OF CLIMATE VARIABILITY AND CHANGE".

Committee on Graduate Work

Jose D. Salas

Dr. Jose D. Salas

David A. Woolhiser

Dr. David A. Woolhiser

Richard E. Eykholt

Dr. Richard E. Eykholt

Jorge Ramirez

Advisor : Dr. Jorge A. Ramirez

Sandra Woods

Department Head/Director

ABSTRACT OF DISSERTATION

PRECIPITATION DOWNSCALING AND ITS USE IN THE ASSESSMENT OF HYDROLOGIC EFFECTS OF CLIMATE VARIABILITY AND CHANGE

The combined use of physically based meteorological and hydrologic modeling can enhance the accuracy and reliability of hydrologic assessments. However, because of the different characteristic spatial and temporal scales of atmospheric and hydrologic processes, and their large spatial and temporal variability, a methodology must be developed for an appropriate coupling of these two kinds of models. In this thesis, a new methodology is developed that couples GCM macro-scale climate model output and distributed watershed rainfall-runoff models through a precipitation downscaling algorithm based on random cascades.

The downscaling model is a composite of a Stochastic Space-Time Disaggregation Model (SSTDM) that preserves the spatial and temporal dependency characteristics and an Intermittency multiplicative Random Cascade Model (IRCM) that incorporates the statistical self-similarity, spatial intermittency, and the spatial storm cluster formation of precipitation. Each of the above sub-models is applied over a specific range of scales. The corresponding scale ranges are non-overlapping and the reference level at which the models are switched is a function of the correlation structure of the observations. High-resolution ($2 \times 2km$) NEXRAD

observations were used for the characterization of the spatial and temporal distribution, the correlation structure, and the statistical self-similarity of precipitation. The scaling analysis demonstrated that a mono-fractal structure of self-similarity of small-scale field less than 32 km is well developed. Based on the results of this analysis process, GCM precipitation was downscaled to the 2 km-scale.

In order to assess the hydrologic impacts of climate variability, the output from the Canadian Climate Center Global Circulation Model was downscaled using the new downscaling scheme described above. The downscaled fields were then used to drive the HEC_HMS, a physically based, semi-distributed hydrologic model. The South Platte Headwaters basin ($2{,}465 km^2$) was selected as the study area for the assessment. Climate output corresponding to the IPCC SRES (Intergovernmental Panel on Climate Change Special Report on Emission Scenarios) "B2" scenario was used for the analysis. Applying the downscaling model to produce precipitation fields at different spatial scales that effectively smoothed the spatial variability led to a reduction of streamflow, so directly applying the GCM precipitation with no downscaling can give rise to gross underestimation of streamflows. Hydrologic response of the South Platte (i.e., streamflows, evapotranspiration, etc.) was simulated for 2 temporal windows (2011-2020 and 2081-2090) corresponding to the above GCM scenario. Results indicate that the JJA runoff volume is decreased 15.37% and the JJA peak flow rate is decreased 18.01%. Much of these reductions are the result of the decrease of JJA precipitation and increase of JJA evaporation.

Boo-Sik Kang
Department of Civil Engineering
Colorado State University
Fort Collins, CO 80523
Summer 2003

ACKNOWLEDGEMENTS

This dissertation could not have been written without Dr. Jorge A. Ramírez who not only served as my supervisor but also encouraged and challenged me throughout my academic program. And I would like to express my sincere appreciation also to my doctoral committee, Dr. Jose Salas, Dr. David A. Woolhiser, and Dr. Richard E. Eykholt for their valuable comments, suggestions, and reviews. I thank Dr. David Fanning in Fanning Consulting and Dr. Thomas Evans in Hydrologic Engineering Center of U.S. Army Corps of Engineers for their kind technical comments at critical moments. The project for this dissertation was partially supported by the National Institute for Global Environmental Change through the U.S. Department of Energy (Cooperative Agreement No. DE-FC03-90ER61010). The data was provided by Global Hydrology Resource Center (GHRC) at the Global Hydrology and Climate Center in NASA, Huntsville, Alabama. I thank them all.

I would like to express my appreciation to Dr. Seok-Ku Ko and other KOWACO staff members for their patience and support. My thanks extend also to Mr. Woo-Gu Kim, Dr. Ick-Hwan Ko, and Dr. Gwang-Man Lee for their careful concern for finalizing my dissertation.

I deliver my love to my American friends; Wells' family, Criders' family, and Shievely's family in Fort Collins. I miss their friendship they showed to my family. Last but not least, I deliver sincere thanks to my parents, brother, and sister for their love and concern. Finally, I thank my wife, Jung-Sun and sweet kid,, Hee-Seok for being always with me with love and patience.

Table of contents

List of Figures

List of Tables

Chapter 1

1. Introduction

1.1. Problem statement

The principal objective of hydrologic science is to understand, characterize and describe the storages and fluxes of water in all components of Earth's physical climate system and their interaction with atmospheric, ecological, geomorphic, geologic, and biogeochemical and other processes. Hydrology describes the spatial and temporal distribution of water in all its phases, as well as the fluxes and storages of moisture. Through realistic assumptions, a natural watershed can be simulated using a mathematical model that converts an external driving force (e.g., rainfall) into a corresponding response (e.g., runoff) as a function of the attributes (temperature, soil characteristics, vegetation, evaporation, infiltration, humidity, wind speed, geographic and geomorphological characteristics, etc.) and actual states (water stage, discharge, soil moisture, precipitable water in the atmosphere, etc.) of the underlying system. However, there are various kinds of uncertainties that cause hydrologic models to provide just an approximation of real phenomena. Limited knowledge of system behavior, errors in hydrologic measurements, imperfect mathematical representation of the real system, imperfect knowledge of the real spatial distribution and nonlinear dynamic evolution of state variables and parameters, time variations in the basin's geomorphologic characteristics, etc., are but a few of the most important sources of uncertainty. The selection of governing equations, the numerical schemes used to solve those equations, and the assumptions made determine the model performance under specific conditions. In an attempt to attain more prompt and accurate results, recent high speed, high capacity computers along with distributed data analysis tools like Geographic Information

System (GIS) tools have triggered the development of new hydrologic models that are distinct from traditional hydrologic models. Hydrologic models have evolved according to the advancement of computing environment, understanding of physical system, data availability, etc. Traditional hydrologic modeling environments are typified by,

- lumped model
- lumped geo- and meteorological data set
- ground-based point observation for precipitation
- local scale watershed

In lumped system models, the flow is computed simply as a function of time, at a particular location and the corresponding lumped variables and parameters are assumed to represent averages of the corresponding variable at the basin scale. Therefore, although lumped parameter models are practically useful at small spatial scales, they are of limited utility to describe hydrologic behavior of large-scale watersheds as a result of their inability to fully characterize the spatial variability of hydrologic variables. In addition, because of the highly non-linear character of hydrologic processes, lumped models also exhibit difficulties in their calibration. On the other hand, contemporary hydrologic modeling environments are typified by,

- distributed model
- remotely sensed distributed geo- and meteorological data set
- distributed data visualizing and analysis tools (GIS)
- incorporating climatic forecasting produced by atmospheric model
- full spectrum of spatial scales (local, regional and continental scales)

In a physically based, distributed modeling system, the flow is computed as a function of space and time throughout the system. Models of this type describe the spatial and temporal evolution of the physical system as a function of principles of conservation of mass, energy and momentum. They subdivide the domain into simple interconnected cells, upon which hydrological quantities can be hypothesized homogeneous. The physically based distributed model is more sophisticated and realistic than the lumped model, but actual application presents several challenges and issues, especially if the surface hydrologic model is coupled to, or driven by output from, an atmospheric model. A few of those challenges are:

- How to deal with the incompatibility between the scale of the input variables and parameters, and the scale of solution of the model equations; or between the scale of atmospheric forecasting model and watershed rainfall-runoff model
- Actual availability of distributed data set
- How to link hydrologic model with distributed data set through GIS interface module
- Numerical effectiveness and stability of distributed hydrologic system
- Consistency in precipitation values between ground observation and remotely sensed observation

On the other hand, global climate issues have been the subjects of major scientific inquiry since the late 20th century. In hydrologic research, these include the hydrological impacts of global climatic variability, anomalies or change over the continental, regional, and local watershed scale. In these cases, the primary concern about successful application of hydrologic watershed models is the scale problem that requires determination of the proper scales leading to reliable outputs. A value of a hydrologic quantity or parameter at a given scale represents an average of a spatially variable quantity or parameter at sub-grid scales. Therefore, information about the sub-grid scale variability is lost in the process. The degree to which the variability is reduced depends on the scale of averaging and the inherent heterogeneity of the original field.

Any kind of scale incompatibility between scales requires the reproduction of the dynamic variability at the micro-scale field when a macro-scale pattern is given. Generally, the dynamic evolution of precipitation in terms of its temporal correlation needs to be emphasized when modeling precipitation at large spatial scales, while when modeling precipitation at small spatial scales, it is the spatial cluster formation and self-similarity of precipitation fields that must be emphasized. The spatial scale at which the modeling emphasis switches between large-scale and small-scale behavior must be determined as a function of the statistical characteristics of the particular precipitation field, and must be incorporated in the modeling approach.

The scale problems arise from 2 kinds of scale inconsistencies, i.e., measurement and model inconsistency. First, field measurements cover a point or local scale area, while the application in the model may be at the larger scale of the grid used to represent the hydrologic process. This is especially true in the characterization of the spatial variability of soil properties and precipitation. The downscaling problem of soil properties arises from the limitation of current techniques and data for measuring soil depth and hydraulic properties in addition to soil moisture. Data assimilation techniques have attempted to combine remotely sensed soil moisture data with other relevant information, such as micrometeorological measurements, land cover data, and soil textural maps. However, a detailed description and treatment of this subject is beyond the scope of this research. This research will focus on the scale problem associated with precipitation. Second, Global Climate Models (GCMs) usually produce precipitation fields at grid dimensions of 200-400 km while the proper resolution required by hydrologic model is a few kilometers at most. Therefore, the scale difference between the 2 models has to be resolved for direct model coupling or for simply using the GCM output as input in the hydrologic application.

This thesis will summarize the state-of-the-art in this field and develop an improved precipitation downscaling model (named 'Stochastic space-time random cascade model'). In addition, using the new downscaling model, a methodology for large-scale continuous streamflow simulation will be presented that will allow assessment of the impacts of climate variability and change on hydrologic system response. This will be achieved using a GIS-based distributed hydrologic model that will be driven using downscaled GCM precipitation.

1.2. Objectives

The overarching objectives of the proposed research are:

1. to develop an improved precipitation downscaling algorithm to be used in integrated analysis and assessment of the hydrologic effects of climate variability and change. The downscaling algorithm will be used to downscale GCM precipitation output from the GCM scale to a scale appropriate for use within surface hydrology models in such a way as to reproduce a realistic spatial and temporal distribution of the precipitation field.
2. to carry out an analysis of the hydrologic effects of climate variability and change by driving a distributed hydrologic model using the downscaled GCM precipitation.

These overarching objectives will be achieved by reaching the following specific goals,

- Identify the characteristics of the spatial and temporal variability of precipitation as a function of scale. The analysis will be done using the $2 \times 2km$ daily NEXRAD data set, which is high resolution (micro-scale) radar observation data for precipitation.
- Based on the spatial and temporal dependency and scaling structure of precipitation field, the space-time precipitation downscaling model will be constructed. The

proposed model will have the ability to preserve the stochastic features of the original micro-scale field and reproduce the spatial intermittency, spatial storm cluster formation and statistical self-similarity of the original field.

- Verify the proposed downscaling model. To do this, the macro-scale precipitation field derived from the NEXRAD, rather than GCM precipitation, is used for input to the model. Then the statistical and scaling features of the simulated micro-scale field will be compared to those of the observation.

- Use the new downscaling algorithm to downscale precipitation from the GCM scale to the scale of the hydrologic model. The GCM data used in this research were provided by CCCma (the Canadian Climate Center for Modeling and Analysis). The GCM precipitation is produced at the scale of $3.75 \times 3.75°(\cong 400 \times 400km)$ and, using the downscaling procedure, it is downscaled to a scale of $2 \times 2km$.

- Predict hydrologic watershed response (i.e., streamflows) by driving a distributed continuous rainfall-runoff model using the downscaled GCM precipitation. The rainfall-runoff model used in this study is HEC-HMS developed by U.S. Army Corps of Engineers. The model is a distributed–parameter, raster (square-grid), 2-dimensional, GIS-based model for simulating event-based or continuous hydrologic response of a watershed. The attractive feature of HEC-HMS for this study is its ability to use raster type distributed precipitation.

- Based on the simulation produced by rainfall-runoff model, the hydrologic assessment for the watershed will be performed through hydrologic frequency analysis. Therefore we can predict the behavior of the underlying watershed under specific climate change scenario.

1.3. Organization of the dissertation

Chapter 1 presents an introduction with the problem description and the research objectives. Chapter 2 describes the background of the research subject. It includes the current issues in the pertinent subject area, demands of this research, the literature review, the current status of the related research area, etc.

Chapter 3 presents the theory of the space-time downscaling model for precipitation. Following a brief overview of existing stochastic disaggregation models, random cascade models and spatial and temporal data analysis, a new stochastic space-time random cascade model is introduced. The new model is verified using NEXRAD observation data. Finally, the model is applied to downscale the macro-scale GCM precipitation to simulate micro-scale precipitation fields.

Chapter 4 presents the application of a GIS-based distributed rainfall-runoff model to examine the hydrologic response of a large-scale basin to climate variability and change scenarios obtained from GCM. The characteristics of the study area (the headwaters of South Platte river basin) are briefly described. The GIS pre-process for HEC-HMS is demonstrated. For model calibration, daily streamflow computed using the actual NEXRAD precipitation is compared to the observation at the basin outlet. After calibration, the model computes the streamflows using the downscaled GCM precipitation data set. The change or variability on streamflow regime due to climate change scenario will be assessed.

Chapter 5 gives the final concluding remarks of this thesis including the grand summary and the recommendations for future research.

Chapter 2

2. Background

2.1. Introduction

The Central U.S. is particularly vulnerable to climate variability and change. The prime driver of this vulnerability is the tight coupling that exists between the climate, vegetation cover and land use. This coupling is strongest in the more arid regions where both natural vegetation and rain-fed crops are water-limited and where midcontinental seasonality causes the great majority of precipitation to fall during the growing season. Most GCM results suggest that under scenarios of a warmer global climate, midcontinental regions such as the central and northern Great Plains may suffer from significantly reduced levels of summer soil moisture. These results, however, are from GCMs with relatively poor representations of the land surface-atmosphere interactions. Regional-scale hydrologic modeling which more accurately represents this coupling is essential to assessments of climate impacts in the Central U.S.

2.2. Climate Modeling (GCMs)

Climate variability refers to short-term (generally decadal or less) climate fluctuations, while Climate change refers to long-term or persistent trends (over decades or more) or shifts in climate. Climate variability and climate change are often described and quantified by Global Climate Models (GCMs). GCMs simulate the physical quantities such as wind speeds, air temperature fields, precipitation, ocean currents, evaporation, and soil moisture, etc. A GCM model is composed of coupled, interacting sub-models, including models to describe processes in the atmosphere, the oceans, the land surface, and the biosphere, and to describe their interactions and feedbacks. Each sub-model deals with the redistribution of mass and energy throughout the climate system. Therefore, GCMs solve a complex set of coupled, non-linear differential equations in a four-dimensional space. Because of computational and other restrictions, these equations are solved using numerical methods on a computational grid that is relatively coarse, especially when compared to the scale at which some of the most important climate processes and interactions occur. Typically, computational grids have sizes of the order $200 \times 200km$ (Figure 2.1).

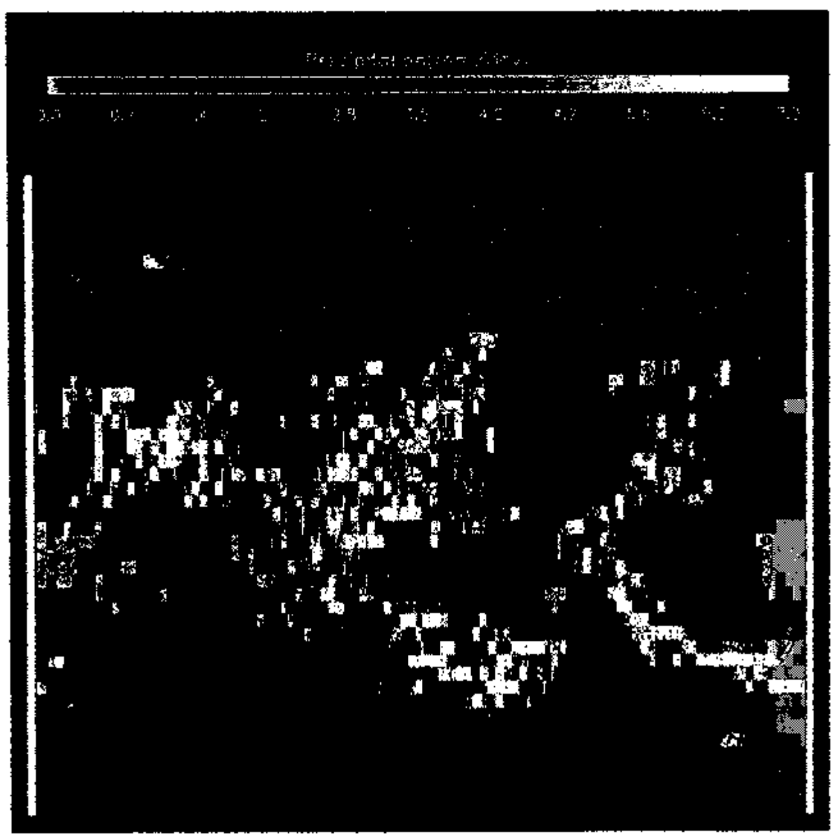

Figure 2-1 A sample GCM precipitation field (CGCM2, 3.75*3.75degree resolution)

The National Assessment report (Gleick, et al. 2000) demonstrates the projected climate variability and change for the United States. It is published by the U.S. Global Change Research

Program and summarizes the current state of the art in climate change science and technology. Around the world, there are more than two dozen groups that are developing models to simulate the climate of the 21st century. These models allow simulations of time-dependent scenarios, based on quantitative relationships, grounded in observational evidence and theoretical understanding. The principal GCMs and their relevant features are summarized in Table 2-1.

Many fundamental processes of hydrological importance, such as those leading to the formation and distribution of clouds and rain-generating storms or those governing soil moisture dynamics, occur on spatial scales smaller than most GCMs are able to resolve. Those phenomena are usually parameterized in rather simplistic ways. Therefore, GCMs are not suitable to simulate and model local variability of climate and hydrological processes. However, GCMs constitute the only tool available to date to predict or forecast quantitatively potential hydrologic regimes under assumed or forthcoming climatic conditions.

Current climate models compute only the vertical balances of energy and water mass at the land surface-atmosphere interface. Thus, at each grid point on the surface, GCMs predict moisture fluxes and changes in water storage (e.g., precipitation, evapotranspiration, soil moisture and groundwater storages.) No lateral redistribution of energy and water mass at the land surface is accounted for by GCMs. Therefore, hydrologic rainfall-runoff models are necessary for redistributing the excess water calculated by GCM on ground surface or predicting available water resources at site of interest.

Model Component or Feature	Canadian Climate Center, Canada (CGCM2)	Hadley Center, United Kingdom (HadCM3)	Max Planck Instiute, Germany (ECHAM4/OPYC3)	Geophysical Fluid Dynamics Lab., USA (GFDL)	National Center for Atmospheric Research (NCAR CSM)
Atmospheric resolution in latitude and longitude	3.75°x3.75° (spectral T32) 10 layers	2.5°x3.75° (grid) 19 layers	2.8°x2.8° (spectral T42) 19 layers	3.75°x2.25° (spectral R30) 14 layers	2.8°x2.8° (spectral T42) 18 layers
Treatment of land surface, evaporation and evapo-transpiration	Modified bucket for soil mosture	Soil layers, plant canopy, and leaf stomatal resistence included	Soil layers, plant canopy, and leaf stomatal resistence included	Simplified bucket for soil moisture	Soil layers, plant canopy, and leaf stomatal resistence included
Includes diurnal cycle	Yes	Yes	Yes	No	Yes
Oceanic resolution in latitude and longitude	1.8°x1.8° 29 layers (based on GFDL MOM1.1)	2.5°x3.75° 20 layers	2.8°x2.8° 9 layers	1.875°x2.25° 18 layers (GFDL MOM1.1)	2.4°x1.2° (variable) 45 layers
Treatment of sea-ice	Thermo-dynamic only	Dynamic and thermo-dynamic	Dynamic and thermo-dynamic	Dynamic and thermo-dynamic	Dynamic and thermo-dynamic
Treatment of atmosphere-ocean coupling	Flux-adjusted	Flux-adjusted	Flux-adjusted	Flux-adjusted	Not Flux-adjusted
Treatment of multiple greenhouse gases	No, CO_2 used as surrogate	No, CO_2 used as surrogate	No, CO_2 used as surrogate	No, CO_2 used as surrogate	Yes
Treatment of sulfate chemistry	Albedo change only	Albedo change only	Albedo change only	Albedo change only	Yes, with reduced sulfur emissions
Equilibrium temperature response of system model to CO_2 doubling	3.5 °C	2.6 °C (4.1 °C for AGCM with simple ocean)	2.6 °C	3.4 °C	2.0 °C

Table 2-1 The summary of characteristics of Global Climate Model

Critical climate variables for water resources assessments include atmospheric temperature, precipitation, evaporation, and soil moisture. Among these, precipitation exhibits a large degree of heterogeneity in space and time. In addition, the physical processes responsible for precipitation are highly non-linear and interact with surface topography, soil moisture and vegetation. These characteristics of precipitation contribute to increasing the degree of uncertainty in GCM prediction. In order to improve the ability of GCMs to predict precipitation, recent atmospheric models are interactively (2-way) coupled with ecological models (e.g., Lu et al., 2001).

The National Assessment report (Gleick, et al. 2000) states that climate models consistently project an increase in global mean precipitation of between 3 and 15% for a temperature increase of 1.5 to $3.5\,^{\circ}C$, but the pattern of changes is likely to vary depending on latitude and geography as storm tracks are altered. On the local pattern of precipitation in the U.S., they demonstrate that there is likely to be an increase in precipitation in the southwestern U.S. as Pacific Ocean temperatures increase, but there is not a clear indication of the trend in southeastern U.S. However, researchers have little confidence in specific regional projections of precipitation because model projections of possible changes in local precipitation are generally mixed over different kinds of models. Therefore, GCM simulations and predictions are recommended by modelers to be used as sensitivity studies or scenarios of possible future climate regimes. And, by using the GCM output to drive a hydrologic watershed model, the same kind of sensitivity analysis can be carried out in the context of water resources at the watershed and local scales. The general process from setting up virtual or future climate conditions to determining scenarios for possible future streamflow regime is illustrated in Figure 2-2.

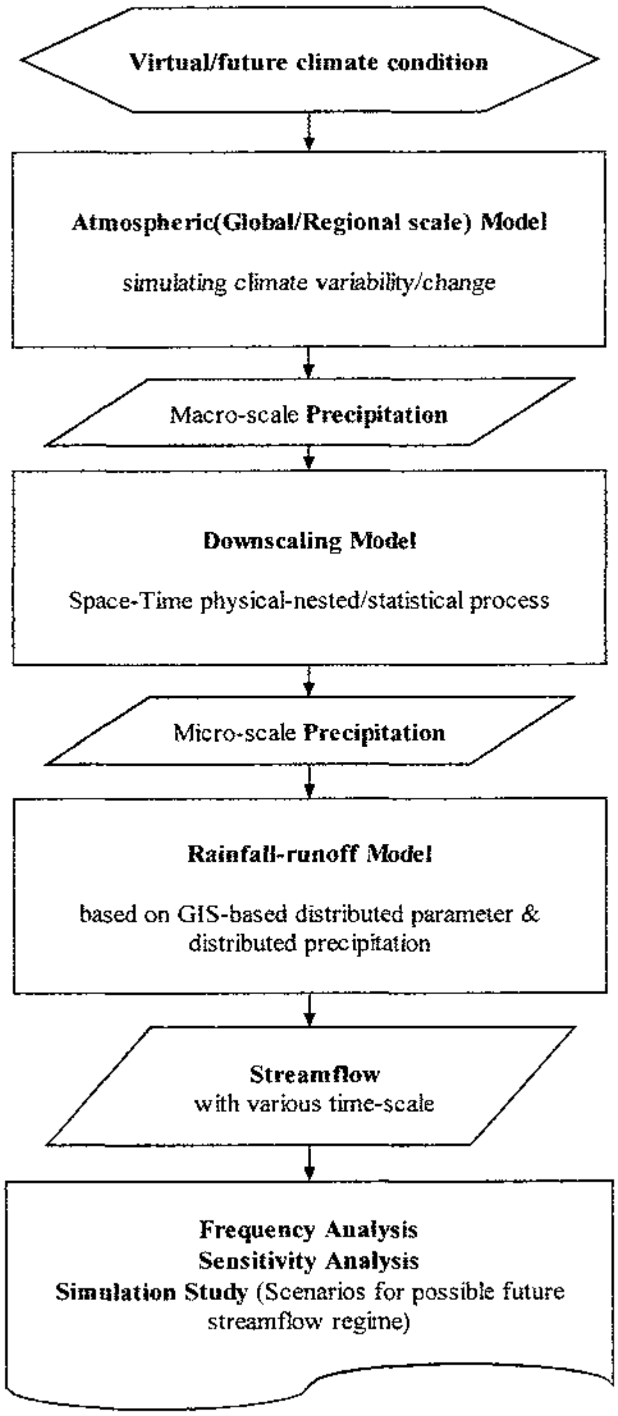

Figure 2-2 The general process of simulating future streamflow regimes

2.3. Watershed Modeling

2.3.1. Watershed Modeling in general

This section presents a brief literature review highlighting the evolution of research on identifying and quantifying the impacts of climate variability and change on streamflow regimes and water resources. First, existing rainfall-runoff models, which constitute the basic tool in watershed analysis, will be introduced, followed by a brief discussion of how the models have been applied to various watershed environments along with the results of climate studies.

Existing rainfall-runoff modeling packages have been developed for specific application purposes. Therefore, watershed models can be classified in various ways. For example, material (reduced scale physical representation of prototype) vs. mathematical models, linear vs. nonlinear models, time-invariant vs. time-variant models, continuous vs. discrete models, analytical vs. numerical models, event-driven vs. continuous process models, and lumped vs. distributed models, etc. Each specific model is associated with an effective range of scales that the model can be used to resolve. The choice of scales depends on the purpose of application, availability of data, geometry of domain, model complexity, accuracy, time and stability of computation, etc.

The temporal dynamics of moisture and their modeling are greatly influenced by the time scale under consideration. System response is closely related to the earth's revolution and rotation. For example, the diurnal pattern of meteorological variables is distinct from the patterns at monthly or seasonal time scales. Spatial scale is another important factor for classifying hydrologic models. Scale (spatial and temporal) is one of the critical factors for proper model selection.

Generally hydrologic models are classified into 3 categories; black box models (BBM), lumped conceptual models (LCM), and physically based distributed models (PDM). BBMs take a systems approach. This type of model focuses on the input-output relationship rather than the physical nature governing system dynamics as defined by the physical laws, the system geometry, the initial and boundary conditions, etc. LCMs, including BBMs, assume the domain as a single homogeneous unit. Thus, the corresponding lumped variables are averaged throughout the spatial domain and all the variables are described as a function of time only. BBM and LCM have been useful for engineering purposes. A few examples include the storage indication method for reservoir routing, the Muskingum method for channel routing, the unit hydrograph method for catchment routing, the rational formula for peak discharge, the index-flood method for determining the magnitude and frequency of peak flows, the Φ–index method for estimation of excess rainfall depth, the Thiessen polygon method for determining the average depth of rainfall, etc. The main advantage of lumped models is their relative simplicity, but they are inadequate when spatial variations of hydrologic components and processes are significant. Therefore, there might be a regional area limit up to which lumped models could be reasonably applied. The rational method, which is used to calculate peak runoff rates in urban storm drainage, has 1.3 to 2.5 km^2 as the upper limit for its applicability (Ponce, 1989). The unit hydrograph method can be confidently applied to watershed areas of $2.5 - 250 km^2$. For watersheds larger than $250 km^2$, overall accuracy is likely to decrease with an increase in watershed area (Ponce, 1989). Example packages of LCMs are the Stanford Watershed Model (SWM), the Sacramento model, the Streamflow Synthesis and Riverflow Regulation (SSARR) model, the HEC-1 model, etc.

PDMs describe system behavior as a function of space and time. The governing equations of PDMs are based on principles of conservation of mass, momentum and energy.

PDMs are often mistakenly called hydraulics routing models. PDMs explicitly account for the spatial and temporal heterogeneity of precipitation, the heterogeneity of the topography, vegetation, soil moisture and soil characteristics. A PDM has to determine the value of each state variable on the continuous space and time domain. The simplest example of a PDM is the kinematic wave model of overland flow. Analytical solutions of the kinematic wave model are often limited to the following conditions. First, the precipitation is assumed to be uniformly distributed in space and time. Second, the storm duration usually exceeds concentration time. Third, the runoff is primarily formed by overland flow and the channel storage processes are negligible. However, the actual hydrologic system is the product of complex climate-watershed interaction with local variations superimposed on considerable global variations of both climate and watershed characteristics and is not easy to be analytically described. Therefore, for practical applications, a PDM has to be discretized over a space-time domain in order to apply a numerical scheme. Numerical solutions can be produced on grid points or pixels on the domain, and the solutions are assumed to be representative or averaged values over finite distances or elements due to their discretization scheme. Thus, most PDMs give rise to lumping or averaging to some extent at the sub-grid scale and the scale at which the lumping of parameters will take place depends on the purpose of the simulation, the level of accuracy, knowledge, skill and experience of the modeler, and financial resources, time and technology available. Distributed models, by their nature, require a vast amount of data and computational resources. However, recently the computational aspects of PDMs have become of lesser importance as a result of advances in high performance computer technology and the development of user-friendly GUI-based software. A more practical limitation on PDMs is the non-availability of distributed hydrologic data. As a result of the advancement of observation techniques, remotely sensed high-resolution digital terrain data, vegetation or soil characteristic data, precipitation and soil moisture data are now available. However, the spatial distribution and dynamic behavior of precipitation and soil moisture among them still represents a scientific challenge at present. Hydrologic examples of this PDM approach are the European Hydrologic Systems (SHE) model, the TOPMODEL, CASC2D, HEC-HMS, etc. A more detailed description and comparison of the above models will be presented in Chapter 4.

2.3.2. Watershed Modeling in conjunction with large-scale climate issues

The development of distributed rainfall runoff process models for large-scale river basins has been the subject of research by hydrologists since the mid-twentieth century. However, assessing the impacts of climate variability and change on hydrologic response and water resources under global climate change conditions has drawn attention of scientists since '90s (e.g., Epstein and Ramirez, 1994; Kite et al. 1994; Miller et al. 1994; Mohseni and Stephan 1998; Olivera et al. 2000; Arora and Boer 2001, etc.). Even though some of the models use distributed precipitation, they are based on limited number of ground observations. Downscaling the GCM precipitation was attained by multi-season, multi-site disaggregation method based on ground observation (Epstein and Ramírez 1994; Kite et al. 1994) or multiple regression based on geographical coordinates and elevation (Yao and Terakawa 1999).

In their work, Epstein and Ramírez (1994) applied daily spatial disaggregation techniques to the downscaling problem for the upper Rio Grande basin in Colorado. Their spatial disaggregation models were used to downscale Canadian Climate Centre GCM temperature and precipitation regimes to site specific locations within the study basin, preserving spatial covariance structures at all spatial scales. They used the Precipitation Runoff Modeling

System (PRMS), a deterministic rainfall runoff model to examine hydrologic sensitivity under the disaggregated climate forcing. Under a doubled CO_2 scenario, an average 3.5 °C in disaggregated GCM temperature and a slight (less than 1.5%) decrease in disaggregated GCM annual precipitation result in significant snowpack accumulation decreases. Peak pack water equivalent decreases as large as 35% are observed. Total annual runoff decreases by an average of 17.7%, increasing during the fall and winter and decreasing in spring and summer. A seasonal shift towards earlier in the year is observed in peak runoff, soil moisture storage and evapotranspiration. Soil moisture increases during winter months and decreases during summer. Evapotranspiration closely follows soil moisture in all seasonal changes.

Kite, et al. (1994) carried out streamflow simulations for the Mackenzie River basin ($1.6\times10^6 km^2$) using the climatological outputs from the CCC GCMII. The operating scales of CCC GCMII were 3.75° and 20 minutes. One GCM pixel covers $72{,}000-92{,}000km^2$ of area which varies depending on latitude. They used simple lumped reservoir parametric (SLURP) distributed watershed model that is similar to the macro-scale water balance model. They subdivided the entire watershed into 5 grouped response units (GRU). Within each GRU, the water balance components of evaporation, overland flow, infiltration and groundwater flow were calculated. The hydrograph at GRU's outlet is obtained considering the travel time between each pixel and basin outlet. Eventually the hydrograph at the main outlet of the basin is calculated from channel routing using non-linear storage function. This model is a distributed model only in the sense that the hydrologic parameters are associated with the distribution of land covers. GCM calculates excess water and soil moisture at the land surface on the basis of the vertical water balance between precipitation, surface evaporation, and the water holding capacity of the soil. In GCMs, the precipitation and surface evaporation are mainly driven by heat and energy dynamics, and tracking lateral, gravity driven flow, like streamflow, is simplified or not considered.

Moseni and Stefan (1998) applied a monthly time-scale simple water budget model to 2 mid-size watersheds, Baptism ($363\,km^2$) and Little Washita ($538\,km^2$) that are located in considerably different climatic zones with different land uses. Baptism watershed is characterized by a cool and humid climate, and by heavily forested areas and by shallow surface soil; while Little Washita watershed is an agricultural watershed with a warm and seasonally dry climate. The water balance components of their model consist of direct runoff, interflow, base flow, snowmelt runoff. In order to make the model flexible for various kinds of climate regimes, they used just 4 calibration parameters: thickness of the uppermost layer of the surface soil, number of rainy days resulting in direct runoff, net radiation and shading factor. Those calibration parameters were spatially lumped over the entire watershed. A 1-month lag between monthly precipitation and baseflow is imposed in the model instead of using accurately routed travel time. Their research shows that for these scales of watersheds, the lumped approach can still produce reasonable monthly runoff simulations.

Yu, et al. (1999) simulated the river basin response to single-storm events by linking HEC-HMS (Hydrologic Modeling System) to the Penn State-NCAR Mesoscale Meteorological Model (MM5) with 3 nested domains. The dynamical downscaling was implemented from a scale of $36\,km$ to a scale of $4\,km$ through triple nesting. Using the distributed precipitation obtained from the dynamical downscaling to drive a distributed watershed model was a notable advance over former methodologies. Their study area is the Upper West Branch of the Susquehana River Basin ($14{,}710\,km^2$). However, their downscaled precipitation shows significant over- or under estimation of the peaks. When considering that the hydrologic model employs a 10-min time step, those differences in temporal evolution of rainfall hyetographs can produce undesirable results in the runoff hydrograph. A similar methodology is employed here, except that the downscaling procedure is based on a random cascade model as opposed to a dynamical model.

Yao and Terakawa (1999) developed a distributed hydrological model. The basin was divided into 1 km-scale squared meshes. The mesh-based precipitation was obtained from gage observations through downscaling using a stepwise regression method. The monthly precipitation is regressed in terms of latitude, longitude, elevation, and the precipitation of the reference location. The monthly regression formula with same coefficients is applied for day of each month with stepwise manner. This downscaling method is straightforward and effective for a watershed that is small enough so that the precipitation of the specific location is highly correlated to that of the reference location. Its main shortcomings are that: a) accuracy decreases as the point of interest moves away from the reference gage station and b) spatial intermittency in the spatial coverage of precipitation cannot be properly simulated. Therefore, the daily runoff in periods of low flow tends to be underestimated.

Generally, in large-scale watersheds, parameters associated with wave celerity and hydraulic geometry, which are required for distributed dynamic routing, cannot be determined easily. Therefore, simple semi-distributed approaches have been preferred instead. In existing large-scale watershed models, the monthly hydrograph is relatively well simulated (e.g., Kite, et al., 1994 and Yao and Terakawa, 1999). Typically, these models use simple interpolation methods (e.g., Thiessen polygons, simple regression, Kriging, etc.) for spatial precipitation description and simulation. For the case of daily runoff, the hydrograph can be fitted to observation through parameter calibration. However, the calibrated parameters cannot always produce accurate hydrograph for precipitation other than what is used for calibration. That is truer for larger-scale watershed models. Runoff tends to be underestimated for uniformly distributed precipitation that does not consider spatial variability. Therefore, as the size of the computational time step decreases, the ability to characterize and account for the spatial variability increases in importance for an accurate simulation of hydrological response.

2.4. Downscaling Issues

One of the major areas of emphasis of this thesis is the development of new downscaling algorithms for precipitation. Downscaling hydrologic variables from macro-scales to micro-scales in space-time has become an important research topic of hydrology (e.g., Wilby and Wigley, 1997), but that subject is rather specific area in the scope of "water behavior in conjunction with climate issues". This section presents only a brief discussion and general background of downscaling. In Chapter 3, a more detailed discussion of space-time precipitation downscaling schemes will be presented.

The most direct and straightforward way of downscaling (in the broad sense) is direct interpolation method. Direct interpolation method is easy to apply and could be effective for smoothly varying fields such as sea level pressure, but not appropriate for highly heterogeneous fields such as precipitation (Cohen and Allsopp 1988). In the narrow sense, downscaling incorporates regional scale variability of the underlying region as well as the heterogeneity and nonlinearity governing the hydrological processes. Downscaling schemes can be classified into 2 general categories; physical process based techniques using nested models and mathematical (or statistical) based techniques using regression, nonlinear dynamics, Markov process or multiplicative random cascades. Wilby and Wigley (1997) classified the downscaling schemes more in detail into 4 categories, namely: regression methods, weather-pattern based approaches, stochastic weather generators, and limited-area modeling. Initially, 'Downscaling' schemes have emerged as a means of interpolating regional scale atmospheric predictor variables (such as a mean sea-level pressure, vorticity, etc.) to station-scale meteorological series (temperature, precipitation, etc.) (e.g., Kim, et al. 1984; Klein 1985; Wigley, et al. 1990, Epstein and Ramirez, 1994). Mostly they use monthly mean and area averages (over $10^5 - 10^6 km^2$) as predictor variables, except for the work of Epstein and Ramírez for which daily values were used. One of the limitations of the regression approach is that it can be useful if a strong relationship between a large-scale parameter and regional climate has been identified. Furthermore, as with many statistical tools, regression approaches could not be used beyond the range of the data used to fit the model. The statistical model is computationally economical but cannot include the local effect explicitly. In contrast, the nested method causes heavy computational burden but can include the local effect. Furthermore, atmospheric processes can be coupled with ecological and hydrological processes. Both methods depend critically on the quality of the large-scale flow field in GCMs. However, the parameters used in physical climate models are often derived from the data obtained in regional experiments, but the resulting approximations are then used everywhere on the globe. Clearly, this procedure yields less reliably simulated local values (von Storch et al. 1993). Marengo et al. (1994) also proposed that improved parameterization of spatially heterogeneous rainfall in each grid box should improve simulations of spatial and temporal variations of evaporation and runoff. However, this approach is still in development and requires not only detailed surface climate data but also high end computer capacity. Meanwhile, the statistical techniques based on multiplicative random cascades have advantages in reproducing the clustering feature, maintaining the statistical characteristics of observed climatic field, the nonlinear dynamics of precipitation field, and have relatively low computational burden.

2.5. Summary

Regional-scale hydrologic modeling which is adequately coupled with output of atmospheric models is essential to assessments of climate impacts in the Central U.S. The use of deterministic, atmospheric, general circulation models to understand climatic variability and potential global climate change under doubled CO_2 forcing has prompted a better understanding of regional and local hydrologic impacts. Because current climate models compute only the vertical balances of energy and water mass at the land surface-atmosphere interface, hydrologic rainfall-runoff models are necessary for laterally redistributing the excess water calculated by GCM on ground surface or predicting available water resources at sites of interest. However, incongruities in model resolutions do not allow for GCM output to be directly used as forcing in the hydrologic models. Therefore, downscaling hydrologic variables from macro-scales to micro-scales in space-time has become an important research topic of hydrology.

Statistical downscaling techniques based on multiplicative random cascades have advantages in reproducing the clustering features, maintaining the statistical characteristics of observed climatic fields, and the nonlinear dynamics of precipitation. Statistically downscaled precipitation fields can be used for sensitivity studies. This thesis will develop a methodology to couple GCM output with large-scale rainfall-runoff model by means of statistical downscaling of GCM precipitation.

Chapter 3

3. Space-time precipitation downscaling

3.1. Introduction

Among all hydrologic variables, precipitation is of paramount importance in the water and energy budgets at the land surface-atmosphere interface and its accurate representation in hydrologic and atmospheric models is critical. Physically, precipitation is the result of intricately interrelated atmospheric components and shows complex spatial and temporal variability. Precipitation phenomena have a wide range of frequency-content features and extreme variability over time scales from a few seconds to years and lengths scales of a few *kms* to several hundred of *kms*. The sensitivity of hydrologic behavior to the variability of the rainfall field is the result of non-linear interactions between the precipitation and the other components of the physical climate system. Understanding, describing and modeling local, regional and global climate and its non-linear interactions with hydrological and biophysical processes are currently some of the most challenging problems in the geosciences. Modeling the space-time structure of precipitation fields is to identify the statistical structure of precipitation variability at a range of space-time scales and to develop precipitation downscaling algorithms and accurate parameterizations of precipitation processes to be used in atmospheric models or coupled atmospheric-hydrologic models. Such modeling is needed in translating the results of a global or climate model down to hydrologic scales through downscaling or through a nested modeling environment. For hydrological applications, high-resolution precipitation fields are required to preserve the statistical characteristics of their variability at all temporal and spatial scales of interest. In particular, the first and second order moments as a function of scale, the second order cross moments across scales, and the intermittency are of great importance and must be preserved.

The precipitation output of meso-scale atmospheric models (e.g., CSU's Regional Atmospheric Modeling System, RAMS) or the available precipitation observations like those from the NEXRAD network are usually at grid sizes that are larger (e.g., $O(10^3 - 10^4 \text{ m})$) than those associated with distributed hydrologic models (e.g., in the order of $10^2 - 10^3$ m). The scales associated with the output from GCMs are even larger (e.g., $O(10^5 \text{ m})$). The land surface system responds to excitations from the atmosphere in the form of precipitation and feeds back moisture into the atmosphere through evapotranspiration. The excitation (e.g., precipitation) and its response (e.g., runoff, latent heat flux) are spatially heterogeneous over a broad range of scales, including sub-grid scales (e.g., $<< O(10^3)$ m). This sub-grid spatial variability has a significant impact on the magnitude and distribution of up-scale, and down-scale land surface fluxes whose interaction is nonlinear. Accounting for this space-time heterogeneity is of paramount importance for hydrologic modeling and for appropriately describing land surface-atmosphere interactions (e.g., Ramírez and Senarath 2000, Ramírez and Finnerty 1996a, 1996b, Pielke and Avissar 1990, Pielke et. al. 1997).

The precipitation field is scale-variant if its space-time behavior depends on the underlying scale and is scale-invariant if its space-time behavior is independent of the underlying scale. Most spatial and temporal behavior of precipitation is scale-variant and the space-time variability of precipitation is a function of storm type, large-scale forcing and physical parameters of the storm environment. However, some scale-invariant feature is embedded in the scale-variant features, i.e., some scale-variant features of the space-time distribution of precipitation field can be expressed in terms of the scale-invariant parameters. If scale-invariant relationships are valid over an objective area, they provide efficient parameterizations over a large range of space-time scales. The scaling-invariant characteristic is especially essential in downscaling algorithms. Another essential aspect is the characterization of the time evolution of the subgrid scale precipitation variability, e.g., at the build-up, maturity and dissipation stage of a storm system of precipitation process. For this task it is particularly useful to connect statistical subgrid scale parameterizations to observables, which can be computed from observed meteorological variables or can be predicted by atmospheric models as the storm evolves. Scaling models explored to date for description of spatial and temporal rainfall include monofractal and multifractal precipitation models (including universal multifractals), generalized scale-invariant multiplicative cascade models and scaling-in-fluctuations models.

Recent advances in the science of climate forecasting models drive hydrologic modelers to incorporate the results of climate simulation models into hydrologic runoff forecasting models. However, because of scale differences between global (or regional) climate models and local hydrologic models, rainfall downscaling is required for coupling these models. In other words, in order to evaluate the local and regional effects of short- and long-term climatic variability, a methodology must be devised to scale down hydroclimatic information from numerical global- and meso-scale atmospheric models or from observations. These methods are alternatively referred to as climate inversion schemes or climate downscaling - disaggregation schemes (e.g. Kim et al. 1984, Wilks 1989, Karl et al. 1990, Lettenmaier and Gan 1990, Wigley et al. 1990, Hay et al. 1992, Epstein and Ramírez 1993, 1994). In a general sense, downscaling schemes can be grouped in two broad categories, *dynamical* and *statistical downscaling* schemes. Wilby and Wigley (1997) classified downscaling schemes in more detail into four categories, namely: regression methods (e.g., Epstein and Ramirez 1994), weather-pattern based approaches, stochastic weather generators, and limited-area modeling.

In *dynamical downscaling* schemes, climate and land-use change scenarios at regional and local scales are developed using sophisticated regional and local atmospheric models, for example, the Regional Atmospheric Modeling System (RAMS) model of Colorado State University (CSU). These models are driven by boundary conditions derived from observations and from the output of larger-scale global atmospheric models. In this way, the atmospheric model acts as a physically-based dynamic interpolator (*e.g.*, physically-based downscaling). In the case of RAMS, it has been coupled to a sophisticated land surface scheme (LEAF-2), to a hydrologic model capable of lateral redistribution of surface water (TOPMODEL), and to a detailed regional ecosystem model (CENTURY). Thus, physical schemes encode multiple, non-linear and complex local and regional interactions and feedbacks, explicitly (e.g., Pielke et. al. 1992; Walko et. al. 2000). However, trying to resolve processes at ever decreasing scales using physically-based models rapidly leads to computational inefficiencies and is limited by poor understanding of physical process behavior at small scales. Other atmospheric models can and have been used for physical downscaling, for example, the NCAR models (e.g., Giorgi and Mearns 1991, Giorgi 1990, etc.) and the Penn State/NCAR mesoscale model, Version 5, (e.g., Dudhia 1993).

In *statistical downscaling* schemes, sub-grid temporal and spatial scale details of climatic variability, in particular precipitation, are obtained by using statistical climate inversion techniques in which the statistical characteristics of the spatial and temporal variability of hydroclimatic fields are preserved as a function of scale. Statistical techniques are commonly based on methods from regression (linear or non-linear) analysis, stochastic processes, nonlinear dynamics, artificial neural networks, Markov processes, multiplicative random cascade models, etc. Each methodology has its unique strengths for reproducing specific statistical features of the fields. Therefore, the process to construct the most efficient combination of methodologies needs to consider the statistical analysis of underlying data set. Generally, modeling using stochastic processes can be useful when a data set shows strong spatial and temporal dependency.

Using the specific tools of scaling analysis, the spatial and temporal distribution of rainfall has been found to exhibit multifractal scaling behavior (Schertzer and Lovejoy, 1987, Gupta and Waymire 1990, Tessier et al., 1993, Carsteanu et al. 1999) since the mid-80's. Schertzer and Lovejoy(1987) first began to explore the theoretical framework of random cascades and multifractal measures to describe the spatial variability of rainfall. The theory of cascades and multifractal measures arose from two distinct sources. The theory of deterministic multifractal measures had its origin in nonlinear dynamical systems, whereas the theory of random multifractal measures was derived from the statistical theory of fully developed turbulent flows governing transfer of energy from some large spatial scale to smaller scales (Kolmogorov, 1962). Multiplicative cascades have been used to generate fractal fields that emulate the scaling exponent spectra observed in rainfall. Multiplicative random cascade model has the advantage of being able to reproduce the scaling (*i.e.*, scale-invariance) features, the clustering, and intermittency that are characteristic of precipitation fields in space and time, while at the same time imposing relatively modest computational burden. The choice of different cascade generators is done according to the scaling spectra that they produce. Notably, models like the "universal multifractals" (Schertzer and Lovejoy, 1987), the β-model (Gupta and Waymire,

1993) or the log-Poisson model (She and Waymire, 1995) were proposed to replace the lognormal model of turbulence (Kolmogorov, 1962). Carsteanu(1997) suggested that introducing dependence among cascade generators based on the "oscillation coefficients" is adequate for temporal rainfall. He also showed the possibility of statistical short-term prediction by analyzing the behavior of rainfall intensity orbits in 2D and 3D pseudo-phase space. One of the significant features of the random cascade model is conservation of the rainfall mass between the cascade levels. Olsson(1998) modeled the temporal small-scale structure of rainfall using a micro-canonical cascade which conserves rainfall mass exactly between successive cascade levels. The previously developed cascade models employed canonical cascades where the mass is on average conserved (Over and Gupta, 1996). Vuruputur (1999) introduced the concept of "dynamic scaling" to construct space-time correlated structure which improved the preservation of the covariance function of the simulated rainfall field. Jothityangkoon (2000) constructed a non-homogeneous random cascade model, which incorporates the spatial gradient of scaling factors.

Another particularly useful tool for looking at a process at different scales in order to study its multiscale structure is the wavelet transform. Wavelet analysis can be especially applied for the situation such that a signal's frequency content changes over time and localization in both frequency and time is needed. Kumar and Foufoula-Georgiou (1993a) proposed a versatile data analysis technique that segregates the large- and small-scale features from the data using wavelet decomposition and a statistical characterization of the small scale features (wavelet coefficients). In applying the above methodology to mid-latitude mesoscale convective storms, Perica and Foufoula-Georgiou (1996) establish the empirical connections between statistical and physical storm characteristics by quantifying relations between the scaling parameters and kinematic and thermodynamic indices of the pre-storm environment. The geophysical application of multifractals and wavelets are summarized by Riedi (1998). Based on an expansion of positive definite wavelets with coefficients belonging to the stochastic cascade, Deidda et al.(1999) developed a multifractal model that is suitable for random generation of synthetic rainfall.

The research reported in this thesis develops a methodology for downscaling of daily precipitation from the spatial scales associated with GCM output to the spatial scales required for hydrologic modeling. In particular, the downscaling procedure will be applied to downscale daily precipitation from a spatial scale of $256 \times 256\,km$ to spatial scale of $2 \times 2\,km$ The verification of the proposed downscaling procedure will be done by inversely disaggregating daily NEXRAD precipitation for the Central U.S. averaged over $256 \times 256\,km$ spatial scale into a $2 \times 2\,km$ scale daily precipitation. The inversely disaggregated precipitation field will be compared to original scale NEXRAD observation. As presented in detail below, the downscaling model will be a composite of a stochastic disaggregation model and an intermittency multiplivative random cascade model. Each of the above components is applied over a specific range of scales. The corresponding scale ranges are non-overlapping and the reference level at which model transition occurs is a function of the correlation structure of the observations, as explained below.

3.2. Data description

The Global Hydrology Resource Center (GHRC) generates $2 \times 2\ km$ daily accumulated precipitation data for the CONtinental United States (CONUS) based upon composites of radar reflectivity data received from WSI (Weather Services International) corporation. The radar reflectivity data provided by WSI is created from the NWS 5 *cm* and 10 *cm* next generation (NEXRAD) radars which are currently operational in the CONUS (*i.e.* WSR-57S, WSR-74C, WSR-88D). The WSI daily radar reflectivity data is in image form with a size of 1887 rows by 3661 columns and has a cell size of $2 \times 2\ km$. Its coverage of the original scan for continental U.S. extends from latitude $20\,N°$ to $53\,N°$ and longitude $130\,W°$ to $60\,W°$. This image has been quality controlled by WSI in real-time before it is received at the GHRC. The current convective Z-R relation used to produce rainfall rates from reflectivity data is taken from Woodley et al. (1975) as equation 3-1.

$$Z = 300R^{1.4} \qquad (3\text{-}1)$$

where Z is reflectivity factor, usually expressed in units of mm^6/m^3 and R is the rainfall rate at the ground expressed in mm/h.

The equation 3-1 is the default WSR-88D convective Z-R relationship which is most accurate during heavy rainfall associated with deep convection. In 1997, the OSF (Operational Support Facility) of NWS (National Weather Service) authorized the use of a Tropical Z-R relationship ($Z = 250R^{1.2}$) developed by Rosenfeld, et al. (1993). The Tropical Z-R relationship should be used to improve PPS (Precipitation Process Subsystem) estimates in tropical convective systems, particularly during land falling hurricanes and tropical storms. The OSF recommends that the Marshall-Palmer relationship ($Z = 200R^{1.6}$), developed by Marshall, et al.

(1955), be used to provide best PPS estimates during general stratiform rainfall events. The best Z-R relationship in cool season stratiform rainfall events depends partly on geographic location. The OSF authorized NEXRAD observation sites to select from two cool season stratiform relationships, $Z = 130R^{2.0}$ for sites east of the continental divide and $Z = 75R^{2.0}$ for sites west of the continental divide (Belville 1999).

The real-time manually quality controlled radar data image is a snapshot received at NASA/MSFC every 15 minutes. This 15-minute radar data comprises 16 levels of reflectivity, every 5 dBZ, beginning at level 1 (0-5 dBZ). The GHRC converts this reflectivity data into a composite daily rainfall total which has the unit of in/day and is eventually organized into 13 classes of rainfall accumulations. The structure of the classification is shown in Table 3-1. As seen in Table 3-1, the value of NEXRAD data is stored as an index which represents a specific range of rainfall values. Therefore, the index-type NEXRAD data is converted to the real-value data by multiplying uniformly distributed random numbers to each rainfall ranges (Table 3-2). Under the specific aggregation (averaging) level, the length of the unit pixel is defined as the "scale". If the dimension of the top scale and the scale of field considered are denoted "l_0" and "l_n", respectively, then the scaling ratio, λ, is defined as l_n / l_0. The scales of aggregation/cascade level are seen in Table 3-3. In this study, the Central U.S. corresponds to the region between latitudes $33.8N°$ to $43.0N°$ and longitudes $105.7W°$ to $95.9W°$ (from east of the Rocky Mountains to the lower Missouri and Arkansas river basins), which comprises the front range of the Rockies and the Central Plains of the U.S. This region corresponds to an area of $1024 \times 1024\ km$, or $512 \times 512\ pixels$.

Class	Rainfall accumulations (inches/day)	Class	Rainfall Accumulations (inches/day)
0	0	7	1.0 – 1.5
1	0 – 0.1	8	1.5 – 2.0
2	0.1 – 0.2	9	2.0 – 3.0
3	0.2 – 0.4	10	3.0 – 4.0
4	0.4 – 0.6	11	4.0 – 5.0
5	0.6 – 0.8	12	> 5.0
6	0.8 – 1.0		

Table 3-1 The NEXRAD RIS8 daily precipitation index structure

Index	Rainfall range [mm/day]	Real value [mm/day]
0	0	0
1	0 – 2.54	$randomu(seed) \times 2.54$
2	2.54 – 5.08	$2.54 + randomu(seed) \times 2.54$
3	5.08 – 10.16	$5.08 + randomu(seed) \times 5.08$
4	10.16 – 15.24	$10.16 + randomu(seed) \times 5.08$
5	15.24 – 20.32	$15.24 + randomu(seed) \times 5.08$
6	20.32 – 25.4	$20.32 + randomu(seed) \times 5.08$
7	25.4 – 38.1	$25.4 + randomu(seed) \times 12.7$
8	38.1 – 50.8	$38.1 + randomu(seed) \times 12.7$
9	50.8 – 76.2	$50.8 + randomu(seed) \times 25.4$
10	76.2 – 101.6	$76.2 + randomu(seed) \times 25.4$
11	101.6 – 127.0	$101.6 + randomu(seed) \times 25.4$
12	> 127.0	$127.0 + randomu(seed) \times 25.4$

*) randomu(seed) : uniformly distributed random number generator

Table 3-2 Data conversion for index-type NEXRAD data *(d) is for disaggregation, **(c) is for random cascade

Aggregation/disaggregation (cascade) level	Scale ($km \times km$)	Scaling ratio, λ	Resolution (pixels in domain)
9/-	1024×1024	2^{0}	1×1
8/-	512×512	2^{-1}	2×2
7/0(d)*	256×256	2^{-2}	4×4
6/1(d)	128×128	2^{-3}	8×8
5/2(d)	64×64	2^{-4}	16×16
4/3(d)	32×32	2^{-5}	32×32
3/1(c)**	16×16	2^{-6}	64×64
2/2(c)	8×8	2^{-7}	128×128
1/3(c)	4×4	2^{-8}	256×256
0/4(c)	2×2	2^{-9}	512×512

Table 3-3 Scales corresponding to aggregation/disaggregation(cascade) levels

3.3. The space-time stochastic random cascade model

3.3.1. Multiscale local fluctuations and correlation structure

The high resolution grid rainfall data provided by observation devices like radar contain considerable statistical information of the underlying characteristics of the spatial and temporal distribution of precipitation and their dependence on spatial and temporal scales. The basic statistics of daily-accumulated precipitation for the region of interest are summarized in Table 3-4 for 1997.

	Mean[mm/day]	Standard deviation [mm/day]	Skewness	Kurtosis
January	0.4007	0.8144	4.2288	27.7202
February	0.7281	1.6141	3.6610	14.9690
March	0.5825	1.4908	4.5283	21.0953
April	0.9885	1.8931	3.3378	11.0510
May	1.1262	2.1597	2.7743	7.4641
June	1.2513	2.3942	2.6719	6.2412
July	1.0091	2.0891	2.8305	8.2071
August	1.1160	2.1511	2.8446	7.4966
September	0.9651	1.8926	3.1989	10.0681
October	0.8030	1.7761	3.6308	12.9215
November	0.5349	1.2211	4.6302	23.8617
December	0.5495	1.3289	3.9488	17.8667

Table 3-4 The basic statistics of NEXRAD precipitation in 1997

The mean and standard deviation are lowest in winter season and highest in summer season. The precipitation field is more positively skewed during winter than during the summer season. The kurtosis, which is a measure of peakedness, also is relatively higher during winter than during summer. These trends in skewness and kurtosis indicate that, during the winter season, storms are characterized by low intensities and correspondingly low gradients spread over large areas (*i.e.*, stratiform precipitation). On the other hand, during the summer season, storms are characterized by high intensities, correspondingly high intensity gradients, spread over relatively small areas (*i.e.*, precipitation of convective nature). Figure 3-1 shows typical scans of NEXRAD precipitation for winter and summer season.

Each radar precipitation field used for this study is composed of 512×512 pixels of high-resolution data ($2 \times 2\ km$). By averaging 4 consecutive non-overlapping pixels of the field (branching number = 4), we can obtain a series of precipitation fields spanning the whole range of scales (from $2 \times 2\ km$ to $256 \times 256\ km$). Each precipitation field is assumed to have relative relationships between the large-scale "local" forcing, r_0, (precipitation value in the pixel at the immediately higher scale) and the small-scale fluctuation, r_{0i}, associated with the large-scale "local" forcing. The distribution of ${}^{r_{0i}}\!/_{r_0}$ is shown in Figure 3-2 for June, July, and August. The global maximum standard deviation of ${}^{r_{0i}}\!/_{r_0}$ is 2 which occurs when r_{0i} is 0, 0, 0,and 4, and the local standard deviation of ${}^{r_{0i}}\!/_{r_0}$ corresponding to specific background rainfall (r_0) forms an envelope curve which exponentially decreases as r_0 increases (Figure 3-2).

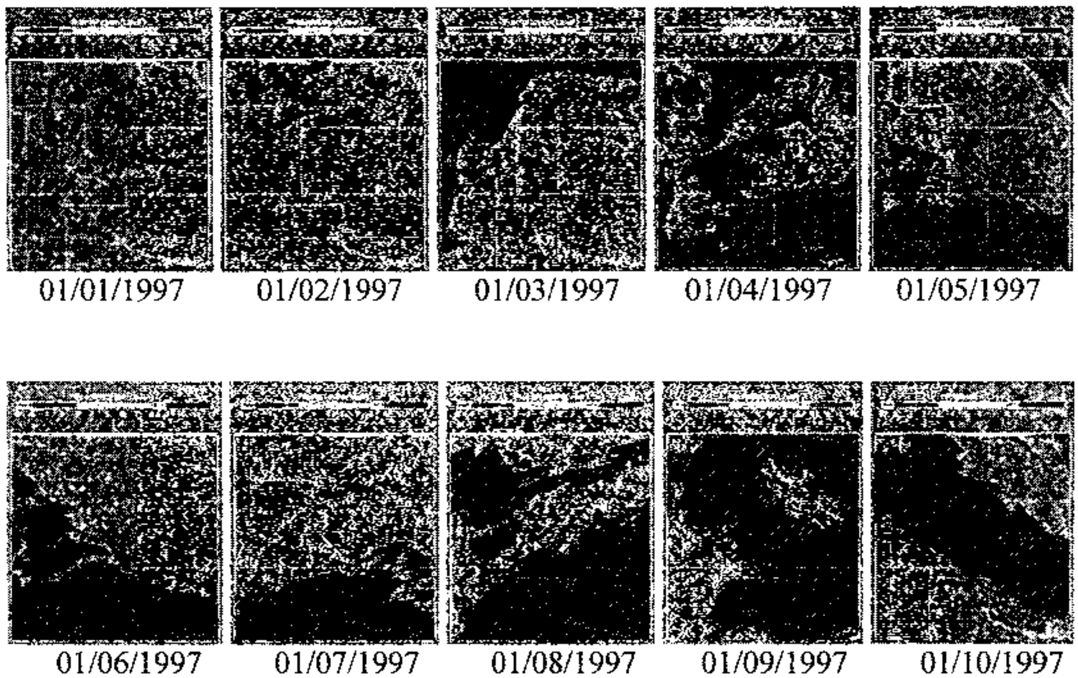

(a) Sample precipitation fields in winter season

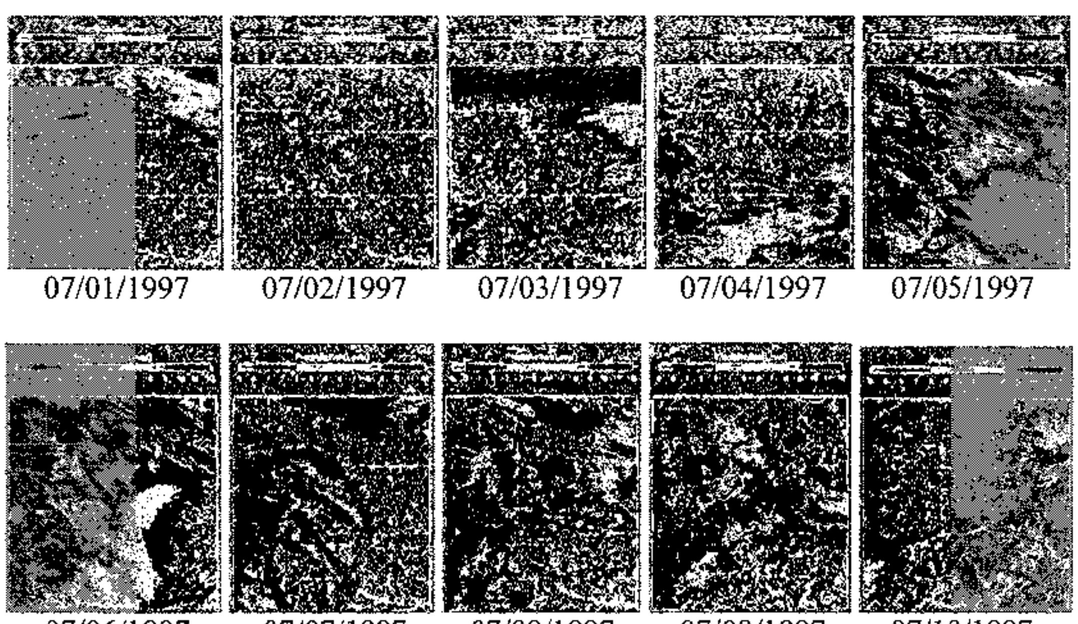

(b) Sample precipitation fields in summer season

Figure 3-1 NEXRAD precipitation fields of winter and summer season

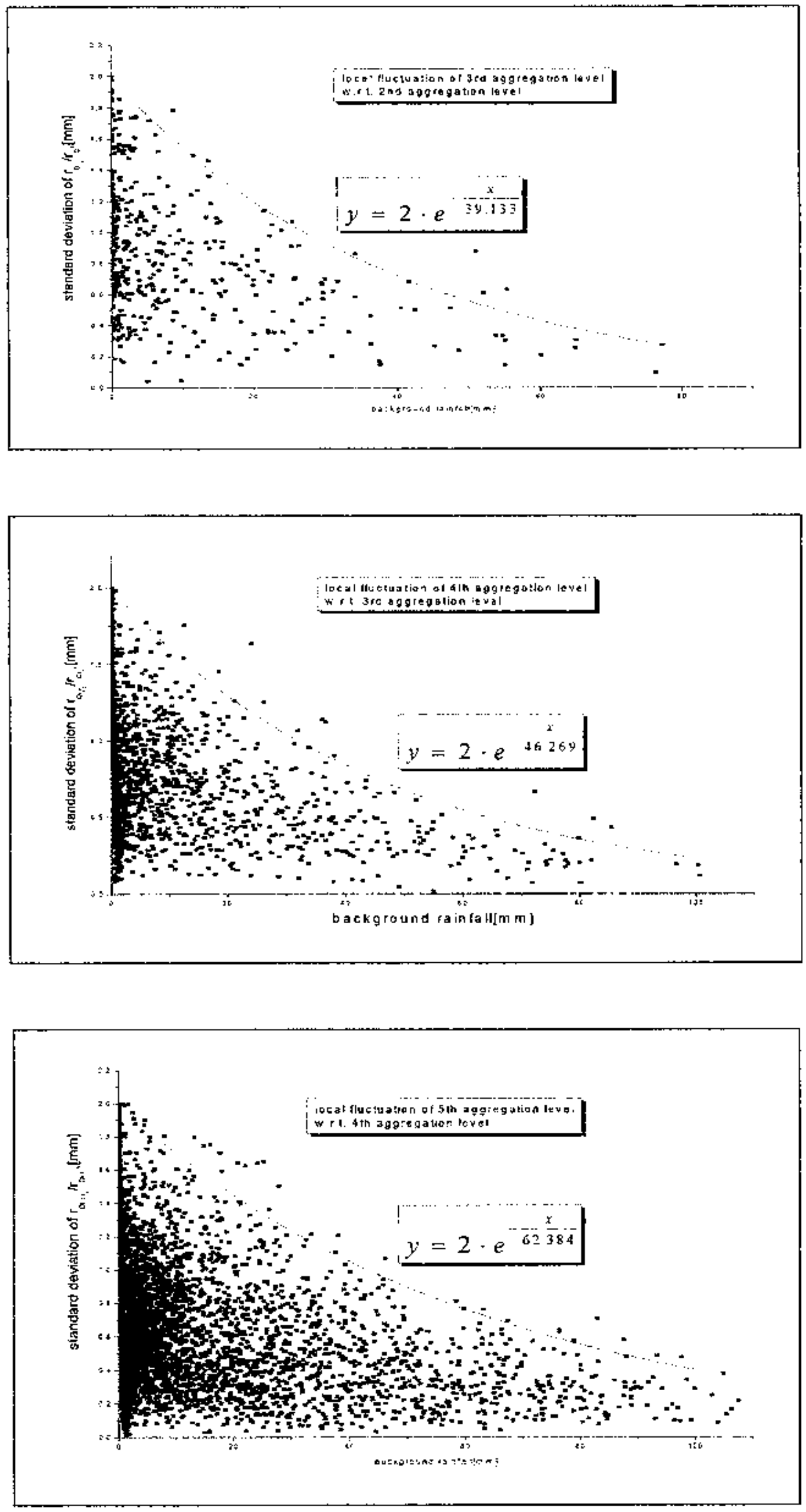

(a) June

Figure 3-2 Distribution of local fluctuation

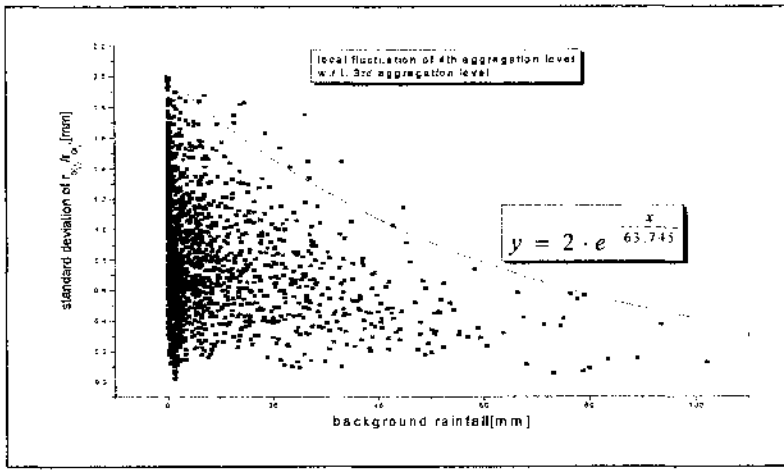

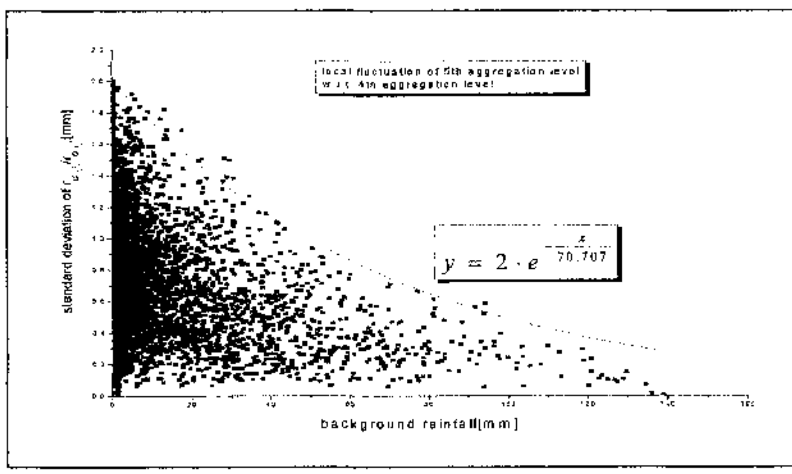

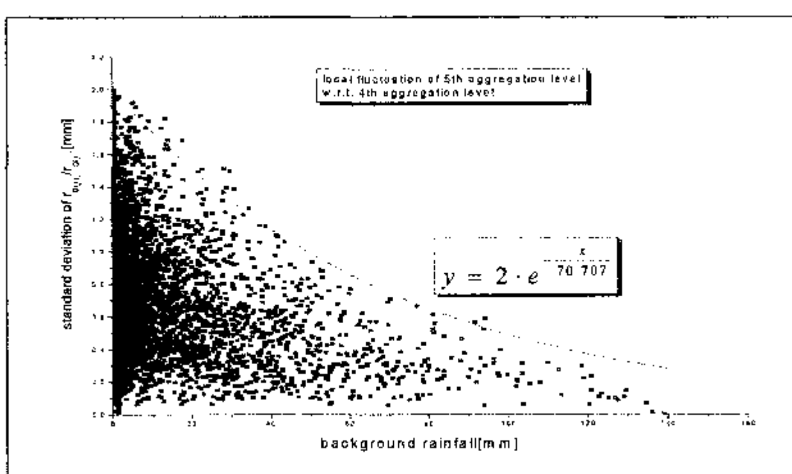

(b) July

Figure 3-2 Distribution of local fluctuation (cont'd)

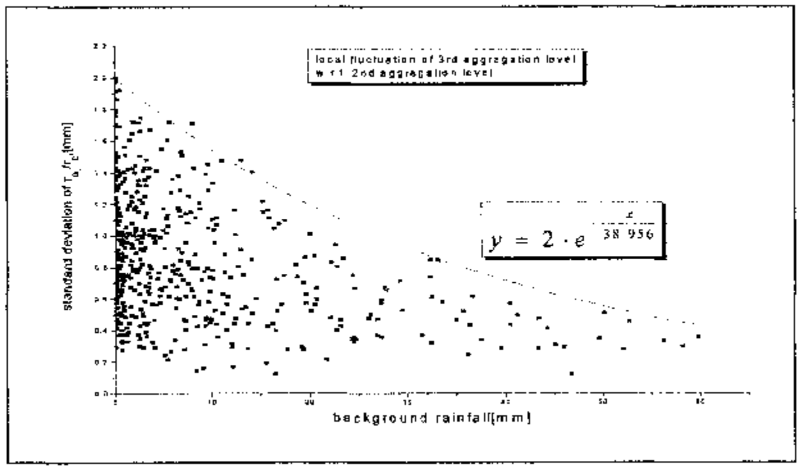

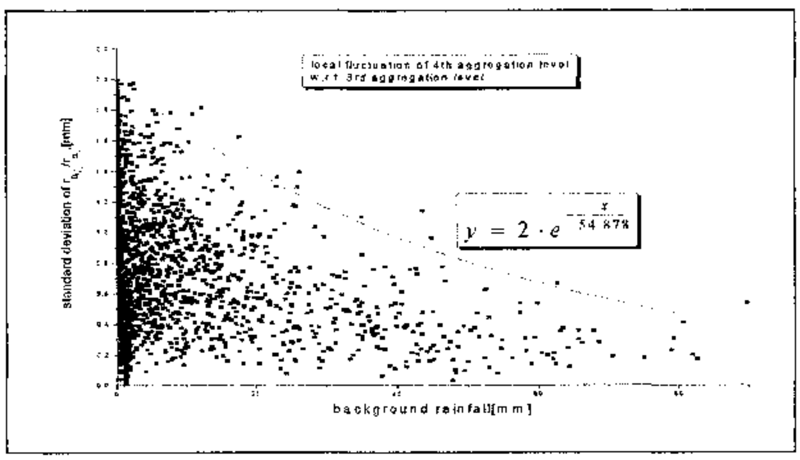

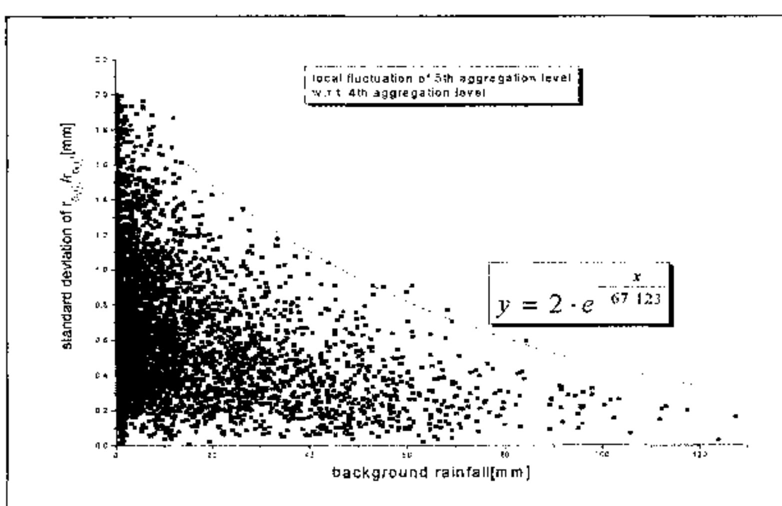

(c) August

Figure 3-2 Distribution of local fluctuation (cont'd)

A sample radar rainfall is plotted on different scales in Figure 3-3. Kumar and Foufoula-Georgiou (1993a) pointed out that small-scale fluctuations (high frequencies and short wave length) exhibit self-similarity. However, at large scales, this behavior breaks down to accommodate the effects of external factors affecting the particular rain-producing mechanism. That is, in the small-scale field, fluctuations are dominated by the small-scale turbulent behavior whereas, in the large-scale field, fluctuations are largely affected by the climatic forcing. Kumar and Foufoula- Georgiou (1993b) tried to segregate large- and small-scale features and identify and estimate the nature of self-similarity in the small-scale features (fluctuations). Unlike the large-scale forcing, the self-similarity that can be found in the small-scale fluctuations is independent of the scale of description of the process. As the grid-scale of the domain of analysis grows, the description of the distribution of variability must rely increasingly on the governing physical process.

The self-similarity that characterizes the distribution of small-scale fluctuations breaks down at a certain scale. Kumar and Foufoula-Georgiou (1993b) suggest that if self-similarity is found to be present in the small scale fluctuations, the upper limit scale over which this behavior holds must be determined, that is, the maximum scale above which physical or other non-scaling stochastic descriptions apply should be established. The idea is that the large-scale features represent the large-scale forcing specific to the particular physical rain producing mechanisms and are scale dependent, whereas when this effect is subtracted the resulting deviations might exhibit properties associated with turbulence (in terms of physics) or scale invariant self-similarity characteristics (in terms of mathematics.) Their experiment shows that the squall line rainfall fluctuations exhibited self-similar characteristics up to a spatial scale of *25-30 km*, based on 1-hour or 10-minutes temporal integration scale.

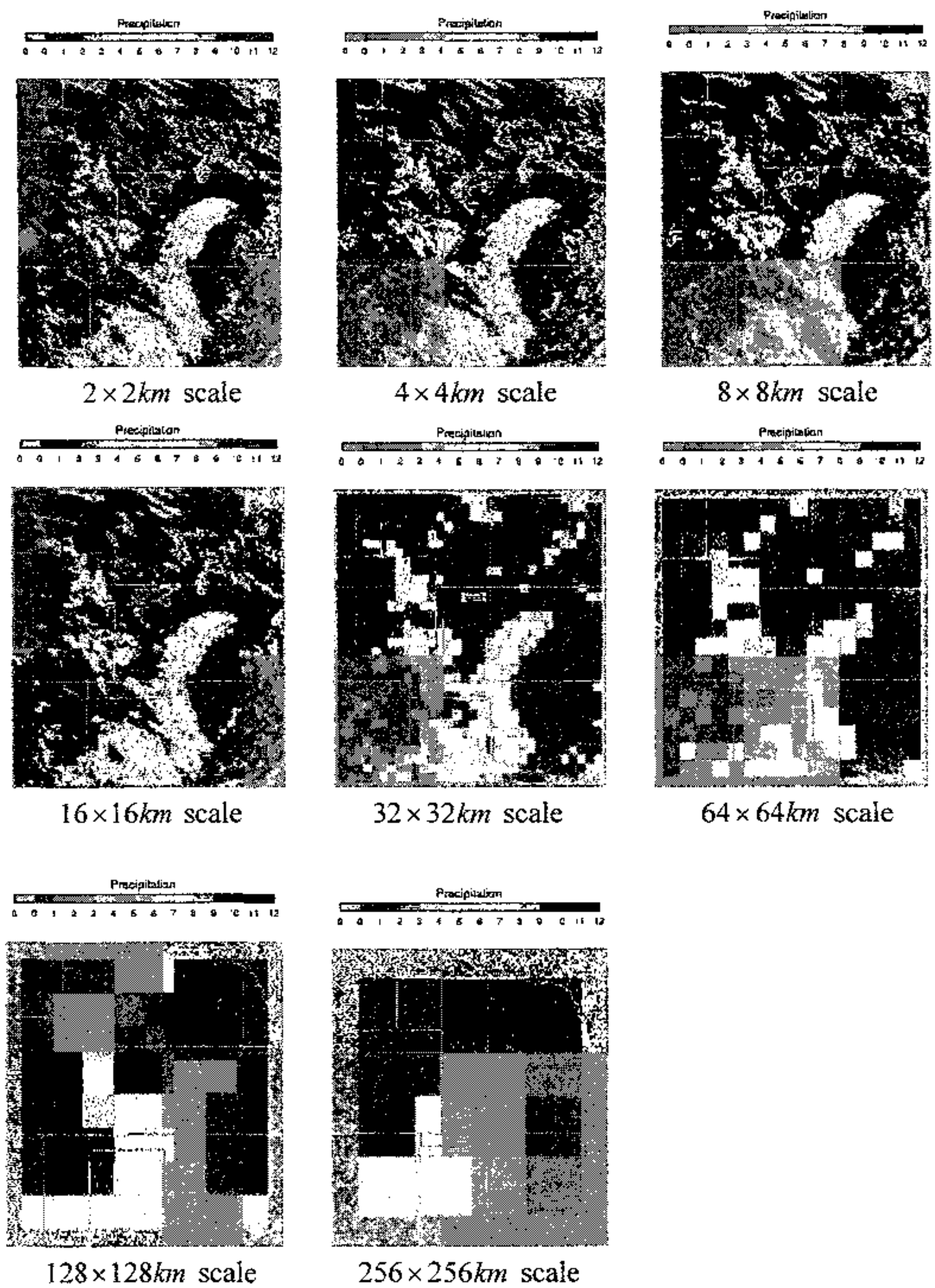

Figure 3-3 NEXRAD observation plotted on different scales (07/06/1997)

Because the random cascade downscaling model takes multiple stages from the highest scale down to the lowest scale, the statistical behavior along the intermediate aggregation levels is very important. In grid precipitation field, it is difficult to examine stochastic features of individual pixels in the entire domain. Therefore, we need to extract ensemble characteristics of the field. *Ensemble characteristic* or *ensemble moment* is a relative concept to *temporal moment*. If one is trying to calculate the temporal average, one would need to calculate the temporal evolution of the quantity. The small-scale spatial distribution (*e.g.*, rainy and non-rainy portion of entire domain and the actual amount of rainfall at a specific pixel in the rainy portion) of grid precipitation is analogous to the Brownian motion of a pollen particle (*e.g.*, the portion associated with the trajectory of the pollen and the actual amount of velocity of the motion of pollen at a specific pixel in the trajectory portion). For the case of Brownian motion of a pollen particle in a fluid, one would need to calculate the motion of all particles within that fluid, because the motions of all these particles are coupled. It is a practically impossible task. Therefore, we need to consider an "ensemble" of "macroscopically identical" systems. "Macroscopically identical" means that all macroscopic variables, such as composition, mass, pressure, and temperature, etc, are identically distributed. Let us now assume that for each (say i^{th}) system of the "macroscopically identical" systems, a researcher measures the quantity $q_i(t; s)$ of a particle, where t and s represent time and space, respectively. With the set of these values, one can calculate the following average value

$$\left\langle q_i^{\,j}(t;s)\right\rangle = \frac{1}{N}\sum_{i=1}^{N} q_i^{\,j}(t;s) \tag{3-2}$$

which is called the ensemble average (for $j=1$) or ensemble moments (for $j=1,2,\ldots$).

It is obvious that this ensemble average is, even for a stationary process, not identical to the time average. The time average is a value obtained from measurements of one particle, whereas the ensemble average values are measured on different particles in different systems. The assumption that these two averages are equal is valid in the theory of systems with an extremely large number of particles. If the two averages are actually equal, one calls the respective stochastic process "ergodic". However, in general, it is not possible to prove the ergodicity for a real physical process. There exists no real proof that for a Brownian particle the two averages are identical. Therefore, one usually assumes ergodicity if there is no hint of "non-ergodic" behavior. It is in many cases possible to make statements about stochastic processes on the basis of plausibility considerations. Whether these statements are actually true or not can usually not be proven within the framework of the theory. It is, therefore, necessary to compare theoretical and experimental results. The most desirable quantities to measure are the probability densities. However, the simplest probability density, which tells something about temporal behavior, is the joint probability of second order (1st and 2nd moment). This is already a function of 3 variables: the 2 stochastic variables and time. Therefore, a correlation function, which depends only on space or time, is useful for tracking the spatial or temporal behavior of a stochastic variable. If we consider an example stationary stochastic process *q(t;s)*, then

$$R_s(\tau) = \frac{\langle q(t;s)q(t+\tau;s)\rangle}{\langle q(t;s)q(t;s)\rangle} \leq 1 \text{ (for stationary process)} \qquad (3\text{-}3)$$

is called the temporal correlation function of the quantity q. and, for a given spatial location s, it is a function only of the lag time τ. Likewise, for a given time, we consider the spatial correlation function of the quantity *q(t;s)* at time t and spatial location s, as follows;

$$R_t(\delta) = \frac{\langle q(t;s)q(t;s+\delta)\rangle}{\langle q(t;s)q(t;s)\rangle} \leq 1 \qquad (3\text{-}4)$$

which for spatially homogeneous fields is only a function of the spatial lag distance δ. The spatial correlograms for July of 1997 from $2\times 2km$ scale to $64\times 64km$ are plotted in Figure 3-4. Each plot in Figure 3-4 contains 9 lines associated with days Jul. 1 - 10, 1997; (Jul. 2 is discarded because of low rainfall) in the beginning of July 1997. In computing correlations the "distance" in grid precipitation is defined between the centers of pixels under consideration. Rather than a point measurement, the pixel value is assumed to be the average value over a pixel. Therefore, the spatial correlation of the grid precipitation field is generally greater than that of point precipitation measurements. For the pixels of the same distance apart, a larger scale precipitation field shows higher spatial correlation. For example, the spatial correlation of the rainfall 1-pixel apart at the $16\times 16km$ scale field tends to be lower than that of the rainfalls 8-pixels apart in $2\times 2km$ scale field. Within a precipitation field of the same scale, the spatial correlation values differ by as much as 50-60% depending on the specific date, indicating that the spatial correlation is related to the larger-scale atmospheric forcing. Figure 3-5 illustrates the lag-1 spatial correlation (Δx = 1 pixel) as a function of aggregation levels for Jul. 1 - 10, 1997 (Jul. 2 is ruled out because of low rainfall). The spatial correlation for the precipitation field lies above 0.85 for $2\times 2\,km$ and $4\times 4\,km$ scale and decreases as a function of scale. However, the lag-1 ($\Delta t = 1day$) temporal correlation is negligible until $64\times 64km$ scale and increases as scale increases from $128\times 128km$ scale (Figure 3-6). The parameter estimation with respect to spatial and temporal dependency structure will be discussed in Chapter 4.

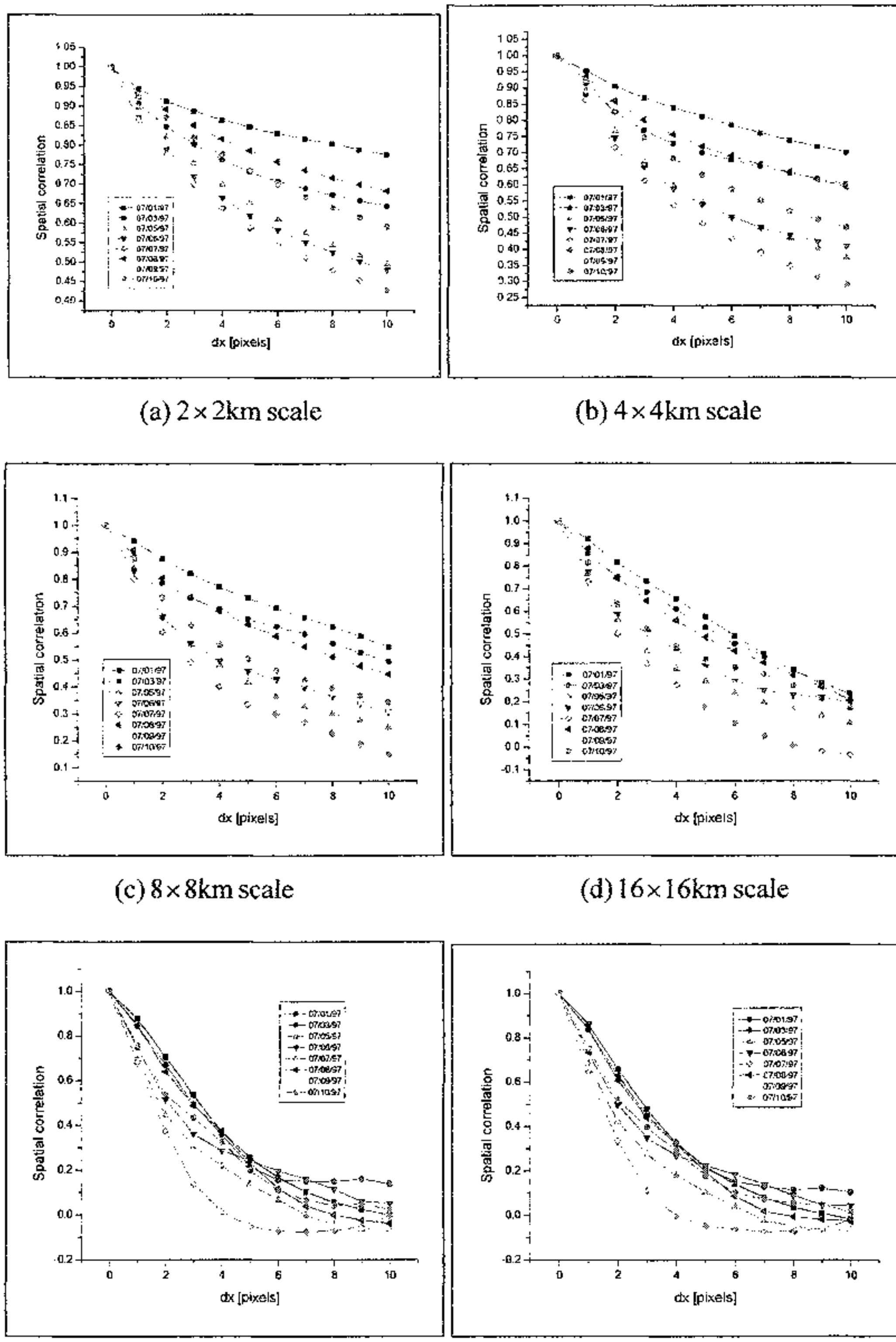

(a) 2×2km scale

(b) 4×4km scale

(c) 8×8km scale

(d) 16×16km scale

(e) 32×32km scale

(f) 64×64km scale

Figure 3-4 Spatial correlogram for the precipitation fields at different scales

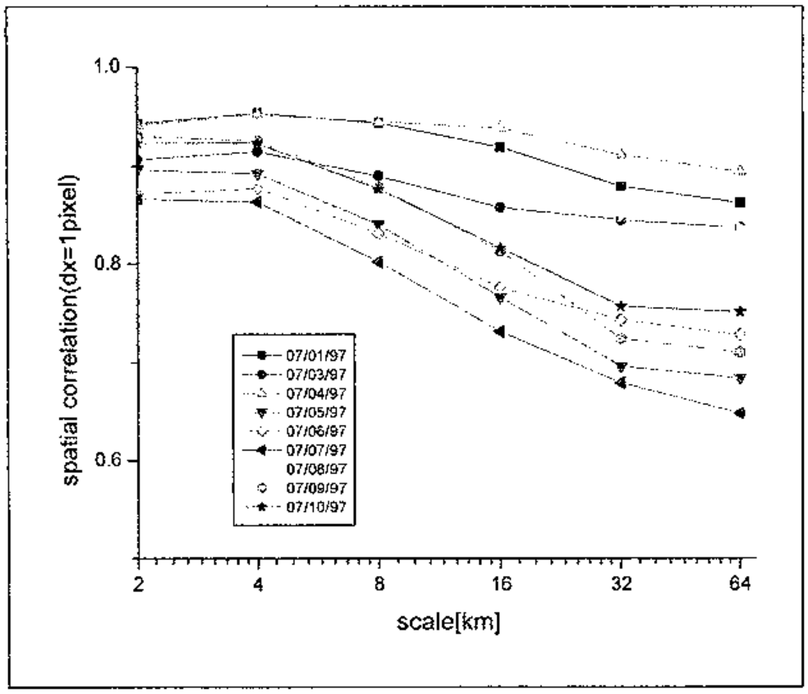

Figure 3-5 Lag-1 Spatial correlation with respect to scales (*dx=1pixel*)

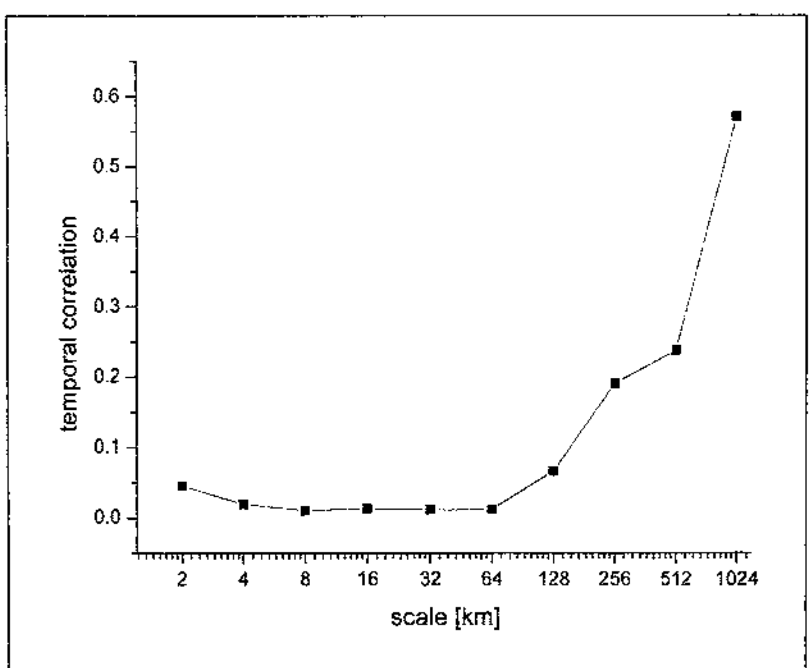

Figure 3-6 Lag-1 Temporal correlation with respect to scales (*dt=1day*)

3.3.2. Scaling features

Self-similarity or scale invariance is a kind of symmetry observed in nature. The simplest form of this symmetry in a statistical context is referred to as simple scaling (*i.e., monofractal)* of the probability distributions. Letting *R(·)* be the rainfall intensity field, this property is expressed as,

$$R(\lambda A) \overset{dist}{=} \lambda^{-\theta} R(A) \tag{3-5}$$

where the equation indicates that the probability density function of the rescaled variable *R(λA)* is equal to that of the original variable *R(A)* except for a factor that is a function of the length scale ratio λ and scaling exponent θ. The scaling exponent θ is the key parameter that characterizes the scaling features of the underlying field. If a measurement has the following mathematical features, the structure of the field is regarded to as a *monofractal.*

1. log-log linearity between statistical moments of order q and length scale λ. That is :

$$\left\langle R_\lambda{}^q \right\rangle = \lambda^{-\theta \cdot q} \left\langle R_0{}^q \right\rangle$$

or equivalently,

$$\log\left\langle R_\lambda{}^q \right\rangle = -(\theta \cdot q) \cdot \log \lambda + \log\left\langle R_0{}^q \right\rangle \tag{3-6}$$

2. a linear change in θ as a function of the moment order q,

$$\frac{d(\theta \cdot q)}{dq} = \theta = aq + c \tag{3-7}$$

The scaling scheme associated with the monofractal is said to be the *simple scaling*. Simple scaling is associated with additive (linear) processes and unique scaling exponents Θ are related to unique fractal dimensions. For example, Figure 3-7 is the plot of ensemble moments of precipitation fields as a function of scale. The data set used for the plot is the NEXRAD rainfall scan of July 1–10 (July 2 is ruled out because of low rainfall), 1997 for the central United States. They show that the NEXRAD precipitation data exhibit linearity between ensemble moments and spatial scales for small-scale fields (less than *32 km* scale), but the linearity breaks down at larger-scale (larger than *64 km* scale). The scaling characteristics of the field below the *32 km* scale are plotted in Figure 3-8. Figure 3-8 is the plot of $\Theta(q)$, the slope of the ensemble moments *vs.* scale function, plotted as a function of the moment order. The linearity of the $\Theta(q)$ indicates that the spatial distribution of daily NEXRAD shows monofractal features (Equation 3-7). In this data set, the theta curve is independent of large-scale forcing.

In hydrologic data fields, it is often found that property (1) holds but the slope function $\frac{d}{dq}\Theta(q)$ in (2) is nonlinear; (*e.g.* Gupta and Waymire 1990, Meng, Ramírez, Salas and Ahuja 1996). This precise structure is called *multifractal*, which requires *multiple scaling*, and has been observed in the spatial variability of rainfall intensities (e.g., Tessier, Lovejoy, and Schertzer 1993, Over 1995), soil moisture (Rodríguez-Iturbe et al. 1995), drainage network slopes (Molnár and Ramírez, 1998), and steady-state and transient infiltration rates (*e.g.*, Meng, Ramírez, Salas and Ahuja, 1996).

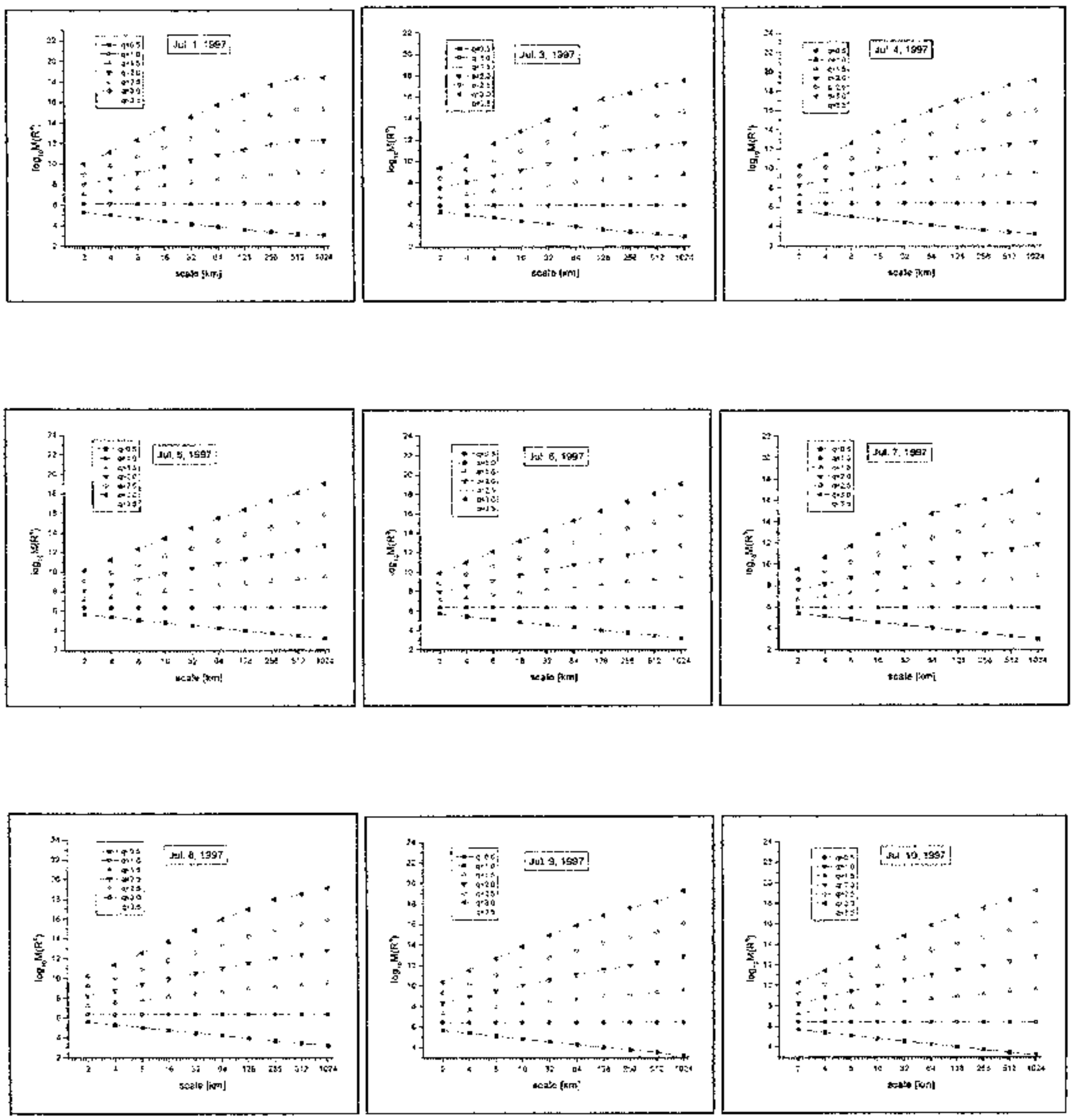

Figure 3-7 The ensemble moments vs. scales

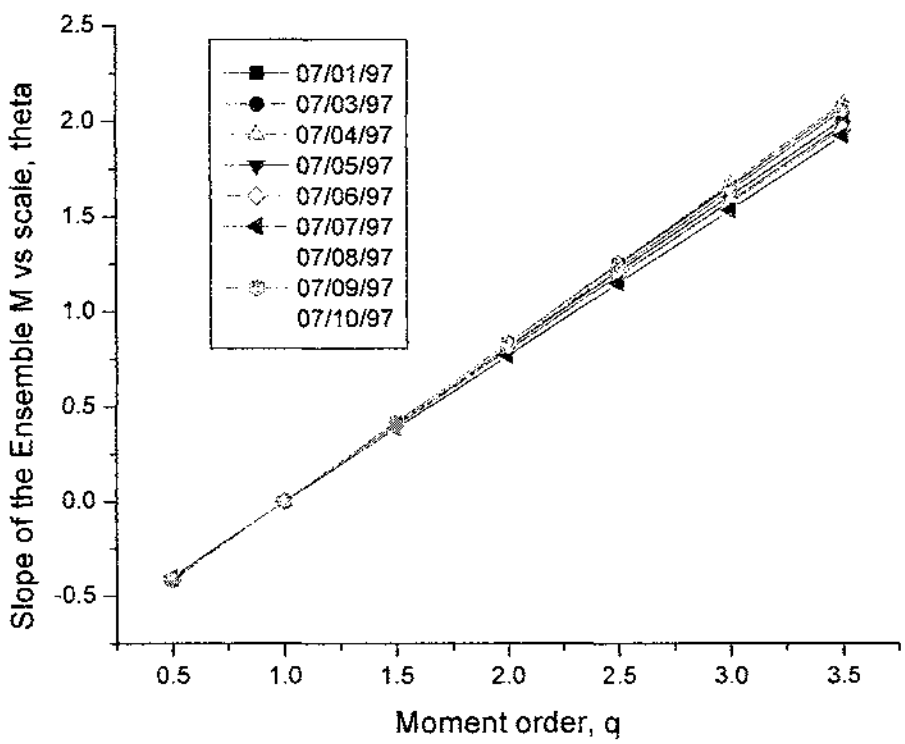

Figure 3-8 Slope Function of the Ensemble Moments of the daily NEXRAD (July 1-10, 1997)

The scaling characteristics of rainfall fields in space and time have been extensively studied. However, most studies have examined the spatial structure separately from the temporal structure. Multifractal structure of the scaling exponents has been found in the spatial distribution of rainfall (Schertzer and Lovejoy 1987, Gupta and Waymire 1990, Tessier et al. 1993); in addition, scale-invariant behavior of the temporal distribution of rainfall has also been found thereafter (e.g., Carsteanu et al. 1999).

3.3.3. The synoptic structure of large-scale precipitation

In sections 3.3.1 and 3.3.2, the spatial and temporal dependence as well as the scaling characteristics were studied for the entire domain. Now, we can do the same analysis for only the rainy portion of the domain. As mentioned, Figure 3-4 implies that the spatial correlation depends on the large-scale forcing. The spatial correlation can be examined for the large-scale forcing, but only for the rainy portion of the field (Figure 3-9 and Table 3-5). The model proposed in later sections will preserve the spatial correlation of the field between 32 *km*- and 128 *km*-scale by means of a stochastic model, whereas the spatial correlation of the field for scales less than 32 *km* will be reproduced through the random cascade model. The temporal correlation for the rainy portion of the domain is shown in Figure 3-10 and Table 3-5. Unlike Figure 3-6, the temporal dependency begins to be significant above 32 *km*-scale. The scaling analysis in section 3.3.2 demonstrated that a monofractal structure is well defined for the small-scale field less than 32 *km*-scale. These results motivate the composite modeling approach porposed in reference to the 32 *km*-scale. Therefore, we construct a Stochastic Space-Time Disaggregation Model (SSTDM) and propose it to describe the process above 32 *km*-scale in order to preserve the spatial and temporal dependency characteristics. At the same time, we construct and apply an Intermittency Random Cascade Model (IRCM) to incorporate the statistical self-similarity, spatial intermittency, and the spatial storm cluster formation. The model structure is illustrated in Figure 3-11.

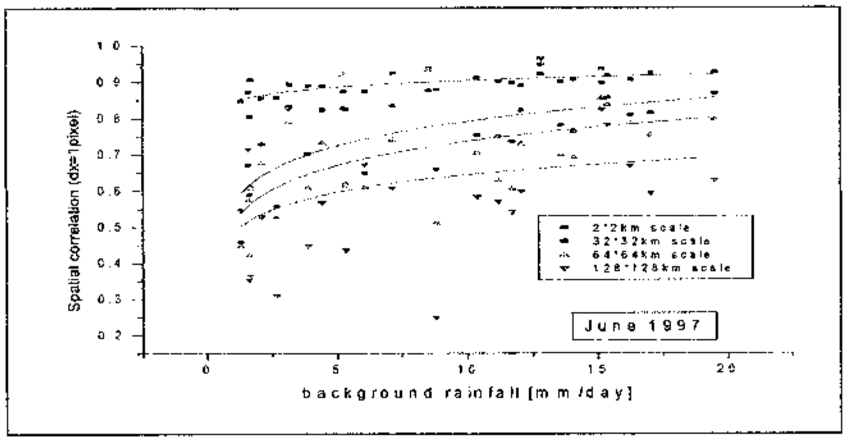

(a) June 1997

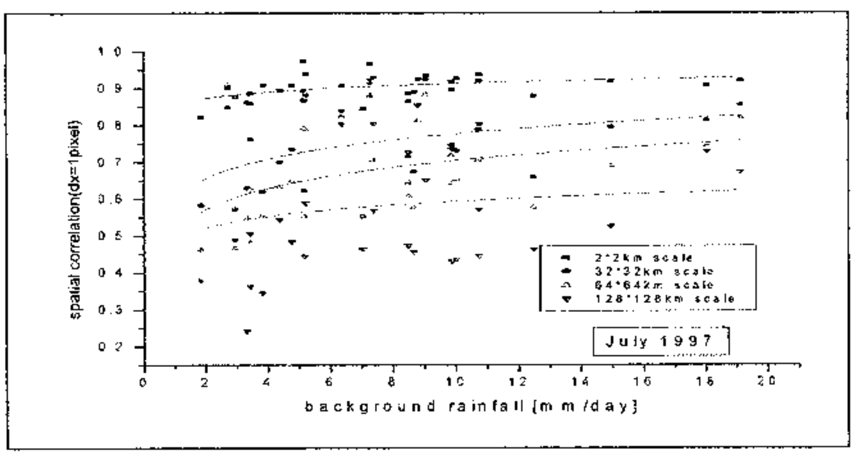

(b) July 1997

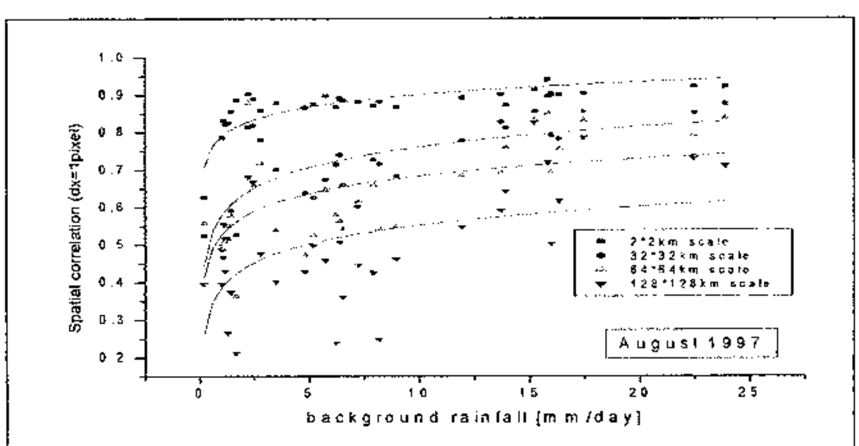

(c) August 1997

Figure 3-9 Lag-1 spatial correlation of the rainy portion of domain

Disaggregation level /scale	Regression formula
1^{st} level $128 \times 128km$	$y = 0.0696\ln(x) + 0.48421$
2^{nd} level $64 \times 64km$	$y = 0.09641\ln(x) + 0.51509$
3^{rd} level $32 \times 32km$	$y = 0.09676\ln(x) + 0.56881$

(a) June 1997

Disaggregation level /scale	Regression formula
1^{st} level $128 \times 128km$	$y = 0.04448\ln(x) + 0.49082$
2^{nd} level $64 \times 64km$	$y = 0.08249\ln(x) + 0.51422$
3^{rd} level $32 \times 32km$	$y = 0.07487\ln(x) + 0.60471$

(b) July 1997

Disaggregation level /scale	Regression formula
1^{st} level $128 \times 128km$	$y = 0.07214\ln(x) + 0.38616$
2^{nd} level $64 \times 64km$	$y = 0.06744\ln(x) + 0.52815$
3^{rd} level $32 \times 32km$	$y = 0.07867\ln(x) + 0.57986$

(c) August 1997

Table 3-5 Regression formulas for Lag-1 spatial correlation within the rainy portion of domain

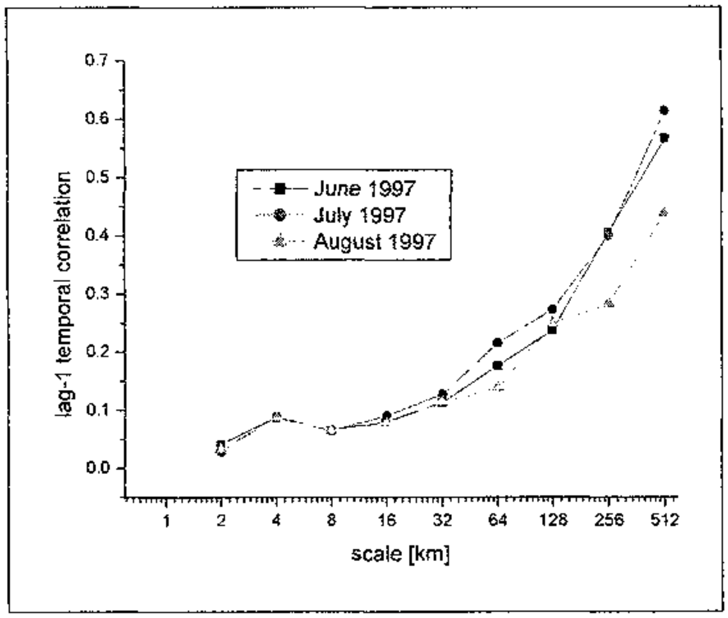

Figure 3-10 Lag-1 temporal correlation for log-transformed rainfall

Disaggregation level	Lag-1 temporal correlation		
	June	July	August
1	0.2372	0.2727	0.2494
2	0.1763	0.2156	0.1383
3	0.1136	0.1275	0.1141

Table 3-6 Lag-1 Temporal correlation for Log-transformed rainfall

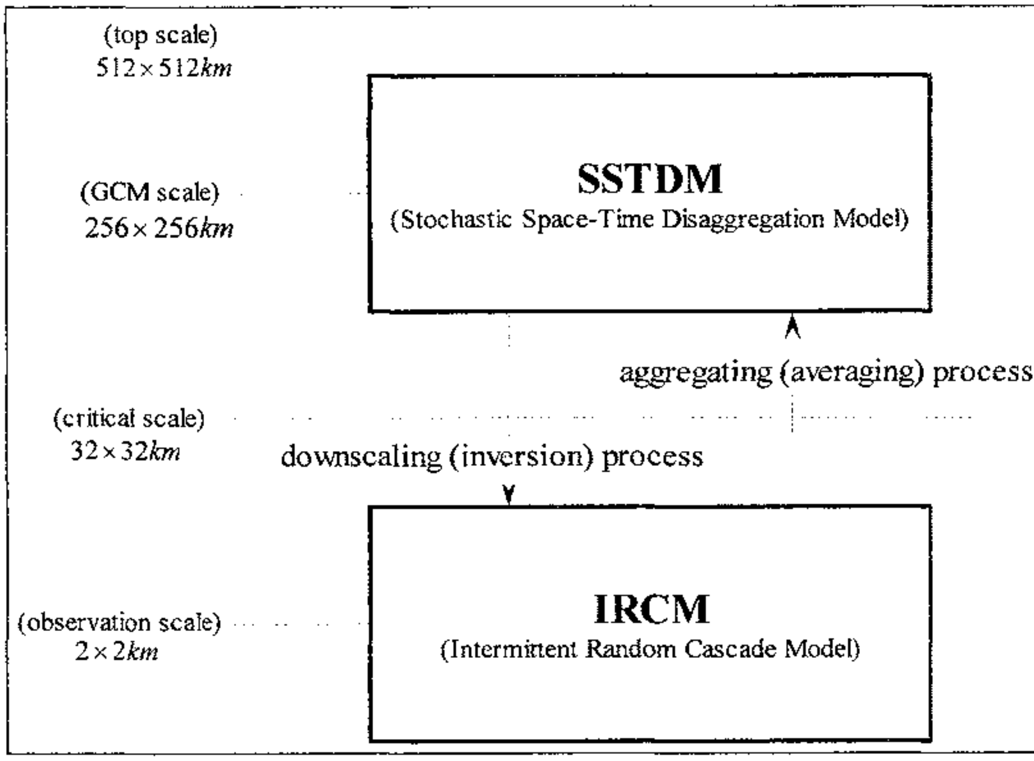

Figure 3-11 General structure of downscaling model

The downscaling process proceeds from the largest spatial scale (256 *km*-scale) to the smallest scale (2 *km*-scale). Based on the specific observations used in this study, the SSTDM proceeds from 256 *km*-scale (0^{th} disaggregation level) down to 32 *km*-scale (3^{rd} disaggregation level). Then, the output of SSTDM is used as the input to the IRCM. The IRCM proceeds from 32-*km* scale (0^{th} cascade level) down to the lowest 2 *km*-scale (4^{th} cascade level). The disaggregation/cascade level and the associated scale or resolution are shown in Table 3-3.

3.3.4. Stochastic Space-Time Disaggregation Model

The grid precipitation field conceptualized in Figure 3-12 is assumed to be correlated temporally and spatially. The lag-1 day temporal correlation is denoted by the parameter ϕ and the lag-1spatial correlation is denoted by the parameter ψ. The lag-1 day temporal correlation (i.e., parameter ϕ) is assumed to vary monthly (or seasonally) and to be a function of scale. The lag-1spatial correlation (i.e., parameter ψ) is assumed to be a function of the background rainfall and scale, too. A stochastic space-time disaggregation model can be constructed to downscale precipitation from a pixel at a given scale (*e.g.*, $r_0(t)$ at the 0^{th} disaggregation level). to the associated pixels at the next higher disaggregation level or consecutive scale in such a way that the lag-1 spatial correlation structure is preserved at every level of disaggregation and between consecutive levels of disaggregation, while at the same time preserving the lag-1 day temporal correlation. If the branching number is 4, there will be 4 precipitation amounts at the consecutive pixels of the next scale (*e.g.*, $r_{01}(t)$, $r_{02}(t)$, $r_{03}(t)$, and $r_{04}(t)$ at the 1^{st} disaggregation level) which will be obtained by downscaling from the pixel of background rainfall (*e.g.*, $r_0(t)$ at the 0^{th} disaggregation level). Based on Figure 3-12, the stochastic model for a pixel at level 1 can be constructed as follows;

$$r_{01}(t) = r_0(t) + a\big(r_{01}(t-1) - r_0(t-1)\big) + b\big(r_0(t) - E[r_0(t)]\big) + c\xi_{01}(t) \tag{3-8}$$

where $\xi_{01}(t)$: is zero mean, unit variance (i.e., standardized) uncorrelated random Gaussian noise, *N(0,1)*.

In order to avoid negative values during the disaggregation process, an alternative form of the model of equation (3-8) can be rewritten for the log-transformed precipitation as follows:

$$\ln r_{01}(t) - \ln r_0(t) = a\big(\ln r_{01}(t-1) - \ln r_0(t-1)\big) + b\big(\ln r_0(t) - \ln E[r_0(t)]\big) + c'\xi_{01}(t) + d$$

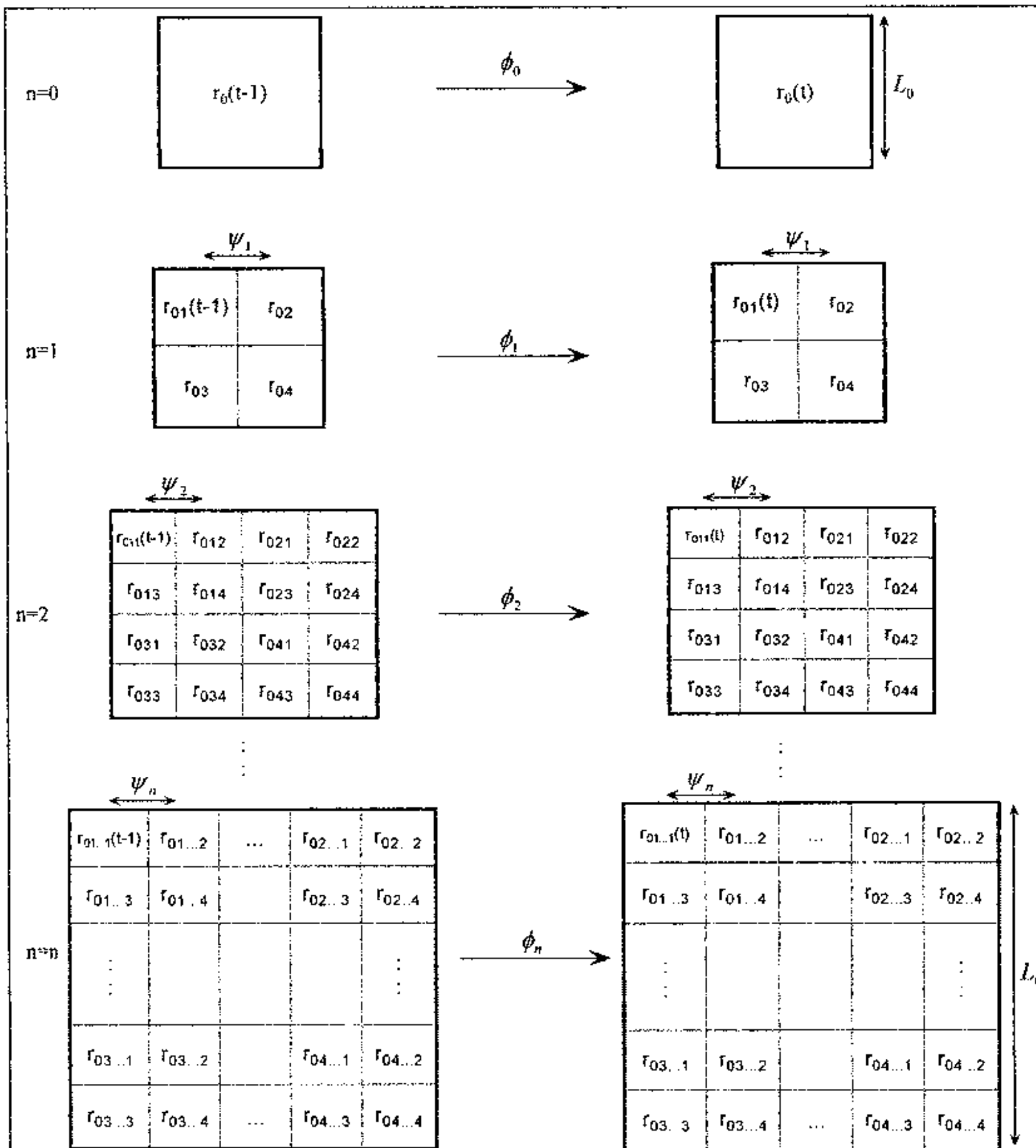

$$\mathbf{Z} = \mathbf{AX} + \mathbf{BY} + \mathbf{CW}$$

$$\mathbf{Z} = \begin{bmatrix} \mu_{0i_1\ldots i_{n-1}1}(t) \\ \mu_{0i_1\ldots i_{n-1}2}(t) \\ \mu_{0i_1\ldots i_{n-1}3}(t) \\ \mu_{0i_1\ldots i_{n-1}4}(t) \end{bmatrix} \quad \mathbf{X} = \begin{bmatrix} \mu_{0i_1\ldots i_{n-1}1}(t-1) \\ \mu_{0i_1\ldots i_{n-1}2}(t-1) \\ \mu_{0i_1\ldots i_{n-1}3}(t-1) \\ \mu_{0i_1\ldots i_{n-1}4}(t-1) \end{bmatrix} \quad \mathbf{Y} = \left[\mu_{0i_1\ldots i_{n-1}}(t)\right] \quad \mathbf{W} = \begin{bmatrix} \xi_{0i_1\ldots i_{n-1}1}(t) \\ \xi_{0i_1\ldots i_{n-1}2}(t) \\ \xi_{0i_1\ldots i_{n-1}3}(t) \\ \xi_{0i_1\ldots i_{n-1}4}(t) \end{bmatrix}$$

$$\mu_{0i_1\ldots i_n}(t) \equiv \ln\left(\frac{r_{0i_1\ldots i_n}(t)}{r_{0i_1\ldots i_{n-1}}(t)}\right) + \frac{s_n^{\,2}}{2}$$

Figure 3-12 The conceptual diagram of SSTDM or $\ln\frac{r_{01}(t)}{r_0(t)} = a\ln\frac{r_{01}(t-1)}{r_0(t-1)} + b\ln\frac{r_0(t)}{E[r_0(t)]} + c'\xi_{01}(t) + d$ (3-9)

It can be shown that if the $\frac{r_{0i}(t)}{r_0(t)}$ follows $N(1,s_1^{\ 2})$ where s_1 is the standard deviation of $\frac{r_{0i}(t)}{r_0(t)}$ at the 1st disaggregation level, then

$$E\left[\ln\frac{r_{0i}(t)}{r_0(t)}\right] = -\frac{s_1^{\ 2}}{2}$$

$$Var\left[\ln\frac{r_{0i}(t)}{r_0(t)}\right] = \ln\left(1+s_1^{\ 2}\right) = \sigma_\mu^{\ 2} \tag{3-10}$$

(e.g., Ang and Tang, 1975). So, we can introduce the dimensionless variable, μ_{0i} defined as

$$\mu_{0i_1} = \ln\frac{r_{0i_1}(t)}{r_0(t)} + \frac{s_1^{\ 2}}{2}$$

Then μ_{0i_1} will follow $N\left(0,\sigma_\mu^{\ 2}\right)$. Equation (3-9) can be rewritten as:

$$\mu_{01}(t) = a\mu_{01}(t-1) + b\mu_0(t) + c'\xi_{01}(t) \tag{3-11}$$

where

$\xi_{0i_1}(t)$: standardized uncorrelated random noise following $N(0,1)$

In equation (3-8), the c coefficient depends on the $r_0(t)$, which is the expected value of $r_{01}(t)$, and depends on the scale and the seasonal large-scale forcing, too. That is,

$$c = f(r_0, \lambda, t) \tag{3-12}$$

However, in equation (3-11), c' is independent of $r_0(t)$. Therefore, c' can be expressed as a function of only the scale and the season (Figure 3-13, Table 3-7), and the parameter estimation procedure is simplified. Perica and Foufoula-Georgiou (1996) and Vuruputur (1999) showed that relative changes in spatial rainfall fluctuations are independent of background intensities. Especially, Vuruputur (1999) used the log difference transformation to study the spatial-temporal statistical organization of rainfall intensity. Expanding equation (3-11) for the

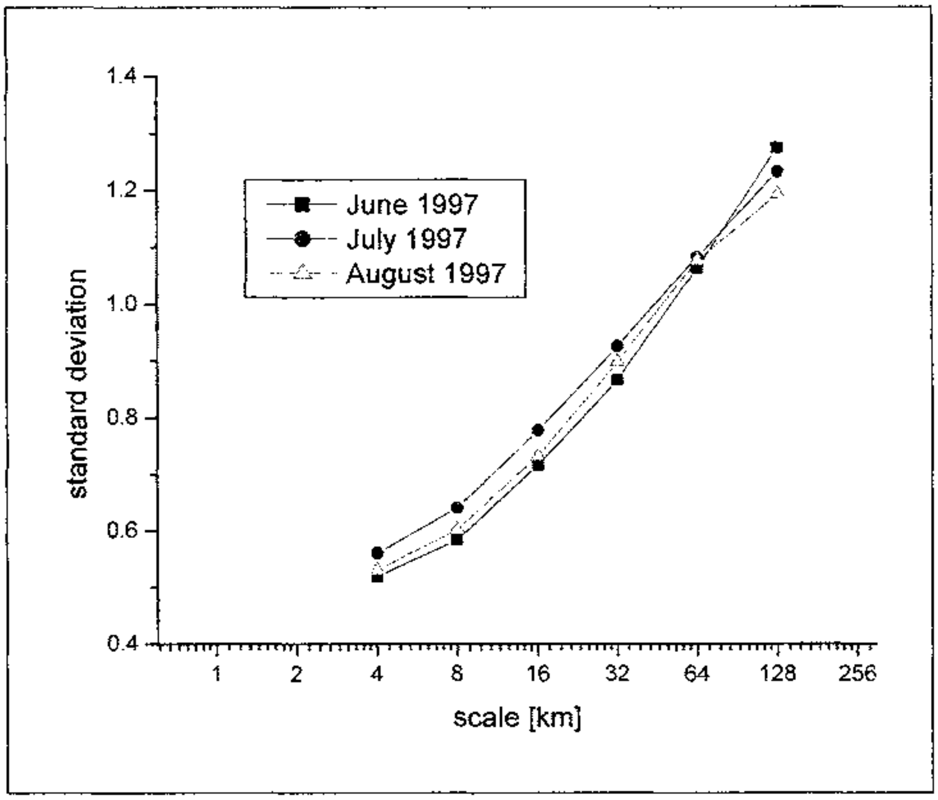

Figure 3-13 Standard deviation of log-transformed rainfall

disaggregation level	standard deviation of log-transformed rainfall		
	June	July	August
1	1.2744	1.2323	1.1930
2	1.0628	1.0825	1.0768
3	0.8655	0.9249	0.8978

Table 3-7 Standard deviation of log-transformed rainfall

pixels associated with the upper disaggregation level, it can be rewritten in matrix form as follows,

$$\mathbf{Z} = \mathbf{AX} + \mathbf{BY} + \mathbf{CW} \tag{3-13}$$

In equation (3-13) and for the first disaggregation level, the $\mathbf{Z}$, $\mathbf{X}$ are (4×1) and $\mathbf{Y}$ is (1×1) dimensionless vectors of the log-transformed rainfall at time *t* and *t-1*, respectively. At the first disaggregation level,

$$\mathbf{Z} = \begin{bmatrix} \mu_{01}(t) \\ \mu_{02}(t) \\ \mu_{03}(t) \\ \mu_{04}(t) \end{bmatrix}, \ \mathbf{X} = \begin{bmatrix} \mu_{01}(t-1) \\ \mu_{02}(t-1) \\ \mu_{03}(t-1) \\ \mu_{04}(t-1) \end{bmatrix}, \text{ and } \mathbf{Y} = [\mu_0(t)]$$

The $\mathbf{W}$ is a (4×1) standardized random noise vector following a N(0,1), *i.e.*,

$$\mathbf{W} = \begin{bmatrix} \xi_{01}(t) \\ \xi_{02}(t) \\ \xi_{03}(t) \\ \xi_{04}(t) \end{bmatrix}$$

$\mathbf{W}$ is uncorrelated with $\mathbf{Z}$, $\mathbf{X}$ and $\mathbf{Y}$. The $\mathbf{A}$ and $\mathbf{C}$ are (4×4) and $\mathbf{B}$ is (4×1) parameter matrices.

The proposed model can be extended sequentially to the n^{th} disaggregation level. At the n^{th} disaggregation level, the model can be written as:

$$\mathbf{Z} = \mathbf{AX} + \mathbf{BY} + \mathbf{CW} \tag{3-14}$$

where the variables can be defined as,

$$\mathbf{Z}=\begin{bmatrix}\mu_{0i_1\ldots i_{n-1}1}(t)\\ \mu_{0i_1\ldots i_{n-1}2}(t)\\ \mu_{0i_1\ldots i_{n-1}3}(t)\\ \mu_{0i_1\ldots i_{n-1}4}(t)\end{bmatrix},\ \mathbf{X}=\begin{bmatrix}\mu_{0i_1\ldots i_{n-1}1}(t-1)\\ \mu_{0i_1\ldots i_{n-1}2}(t-1)\\ \mu_{0i_1\ldots i_{n-1}3}(t-1)\\ \mu_{0i_1\ldots i_{n-1}4}(t-1)\end{bmatrix},\ \mathbf{Y}=\lfloor\mu_{0i_1\ldots i_{n-1}}(t)\rfloor,\mathbf{W}=\begin{bmatrix}\xi_{0i_1\ldots i_{n-1}1}(t)\\ \xi_{0i_1\ldots i_{n-1}2}(t)\\ \xi_{0i_1\ldots i_{n-1}3}(t)\\ \xi_{0i_1\ldots i_{n-1}4}(t)\end{bmatrix}$$

and

$$\mu_{0i_1\ldots i_n}(t)\equiv\ln\left(\frac{r_{0i_1\ldots i_n}(t)}{r_{0i_1\ldots i_{n-1}}(t)}\right)+\frac{s_n^{\ 2}}{2}$$

where r is daily rainfall accumulation and the index $i_1,\ldots,i_n$ can have integer value from 1 to b (=4 in 2-dimensional space).

The initial disaggregation at the initial time is implemented with $\mathbf{X}$ set to $\mathbf{0}$, i.e.,

$$\mathbf{Z}=\mathbf{BY}+\mathbf{CW}. \tag{3-15}$$

The parameter matrices $\mathbf{A}$, $\mathbf{B}$, and $\mathbf{C}$ can be obtained as a function of the variances and covariances of $\mathbf{Z}$, $\mathbf{X}$, $\mathbf{Y}$ and $\mathbf{W}$ as follows.

- The parameter matrices $\mathbf{A}$, $\mathbf{B}$

Post-multiply the equation (3-14) by the transpose of vector $\mathbf{X}$, $\mathbf{X}^T$ to obtain:

$$\mathbf{ZX}^\mathbf{T}=\mathbf{AXX}^\mathbf{T}+\mathbf{BYX}^\mathbf{T}+\mathbf{CWX}^\mathbf{T} \tag{3-16}$$

Post-multiply the equation (3-14) by the transpose of vector $\mathbf{Y}$, $\mathbf{Y}^\mathbf{T}$ to obtain:

$$\mathbf{ZY}^\mathbf{T}=\mathbf{AXY}^\mathbf{T}+\mathbf{BYY}^\mathbf{T}+\mathbf{CWY}^\mathbf{T} \tag{3-17}$$

To obtain the values of the parameter $\mathbf{A}$ and $\mathbf{B}$, apply the expectation operator on both sides of the equation (3-16) and (3-17). Apply the expectation operator on both sides of the equation (3-16) and (3-17) to obtain

$$\mathbf{S_{ZX}}=\mathbf{AS_{XX}}+\mathbf{BS_{YX}}+\mathbf{CS_{WX}} \tag{3-18}$$

$$\mathbf{S}_{ZY} = \mathbf{A}\mathbf{S}_{XY} + \mathbf{B}\mathbf{S}_{YY} + \mathbf{C}\mathbf{S}_{WY} \tag{3-19}$$

where $\mathbf{S}_{ZX}$, $\mathbf{S}_{ZY}$, $\mathbf{S}_{XX}$, $\mathbf{S}_{XY}$, $\mathbf{S}_{YX}$, $\mathbf{S}_{YY}$, $\mathbf{S}_{WX}$, and $\mathbf{S}_{WY}$ are covariance matrices whose elements are covariances between the corresponding index variables. Because the $\mathbf{W}$ is independent of $\mathbf{X}$ and $\mathbf{Y}$, $\mathbf{S}_{WX} = \mathbf{S}_{WY} = \mathbf{0}$, the equation (3-18) can be rewritten for $\mathbf{A}$:

$$\mathbf{A} = \mathbf{S}_{ZX}\mathbf{S}_{XX}^{-1} - \mathbf{B}\mathbf{S}_{YX}\mathbf{S}_{XX}^{-1} \tag{3-20}$$

Substituting the equation (3-20) into (3-19) and solving for $\mathbf{B}$ gives

$$\mathbf{S}_{ZY} = \mathbf{S}_{ZX}\mathbf{S}_{XX}^{-1}\mathbf{S}_{XY} - \mathbf{B}\mathbf{S}_{YX}\mathbf{S}_{XX}^{-1}\mathbf{S}_{XY} + \mathbf{B}\mathbf{S}_{YY}$$

so

$$\mathbf{B} = \left(\mathbf{S}_{ZY} - \mathbf{S}_{ZX}\mathbf{S}_{XX}^{-1}\mathbf{S}_{XY}\right)\left(\mathbf{S}_{YY} - \mathbf{S}_{YX}\mathbf{S}_{XX}^{-1}\mathbf{S}_{XY}\right)^{-1} \tag{3-21}$$

Substituting the equation (3-21) into (3-20) leads to,

$$\begin{aligned}\mathbf{A} &= \mathbf{S}_{ZX}\mathbf{S}_{XX}^{-1} - \left(\mathbf{S}_{ZY} - \mathbf{S}_{ZX}\mathbf{S}_{XX}^{-1}\mathbf{S}_{XY}\right)\left(\mathbf{S}_{YY} - \mathbf{S}_{YX}\mathbf{S}_{XX}^{-1}\mathbf{S}_{XY}\right)^{-1}\mathbf{S}_{YX}\mathbf{S}_{XX}^{-1} \\ &= \left[\mathbf{S}_{ZX} - \left(\mathbf{S}_{ZY} - \mathbf{S}_{ZX}\mathbf{S}_{XX}^{-1}\mathbf{S}_{XY}\right)\left(\mathbf{S}_{YY} - \mathbf{S}_{YX}\mathbf{S}_{XX}^{-1}\mathbf{S}_{XY}\right)^{-1}\mathbf{S}_{YX}\right]\mathbf{S}_{XX}^{-1}\end{aligned} \tag{3-22}$$

The equations (3-21) and (3-22) can be used to estimate the parameter matrices $\mathbf{A}$ and $\mathbf{B}$ as a function of the covariance matrices $\mathbf{S}_{ZX}$, $\mathbf{S}_{ZY}$, $\mathbf{S}_{XX}$, $\mathbf{S}_{XY}$, $\mathbf{S}_{YX}$, $\mathbf{S}_{YY}$, $\mathbf{S}_{WX}$, and $\mathbf{S}_{WY}$.

The Parameter Matrix $\mathbf{C}$

In order to estimate the parameter matrix $\mathbf{C}$ proceed as follows. Post-multiply the equation (3-17) by the vector $\mathbf{Z}^T$ to obtain,

$$\mathbf{ZZ}^{\mathrm{T}} = (\mathbf{AX}+\mathbf{BY}+\mathbf{CW})(\mathbf{AX}+\mathbf{BY}+\mathbf{CW})^{\mathrm{T}}$$

and

$$\begin{aligned}\mathbf{ZZ}^{\mathrm{T}} = {} & \mathbf{AXX}^{\mathrm{T}}\mathbf{A}^{\mathrm{T}} + \mathbf{AXY}^{\mathrm{T}}\mathbf{B}^{\mathrm{T}} + \mathbf{AXW}^{\mathrm{T}}\mathbf{C}^{\mathrm{T}} + \\ & \mathbf{BYX}^{\mathrm{T}}\mathbf{A}^{\mathrm{T}} + \mathbf{BYY}^{\mathrm{T}}\mathbf{B}^{\mathrm{T}} + \mathbf{BYW}^{\mathrm{T}}\mathbf{C}^{\mathrm{T}} + \\ & \mathbf{CWX}^{\mathrm{T}}\mathbf{A}^{\mathrm{T}} + \mathbf{CWY}^{\mathrm{T}}\mathbf{B}^{\mathrm{T}} + \mathbf{CWW}^{\mathrm{T}}\mathbf{C}^{\mathrm{T}}\end{aligned} \tag{3-23}$$

The $\mathbf{W}$ is a vector of zero mean, unit variance, uncorrelated random variables, so that the covariance matrix $\mathbf{S}_{\mathbf{WW}}$ is an identity matrix and because the $\mathbf{W}$ is independent of $\mathbf{X}$ and $\mathbf{Y}$, $\mathbf{S}_{\mathbf{WX}} = \mathbf{S}_{\mathbf{WY}} = \mathbf{0}$. Therefore, taking expectations on both sides of the equation (3-23) to obtain

$$\mathbf{S}_{\mathbf{ZZ}} = \mathbf{AS}_{\mathbf{XX}}\mathbf{A}^{\mathrm{T}} + \mathbf{AS}_{\mathbf{XY}}\mathbf{B}^{\mathrm{T}} + \mathbf{BS}_{\mathbf{YX}}\mathbf{A}^{\mathrm{T}} + \mathbf{BS}_{\mathbf{YY}}\mathbf{B}^{\mathrm{T}} + \mathbf{CS}_{\mathbf{WW}}\mathbf{C}^{\mathrm{T}} \tag{3-24}$$

$$\mathbf{CC}^{\mathrm{T}} = \mathbf{S}_{\mathbf{ZZ}} - \mathbf{AS}_{\mathbf{XX}}\mathbf{A}^{\mathrm{T}} - \mathbf{AS}_{\mathbf{XY}}\mathbf{B}^{\mathrm{T}} - \mathbf{BS}_{\mathbf{YX}}\mathbf{A}^{\mathrm{T}} - \mathbf{BS}_{\mathbf{YY}}\mathbf{B}^{\mathrm{T}} \tag{3-25}$$

The parameter matrix $\mathbf{C}$ can be obtained from the product of $\mathbf{CC}^{\mathrm{T}}$ following the procedure indicated below.

If $\mathbf{C}$ is a real matrix, the matrix

$$\mathbf{G} = \mathbf{CC}^{\mathrm{T}} \tag{3-27}$$

is called Gram matrix of $\mathbf{C}$. In order for $\mathbf{CC}^{\mathrm{T}}$ to be decomposable, $\mathbf{CC}^{\mathrm{T}}$ has to be a positive definite symmetric matrix. The elements of correlation matrices should be carefully tuned to avoid non-positive definiteness of $\mathbf{CC}^{\mathrm{T}}$. Strictly speaking, a matrix is "positive definite" if all of its eigenvalues are positive. Eigenvalues are the elements of a vector, $\mathbf{d}$, which results from the decomposition of a square matrix, $\mathbf{T}$, as:

$$\mathbf{T} = \mathbf{d}^T\mathbf{F}\mathbf{d} \tag{3-28}$$

This definition cannot be checked numerically. To an extent, however, we can test the positive definiteness in terms of the sign of the "determinant" of the matrix. The determinant is a scalar function of the matrix. In the case of symmetric matrices, such as covariance or correlation matrices, positive definiteness will only hold if the matrix and every "principal submatrix" has a positive determinant. "Principal submatrices" are formed by removing row-column pairs from the original symmetric matrix. There are some other equivalent definitions that can be used, for example;

i. All pivots in Gaussian elimination without pivoting must be positive

ii. All principal minors of F must be positive, i.e., let Fk denote the submatrix made up of the first k rows and columns of F. If $\mathbf{F} \in \mathbf{R}^{n\times n}$, then $|\mathbf{F_k}|, k = 1,\ldots,n$, are the principal minors of F.

A matrix which fails this test is "not positive definite". If the determinant of the matrix is exactly zero, then the matrix is "singular" (Wothke, 1993).

Observe that if we are not interested in explicitly preserving the lag-1 temporal correlation between $[\mu_{0i_n}(t)]$ and $[\mu_{0i_n}(t-1)]$ at all scales, that is, if $\mathbf{A}$ is zero, the equations (3-21), (3-22) and (3-26) reduce to the well known parameter estimation equations of the temporal disaggregation model of Valencia and Schaake (1972); which was used for spatial downscaling in the context of climate change impact analysis by Epstein and Ramírez (1994). The Valencia and Schaake's model was developed for multi-site, multi-season point streamflow and revised to include linkages with the past season by Mejia and Rousselle (1976). Because this model originally produces seasonal streamflow from annual streamflow and can be extended to monthly or smaller time intervals, the spatial or temporal intermittency of rainfall is not critically considered. In this study, the proposed model of Equation 3-13 will be applied within a range of scales for which the spatial intermittency is assumed to be negligible as indicated by our data analysis (in our case study this scale ranges from 128 *km*-scale to 32 *km*-scale, as will be shown later).

Under assumptions of homogeneity and isotropy, the covariance matrices can be constructed as follows. Once the background precipitation (the precipitation of upper scale field that corresponds to the frame of 4 consecutive pixels of the underlying field) is determined, the spatial correlation ($\Delta x = 1\ pixel$) of the fields associated with each scale can be obtained from the regression formula (Figure 3-9 and Table 3-5). In this grid precipitation field, the spatial correlation between pixels facing diagonally is assumed to be the same as the correlation between pixels facing horizontally or vertically (Figure 3-12). The homogeneity and isotropy assumptions are necessary for the positive definiteness of the Gram matrix. The lag-1 spatial correlation of $\Delta x = 1 pixel$ with respect to background rainfall and lag-1 temporal correlation with respect to scale are presented in Figure 3-8 and Figure 3-9, respectively. Details of the derivation of $\mathbf{S}_{XX}$, $\mathbf{S}_{ZZ}$, $\mathbf{S}_{XX}$, $\mathbf{S}_{YY}$, $\mathbf{S}_{ZX}$, and $\mathbf{S}_{XY}$ are shown in Appendix B.

The spatial distribution of grid rainfall consists of groups of storm clusters. Figure 3-9, which is the lag-1 temporal correlation of log precipitation for pixels within storm clusters, shows that the critical scale is 32 *km*. Below the critical scale, the distribution of precipitation does not depend strongly on the temporal correlation. Instead, what becomes important at smaller scales is the statistical self-similarity and spatial intermittency.

3.3.5. Intermittent random cascade model

In this section, we will describe the cascade structure of the rainfall field, and how this cascade structure is defined and used for rainfall generation (i.e., downscaling). Multiplicative random cascades have been used to generate fractal fields that emulate the spectrum of scaling exponents of observed rainfall (Lovejoy and Scherzler 1992, Gupta and Waymire 1993, Over and Gupta 1996). The choice of different cascade generators is done according to the scaling spectra that they produce. Notably, models like the "*universal multifractals*" (Schertzer and Lovejoy 1987), the β-model (Gupta and Waymire, 1993) or the log-Poisson model (She and Waymire 1995) were proposed as alternatives to the lognormal model of turbulence (Kolmogorov 1962). The discussion of the random cascade model presented below follows closely those presented by Gupta and Waymire (1993), Over (1995), Over and Gupta (1996), Molnár (2000), and Kang and Ramírez, (2001).

Discrete random cascades distribute mass on successive regular subdivisions of a d-dimensional cube. A schematic of this process is shown in Figure 3-14. The initial pixel, with length scale L_0, is subdivided at each level into b equal parts, where b ($\geq 2^d$ where d is dimension, i.e., 2 for 2-dimensional space, 3 for 3-dimensional space and so on) is called the branching number. The i^{th} pixel at the n cascade (subdivision) level is denoted by Δ^i_n (there are $i = 1, \ldots, b^n$ sub-pixels at level n). The length scale of the sub-pixel Δ^i_n is denoted l_n, and the dimensionless spatial scaling ratio is defined as:

$$\lambda_n = l_n / l_0 = b^{-n/d} \tag{3-29}$$

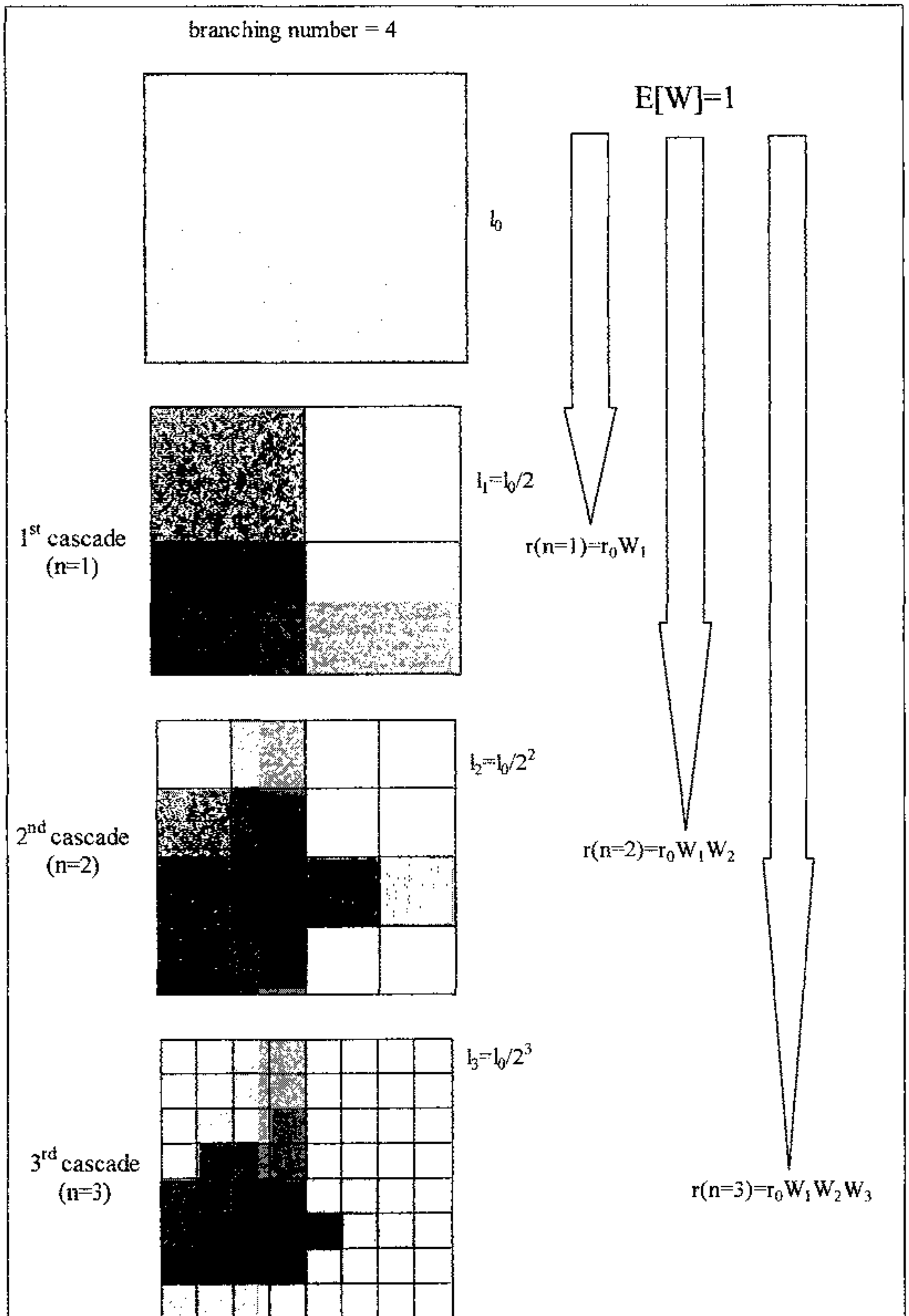

Figure 3-14 Schematic diagram of intermittent random cascade model

Let the non-random initial rainfall intensity be $r_0\ (= r(\Delta_0))[LT^{-1}]$, which is assigned to the initial pixel at the largest scale level. The sub-pixels Δ_1^i, i=1, 2,…, b at the first cascade level are assigned the intensity $r_0 W_1(i)$, where the *W's* are independent and identically distributed random variables, the *cascade generator*, whose expected value is one but which can take on the value of zero. Likewise, the rainfall intensity at the 2nd cascade level is $r_0 W_1(i) W_2(i)$. This multiplicative process continues through all cascade levels, and eventually, at the n^{th} cascade level, the rainfall intensity in sub-pixel Δ_n^i is:

$$r(\Delta_n^i) = r_0 \prod_{j=1}^{n} W_j(i)$$

The rainfall intensity, $r(\Delta_n^i)$, can be disaggregated still into smaller-scale pixels and the downscaling process must ensure that $r(\Delta_n^i)$ is preserved. In other words, the average of the rainfall intensities of sub-pixels in Δ_n^i must converge to $r(\Delta_n^i)$. Let the average rainfall intensity in the pixel Δ_n^i after k - n $(k \geq n)$ levels further than n levels as $r_k(\Delta_n^i)$, then

$$\begin{aligned} r_k(\Delta_n^i) &= r_n(\Delta_n^i) \prod_{j=n+1}^{k} W_j(i) \quad (k \geq n) \\ &= \left(r_0 \prod_{j=1}^{n} W_j(i)\right) \prod_{j=n+1}^{k} W_j(i) \\ &= r_0 \prod_{j=1}^{k} W_j(i), \qquad \text{for } i = 1, 2, \ldots, b^n \qquad (3\text{-}30) \end{aligned}$$

If k is much greater than n, k is referred to as the cascade level of high frequency disaggregation and n is the cascade level of low frequency disaggregation. If the distribution of

W is non-negative with $\langle W \rangle = 1$, then rainfall intensity is conserved on the average at all levels in the random cascade. The mass, $m(\Delta_n^i)$, in a pixel of n^{th} cascade level is the product of the rainfall intensity and the pixel area.

$$m(\Delta_n^i) = l_n^{\ d} \cdot r(\Delta_n^i)$$

Then, equation (3-30) can be rewritten in terms of mass, as follows

$$m_k(\Delta_n^i) = l_n^{\ d} r_0 \prod\nolimits_{j=1}^{k} W_j(i), \qquad \text{for } i = 1, 2, \ldots, b^n$$

The cascade limit mass, m_∞, can be obtained by letting k go to infinity.

$$m_\infty(\Delta_n^i) = \lim_{k \to \infty} m_k(\Delta_n^i) = l_n^{\ d} r_0 \prod\nolimits_{j=1}^{\infty} W_j(i) \equiv l_n^{\ d} r_0 Z_\infty(i) \qquad \text{for } i = 1, 2, \ldots, b^n \quad (3\text{-}31)$$

The *i.i.d.* random variable Z_∞ introduced in Equation (3-31) is defined as the infinite product of the cascade generators. Therefore, the statistical characteristics of the limit measure depend on the distribution of W *and/or* Z_∞.

Most noteworthy is that the cascade limit mass $m_\infty(\Delta_n^i)$ is given by the product of a large scale, low-frequency component $m_n(\Delta_n^i)$ and a sub-grid scale, high frequency component $Z_\infty(i)$ (Equations 3-30 and 3-31). As seen from the definition of Z_∞, its mathematical behavior is governed by the characteristics of products of Ws. In order to investigate the moment characteristics of W, let's consider the qth order moment ($M_n(q)$) of the mass:

$$\begin{aligned} M_n(q) &= \sum_{i=1}^{b^n} m_\infty^{\ q}(\Delta_n^i) \\ &= \sum_{i=1}^{b^n} l_n^{\ dq} r_\infty^{\ q}(\Delta_n^i) \\ &= \sum_{i=1}^{b^n} l_n^{\ dq} \left(r_0 \prod_{j=1}^{n} W_j^i(\Delta_n^i) \right)^q \end{aligned}$$

For large n, the sample moments would be asymptotic to their ensemble moments.

$$\langle M_n(q)\rangle = l_n^{dq} r_0^{q} b^{n} \langle W^q \rangle^n = l_0^{dq} b^{(1-q)n} r_0^{q} \langle W^q \rangle^n \tag{3-32}$$

Taking logarithms of both sides of the above equation gives,

$$\log_b \langle M_n(q)\rangle = q \log_b r_0 + dq \log_b l_0 + n\{\log_b \langle W^q \rangle - (q-1)\} \tag{3-33}$$

From the definition of scaling ratio, λ_n, (equation 3-29),

$$n = -d \log_b \lambda_n \tag{3-34}$$

Inserting equation 3-34 into the equation 3-33 gives,

$$\log_b \langle M_n(q)\rangle = -d(\log_b \langle W^q \rangle - (q-1))\log_b \lambda_n + q \log_b (r_0 l_0^{\,d}) \tag{3-35}$$

Equation 3-35 indicates that there is a *log-log* relationship between the ensemble moment, $\langle M_n(q)\rangle$, and the scaling ratio, λ_n. The slope of this relationship is defined by the so-called τ-function,

$$\tau(q) = d(\log_b \langle W^q \rangle - (q-1)) \tag{3-36}$$

Kahane and Peyriere (1976) introduced the Mandelbrot-Kahane-Peyriere (so-called MKP) function, $\chi_b(q)$ as,

$$\chi_b(q) = \log_b \langle W^q \rangle - (q-1) \tag{3-37}$$

The MKP function is identical to the τ-function except for the multiplicative factor d. Therefore,

$$\tau(q) = d\chi_b(q) \tag{3-38}$$

The MKP function characterizes the distribution of the cascade generator W and the scaling properties of rainfall. The distribution of the fluctuation is determined by that of the random cascade generator, W. The important characteristics of the MKP function were explored by Madelbrot (1974). The MKP function is always convex and the pattern can fall into the following 3 classes (Figure 3-15. adapted from Mandelbrot, 1974):

(a) Regular class : $\chi_b^{(1)}(1) < 0,\ \chi_b(2) < 0, \alpha_1 = \infty$

(b) Irregular class : $\chi_b^{(1)}(1) < 0,\ \chi_b(2) < 0,\ \ 1 < \alpha_1 < \infty$

(c) Degenerate class : $\chi_b^{(1)}(1) > 0,\ \chi_b(2) > 0,\ \ 0 < \alpha_1 < 1$

where $\chi_b^{(1)}(\cdot)$ represents the first derivative of $\chi_b(\cdot)$ and α_1 is denoted as the second zero of the MKP function.

The 'regular' class includes all *W* that are bounded by *b*. The birth-death (or 0-1) model belongs to the 'regular' class because the value of the cascade generator is either 0 or 1. The regular class has finite moments of every order. The 'degenerate' class corresponds to *W's* that are 'more scattered than is likely in nature'. Under degenerate conditions, the second zero of MKP function is less than 1 and the resulting fluctuation vanishes as λ goes to zero. The 'irregular' class includes all *Y's* that are 'not too scattered but nevertherless can exceed *b*'. In the case of the log-normal random cascade model that will be presented below, one has to consider the degenerate or the irregular condition. The following theorem suggested by Kahane and Peyriere (1976) refers to the conditions of MKP function for convergence of the limit measure.

Theorem 3-1 (Kahane and Peyriere, 1976)

Let *W* be the generator of a discrete *i.i.d.* random cascade with MKP function $\chi_b(q)$ and branching number *b*, then

(a) If $\chi_b^{(1)}(1) < 0$, then $Z_\infty > 0$ and $\langle Z_\infty \rangle = 1$, where $\langle\cdot\rangle$ designates the ensemble average.

(b) For any q (>1), $m_\infty(J) < 0$ has a finite moment of order q if and only if $q < q_c$, where $q_c = \inf\{q \geq 1; \chi_b(q) \geq 0\}$ and J represents the space in which mass is measured. Moreover, $\langle Z_\infty{}^q \rangle$ exists for all $q > 0$ if and only if W is essentially bounded by b and $P(W = b) = \frac{1}{b}$.

(c) If $\langle Z_\infty \log Z_\infty \rangle < \infty$, then the limit measure m_∞ is almost surely supported by a Borel subset of J of Haussdorf dimension $D = -d\chi_b{}^{(1)}(1)$.

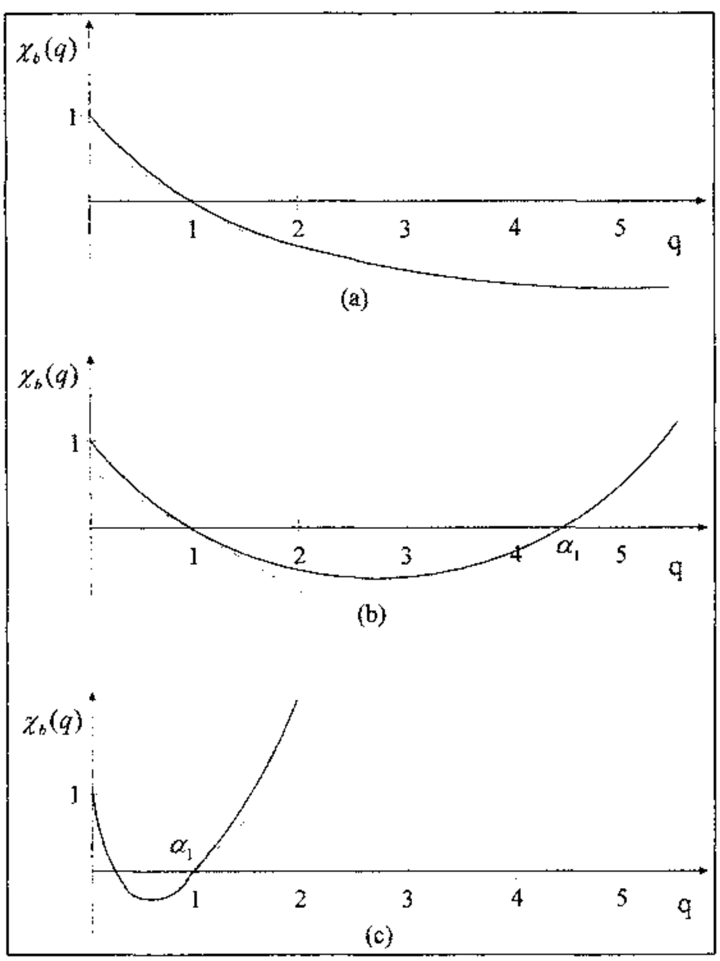

Figure 3-15 Classes of MKP function

Various forms of generators for constructing the cascade structure satisfy the existence and convergence conditions. However, from a practical point of view, we need a generator that, on the one hand, has a sufficient number of adjustable parameters and, on the other hand, is simple enough to be manipulated analytically. In this respect, the log-normal generator, which will be described later in this section, has been shown to be a good candidate for this role (Over 1995). In the study of intermittent turbulence, many researches have considered log-normality to be a pragmatic assumption for turbulent dissipation (Kolmogorov 1962, Oboukov 1962, Mandelbrot 1972).

If there is a *log-log* linear relationship between the ensemble moment and the scaling ratio, then the slope can be calculated easily from the observation data especially when $q=0$. From equation (3-36), the slope function is defined as,

$$\tau(0) = \lim_{\lambda_n \to 0} -\frac{\log_b M_n(0)}{\log_b \lambda_n} = d\left(1 + \log_b \left\langle W^0 \right\rangle\right) \qquad (3\text{-}39)$$

where W can be 0 or a positive real value.

In data analysis, the scaling of the sample moments is used to estimate the $\tau(0)$ function and the distribution of the cascade generator, from which parameters of the cascade model can be inferred.

For intermittent rainfall data (in both temporal and spatial domains) it is desirable that the probability that W=0 be positive. For this purpose an *intermittent model* using the cascade generator W is described here (after Over 1995). In this case W is written as a composite generator,

$$W = BY \qquad (3\text{-}40)$$

where B is an intermittency generator of the so-called *β-model* and Y is a strictly positive log-normal random variable and has the form of $Y = b^{\gamma+\varepsilon X}$. The B and Y are independent cascade generators. The model has the mathematical form of :

$$P(W=0) = 1-b^{-\beta} \quad \text{and} \quad P(W = b^{\beta}Y = b^{\beta}\cdot b^{\gamma+\varepsilon X}) = b^{-\beta} \tag{3-41}$$

The γ is derived to be (Over, 1995):

$$\gamma = -\frac{\varepsilon^2 \log b}{2}$$

The final form of log-normal random cascade model is,

$$P(W=0) = 1-b^{-\beta} \quad \text{and} \quad P(W = b^{\beta}Y = b^{\beta-\frac{\varepsilon^2 \ln b}{2}+\varepsilon X}) = b^{-\beta} \tag{3-42}$$

where X is a standardized Gaussian random variable.

Physically, β is the statistical self-similarity parameter, which is scale-invariant and characterizes the spatial intermittency of the precipitation distribution. Therefore, the rainy fraction of the underlying field can be represented in terms of β. However, Figure 3-2 and Table 3-8 show that the rainy fraction (f_r) is scale-variant. The scale-variant feature of the rainy fraction can be simulated through a combination of a scale-invariant parameter, β, and a scale variant component, i.e., $f_r = b^{-n\hat{\beta}} = (b^{-n})^{\beta}$. The parameter β can be estimated as a function of the MKP functions or the τ-function as suggested by Over (1995) as follows,

$$\hat{\beta} = 1 - \frac{\tau(0)}{d} \tag{3-43}$$

where $\tau(\cdot)$ is the slope function of the moment-scale plot. For ease of computation of $\hat{\beta}$ from observation data, equation (3-43) can be equivalently rewritten as follows,

$$\hat{\beta} = 1 - \frac{\tau(0)}{d} = 1 - \frac{\frac{\log_b M_n(0)}{n/d}}{d}$$

$$= 1 - \frac{\log_b\left(\sum_{i=1}^{b^n} m_\infty{}^0(\Delta_n^i)\right)}{n}$$

$$= 1 - \frac{\log_b(b^n f_r)}{n}$$

$$= -\frac{\log_b f_r}{n} \qquad (3\text{-}44)$$

where f_r is rainy fraction of the precipitation field at n^{th} cascade level

Scale [km]	Rainy fraction of original rainfall field	Rainy fraction calculated from $\beta = 0.0134$
256	1	1
128	1	0.9822
64	0.9961	0.9635
32	0.9873	0.9458
16	0.9595	0.9284
8	0.9202	0.9113
4	0.8816	0.8945
2	0.8458	0.8781

Table 3-8 Comparison of rainy fractions

As implied by equation (3-44), β is represented in terms of the rainy fraction of the observation scale (lowest scale) and the total number of cascade levels. In other words, the rainy fraction of each cascade level can now be described as a function of the scale-invariant β and the cascade level (scale variant). Table 3-8 compares the rainy fraction of the original NEXRAD observations and the one computed from estimated β. As indicated, the scale-variant feature of rainfall field is adequately represented by the scale-invariant β.

The MKP function of the log-normal model is (Over, 1995):

$$\chi_b(q) = (\beta - 1)(q - 1) + \frac{\varepsilon^2 \ln b}{2}(q^2 - q) \tag{3-45}$$

From this MKP function, the degenerate condition gives

$$\chi_b^{(1)}(1) = (\beta - 1) + \frac{\varepsilon^2 \ln b}{2} > 0 \quad \rightarrow \quad \beta > 1 - \frac{\varepsilon^2 \ln b}{2}$$

and

$$\chi_b(2) = (\beta - 1) + \varepsilon^2 \ln b > 0 \quad \rightarrow \quad \beta > 1 - \varepsilon^2 \ln b$$

In section 3.3.6, ε will be estimated 0.12. Then, the degenerate condition is $\beta > 0.98$ which implies that almost all the pixels are in dry. Considering the range of β in our case (Figure 3-16), the degenerate condition is not critical.

The parameter ε can be estimated from the second derivative of $\tau(q)$ using the following formula:

$$\hat{\varepsilon} = \sqrt{\frac{\chi^{(2)}(q)}{\ln b}} = \sqrt{\frac{\tau^{(2)}(q)}{d \ln b}} \tag{3-46}$$

The second derivative of $\tau(q)$ can be calculated from data. The definition of $\tau(q)$ is,

$$\tau(q) = \lim_{n \to \infty} \frac{\log_b M_n(q)}{n/d} = \lim_{n \to \infty} \frac{\ln \sum_{i=1}^{b^n} m_\infty{}^q(\Delta_n^i)}{\frac{n}{d} \ln b}$$

where n is the number of cascades.

Before deriving the first and second derivative of $\tau(q)$, we have to figure out the first derivative of the function $\ln m^q$

When $f(q) = m^q$ then,

$$\frac{d(\ln f)}{dq} = \frac{d(q \ln m)}{dq}$$

This can be rewritten as

$$\frac{1}{f} \cdot \frac{df}{dq} = \ln m$$

Eventually,

$$\frac{df}{dq} = f \ln m$$

From the above equation, the first derivative of $\tau(q)$ will be

$$\tau^{(1)}(q) = \frac{d}{dq} \lim_{n\to\infty} \frac{\ln \sum_{i=1}^{b^n} m_\infty^q(\Delta_n^i)}{\frac{n}{d}\ln b} = \lim_{n\to\infty} \frac{\frac{d}{dq} \ln \sum_{i=1}^{b^n} m_\infty^q(\Delta_n^i)}{\frac{n}{d}\ln b}$$

$$= \lim_{n\to\infty} \frac{\sum_{i=1}^{b^n} m_\infty^q(\Delta_n^i) \cdot \ln m_\infty(\Delta_n^i)}{\frac{n}{d}\ln b \cdot \sum_{i=1}^{b^n} m_\infty^q(\Delta_n^i)}$$

And

$$\tau^{(2)}(q) = \frac{d}{dq} \lim_{n\to\infty} \frac{\ln \sum_{i=1}^{b^n} m_\infty^q(\Delta_n^i) \cdot \ln m_\infty(\Delta_n^i)}{\frac{n}{d}\ln b \cdot \sum_{i=1}^{b^n} m_\infty^q(\Delta_n^i)}$$

$$= \lim_{n\to\infty} \frac{\left[\sum_{i=1}^{b^n} m_\infty^q(\Delta_n^i)(\ln m_\infty(\Delta_n^i))^2\right]\left[\sum_{i=1}^{b^n} m_\infty^q(\Delta_n^i)\right] - \left[\sum_{i=1}^{b^n} m_\infty^q(\Delta_n^i)\ln m_\infty^q(\Delta_n^i)\right]^2}{\frac{n}{d}\ln b\left[\sum_{i=1}^{b^n} m_\infty^q(\Delta_n^i)\right]^2}$$

The scaling of the intermittent log-normal model is represented as :

$$\log_b\langle M_n(q)\rangle = q\log_b R_0 - d(\log_b \lambda_n)(\log_b\langle W^q\rangle - (q-1))$$

$$= q\log_b R_0 - d(\log_b \lambda_n)\left((\beta-1)(q-1) + \frac{\varepsilon^2 \ln b}{2}(q^2-q)\right) \qquad (3\text{-}47)$$

Comparing equation (3-47) with equation (3-6), we can find:

$$\theta\cdot q = d\left((\beta-1)(q-1) + \frac{\varepsilon^2\ln b}{2}(q^2-q)\right)$$

$$\theta = \frac{d(\theta\cdot q)}{dq} = d\left[\varepsilon^2(\ln b)q - \frac{\varepsilon^2\ln b}{2} + (\beta-1)\right] \qquad (3\text{-}48)$$

Therefore, the intermittent log-normal model can be applied to fields that follow simple scaling.

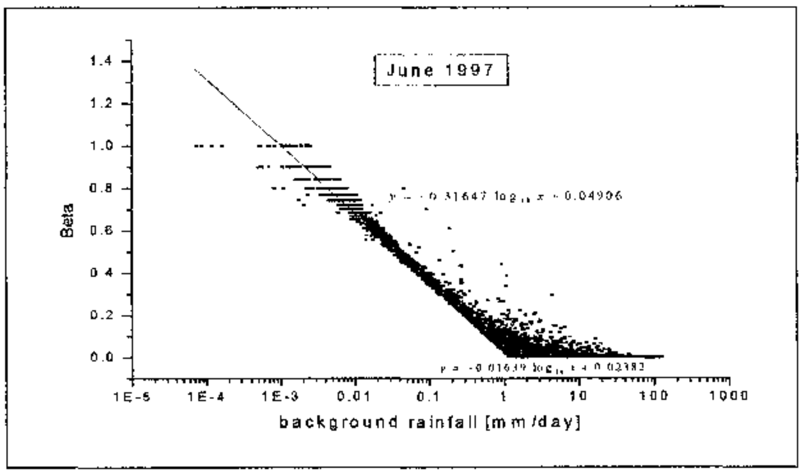

(a) June

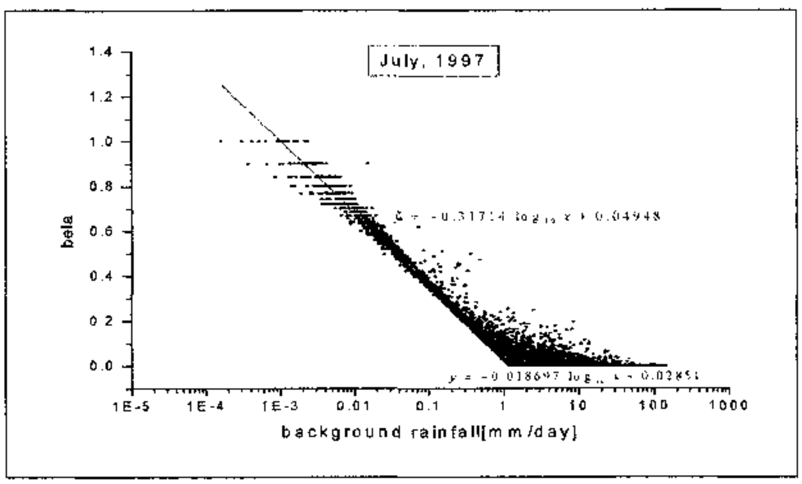

(b) July

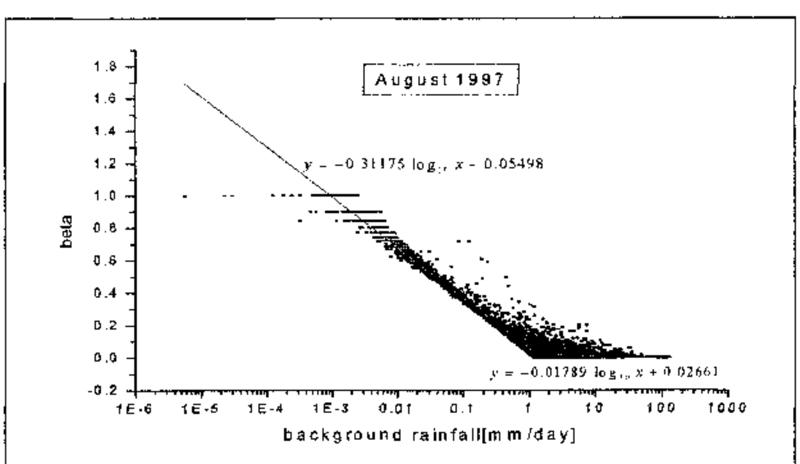

(c) August

Figure 3-16 Beta vs. background rainfall

3.3.6. Application and results

This model was tested on the precipitation field of July, 1997 corresponding to the same NEXRAD data set used for data analysis. The geographical area includes the Front Range of the Rocky Mountains and the Great Plains of the Central United States in eastern Colorado, Nebraska, Kansas, Oklahoma and parts of Wyoming, New Mexico, and Texas. By means of our proposed downscaling procedure, our objective is to simulate observation scale precipitation fields from the GCM scale precipitation field in such a way that the simulated fields are statistically indistinguishable from the observations including scaling characteristics in space and time. The observation field is composed of 512×512 pixels with a pixel size of $2 \times 2\,km$ and encompasses 9 cascade levels. The significant scale is $32 \times 32\,km$, which corresponds to 5^{th} cascade level. The GCM scale corresponds to $128 \times 128\,km$, (*i.e.*, 3^{rd} cascade level.) Therefore, the SSTDM was applied from 3^{rd} to 5^{th} cascade level and the IRCM was applied from 6^{th} cascade level down to the 9^{th} cascade level. The process is illustrated in Figure 3-11.

The SSTDM has 3 parameters (ϕ, ψ, σ) that need to be estimated. All of these parameters were revealed to be dependent on scale. The fluctuation parameter (σ) is uniformly distributed over the large-scale forcing and depends only on scale (see Figure 3-13 and Table 3-7). The lag-1 spatial correlation, characterized by the parameter ψ, is found to be scale dependent and to depend also on the large scale forcing, as seen on Figure 3-9. Regression equations for ψ are shown in Table 3-5. Figure 3-10 and Table 3-6 show the lag-1 temporal correlation, ϕ, of the log-transformed precipitation data as a function of disaggregation level.

The IRCM has 2 parameters (β , ε) that need to be estimated. Figure 3-16 illustrates that the intermittency parameter, β, exhibits piecewise semi-log relationship with background rainfall. The quadratic form of the MKP function (Figure 3-15) implies that the second derivative theoretically should be constant. However, the second derivative computed from the observations has density distribution centered around 0.01 (see Figure 3-17). The fluctuation parameter, ε , of IRCM can be computed as follows using Equation 3-32:

$$\hat{\varepsilon} = \sqrt{\frac{\tau^{(2)}(q)}{2\ln b}} = \sqrt{\frac{0.04}{2\ln 4}} = 0.12$$

With these parameters, a test simulation for downscaling of large-scale precipitation fields is carried out for June, July and August of 1997. The large-scale field used for this test is generated by resampling the original NEXRAD observations from a $2 \times 2\ km$ -scale to a $256 \times 256\ km$ -scale field.

Figure A-A1 ~ A-A3 (in Appendix) compare observed and simulated precipitation fields for the period June – August of 1997. Figure 3-18 compares the observed and simulated mean precipitation of the entire domain throughout the period June to August of 1997. The mean precipitation of the original field is preserved throughout the whole period. Even though there are some outliers in the time series plot of the standard deviation (see Figure 3-19), the overall behavior of the spatial fluctuation is well reproduced. As indicated earlier, the random cascade parameter is a measure of the fraction of wet surface of the underlying field. The wet fraction is successfully delineated through the statistical self-similarity parameter, β (see Figure 3-20). The spatial correlation structure of the simulated field for *dx=1 pixels* at 16 km-scale shows that the temporal fluctuation of the spatial correlation of the simulation is less than that of observation (see Figure 3-21). This may be because the temporal evolution of spatial correlation is not explicitly incorporated in the random cascade model. The evolution of spatial correlation as a function of large-scale forcing is considered in the stochastic disaggregation model from top (128 *km*) down to the critical scale (32 *km*). The trend of the spatial correlation patterns of the observation is quite well reproduced. The lag-1 (day) temporal correlations for the months of June, July and August as a function of spatial scale is presented in Figure 3-22. The stochastic disagrregation model was driven from the 128 *km*-scale and down to the 32 *km*-scale. They reasonably reproduce the observed pattern of NEXRAD precipitation over the entire range of spatial scales.

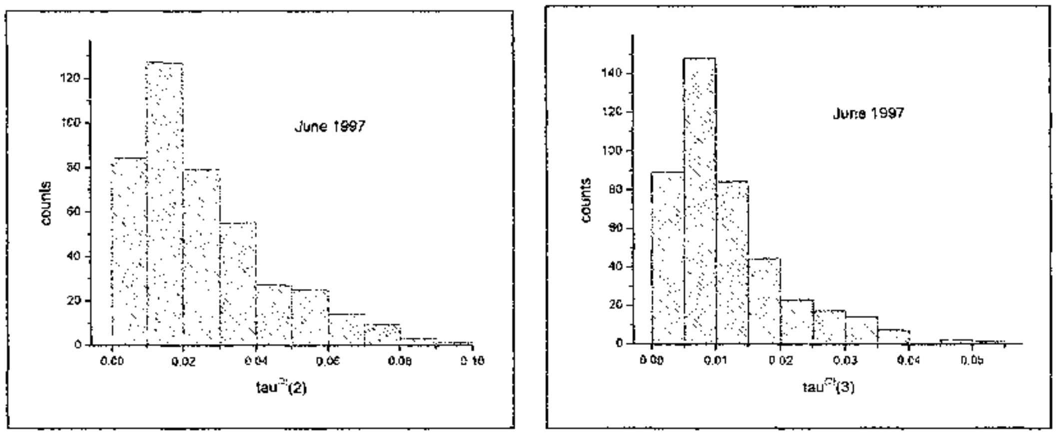

(a) June

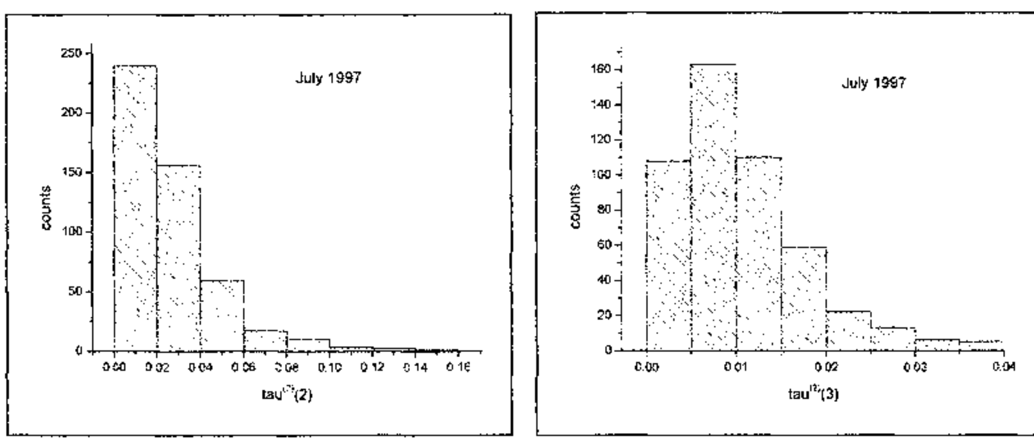

(b) July

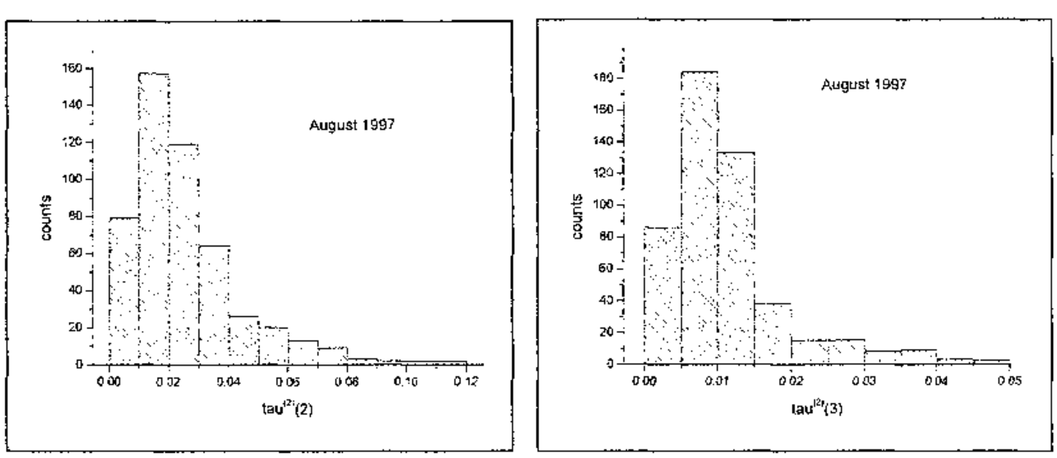

(c) August

Figure 3-17 The density plot for $\tau^{(2)}(q)$

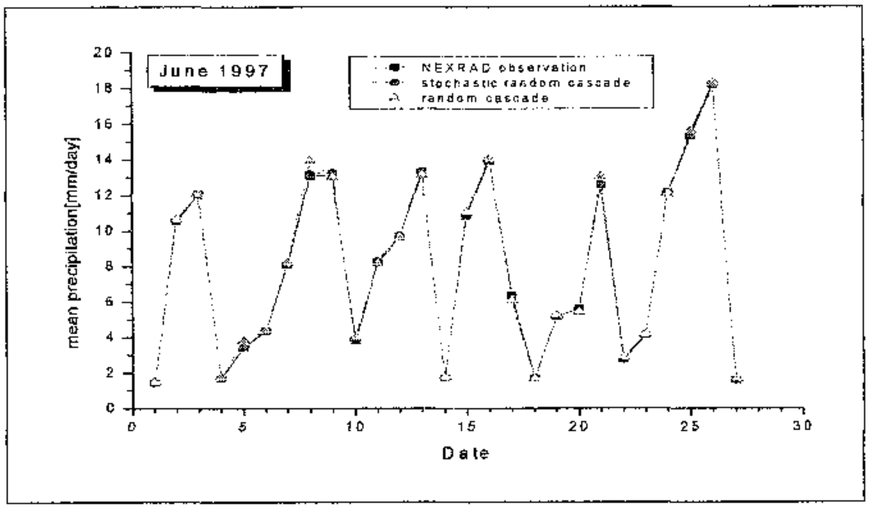

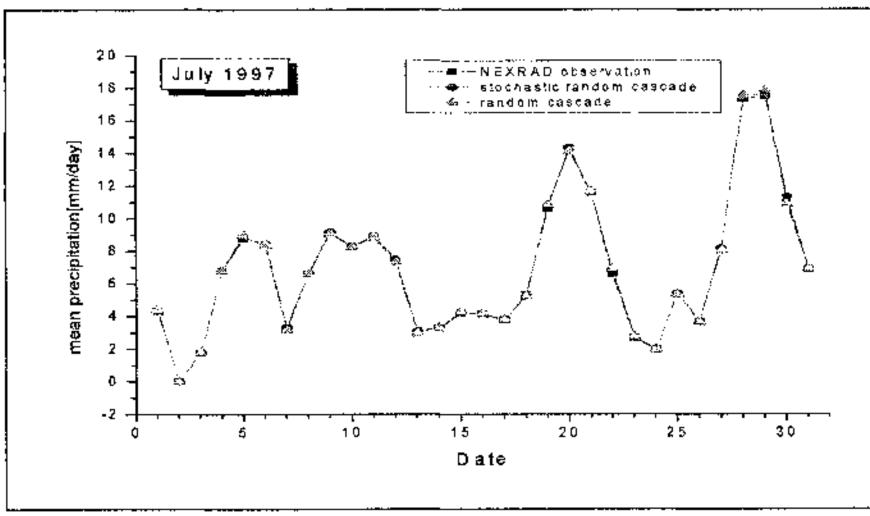

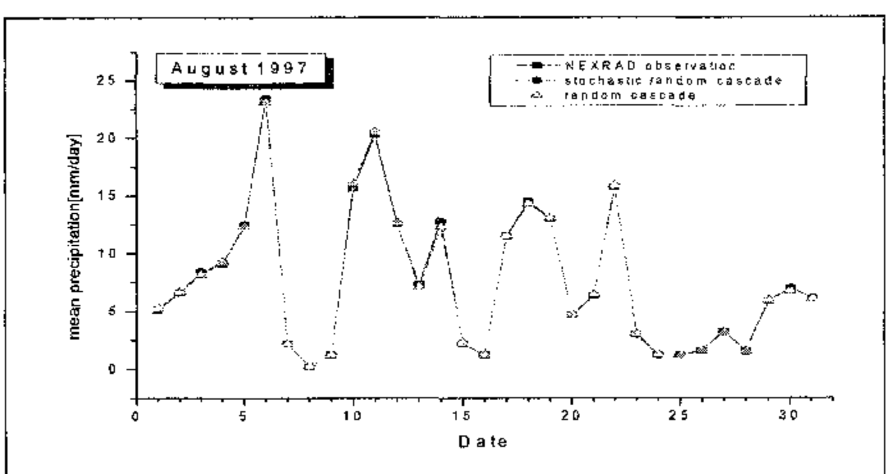

Figure 3-18 Comparison of mean precipitation of the entire field

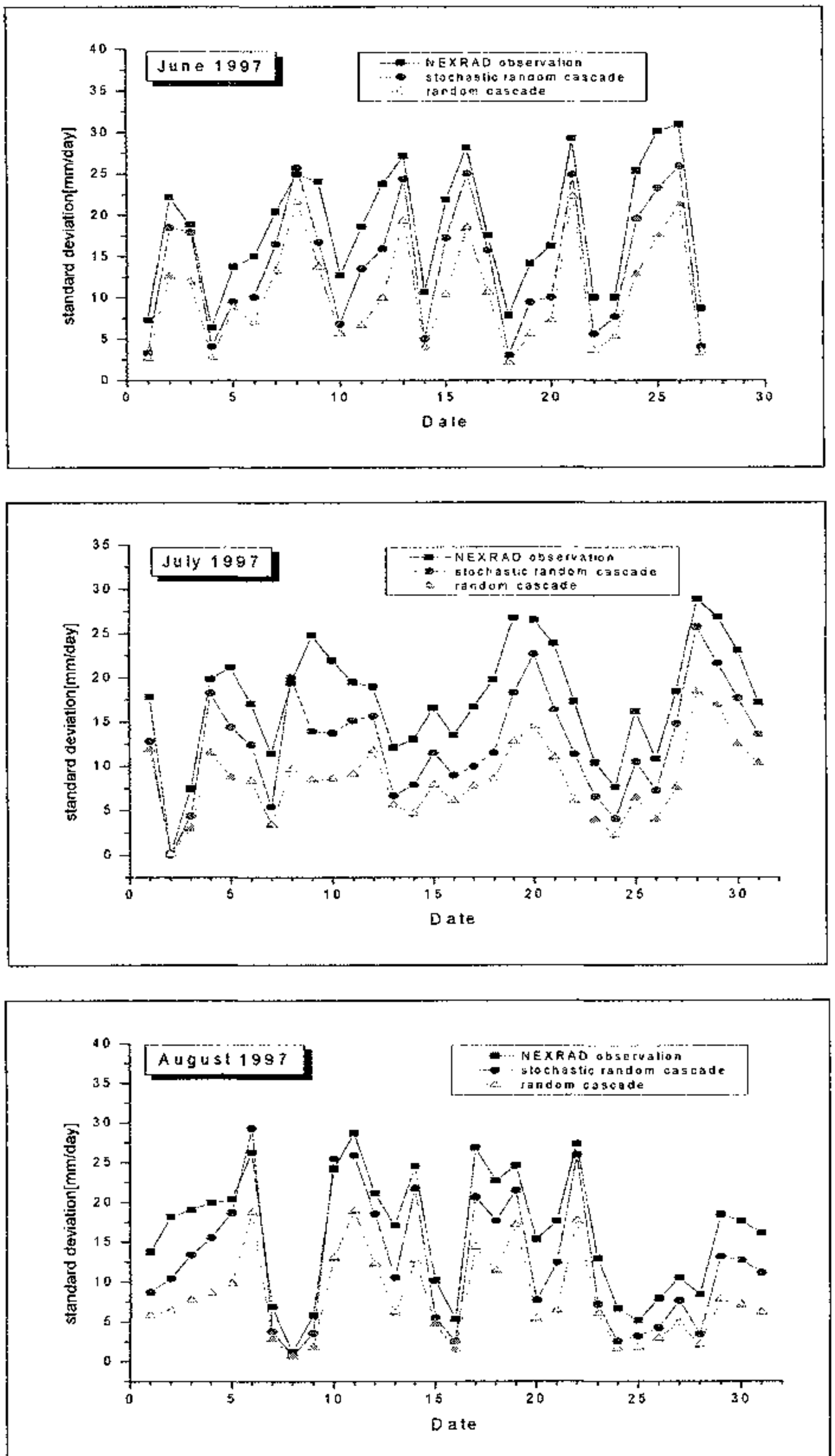

Figure 3-19 Comparison of standard deviation of the entire field

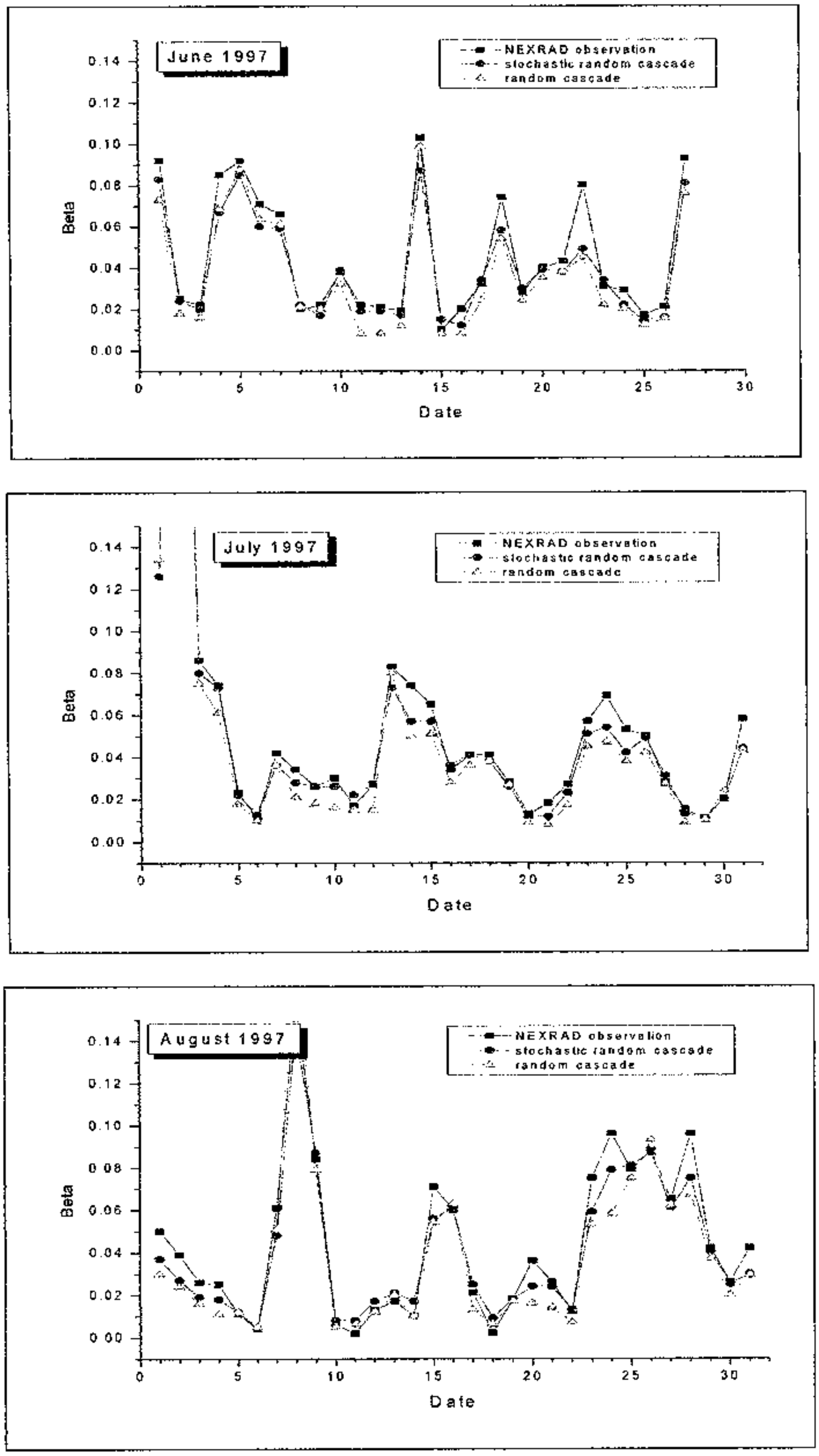

Figure 3-20 Comparison of self-similarity parameter of the entire field

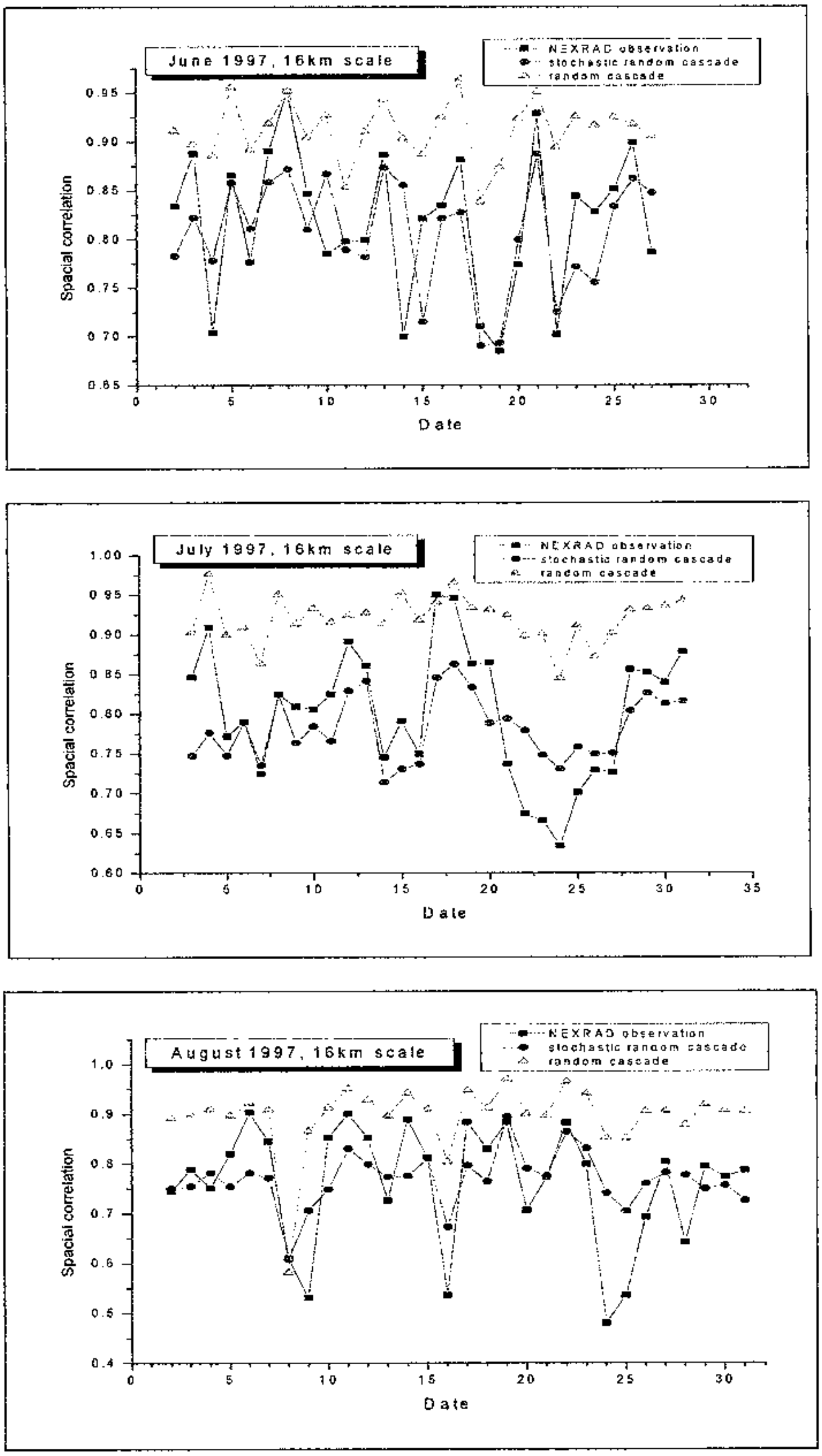

Figure 3-21 Comparison of spatial correlation between NEXRAD and simulation(16 km scale)

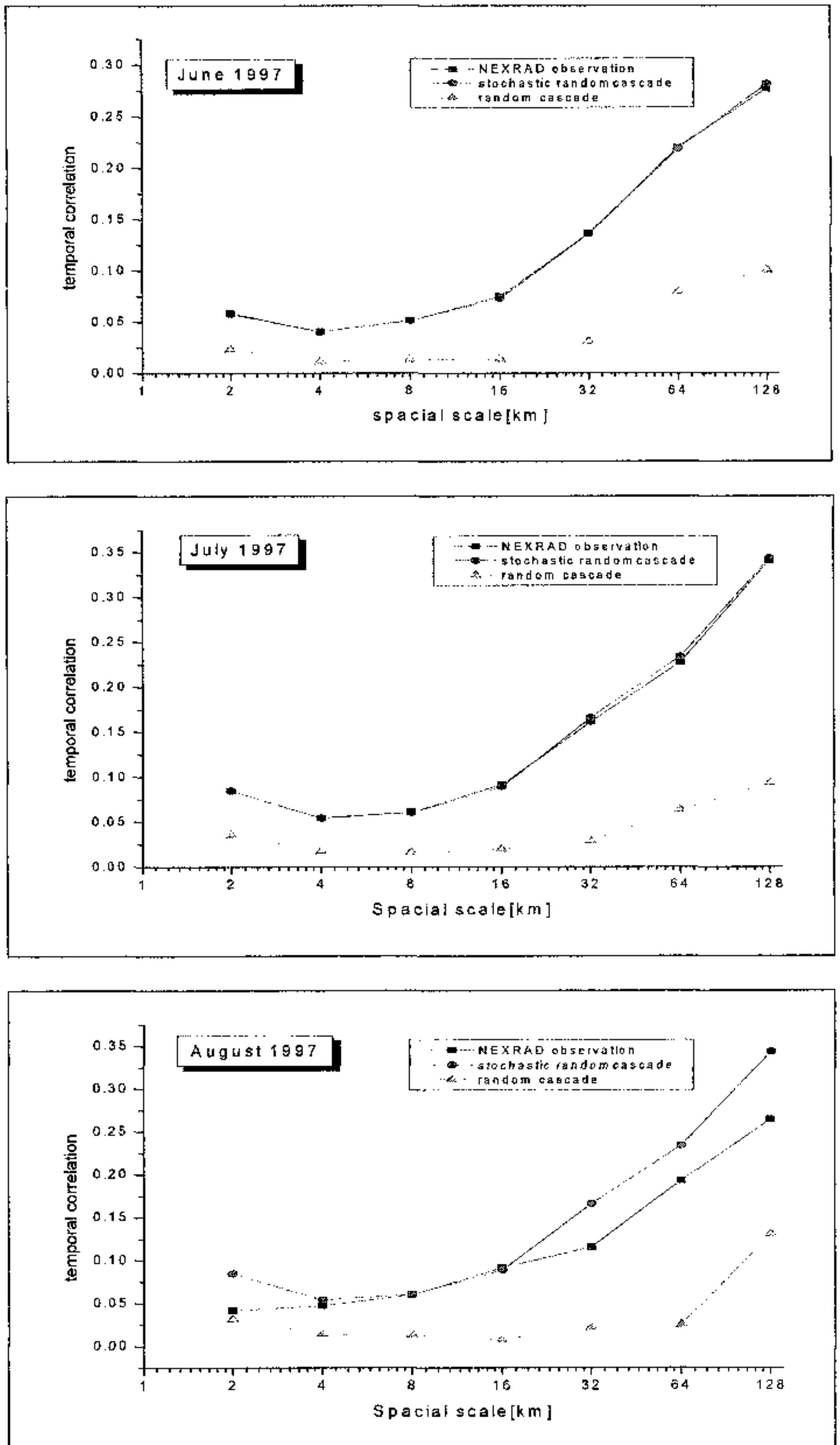

Figure 3-22 Comparison of lag-1 (day) temporal correlation between NEXRAD and simulation

3.4. Summary

In this Chapter, a methodology for downscaling of daily precipitation from the spatial scales associated with GCM output to the spatial scales required for hydrologic modeling was developed.

The downscaling model is a composite of a Stochastic Space-Time Disaggregation Model (SSTDM) to preserve the spatial and temporal dependency characteristics and an Intermittency Multiplicative Random Cascade Model (IRCM) to incorporate the statistical self-similarity, spatial intermittency, and the spatial storm cluster formation. Each of these two sub-models was applied over a specific range of scales. The corresponding scale ranges are non-overlapping and the reference level at which models are swiched is a function of the correlation structure of the observations. The statistical tests show that above 32-*km*-scale the precipitation field exhibits a statistically significant temporal correlation structure and a spatial correlation structure that is a function of scale of the field under consideration. The scaling analysis also demonstrated that a the small-scale field at scales less than 32 *km* exhibits a well-developed monofractal structure of self-similarity.

The SSTDM has 3 parameters (ϕ, ψ, σ) to be estimated. All of these parameters were revealed to be dependent on scale. The fluctuation parameter (σ) is uniformly distributed over the large-scale forcing and depends only on scale. The lag-1 (pixel) spatial correlation, characterized by the parameter ψ, is found to be scale dependent and to depend also on the large scale forcing. The lag-1 temporal correlation, ϕ, of the log-transformed precipitation data was suggested as a function of disaggregation level.

The IRCM has 2 parameters (β, ε) to be estimated. The intermittency parameter, β, exhibits piecewise semi-log relationship with background rainfall. Even though the quadratic form of the MKP function implies that the second derivative theoretically should be constant, the second derivative computed from the observations has a density distribution centered around 0.01. Therefore, the fluctuation parameter, ε, of IRCM can be computed as 0.06.

The downscaling procedure will be applied to downscale daily precipitation from a spatial scale of $256 \times 256\,km$ to spatial scale of $2 \times 2\,km$. The verification of the proposed downscaling procedure will be done by inversely disaggregating daily NEXRAD precipitation for the Central U.S. resampled over $256 \times 256\,km$ spatial scale into a $2 \times 2\,km$ scale daily precipitation. The inversely disaggregated precipitation field will be compared to original scale NEXRAD observation.

With these parameters, a test simulation for downscaling of large-scale precipitation fileds is carried out for June, July and August of 1997. The large-scale field used for this test is generated by resampling the original NEXRAD observations from a $2 \times 2\,km$-scale to a $256 \times 256\,km$-scale field. It is shown that the mean precipitation of the original field is preserved throughout the whole period. Even though there are some outliers in the time series plot of the standard deviation, the overall behavior of the spatial fluctuation is well reproduced. The wet fraction is successfully delineated through the statistical self-similarity parameter, β. The spatial correlation structure of the simulated field for *dx=1 pixels* at 16 km-scale shows that the temporal fluctuation of the spatial correlation of the simulation is less than that of the observation. This may be because the temporal evolution of spatial correlation is not explicitly incorporated in the random cascade model. The evolution of spatial correlation as a function of large-scale forcing is considered in the stochastic disaggregation model from top (128 *km*) down to the critical scale (32 *km*). The trend of the spatial correlation patterns of the observation is quite well reproduced. The lag-1 (day) temporal correlations for the June, July and August were presented as a function of spatial scale. The simulation using the new proposed model was considered to reasonably follow the pattern of NEXRAD observations over the entire range of spatial scales.

Chapter 4

4. Streamflow Prediction with Distributed Precipitation Field

4.1. Background

This chapter presents the methodology for simulating watershed response using the precipitation scenarios produced by a GCM. As mentioned in Chapter 2, the spatial scale ($200 \sim 300km$) of GCMs is usually much greater than that of hydrologic rainfall-runoff models. In a GCM, each grid is considered as a single homogeneous unit. However, there is a great deal of spatial variability present in hydrologic variables, driving forces, and process interactions occurring at sub-grid scales, that is, at scales smaller that the typical GCM scale. This spatial variability gives rise to significant effects on the streamflow response. Therefore, distributed hydrology models are required. In a distributed model, flow is calculated as a function of space and time throughout the system. A truly distributed model of a process is possible only if the process can be described by an equation having an analytical solution (Muzik 1996). For certain conditions of the system, an example of such a model is the kinematic wave model of overland flow. However, the vast majority of hydrologic equations cannot be solved analytically for the varied watershed conditions encountered in practice. In that case, these equations must be solved numerically on a discretized space-time domain. Therefore, numerical solutions assign average values over finite space-time intervals or elements corresponding to their particular discretization scheme. Thus most distributed models go through some degree of lumping. The model results can be sensitive to the scale of lumping, which can vary widely from distances measured in centimeters to areas of a watershed. The choice of scale of distributed elements will generally depend on the purpose of the simulation, the technology available, the size of watershed, the data availability, the level of accuracy required, and the knowledge, skill and experience of the modeler, etc. Conceptualizing the runoff producing mechanism is crucial for model developing or determination of proper models for a specific situation. According to Beven and Kirkby (1979), there are 4 major processes in runoff formation in a uniform basin.

i) Infiltration excess runoff: This type of runoff is also called "Hortonian runoff" and occurs every time rainfall intensity exceeds the infiltration capacity of the soil near the surface of the soil. As a result of this excess, the soil surface becomes saturated. This process is thought to have considerable relevance in areas of little vegetation cover with low values of hydraulic conductivity and in regions of high rainfall intensity. The use of physically based equations for the estimation of infiltration capacity is of importance for a better simulation of the surface runoff phenomenon. Available infiltration models can vary from approximate solutions of the Richards' equation (1931), such as the model proposed by Philip (1957), to exact analytical solutions of approximate physical models, such as the model proposed by Green-Ampt (1911). The Green-Ampt model was applied to a steady rainfall input by Mein and Larson (1973). And Chu (1978) demonstrated the applicability of the model for use under conditions of unsteady rainfall.

ii) Saturation excess runoff: This type of runoff is also called "Dunne runoff". According to Dunne (1978), this type of runoff occurs when the soil surface becomes saturated from below as a result of infiltration and downslope surface flow. This mechanism is particularly evident near channel wet lands which tend to expand or contract during and between rainfall events. This mechanism is, therefore, more suitable to surface runoff production in those wet areas rich in vegetation, typified by convergent topography and with shallow water tables. This source of overland flow contributes directly to the storm hydrograph. One of the most used models for the estimation of saturation excess runoff is the so-called TOPMODEL, proposed by Beven and Kirkby (1979). The TOPMODEL has strength in offering conceptual simplifications with respect to the initial water table profile and the soil moisture profile in the unsaturated zone above the water table. The TOPMODEL is based on some key assumptions as indicated briefly below (Figure4-1):

a) The actual lateral flow(q) is proportional to the specific catchment area (a) and is related to the equilibrium steady-state recharge rate (R), i.e.,

$$q = Ra$$

b) The saturated hydraulic conductivity (K) at a given point on a hill slope decreases along the depth of soil profile according to an exponential law, i.e.,

$$K = K_0 e^{-fz_i}$$

c) For small ground surface slopes, the local hydraulic gradient of the groundwater aquifer is assumed parallel to the local slope, and is denoted by tanβ. The downslope flow below the water table at a depth, z_i, is the product of transmissivity (T) and $\tan\beta$:

$$q = T(z_i) \cdot \tan\beta$$

iii) Downslope lateral flow of saturated or unsaturated groundwater. Subsurface flow velocities are commonly too slow to contribute appreciably to the peak of the storm hydrographs although in volume terms subsurface flow may dominate the overall response of the basin in providing the hydrograph tail and base flows.

Regardless of the complexity of the model, streamflow is calculated based on these runoff formation concepts. As noted in the literature, the fully physically and dynamically based deterministic models require huge amounts of data, sophisticated computing resources and a comprehensive understanding of the physical nature of the underlying watershed. These requirements place limits on the practical application of the models. Therefore, many of the existing distributed rainfall-runoff models are based on a compromise between a fully distributed approach and a lumped approach, and exhibit some degree of lumping in space and time.

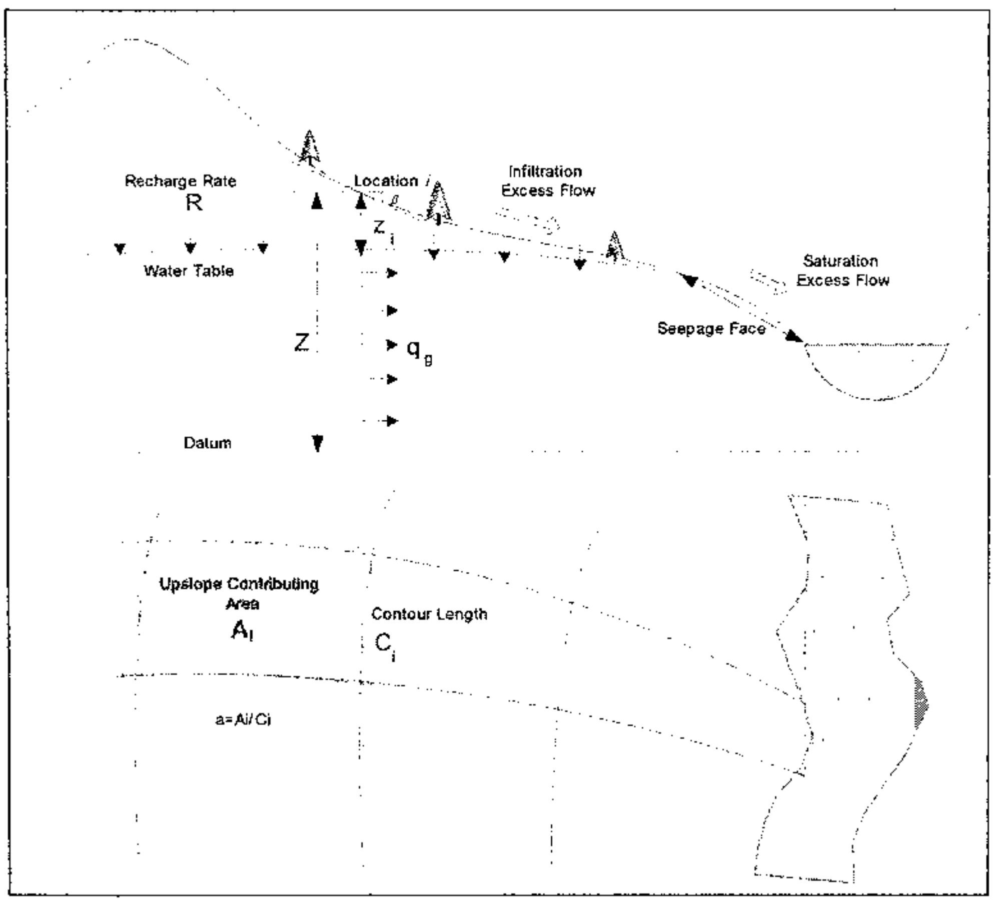

Figure 4-1 The conceptual diagram of TOPMODEL

4.2. Distributed Hydrologic Model (HEC_HMS)

The HEC-HMS is an upgraded version of the HEC-1 Flood Hydrograph package. Whereas HEC-1 takes a lumped approach and simulates event-based hydrographs, HEC-HMS has a capability for producing continuous hydrographs over long periods of time and spatially distributed runoff computation using a grid cell depiction of the watershed and quasi-distributed linear transform (ModClark) of cell-based precipitation and infiltration. The key hydrologic features for an analysis using the HEC-HMS are similar to the HEC-1. As opposed to the traditional lumped models, HEC-HMS is a distributed model requiring gridded data. Currently, there exist readily available sources for gridded precipitation data (e.g., NWS NEXRAD weather radar), topographic and land use/land cover data from the United States Geological Survey (USGS), and soils data from the National Resource Conservation Service. Watershed elements considered in the HEC-HMS include: sub-basin, reach, junction, reservoir, diversion, source and sink. Hydrologic modeling of watershed elements considers hydrologic losses, runoff transformation, open-channel routing, baseflow routing, etc., and each of these processes can be modeled using optional schemes to be selected by user.

The *sub-basin loss* methods available in HEC-HMS include: a) deficit and constant, b) Green and Ampt, c) gridded SCS curve number, d) gridded Soil Moisture Accounting (SMA), e) initial and constant, f) SCS curve number, and g) Soil Moisture Accounting(SMA). The gridded SCS curve number and the gridded Soil Moisture Accounting can only be used with the ModClark transform. The *sub-basin transform* methods consist of a a) conceptual kinematic wave model, b) the ModClark quasi-distributed linear transform, and c) empirical unit hydrograph techniques including Clark, Snyder, SCS, and user-specified. Because of the use of grid precipitation in this research, the combination of the gridded Soil Moisture Accounting (SMA) and the ModClark quasi-distributed linear transform is pertinent to our application and is selected. Therefore, the gridded SMA algorithm will be described first.

The SMA algorithm simulates the movement of water in and out of the vegetation canopy layer, the surface interception storage, the soil profile and any groundwater layers. This includes the transfer and changes in storage over time of water moving through the media. The SMA algorithm also computes an outflow of both surface runoff and groundwater flow and loss due to evapotranspiration (ET) and deep percolation, from the area to which it is applied. Even though the SMA algorithm is defined as a quasi-physical model meaning that the model components represent the physical characteristics of the watershed, these parameters may or may not be directly correlated with measured or observed physical conditions. The SMA algorithm is a lumped model in that the parameters approximate the combined physical characteristics for a given watershed. The SMA algorithm can be used in a more distributed fashion if the area over which it is applied is more detailed within a watershed. The SMA algorithm uses a series of storage volumes to keep track of the current volume of water in each land-based component of the hydrologic cycle. The storage volumes represented in the model are 3 fixed storage volumes of canopy interception, surface interception, soil profile; and a variable number of groundwater layers (Figure 4-2). Inflow and outflow fluxes control the amount of water lost or added to each of these storage components. These fluxes include ET, infiltration, percolation, surface runoff, and groundwater flow.

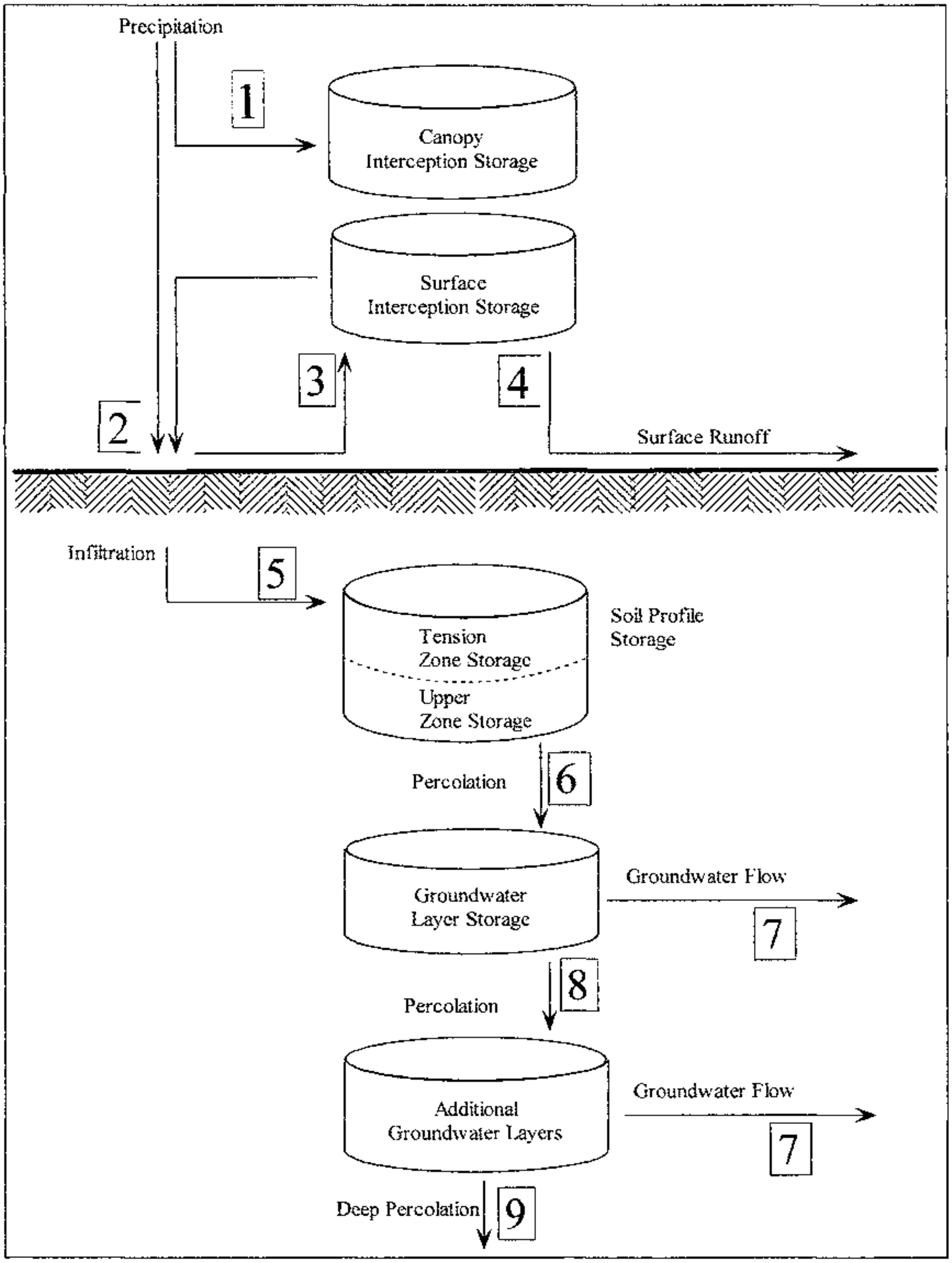

Figure 4-2 Conceptual diagram of SMA model during precipitation period

- *Canopy-interception storage*: Canopy-interception storage represents the fraction of precipitation that is captured by trees, shrubs, and grasses, and does not reach the soil surface. Precipitation is the only inflow into this storage volume (Figure 4-2 [1]). When precipitation occurs, it first fills canopy interception storage. Only after this storage is filled, precipitation becomes available for filling other storage volumes below this layer. Water is held in canopy-interception storage until it is removed by evaporation.

- *Surface-interception storage*: Surface-interception storage is the volume of water held in shallow surface depressions. Inflow to this storage comes from precipitation not captured by canopy interception and in excess of the infiltration rate (Figure 4-2 [3]). Outflows from surface-interception storage are infiltration to the soil profile or ET (Figure 4-2 [2]). Any contents in surface depression storage at the beginning of the time step are subject to infiltration. Only if the precipitation available for infiltration exceeds the potential infiltration rate, the water that has not infiltrated fills surface interception storage. Once the volume of surface interception is exceeded then the remaining excess water contributes to surface runoff (Figure 4-2 [4]).

- *Soil profile storage*: The soil profile storage represents water stored in the top layer of the soil. Inflow is infiltration from the surface (Figure 4-2 [5]). Outflows are percolation to a lower groundwater layer or ET (Figure 4-2 [6]). The soil profile zone is conceptualized as two regions, the tension zone and the upper zone. The tension zone is defined as the area that will lose water only to ET but not to percolation, whereas the upper zone is defined as the portion of the soil profile that will lose water to ET and/or percolation. In the tension zone, water is attached to soil particles and in the upper zone water is held in the pores of the soil matrix. ET occurs from the upper zone first and tension zone last.

- *Groundwater storage*: Precipitation that succeeds in moving from the soil layer down into the underlying bedrock will at some point reach an area of permanent saturation that is known as the groundwater. Water flows horizontally through the groundwater layer until it reaches a river, lake or ocean. Typical groundwater flow velocities lie in the range of 250 to 0.001 meters per day. Losses from a groundwater storage layer are due to groundwater flow or to percolation from one groundwater layer to another. Percolation out of groundwater storage either percolates to a "lower" groundwater zone (Figure 4-2 [8]),, or, if it is the "lowest" groundwater zone, it contributes to deep percolation and is lost from the system (Figure 4-2 [9]), because aquifer flow is not modeled in the SMA.

- *Flow components*: The SMA model computes fluxes into, out of, and between the storage volumes. These fluxes can take the form of precipitation, ET (evapotranspitation), infiltration, percolation, surface runoff, groundwater flow. Precipitation is the original source of input for the storage volumes in the model whereas ET is the loss from storage components of the system. The model assumes that these two processes (precipitation and ET) are not occur at the same time so that only one of these two processes proceeds for a given time step. Any evaporation occurring during precipitation events is assumed to be removed before the precipitation volume is supplied to the model.

Flow into and out of storage layers is computed for each time step in the HEC-HMS SMA model. There are two orders of computation based on whether precipitation or ET is occurring. No evapotranspiration is assumed to occur during precipitation events. The order of computation during precipitation is shown in Figure 4-2 and described briefly as follows (Bennet, 1993):

① A precipitation increment first fills canopy-interception storage.

② Precipitation in excess of canopy interception combined with any water in surface storage at the beginning of the time step becomes available for infiltration.

③ If the combination of these two exceeds a calculated potential infiltration volume, the volume of water greater than the infiltration volume returns back to surface-interception storage.

④ When surface interception storage is full, the excess becomes surface runoff and routed out of the SMA model.

⑤ The volume of water available for infiltration less than the potential infiltration volume fills the soil profile.

⑥ Water in the soil profile then percolates to the first groundwater layer.

⑦ Groundwater flow is routed out of the first groundwater layer.

⑧ The remaining water is available for percolation to the next deeper groundwater layer.

⑨ Routing and then percolation continues from each groundwater layer until the "lowest" layer in the system is reached, and percolation is to a deep aquifer and is an output from the model.

The order of computation during dry period is shown in Figure 4-3 and described briefly as follows:

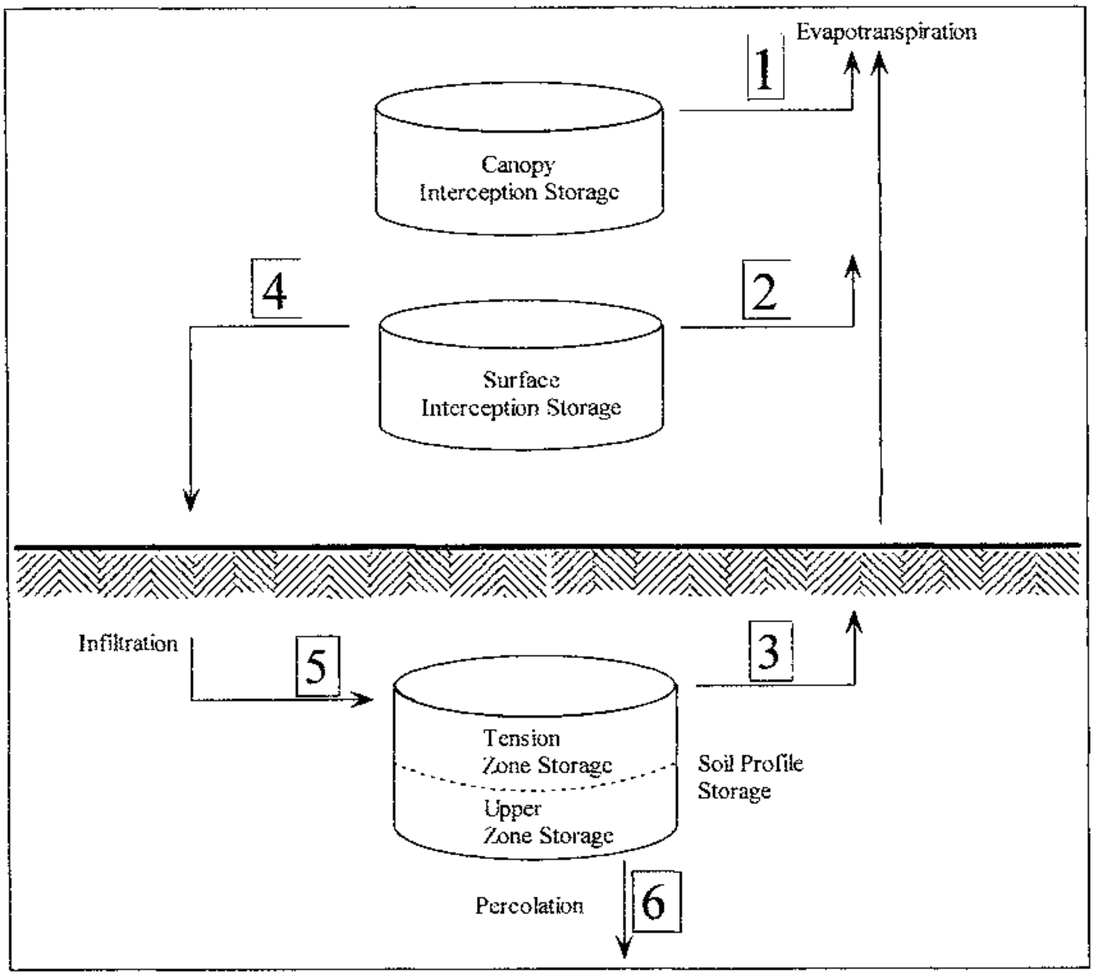

Figure 4-3 Conceptual diagram of SMA model during precipitation period

① Potential evapotranspiration is first satisfied from canopy storage.

② Surface storage is then depleted once the canopy storage is empty and if the potential ET has not been met.

③ Water is next removed from the tension zone and/or the Upper Zone of the soil profile storage if the potential ET is not satisfied.

④ Any water remaining in surface storage is available for infiltration.

⑤ The water that has infiltrated fills the soil profile.

⑥ Model simulations continue for percolation and groundwater as in precipitation periods.

A total of 3 different methods for *baseflow* are available: a) constant monthly, b) linear reservoir, and c) recession. The linear reservoir method can be used for only sub-basins using the soil moisture accounting or gridded soil moisture accounting loss methods. Recession method is suitable for watersheds where the volume and timing of baseflow is strongly influenced by precipitation events.

Channel routing for reach elements can be accomplished with one of 6 different methods: a) Kinematic wave, b) lag, c) modified Puls, d) Muskingum, e) Muskingum-Cunge 8-point section, and f) Muskingum-Cunge standard section.

The meteorological model requires precipitation and evapotranspiration data. Precipitation can be provided using one of 6 different methods: a) User Hyetograph, b) User gage weighting, c) inverse-distance gage weights, d) gridded precipitation, e) frequency storm, and f) standard project storm. The HEC-HMS uses an Evapotranspiration (ET) zone which is a conceptual area that is homogeneous with respect to evapotranspiration process and has no defined boundaries. All sub-basins in the same ET zone are supposed to have the same evaporation. An ET zone can be a discontinuous region. If sub-basin elements are set to use the soil moisture accounting loss method, the monthly average evapotranspiration method must be applied.

4.3. GIS preprocessing

The key features of distributed hydrologic models are a distributed hydrologic process description coupled to distributed input data sets, including geo-spatial information, precipitation, and physical basin characteristics. Extracting geo-spatial information from DEMs (Digital Elevation Model datasets) and preparing the input files for HMS can be achieved by GeoHMS, which is a GIS interface module and can be plugged into ArcView. The background map file that can be imported by HEC-HMS is created by Geo-HMS. Data processing also can be done semi-automatically without the HEC-GeoHMS extension by a skilled GIS specialist using GIS software or automatically by someone with a basic working knowledge of ArcView using the HEC-GeoHMS ArcView extension.

Unfortunately, HEC-GeoHMS and HEC-HMS do not currently process the grid-based precipitation data so that HEC-HMS can use it. At this stage, it is not practical for most hydrologists to process the grid-based precipitation independently. The HEC-HMS program requires gridded precipitaton data in a HEC-DSS (Data Storage System) file format. The current version (January 2001) of the HEC-HMS or HEC-GeoHMS does not have the capability to convert the grid data into a DSS file format. Therefore, the DSS file for the grid precipitation data has to be created by an external conversion program.

The grid-cell file required by the ModClark transform method could be produced by the external program called "GridParm". However, the GridParm runs only on Sun workstations equipped with ArcInfo and the grid extension. The latest version of GeoHMS has a module for creating grid cell parameter file by default.

4.3.1. South Platte River Basin

The South Platte River basin is located in the southwest corner of the Missouri River Basin. It lies between the latitudes 101° and 107° and between the longitudes 38° and 42° in the states of Colorado, Wyoming and Nebraska. The basin is enclosed by the Continental Divide on the west, the North Platte River Basin to the north, the Arkansas River Basin to the south, the Republican River Basin to the southeast and the Lower Platte River Basin to the east. Figure 4-4 shows a synoptic view and longitudinal river profile of the South Platte watershed. The total basin area is 62,936 km^2, which makes up 4.6% of the total drainage area of the Missouri River. The longest flow length is about 711 km.

Principal western tributaries that flow into the river are listed below, Tarryall Creek, North Fork South Platte River, Bear Creek, Clear Creek, St. Vrain Creek, the Big Thompson River, the Cache La Poudre River and North Fork Cache La Poudre River. These streams head eastward from the Continental Divide and have relatively steep bed slopes. The tributaries that drain to the north into the river are Plum, Cherry, Boxelder, Kiowa, Bijou, Badger, and Beaver Creeks and the ones to the south are Lone Tree, Crow, Wildcat, Pawnee, Cedar, and Lodgepole Creeks. Nearly the entire Lodgepole Creek watershed lies in Wyoming and Nebraska.

The natural vegetation of the South Platte consists of grasses, herbs, shrubs, and woodland and conifer forest ranging from the short grass type of the plains to alpine forests. The topography is a critical factor for the type and coverage of vegetation. The mountain peaks and ranges above 3,350 m are generally treeless and

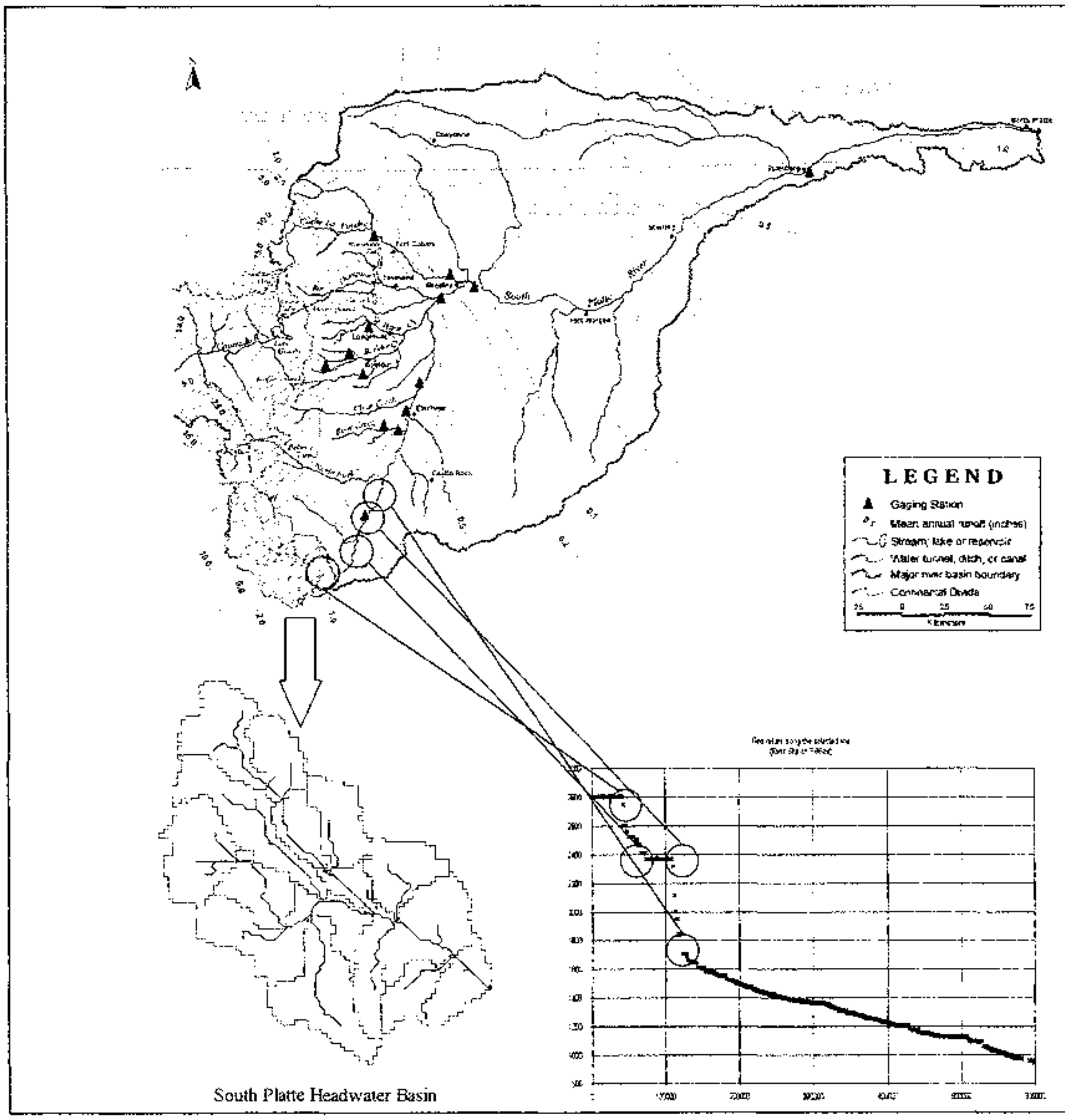

Figure 4-4 Synoptic view and longitudinal river profile of South Platte Watershed

have only a few hardy shrubs and grasses that survive the harshness of the high altitude climate. Below timberline the mountain slopes are covered with spruce, yellow pine, fir, juniper and aspen. The mountain valleys generally have a good covering of grass and shrubs and the streams flowing along the valley are bordered by willows and other shrubs. The foothills and the plains area that still remain in native vegetation are covered with native grasses and occasional clumps of deciduous trees. Cottonwoods and willow brush are found along the streams. All of the herbaceous growth and much of the shrub and woodland growth are regarded as important for both livestock and wildlife.

Three distinct geographic regions define the climate of the basin. Weather conditions vary widely between geographic regions but in general are relatively uniform in each of the mountains, the foothills, and the plains regions. The mountains region has a severe climate with heavy snowfall and a short growing season. The precipitation varies with the altitude and the aspect of slope and generally increases toward the higher elevations. The greatest precipitation, greater than 127*cm* annually, falls on the mountains of the Continental Divide that separate the watersheds of the Cache La Poudre River, the Big Thompson River, and St. Vrain Creek from the Colorado River Basin. The least precipitation also occurs in the mountainous region. South Park, shielded by surrounding high ranges, only receives approximately 28*cm* annually. The climate of the foothills region is a transition between the climates of the plains and of the mountains. Precipitation ranges between 38 to 51*cm* on the average and is less than in the mountains. Both summer and winter temperatures are more moderate that in either the plains or mountainous regions and day-to-day weather is comparatively uniform. The climate of the plains is characterized by low relative humidity, light rainfall, warm summers, cold winters, strong wind, and considerable temporal variability of annual precipitation. Near the foothills, the precipitation averages about 38*cm* annually. It decreases eastward to a low of about 30*cm* in the vicinity of Greeley then increases to nearly 48*cm* as the eastern end of the basin is approached. Most of the precipitation in the plains region falls in the form of rain from April through September.

The water resources of the South Platte River Basin consist of surface runoff originating within the basin, importations from other basins, and ground water. Most of the surface runoff is contributed by the high mountain sub-watersheds of the main river and its major tributaries. Surface water supplies are appropriated several times over by direct diversion and storage rights. Because only a portion of the water is used consumptively, each time it is applied for irrigation, municipal, and industrial purposes the residual passes down the river to serve other needs. Through this process water is used and reused many times before it leaves the basin.

According to the classification of the USGS, the South Platte River basin is a part of the Missouri region and consists of 19 sub-basins. Among these, the Headwaters basin (HUC #10190001) is located at most upstream of the South Platte River (Figure 4-4) and virgin flow is relatively well preserved. The hydrologic analysis presented in this dissertation will be performed for the Headwaters basin (HUC #10190001). The outlet of the Headwaters basin corresponds to the streamflow gaging station of the South Platte River near Lake George (USGS06696000), which is located at Park County, Colorado, 38°54'19" in latitude and 105°28'22" in longitude. The drainage area of HUC #10190001 is 2465 km^2 and the datum of the gage is 2,578 m above sea level.

4.3.2. GIS preprocessing for HEC-HMS using HEC-geoHMS

4.3.2.1. Preparation of DEM data

The quantitative assessment of hydrologic processes depends on the topographic configuration of the landscape, which is one of several controlling boundary conditions. Digital Elevation Models (DEMs) are usually stored in one of three data structures. These structures are grid structures, Triangulated Irregular Network (TIN) structures, and contour-based structures. Each of these DEM structures has its advantages and disadvantages. Square-grid DEMs are most widely used because of their simplicity, ease of use and computational efficiency. However, the grid size is dependent on certain computed landscape parameters and is difficult to be adjusted to changes in the size of landscape characteristics. TINs overcome these disadvantages to some extent; however, the computation of landscape attributes from TINs is more complex than for square-grid DEMs. Topographic representation of contour-based data structure is generally referred to as a Digital Line Graph (DLG). DLG provides better outlines of landscape features than grid structures and are well suited to define streamlines of surface runoff.

A gridded DEM file contains topographic elevations sampled on a uniform grid spacing. Typically, the horizontal grid spacing comes out to about every 30 meters for 7.5 minute DEMs, 3 arc-seconds (about 100m) for 1 degree DEMs and 30-arc seconds (approximately 1 kilometer) for GTOPO30. 7.5-minute DEM (30 x 30 m data spacing cast on Universal Transverse Mercator (UTM) projection or 1×1 arc-second data spacing) provides coverage in 7.5×7.5 minute blocks. This type of DEM provides the same coverage as a standard USGS 7.5 minute map series quadrangle for the Contiguous United States, Hawaii, and Puerto Rico. These DEMs are made available to the public by the USGS. 1-degree DEM (3×3 arc-second data spacing) provides coverage in 1×1 degree blocks. Using two DEM files of this type (three in some regions of Alaska) would provide the same coverage as a standard USGS 1×2 degree map series quadrangle. The basic elevation model is produced by or for the Defense Mapping Agency (DMA), but is distributed by USGS in the DEM data record format. These are available for download at no cost from the USGS. GTOPO30 is a global digital elevation model (DEM) resulting from a collaborative effort led by the staff at the U.S. Geological Survey's EROS Data Center in Sioux Falls, South Dakota. Elevations in GTOPO30 are regularly spaced at 30-arc seconds (approximately 1 kilometer). GTOPO30 was developed to meet the needs of the geospatial data user community for regional and continental scale topographic data. GTOPO30 is a global data set covering the full extent of latitude from 90 degrees south to 90 degrees north, and the full extent of longitude from 180 degrees west to 180 degrees east. The horizontal grid spacing is 30-arc seconds (0.008333 degrees), resulting in a DEM having dimensions of 21,600 rows and 43,200 columns. To facilitate electronic distribution, GTOPO30 has been divided into 33 smaller pieces, or tiles. The area from 60 degrees south latitude to 90 degrees north latitude and from 180 degrees west longitude to 180 degrees east longitude is covered by 27 tiles, with each tile covering 50 degrees of latitude and 40 degrees of longitude. Antarctica (90 degrees south latitude to 60 degrees south latitude and 180 degrees west longitude to 180 degrees east longitude) is covered by 6 tiles, with each tile covering 30 degrees of latitude and 60 degrees of longitude. The tiles names refer to the longitude and latitude of the upper-left (northwest) corner of the tile. Other sources of DEM data are listed in Appendix B. In this research, the GTOPO30 data is used for terrain analysis for South Platte Headwaters basin. The data is originally stored in geographic coordinates (latitude/longitude) and is referenced to the World Geodetic Survey (WGS) system of 1984 (WGS84). The basic elevation unit is meters. Neither ArcView nor ArcInfo support the conversion of signed image data; therefore the negative 16-bit signed values of original GTOPO30 will need to be adjusted after grid conversion. The data conversion and parameters for SHG map projection are illustrated in Appendix C.

4.3.2.2. Preparation of Sub-basin and Stream Network

The GTOPO30 covers continental United States with 4 consecutive tiles : W140N90, W140N40, W100N90, W100N40. These tiles are merged into one theme. The South Platte watershed lies in Colorado, Wyoming, and Nebraska. The shapefile format of U.S. states boundary map can be obtained from the National Atlas (http://nationalatlas.gov/statesm.html). The states map must be projected to Albers Equal Area projection using ArcToolbox, too, then it be overlaid on the merged DEM. The 3 states (Colorado, Wyoming, and Nebraska) are clipped from the merged DEM theme. The next task is to identify the portion of South Platte Headwater basin. To do so, the Hydrologic Units map must be prepared. The shapefile format of 1:2,000,000 USGS Hydrologic Unit boundaries of the United States is available in the Geography Network (http://www.geographynetwork.com/data/). The hydrology units map is geographically coordinated and needs to be projected to Albers Equal Area, also. Once the South Platte watershed is clipped from the 3-states DEM theme, the Headwaters study basin can be identified by defining the streamflow gaging station of South Platte River near Lake George (USGS06696000) as the outlet of the sub-basin (Figure 4-5). The river network layer can be laid over the theme. The 1:2,000,000 scale DLG files of the US streams can be obtained from USGS (http://water.usgs.gov/GIS/metadata/usgswrd/stream.html).

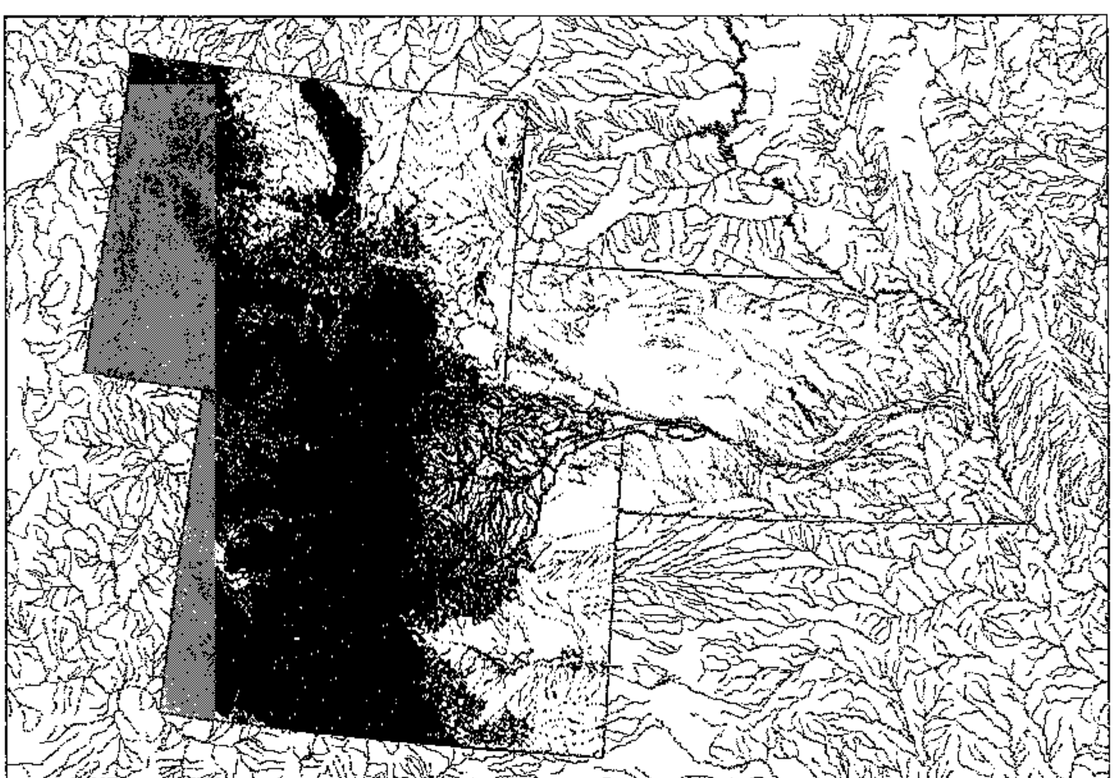

Figure 4-5 DEM clipping from the original GTOPO30

4.3.2.3. Terrain Processing using HEC-GeoHMS

The derived channel network from 1km-resolution GTOPO30 reveals obviously incorrect links in certain areas, especially in the vicinity of reservoirs (Figure 4-6); therefore, it was decided that burning the streams into the DEM would be necessary to obtain an accurate depiction of the stream network. Burning in of streams involves taking the DLG stream network and converting it into a grid in the same map projection as the DEM onto which the streams will be burned. Once the stream grid is overlaid onto the DEM, all points on the DEM except for the grid associated with the stream network are raised an arbitary value. Burning in streams accomplishes two things. First, it ensures that a more accurate stream network will be created from the DEM. Second, it guaranties that once water enters a part of the stream network, it will stay within the network and eventually flow off the DEM (Figure 4-7).

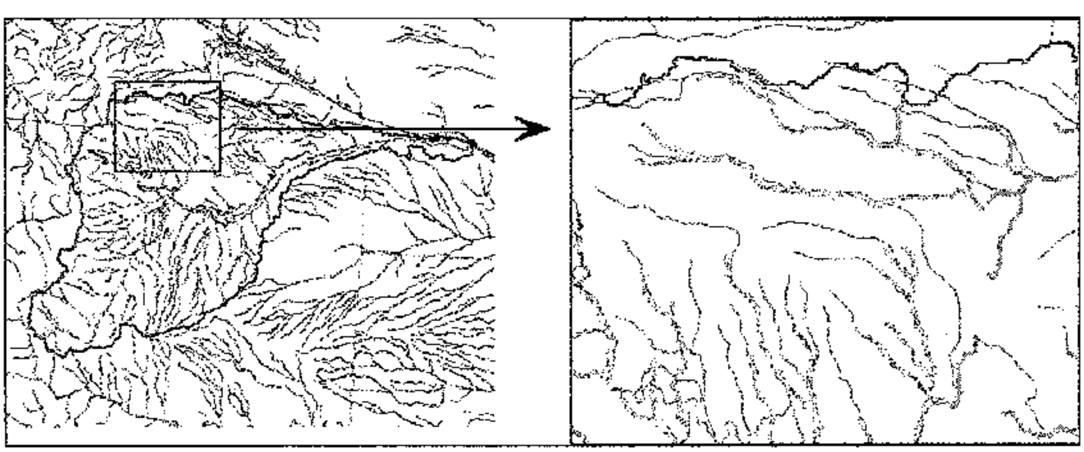

Figure 4-6 Derived stream network (green) *vs.* real stream network (blue)

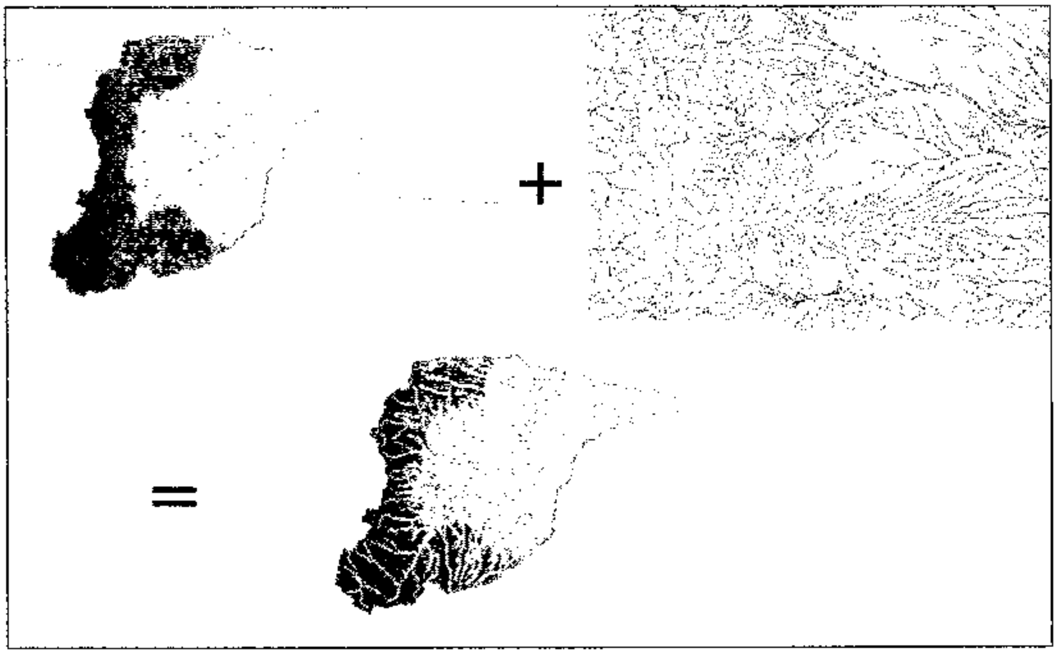

Figure 4-7 Burning in of a stream network into a DEM

All DEM files possess sinks or pits, places where water gets trapped. If water falls onto any of the cells in the DEM, the water should be able to flow to the edge of the DEM via some route. Because pits trap water and hinder flow, they can lead the network extraction process to produce the wrong flow direction. Thus, the Fill Sinks function eliminates all pits from the DEM by raising pit cell elevations so as to level the pits with the surrounding terrain. While it is necessary for all pits to be removed, the inaccuracies of the DEM data set will create some pits that are not really there. This is actually not a problem because pits, in most cases, exist in minor scales, and smoothing them out of the DEM will not significantly alter the flow patterns in the DEM. Only tiny sinks will be filled, since large sinks, such as lakes, are real sinks which we do not wish to remove from the DEM.

When rainfall occurs on a pixel on the DEM, it may flow along one of 8 different directions to an adjacent grid cell depending upon which direction offers steepest descent. The pre-processing also includes the generation of a flow direction grid file. This flow direction grid indicates the direction in which water will flow from each point on the elevation grid. Then, a flow accumulation grid is produced from the flow direction grid. Each value on the flow accumulation grid represents the number of grid cells that the grid cell in question drains. The flow accumulation grid plays key role in the Stream Definition calculation. The user can appoint how many cells must be upstream of a given cell for that cell to be considered part of the stream network. Obviously, all cells belong to the stream network, but only the cells that drain a significant (i.e., a threshold) number of cells should be considered a river or a stream or some other sort of drainage mechanism. This last procedure allows the extraction of the stream network (Figure 4-8).

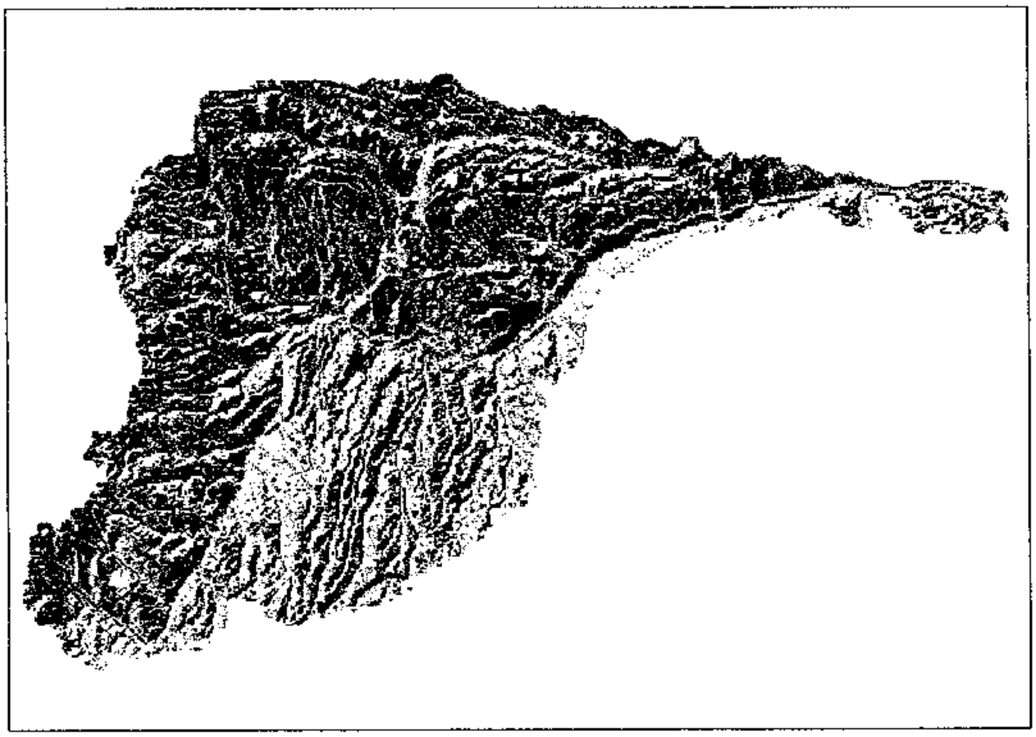

Figure 4-8 Flow direction associated with grid aspect

Using the derived channel network, the sub-basins boundary can be delineated. The accuracy of the channel network can be confirmed by comparing the areas of sub-basins delineated from the derived channel network (Table 4-1). The absolute maximum, absolute minimum and average errors are 3.2, 0.06, and 0.55%, respectively. This result indicates that the stream network which was burned into the original DEM has enough detail to model the region of interest properly.

The grid structure is excellent for cell-based analysis (Figure 4-9), however, vector data are easier to use and store. Therefore, grids are usually employed to develop a data set, and the final product is then converted to vector format. Since a vector polygon does not necessarily have a square shaped border like the grid, when a grid is converted to a polygon, a 'dangling polygon' may be created on the edge of an existing polygon. This dangling polygon is a tiny watershed that does not exist, and should be dissolved into the parent watershed polygon to which that drainage area really belongs.

Unit : km^2

Gaging station	Area(by USGS)	Area(derived from topology)	Error(%)
Paxton, NB	62,160	60,183	3.2
Julesburg, CO	60,070	58,879	2.0
Crook, CO	49,826	49,474	0.7
Balzac, CO	43,646	43,164	1.1
Fort Morgan, CO	38,358	38,382	-0.06
Weldona, CO	34,304	34,011	0.9
Masters, CO	31,533	31,977	-1.4
Fort Lupton, CO	12,976	12,935	0.3
Henderson, CO	12,207	12,183	0.2
Waterton, CO	6,788	6,814	-0.4
South Platte, CO	6,680	6,689	-0.1
Cheesman Lake, CO	4,538	4,625	-1.9
Lake George, CO	2,494	2,455	1.6
average			0.55

Table 4-1 Comparison of sub-basin areas certified by USGS and derived from topology

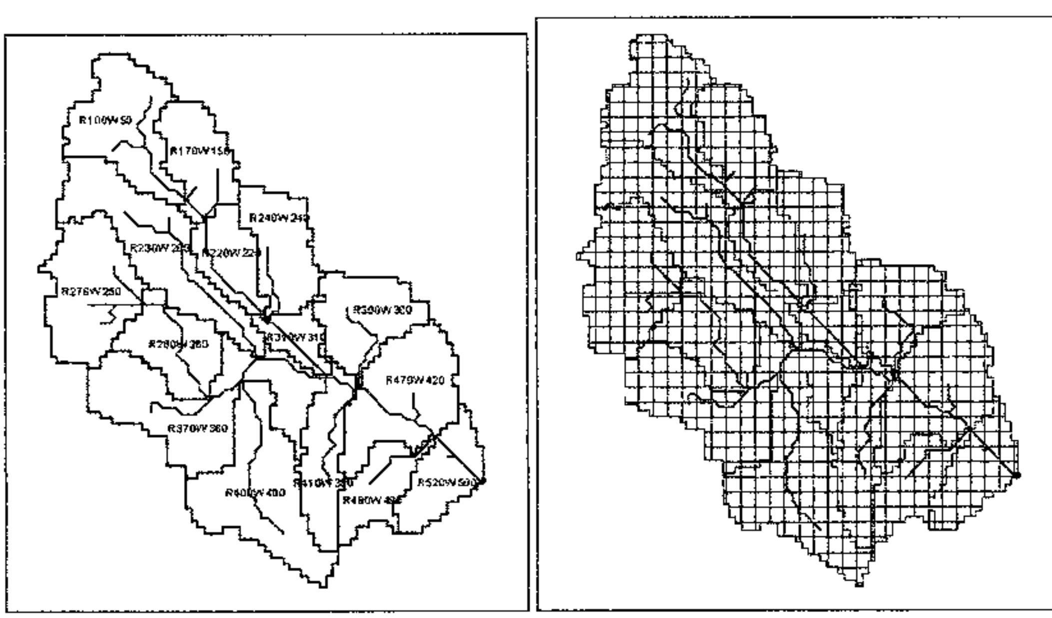

Figure 4-9 South Platte Headwaters basin on SHG grids

4.3.2.4. Preparation of State Soil Geographic (STATSGO) database

The U.S. Department of Agriculture's (USDA) Natural Resources Conservation Service (NRCS), formerly the Soil Conservation Service (SCS), established three soil geographic data bases representing kinds of soil maps. The maps are produced from different intensities and scales of mapping. The 3 soil geographic data bases are the Soil Survey Geographic (SSURGO) data base, the State Soil Geographic (STATSGO) data base, and the National Soil Geographic (NATSGO) data base. Among those, the STATSGO data base was designed primarily for regional, multistate, river basin, State, and multicounty resource planning, management, and monitoring. The mapping scale for a STATSGO map is 1:250,000. The level of mapping is designed to be used for broad planning and management uses covering state, regional, and multi-state areas. Map unit delineations match at state boundaries. States have been joined as one complete seamless data base to form statewide coverage. STATSGO data are available in the USGS DLG format.

The union product of STATSGO and sub-watershed themes provides the information concerning what types of soils are present in each sub-basin area (Figure 4-10). The most dominant map unit identification number (muid) is CO338 that occupies 42.2% of the Headwaters basin (Table 4-2). The CO338 contains 19 soil components. Most of them are well drained loam or sandy loam. The average bed rock depth is 153*cm* (about 60*inches*) deep. The remaining *muid*'s are CO337 (19.5%), CO303 (16.4%), CO411 (7.1%), etc. The soil component and map unit table, which are loaded when the STATSGO theme is imported, provide detailed information of characteristics of the specific soil component. Table A-F1 summarizes the characteristics of soil components necessary for determining parameter values of the rainfall-runoff model. The definition of soil data elements used in Table A-F1 is given in Table A-F2.

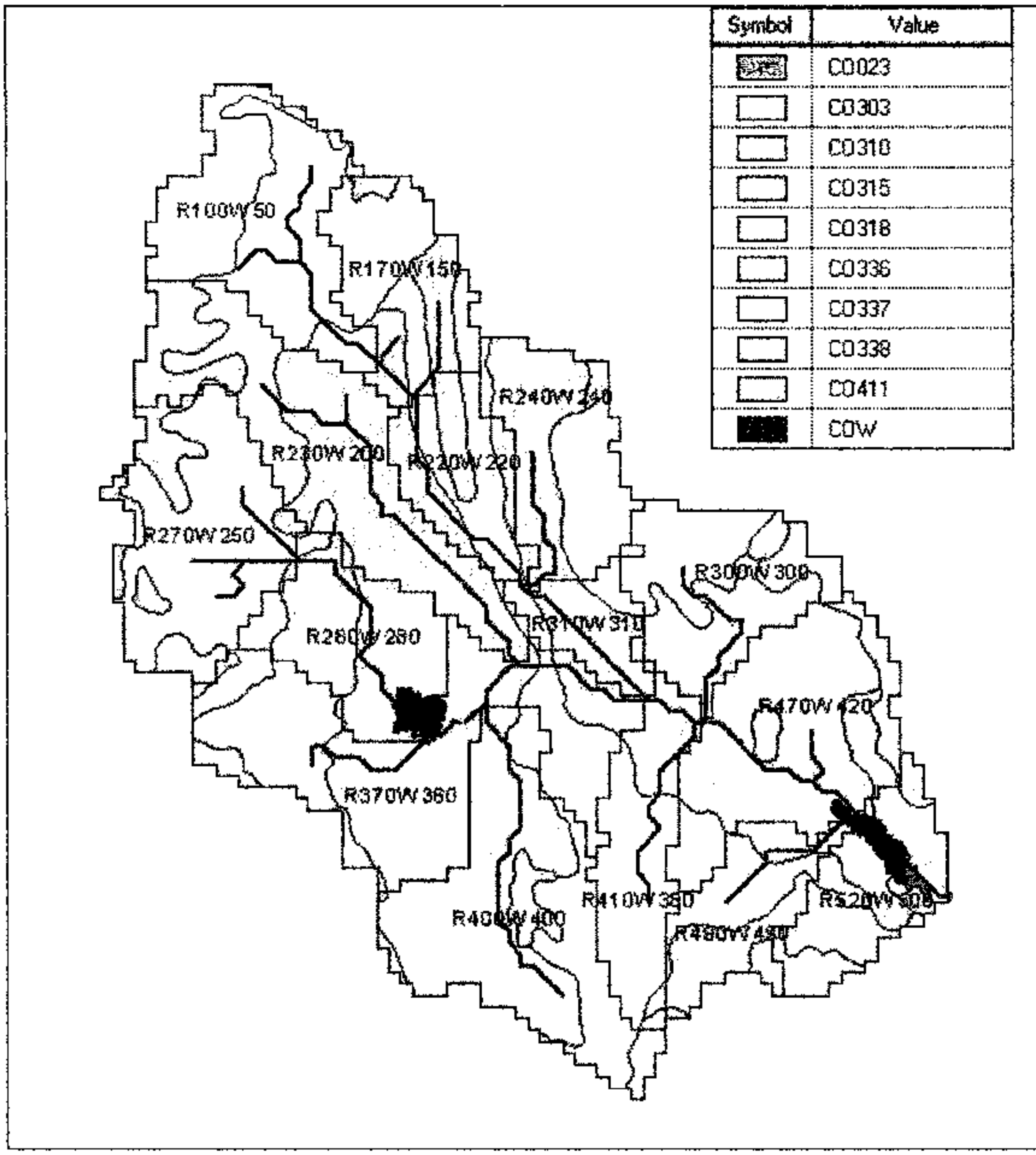

Figure 4-10 STATSGO map for South Platte Headwaters basin

Watershed	muid	area	%	Watershed	muid	area	%
R100W50	CO023	0.313	0.16	R310W310	CO337	17.42	30.39
	CO303	100.42	51.48		CO338	39.91	69.61
	CO411	81.09	41.57		total	57.33	100.00
	CO338	13.24	6.79	R370W360	CO303	13.78	4.76
	total	195.06	100.00		CO315	13.19	4.55
R170W150	CO303	54.23	43.34		CO336	65.75	22.70
	CO338	23.15	18.50		CO337	44.55	15.38
	CO441	4.57	3.65		CO338	148.87	51.39
	CO337	27.56	22.02		COW	3.53	1.22
	CO338	15.63	12.49		total	289.67	100.00
	total	125.14	100.00	R400W400	CO310	13.92	5.48
R220W220	CO337	43.88	45.16		CO315	11.56	4.55
	CO338	53.29	54.84		CO337	67.98	26.75
	total	97.17	100.00		CO338	160.69	63.23
R230W200	CO303	57.94	23.75		total	254.15	100.00
	CO411	40.54	16.62	R410W380	CO315	2.22	1.81
	CO336	1.44	0.59		CO318	2.26	1.85
	CO337	2.26	0.93		CO337	84.95	69.44
	CO338	141.81	58.12		CO338	32.91	26.90
	total	243.99	100.00		total	122.34	100.00
R240W240	CO310	4.53	3.37	R470W420	CO310	21.39	9.97
	CO337	59.01	43.96		CO315	18.77	8.75
	CO338	70.69	52.66		CO337	19.34	9.01
	total	134.23	100.00		CO338	154.13	71.81
R270W250	CO303	156.38	76.08		COW	1	0.47
	CO336	1.01	0.49		total	214.63	100.00
	CO338	3.32	1.62	R490W490	CO315	7.9	8.13
	CO411	44.83	21.81		CO318	34.91	35.92
	total	205.54	100.00		CO337	38.88	40.01
R280W280	CO303	12.94	9.79		CO338	14.56	14.98
	CO336	49.5	37.46		COW	0.93	0.96
	CO338	63.13	47.78		total	97.18	100.00
	COW	6.57	4.97	R520W500	CO310	27.12	24.24
	total	132.14	100.00		CO315	21.09	18.85
R300W300	CO310	6.29	4.87		CO318	27.01	24.15
	CO315	1.74	1.35		CO337	7.14	6.38
	CO337	57.69	44.69		CO338	18.69	16.71
	CO338	63.36	49.09		COW	10.81	9.66
	total	129.08	100.00		total	111.86	100.00

Table 4-2 STATSGO soil distribution of sub-basins of South Platte Headwaters basin

4.3.2.5. Grid rainfall processing

The NEXRAD data during 1 June 1997 to 31 August 1997 was used for HMS calibration. Then, the downscaled GCM grid precipitation of 20 years total was used for simulating several climate change scenarios. In HMS, the grid-based rainfall data must be in the HEC-DSS (Data Storage System) format.

The HEC-DSS was first conceived and designed in 1979 by Arthur F. Pabst, Mark G. Lewis, and Rochelle Barkin. DSS was developed to meet the specific needs of applications in water resources studies. In order to efficiently manage large amounts of related data for practical applications, routines have been developed which organize and transfer data in blocks of continuous data. For example, each block of data for time series applications consists of a record of a time-dependent variable for a day or month or year. By storing data in this manner, an entire year of daily flows (or block of data) can be handled as a single element and accessed by one "search" of the data base. Other routines deal with tables of paired data, such as stage-discharge, stage-damage or discharge-frequency relationships. HEC-DSS uses a block of sequential data as the basic unit of storage. This concept results in a more efficient access of time series or other uniquely related data. HEC-HMS data conversion process is explained in Appendix E.

4.3.2.6. Preparation of HMS parameter files

The grid-cell parameter file represents sub-basins as grid cells for the distributed-modeling approach. The HMS requires a ModClark parameter file for use in conjunction with grid-based rainfall in the DSS format. Before HEC-GeoHMS, the parameter file was created by GridParm, which generates terrain grids from DEM using Arc/Info AMLs. GridParm only runs on Sun workstations equipped with Arc/Info and the grid extension. The GeoHMS is now prefered over the GridParm because of its ease of use. The grid-cell parameter file is produced by intersecting a grid with the sub-basin. In other words, the parameter file contains values for hydrologic properties of cells defined by the intersection of a set of watershed boundaries with cells in the SHG grid. Each grid cell contains the information of X and Y coordinates, grid-cell travel distance to outlet, grid-cell area. The cell resolution for the SHG grid used in this research is 2,000 m, which is consistent with the NEXRAD resolution. Additionally, HMS requires a background map file (mapfile.map), which captures the geographic information of the sub-basin boundaries and stream alignments in an ascii text file that can be read by HMS.

4.3.2.7. Snowmelt Runoff

Precipitation in the form of snow and snowmelt runoff are important processes in mountainous areas at high altitude. The snowfall season length characteristics depend on location (i.e., latitude), the aspect of slope, surface elevation, etc. and generally increases toward the higher elevations. Most snow precipitation in the plains of the conterminous U.S. falls from October to March, but in the mountainous areas it occurs from September to May. Therefore, snowmelt runoff can have significant effects on the streamflows during June or even after June. These effects are often similar to floods induced by heavy rainfall in the sense that there can be sudden increases of streamflow as the atmospheric temperature rises sharply. However, soil moisture, groundwater flow conditions, etc, can differ a lot from the events of rainstorms.

The target season of rainfall-runoff analysis in this research is from June to August, which in the study basin usually exhibits the most intense rainfall in the year. During this time, most precipitation in the study basin occurs in the form of rainfall, and that was one of the main reasons for selecting the season of analysis. However, streamflow may still be affected by the condition of the remaining snowpack in the basin and consequent snowmelt runoff. If we need consider snowmelt runoff process in modeling streamflow, the portion of streamflow contributed by snow melting needs to be identified over time and space first so that we can decide how significant the snow melting process is in the specific time and region. In this research, however, the snow melting process could not be explicitly incorporated in the rainfall-runoff analysis for several reasons. First, the focus of this research is rainfall variability in space and time and as a function of scale, and the impacts of changes in that variability on streamflow response. Therefore, the selection of the season and study basin was made so as to minimize the likelihood of snowmelt runoff influence. Second, limitation of data availability for snowmelt runoff process calibration, e.g. separation of snow melting flow from the surface water hydrograph, soil moisture conditions, snow accumulated in the study area, etc. As a result of these choices, the distributed hydrologic model (HEC-HMS) used was selected based on its ability to simulate the spatial variability of rainfall and it in fact cannot handle snow melting process. The main objective of this research is to examine the relative dynamic behavior of streamflow patterns as a result of precipitation change or variability.

4.4. Calibration of HEC-HMS Model for South Platte Headwaters Basin

Before running the HMS model, a 'Basin model', a 'Meteorological model', and a 'Control specifications' must be configured. The HMS schematic diagram with watershed map is loaded in the basin model (Figure 4-11). The entire Headwaters basin consists of 15 sub-basins and the Soil Moisture Accounting (SMA) units corresponding to each sub-basin need to be specified for canopy, surface, soil profile, and groundwater, etc. The model parameters for 'Loss rate', 'Transform of excess rainfall', 'Baseflow', and 'Channel routing' must be assigned. The observation values of streamflow at the basin outlet need to be available for the purpose of calibration and comparison.

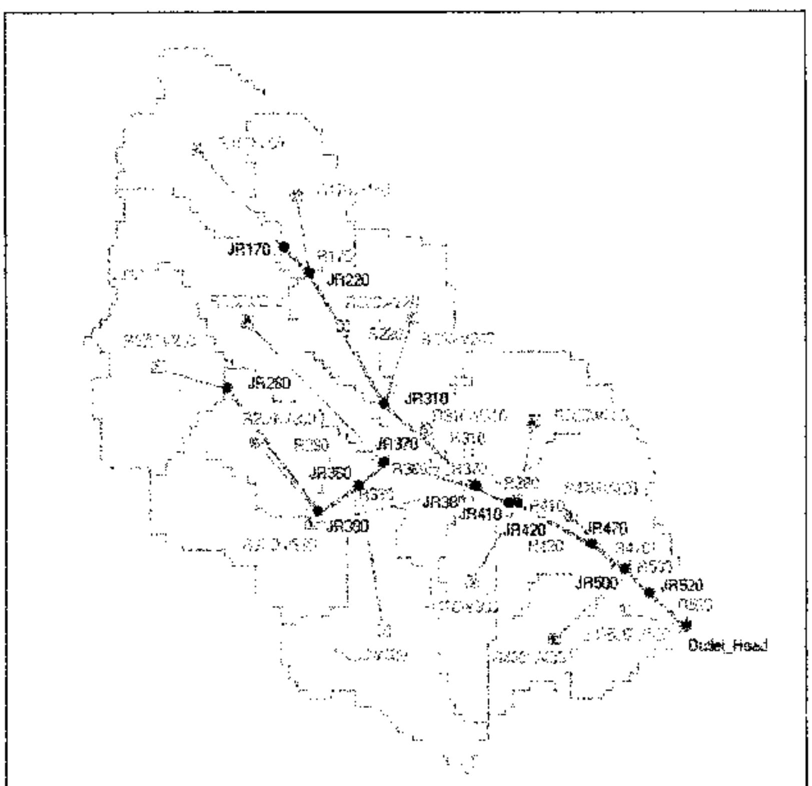

Figure 4-11 HMS schematic diagram for Headwaters basin

As mentioned in Section 4.2, even though the SMA model components represent the physical characteristics of the watershed, these parameters may or may not be directly correlated with measured or observed physical properties. That is because the SMA algorithm applies a degree of lumping to its parameters in approximating the combined physical characteristics for a given watershed. The initial SMA units and initial storage as a percentage of capacity for each layer are shown in Table 4-3.

Canopy interception	
- initial storage (%)	20
- storage capacity (mm)	2
Surface depression	
- initial storage (%)	50
- storage capacity (mm)	5
- soil infiltration max. rate (mm/hr)	2
Soil profile	
- initial storage (%)	70
- storage capacity (mm)	10
- tension zone capacity (mm)	2
- percolation max. rate (mm/hr)	1
Groundwater1	
- initial storage (%)	100
- storage capacity (mm)	20
- percolation max. rate (mm/hr)	0.5
- storage coefficient (hr)	30
Groundwater1	
- initial storage (%)	100
- storage capacity (mm)	20
- percolation max. rate (mm/hr)	0.5
- storage coefficient (hr)	30

Table 4-3 Initial estimate for SMA units and initial storage capacity

Rainfall radars are very useful for areas that do not have a sufficient number of gaging stations. However, the radar measurement has various sources of error including, for example, (1) varying atmospheric conditions between the radar and the hydrometeors, (2) distance from the radar to the hydrometeors, (3) hydrometeor characteristics, and (4) radar characteristics, etc (Bedient and Huber, 2002). Atmospheric conditions between the radar and the rain producing target affect the efficiency with which precipitation returns energy back to the radar. Backscattering and absorption of the radar signal by the raindrops in the intervening atmosphere reduce, or attenuate, the signal strength. With distance, signal strength is further attenuated, making accurate rainfall rate estimation difficult. The radar operator does not exactly know the size of the raindrops or the number of drops of each size; known as the Drop Size Distribution (DSD), which affects the strength of the return signal. Most important, radar measures reflectivity at heights extending to 15 km in the atmosphere, where water droplets may co-exist between liquid and frozen states. The rainfall rate depends not only on the DSD but also on the fall velocity of the raindrops. Downdrafts (updrafts) during a thunderstorm can cause a localized increase (decrease) in fall velocity of rainfall. These localized effects, among others, cause precipitation rates estimated aloft by radar to differ from rainfall rates measured on the ground at point locations of the gages. However, accurate and precise rainfall measurement can be attained through the combined use of the radar and ground rain gage networks. The radar measurement can be consistent to ground gage observations by removing systematic and random errors (Bedient and Huber, 2002). For effective radar-to-gage calibration, there must be some extent of rain gage network. The Headwaters basin has 6 rainfall gage stations (Figure 4-12 and Table 4-4). However, just 2 (Antero Reservoir and Lake George) of them have records for the year 1997. The time series of rainfall between the averaged NEXRAD for the entire Headwaters basin and point observation at the 2 stations is compared in Figure 4-13. Considering the 15 sub-basins in the Headwaters basin, 2 stations are not enough to carry out effective radar-to-gage calibration. Therefore, in this study, the systematic and random errors embedded in the NEXRAD are subject to lumping in the calibration of the parameters of HMS model.

The final calibration of the HMS model to the 1997 JJA NEXRAD precipitation is shown in Table 4-5. The hydrograph at the outlet of the basin (S. Platte River near Lake George) and the calculation summary table are given in Figure 4-14 and Table 4-6, respectively. The global summary of HMS results includes the peak discharge, the time of peak, volume, and the drainage area of each one of the hydrologic elements. There are 7 streamflow gage stations within the Headwaters basin (Table 4-4). Two of them (Four mile creek near Fairplay, and S Platte River near Lake George) are located at the outlet of sub-basins, but the Four mile Creek has records just for 1978-1980. Therefore, the streamflow gage station that can be used for calibration is only the South Platte River near Lake George (station ID : 06696000). The lack of additional gage stations hinders a more accurate tuning of the sub-basin hydrographs. The hydrographs of Figure 4-14 show a reasonable fit between simulated and observed hydrographs in terms of amount and timing of the peak flows except for the 3rd peak (Jul. 18 – Aug. 4). Considering the rainfall pattern of the sub-basins, the R310W310 and R270W250 would lead to the shape of the 3rd peak in Figure 4-14. However, the absolute rainfall amounts of the hyetograph during that period in those 2 sub-basins were not high enough. The recession rate of the hydrograph follows the observations except for the period between Aug. 20 – 31.

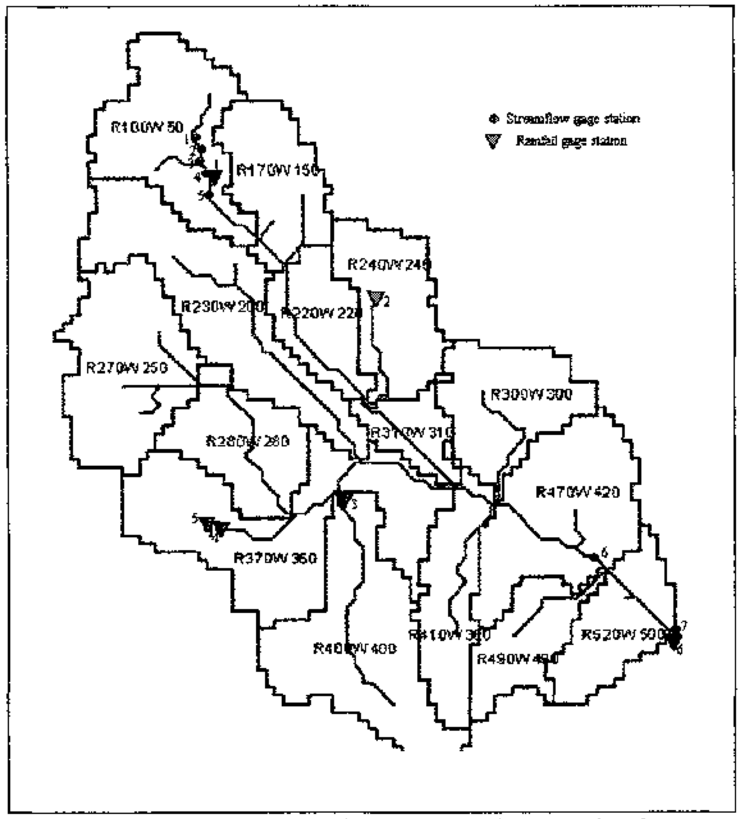

Figure 4-12 Rainfall and streamflow gage stations in Headwaters basin

Streamflow gaging station					
	Sta. ID	Station Name	Latitude	Longitude	Elev.(ft)
1	06693800	Mosquito creek near Alma, CO	39:16:12	106:03:02	10,220.0
2	06693980	Middle Fork S. Platte river above Fairplay, CO	39:14:12	106:01:43	10,050.0
3	06694700	Four mile creek near Fairplay, CO	39:11:04	106:03:47	10,250.0
4	06694400	South Fork S. Platte river above Fairplay, CO	39:04:57	106:02:52	9,470.0
5	06694100	Middle Fork south Platte river near Hartsel, CO	39:01:20	105:45:29	8,796.0
6	06695000	S Platte river above 11mile canyon near Hartsel, CO	38:58:03	105:34:51	8,612.8
7	06696000	S Platte river near Lake George, CO	38:54:19	105:28:22	8,458.0
Rainfall gaging station					
1	2814	Fairplay, CO	39:14:00	106:00:00	10,000.0
2	1811	Como 13 SSE, CO	39:09:00	105:47:00	9,500.0
3	3811	Hartsel, CO	39:02:00	105:48:00	8,870.0
4	263	Antero Reservoir, CO	38:59:00	105:53:00	8,920.0
5	258	Antero Junction 3 NNE, CO	38:58:00	105:57:00	9,030.0
6	4742	Lake George 8 SW, CO	38:54:00	105:28:00	8,520.0

Table 4-4 The rainfall and streamflow gaging stations in Headwaters basin

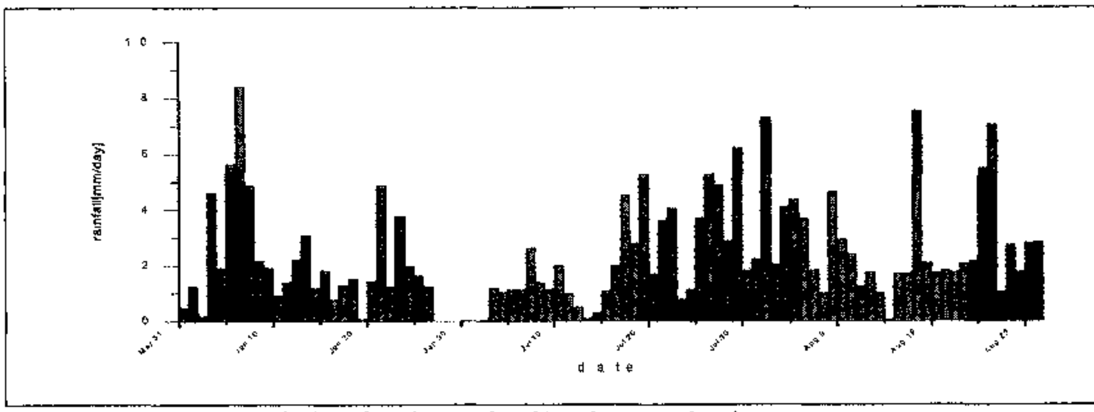

(a) NEXRAD average rainfall for the entire Headwaters basin

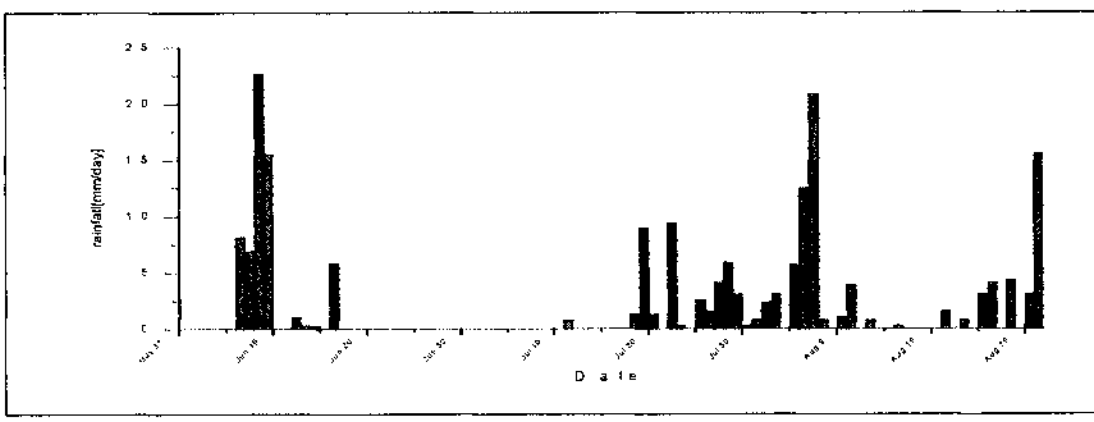

(b) ground observation at Antero reservoir

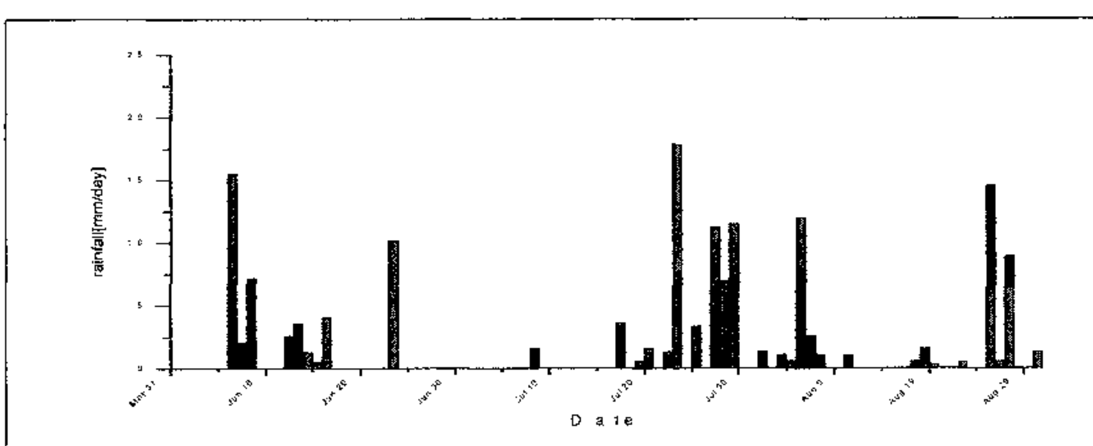

(c) ground observation at Como 4

Figure 4-13 Rainfall observations in Headwaters basin

Initial storage					
Sub-basin	Canopy	Surface	Soil profile	Groundwater1	Groundwater2
R100W50	20	50	70	100	100
R170W150	20	50	70	100	100
R230W200	20	50	70	100	100
R270W250	20	50	70	100	100
R310W310	20	50	70	100	100
R220W220	20	50	70	100	100
R240W240	20	50	70	100	100
R470W420	20	50	70	100	100
R410W380	20	50	70	100	100
R370W360	20	50	70	100	100
R300W300	20	50	70	100	100
R280W280	20	50	70	100	100
R520W500	10	30	50	100	100
R490W490	20	50	70	100	100
R400W400	20	50	70	100	100

Soil Moisture Accounting units						
SMA unit	Canopy	Surface		Soil Profile		
	Storage capacity(mm)	Storage capacity(mm)	Soil Infiltration Max. Rate(mm/hr)	Storage capacity(mm)	Tension Zone capacity(mm)	Percolation Max. Rate(mm/hr)
R520W500	1	5	2	10	2	1
R470W420	2	7	2	15	4	3
R300W300	2	7	2	10	3	2
R100W50	2	5	2	5	2	1
R170W150	2	5	2	5	2	1
R400W400	1	1	1	3	2	0.5
R370W360	2	3	2	2	1	0.5
R280W280	2	5	2	5	2	0.5
R490W490	0.5	0.5	0.5	1.2	1	0.5
R230W200	1	2	1	3	1	0.5
R270W250	0.5	2	1	2	1	0.5
R310W310	0.5	0.5	0.5	2	1	0.5
R220W220	1	2	1	4	3	0.5
R240W240	2	5	2	5	2	1
R410W380	1	5	3	10	3	2

Table 4-5 Calibrated parameters of HMS model

Soil Moisture Accounting units						
SMA unit	Groundwater1			Groundwater2		
	Storage capacity(mm)	Percolation Max. Rate(mm/hr)	Storage coefficient (hr)	Storage capacity(mm)	Percolation Max. Rate(mm/hr)	Storage coefficient (hr)
R520W500	20	0.5	30	40	0.5	50
R470W420	25	0.5	30	40	0.5	50
R300W300	20	0.5	30	40	0.5	50
R100W50	20	0.5	30	40	0.5	50
R170W150	20	0.5	30	40	0.5	50
R400W400	20	0.5	30	40	0.5	50
R370W360	15	0.5	30	40	0.5	50
R280W280	15	0.5	30	40	0.5	50
R490W490	10	0.5	30	40	0.5	50
R230W200	15	0.5	30	40	0.5	50
R270W250	10	0.5	30	40	0.5	50
R310W310	10	0.5	30	40	0.5	50
R220W220	15	0.5	30	40	0.5	50
R240W240	20	0.5	30	40	0.5	50
R410W380	20	0.5	30	40	0.5	50

	ModClark transform		**Groundwater recession**		
Sub-basin	Time of Concentration (hrs)	Storage Coefficient (hrs)	Initial Flow (cms)	Recession Ratio	Threshhold Flow (cms)
R100W50	40	150	0.1	0.99	2
R170W150	20	130	0.1	0.99	2
R230W200	40	120	0.1	0.92	2
R270W250	60	150	0.5	0.99	2
R310W310	40	110	0.1	0.99	2
R220W220	40	80	0.1	0.94	2
R240W240	40	80	0.1	0.90	2
R470W420	120	150	0.1	0.8	2
R410W380	65	120	0.1	0.85	2
R370W360	100	120	0.1	0.99	2
R300W300	120	150	0.1	0.8	2
R280W280	80	120	0.1	0.85	2
R520W500	150	140	0.1	0.9	2
R490W490	100	150	0.1	0.98	2
R400W400	60	100	0.1	0.995	2

Table 4-5 Calibrated parameters of HMS model (cont'd)

	Muskingum channel routing		
Reach	K (hrs)	X	Number of sub-reaches
R170	2	0.2	1
R220	6	0.2	1
R360	8	0.2	1
R370	25	0.2	1
R310	5	0.2	1
R380	10	0.2	1
R410	2	0.2	1
R280	10	0.2	1
R390	12	0.2	1
R420	35	0.2	1
R470	20	0.2	1
R500	20	0.2	1
R520	25	0.2	1

Table 4-5 Calibrated parameters of HMS model (cont'd)

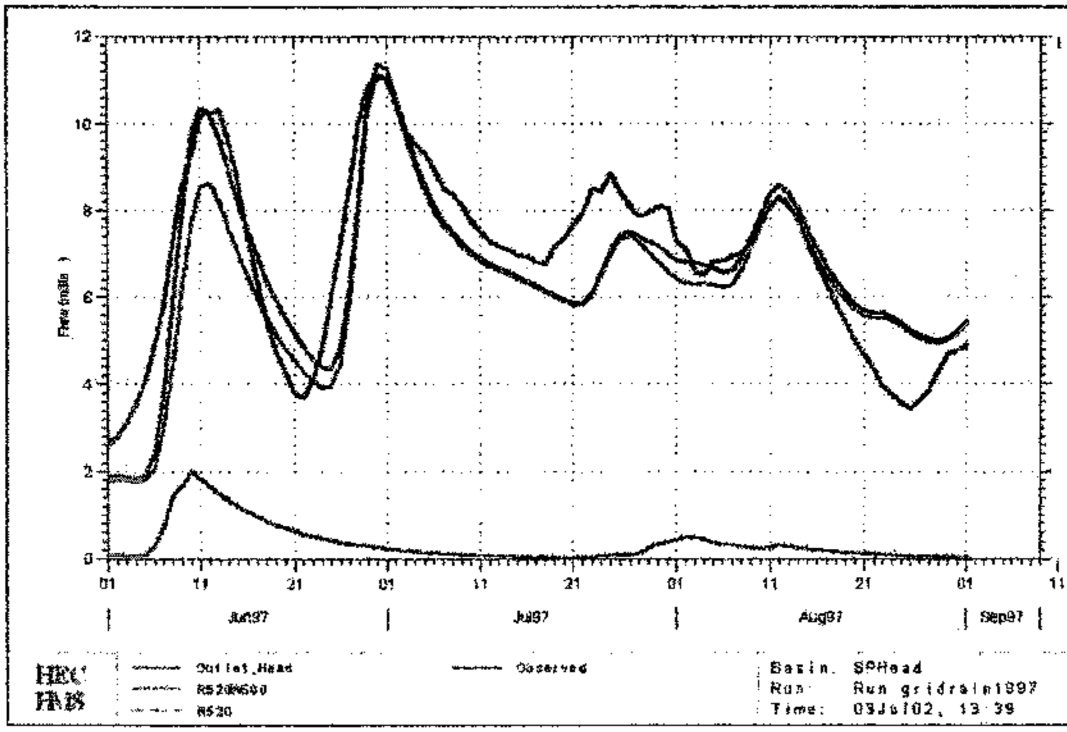

Figure 4-14 The hydrograph at the outlet of Headwaters basin

```
Project : Headwaters
Run Name : Run gridrain1997
Start of Run : 01Jun97 00:00        End of Run   : 31Aug97 24:00
Basin Model : SPHead                Met. Model   : Met 1997gridrain
Control Specs : Control 1997
```

Hydrologic Element	Peak Discharge (cms)	Time of Peak	Volume (1000 m^3)	Drainage Area (km^2)
R270W250	0.5	31 May 97	2780.9	205.539
JR280	0.5	31 May 97	2780.9	205.539
R280	0.5	31 May 97	2790.4	205.539
R280W280	1.0446	04 Aug 97	653.53	132.132
JR390	1.3537	04 Aug 97	3443.9	337.671
R390	1.3001	05 Aug 97	3459.3	337.671
R400W400	0.53395	08 Aug 97	2884.7	254.477
JR360	1.7123	05 Aug 97	6344.0	592.148
R360	1.7522	05 Aug 97	6347.0	592.148
R230W200	1.7372	24 Jun 97	2582.8	243.990
JR370	2.5042	24 Jun 97	8929.8	836.138
R370	2.3462	25 Jun 97	8941.8	836.138
R100W50	1.5257	23 Jun 97	6861.4	195.052
JR170	1.5257	23 Jun 97	6861.4	195.052
R170	1.6183	24 Jun 97	6856.2	195.052
R170W150	5.8959	23 Jun 97	10786	125.141
JR220	7.2834	23 Jun 97	17642	320.193
R220	7.2149	24 Jun 97	17602	320.193
R220W220	1.3085	23 Jun 97	1293.8	97.177
R240W240	0.27407	04 Aug 97	423.46	134.230
JR310	8.3916	24 Jun 97	19320	551.600
R310	8.7550	24 Jun 97	19285	551.600
R370W360	1.3065	06 Aug 97	1949.9	292.229
R310W310	0.38547	19 Jul 97	1154.0	57.327
JR380	11.181	24 Jun 97	31331	1737.294
R380	10.602	25 Jun 97	31264	1737.294
JR410	10.602	25 Jun 97	31264	1737.294
R410	10.773	25 Jun 97	31251	1737.294
R410W380	0.13486	05 Jun 97	111.48	122.345
R300W300	0.84535	08 Jun 97	644.12	144.716
JR420	10.833	25 Jun 97	32007	2004.355
R420	9.5203	26 Jun 97	31777	2004.355
JR470	9.5203	26 Jun 97	31777	2004.355
R470	9.2245	27 Jun 97	31640	2004.355
R490W490	3.3502	24 Jul 97	15380	97.177
R470W420	4.4286	08 Jun 97	3732.4	214.627
JR500	11.741	27 Jun 97	50753	2316.159
R500	11.497	28 Jun 97	50472	2316.159
JR520	11.497	28 Jun 97	50472	2316.159
R520	11.121	29 Jun 97	50143	2316.159
R520W500	2.0146	09 Jun 97	2845.7	111.858
Outlet_head	11.376	29 Jun 97	52989	2428.017

Table 4-6 Global summary of HMS results

4.5. Simulation of Hydrologic Response under a Changed Climate Scenario

4.5.1. GCM model (CGCM2 by CCCma)

The hydrologic cycle is an integrated and dynamic component of the Earth's geophysical climate system and both affects and is affected by climatic conditions. Changes in the Earth's radiation balance affect winds, temperatures, atmospheric energy distribution, and water transport, cloud dynamics and more. Changes in temperature affect evapotranspiration rates, cloud characteristics and extent, soil moisture, and snowmelt regimes. Changes in precipitation affect the timing and magnitude of floods and droughts, shift runoff regimes, and alter groundwater recharge regimes. Synergetic effects alter cloud formation, vegetation patterns and growth rates, and soil conditions. At a larger scale, climate changes can affect major regional atmospheric circulation patterns and storm frequencies and intensities. All of these factors are, in turn, very important for decisions about water and land-use planning and management. One of the two major objectives of this thesis is to develop a methodology for predicting streamflow regime changes or future available water resources under a changed climate scenario as predicted by a General Circulation Model (GCM). General circulation models are limited in their ability to accurately simulate important aspects of the hydrologic cycle, for example lateral redistribution of excess precipitation over the land surface. Furthermore, many fundamental hydrologic processes, such as the formation and distribution of clouds and rain-generating storms or watershed soil-moisture dynamics, occur on spatial scales smaller than most GCMs are able to resolve. We thus know less about how the water cycle will change than we would like to know in order to make decisions about how to plan, manage, and operate water systems. Climate models attempt to represent the full climate system from first principles on large scales. Physical "parameterizations" are used to approximate the effects of unresolved small scale processes because it is not currently feasible to include detailed representations of these processes in present day models. Caution is therefore needed when comparing climate model output with observations or analyses on spatial scales shorter than several grid lengths (approximately 1000 to 1500 km in mid-latitudes), or when using model output to study the impacts of climate variability and change. The reader is further cautioned that estimates of climate variability and change obtained from climate model results are subject to sampling variability. This uncertainty arises from the natural variability that is part of the observed climate system. Even though the issues described above hinder modelers in their use of GCM outputs in real time streamflow predictions, the GCM rainfall is still useful for sensitivity studies or to assess the likely impacts of scenarios of possible future climates.

Table 2-1 summarizes current major GCMs. This study uses output from the CGCM2 model of the Canadian Climate Center for modeling and analysis (CCCma). The second version of the Canadian Global Coupled Model (CGCM2), is based on the earlier CGCM1, but with improvements aimed at addressing shortcomings identified in the first version. In particular, the ocean mixing parameterization has been changed from horizontal/vertical diffusion scheme to the isopycnal/eddy stirring parameterization of Gent and McWilliams (1990), and sea-ice dynamics has been included following Flato and Hibler (1992). In addition, other technical modifications were made in the ocean spin-up and flux adjustment procedure. A description of CGCM2 and a comparison, relative to CGCM1, of its response to increasing greenhouse-gas forcing can be found in Flato and Boer (2000).

Figure 4-15 shows the global, annual mean surface air temperature change simulated by CGCM1 and CGCM2, when forced with the widely-used "IS92a" (1% per year increase) scenario. The two models agree rather closely in terms of their global mean response. Also shown in the figure are time series obtained using the newer IPCC SRES "A2" and "B2" forcing scenarios. The scenario 'IS92a' and 'IPCC SRES' will be discussed below.

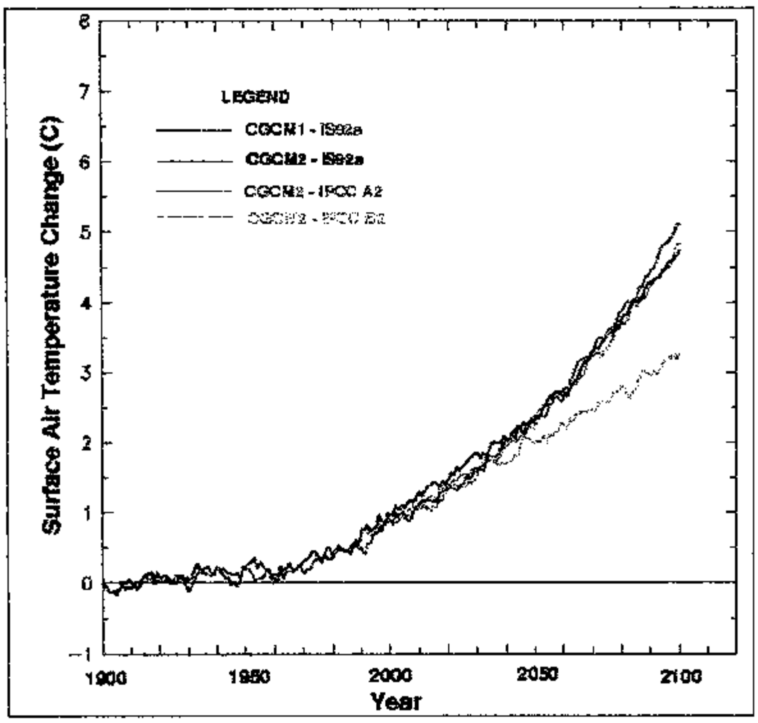

Figure 4-15 Global annual average surface temperature change, relative to 1900-1929 average as produced by CGCM1 and CGCM2 for various forcing scenarios

The CCCma coupled models, CGCM1 and CGCM2, represent the net radiative effect of all greenhouse gases by means of an *equivalent* CO_2 concentration. The *equivalent* CO_2 concentration is necessarily higher than the observed CO_2 concentration since it represents the climate forcing due to CO_2 and also the forcing associated with all other greenhouse gases. In transient climate change simulations, the change in greenhouse gas forcing is represented in the model as a perturbation relative to the 330*ppmv equivalent* CO_2 concentration used in the *control* simulation. That is, 330*ppmv* is taken as a reference value, and climate change simulations involve changes relative to this value. *Equivalent* CO_2 values from 1850 to 1990 are based on historical changes in greenhouse gas forcing provided by the Hadley Center. From 1990 onward, 3 different scenarios are employed by the CCCma.

IPCC IS92a

The 'IS92a' scenario has effective CO_2 concentration increasing at 1% per year after 1990. In the model, the concentrations are specified by linear interpolation between specified values at 2000, 2025, 2050 and 2100. The IPCC IS92a scenario specifies equivalent greenhouse gas (GHG) concentrations and sulphate aerosol loadings from 1850 to 2100.

IPCC SRES 'A2' and 'B2'

The IPCC Special Report on Emission Scenarios (SRES) provides 40 different scenarios that are deemed *equally likely*. For the Third Assessment Report, the IPCC facilitated the conversion of two of these emission scenarios (A2 and B2) into concentration scenarios for use in climate simulations. The forcing changes implied by the concentrations were used to scale the equivalent CO_2 values to be consistent with the 1990 value in the IS92a simulation. The A2 scenario envisions population growth to 15 billion by the year 2100 and rather slow economic and technological development. It projects slightly lower GHG emissions than the IS92a scenario, but also slightly lower aerosol loadings, such that the warming response differs little from that of the earlier scenario. The B2 scenario envisions slower population growth (10.4 billion by 2100) with a more rapidly evolving economy and more emphasis on environmental protection. It therefore produces lower emissions and less future warming. Climate change results based on the A2 and B2 scenarios are also discussed in the IPCC Third Assessment Report. Because of the data availability, only IPCC SRES B2 scenario is used in this research. The B2 scenario produces less warming than the A2 or earlier GHG+A results. A total of 111 years of monthly data is available from the CCCma web site. However, daily data can be obtained through direct order. The data set for IPCC SRES B2 used in this study consist of 4 different time windows (1975-1995, 2011-2030, 2041-2060, 2071-2090). Figure 4-16 shows the increasing temperature trend of CGCM2 simulation for Central US and South Platte river basin. Because the South Platte river basin is located in the northwest section of the Central US, the time series for South Platte river is shifted lower about $2\,^{\circ}C$ from the time series of the Central US. Despite the significant shift in temperature, the rainfall pattern stays consistent. However, the net water balance (precipitation minus evaporation) does not exhibit any significant shift (see Figure 4-17).

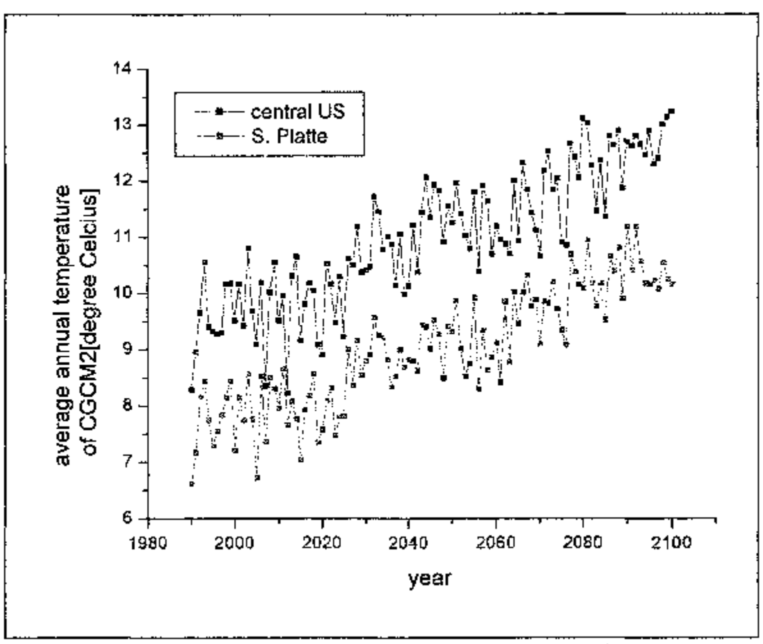

Figure 4-16 Average annual temperature of CGCM2 simulation

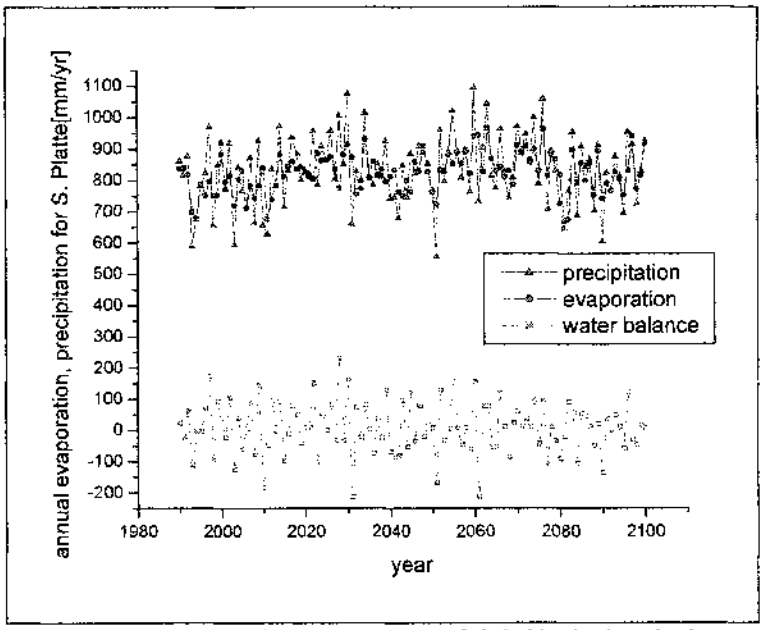

Figure 4-17 Average annual temperature of CGCM2 simulation

4.5.2. Streamflow simulations and results

Now we may consider further the hydrographs for 1997 NEXRAD precipitation. The scale of daily NEXRAD precipitation is 2 *km*. We can resample the precipitation fields based on different scales from the same source of NEXRAD precipitation as we did in section 3.3.1. If the ground surface is unsaturated, the runoff ratio, that is, the fraction of precipitation that becomes runoff ($R \equiv \frac{Q}{E(P)}$), will be less than one. In other words, some portion of precipitation is lost to infiltration and the degree of loss depends on the spatial variability of soil moisture and precipitation. In the HEC-HMS model, the initial soil moisture storage is assumed constant and some amount of lumping is reflected in estimating the parameters of the Soil Moisture Accounting (SMA) units. Therefore, it is hard to analyze the sensitivity of stream runoff to spatial variability of soil moisture. However, an analysis of the sensitivity of streamflow to the spatial variability of precipitation can be performed by forcing the model with the precipitation fields of different scales that have different spatial variabilities (Figure 4-18). The initial storage listed in Table 4-5 shows that the ground surface of South Platte Headwaters basin is assumed to be partially saturated at the initial stage. Because the infiltration capacity of ground surface acts as a threshhold, Figure 4-18 indicates that the high degree of spatial variability of rainfall leads to a high amount of excess rainfall and streamflow. Figure 4-19 is the sensitivity curve of the runoff volume and peak flow rate at the outlet of the Headwaters basin. Both variables appear to decrease logarithmically as a function of the scale of the rainfall field forcing. While the peak flow rate decreases linearly, the runoff volume decreases non-linearly in the semi-log domain. The rate of decrease of the runoff volume decreases as the scale of the rainfall field decreases. As shown in these graphs, for finer scales, the runoff volume is more sensitive to the scale of the rainfall field

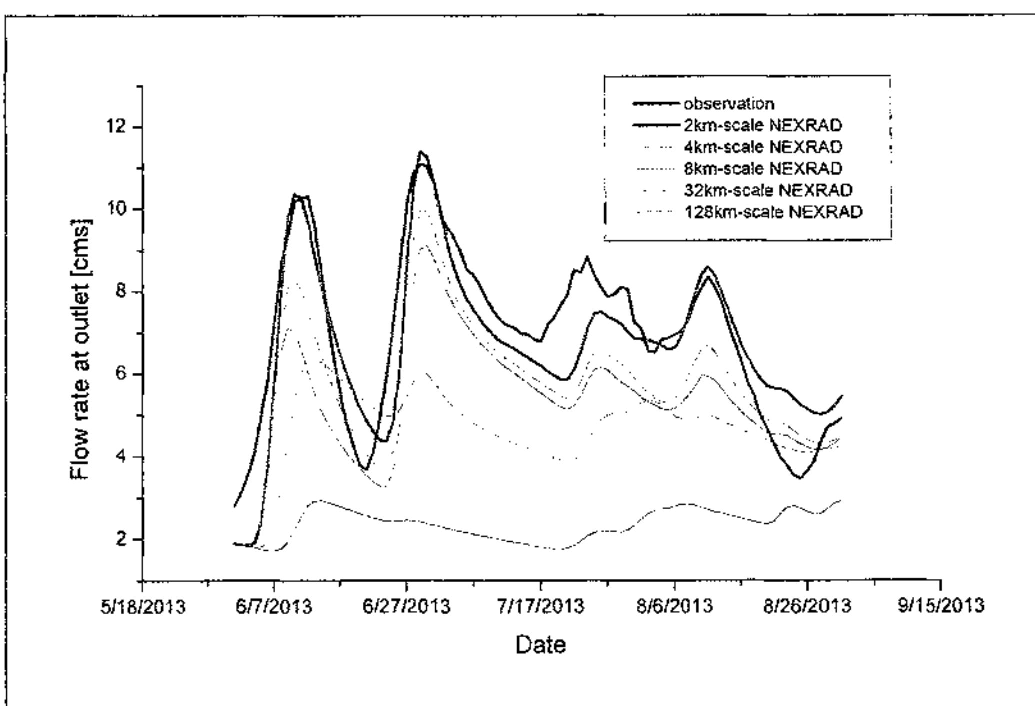

Figure 4-18 The hydrographs of 1997 NEXRAD JJA precipitation

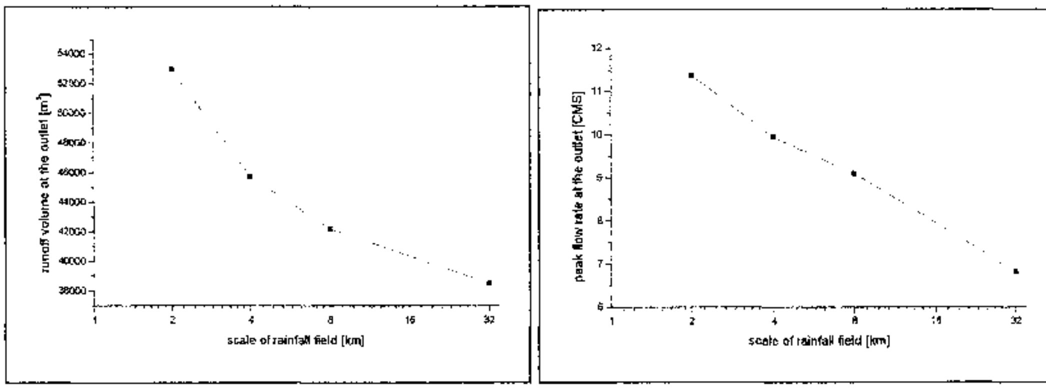

Figure 4-19 The sensitivity of runoff volume and peak flow rate to scale (e.g., degree of variability) of rainfall fields

than peak flow rate is; whereas, for coarser scales, the peak flow rate is more sensitive to the scale of the rainfall field than the runoff volume. Before proceeding to the streamflow prediction using GCM precipitation, the annual pattern of GCM precipitation is compared to the historical records of gage observations of the South Platte River basin.

When setting up climate change scenarios for GCM, from 1990 onward, an increase of 1% or less per year (it varies with the specific scenario) of the equivalent CO_2 is assumed. Based on this assumption, climate models constantly project an increase in global mean precipitation of between 3 to 15% for a temperature increase of 1.5 to 3.5 $°C$. But these global average changes hide significant differences in regional precipitation patterns. Some large areas with increases or decreases in precipitation may have areas where precipitation changes in opposite direction (WSAT, 2000). Figure 4-20 shows that there is significant inconsistency between absolute values of GCM precipitation and historical records of gage observation. Nevertheless the relative variability in GCM precipitation can be respected. During 1990 to 2000, the climate conditions for running model are similar to those for the precipitation observations, but the model simulation value shows bias from the observation which needs to be adjusted. Therefore, the GCM precipitation needs to be tuned to the local region by shifting the whole series by the difference or amount of bias between GCM precipitation and gage observation in 1990 to 2000 (Figure 4-20).

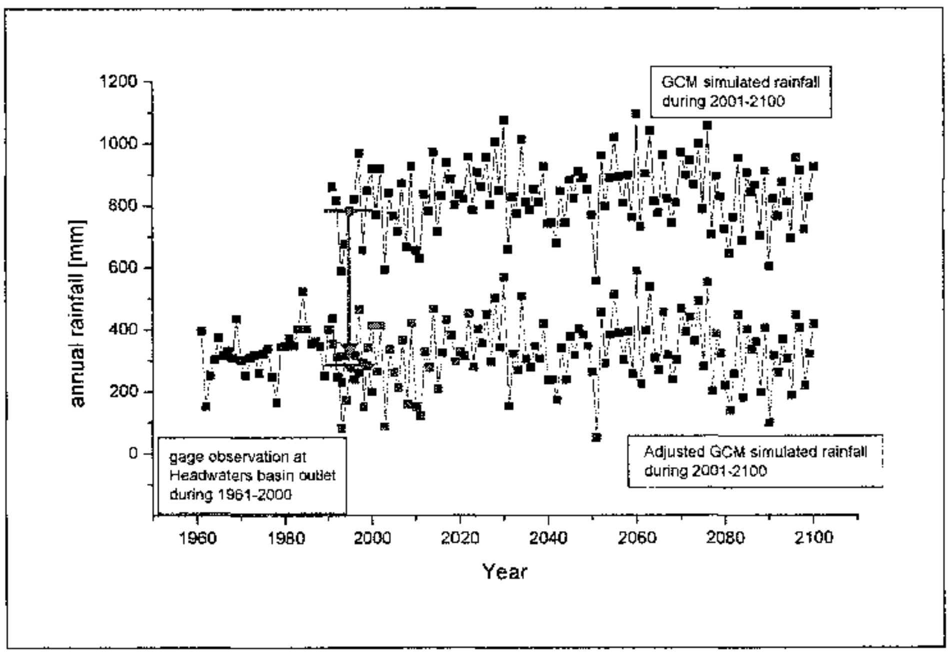

Figure 4-20 The comparison of GCM rainfall and historical observation of gage rainfall

In order to predict streamflows from GCM precipitation, the CCCma simulation is first downscaled using the methodology described in Chapter 3. Then, with the parameters calibrated for 1997 JJA NEXRAD, the hydrographs were produced for the CCCma scenarios. We did streamflow prediction for 2 temporal windows (2011-2020 and 2081-2090) of GCM precipitation. For each year, 10 hydrographs were simulated for 10 different spatial distributions of precipitation that are assumed to have common large-scale forcing (total precipitation).

Therefore, 200 hydrographs were computed for the year 2011 to 2020 and 2081 to 2090 (Figure A-H1). Because each of the 10 hydrograph simulations of a specific year have the same temporal distribution of rainfall, they have similar shapes (e.g., time to peak). However, the magnitude of total runoff or peak flow vary according to the spatial distribution of the rain fields. Figure 4-21 compares the coefficient of variation of the peak flows and runoff volumes and illustrates that the coefficient of variation of peak flow is higher than those of runoff volumes over most of the years. That means the distribution of peak flow rate is more scattered over the simulations and more sensitive to the spatial variability of rainfall than total runoff volume is.

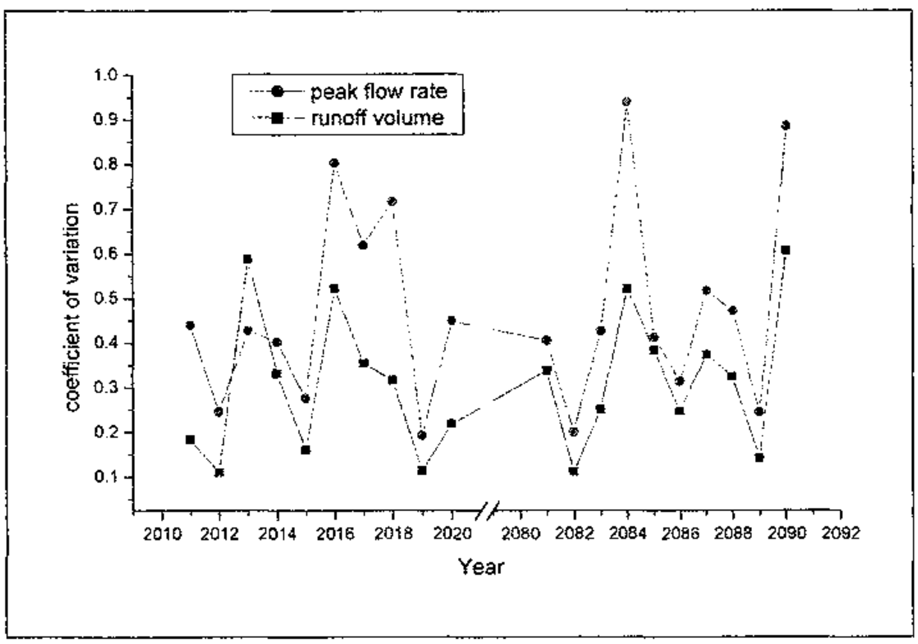

Figure 4-21 The coefficient of variation of the GCM hydrograph prediction

Figures 4-22 and 4-23 show the statistics of the simulated GCM precipitation and evaporation for 2 temporal windows of the data set. The comparison is made for annual values and JJA (June-July-August) values. These figures show that the annual evaporation is increased 4.65% due to temperature increases, whereas the average annual precipitation is not changed significantly. The JJA evaporation is increased 4.19%, whereas the JJA precipitation is decreased 4.2%, which results in the reduction of streamflow runoff in the latter 10 years. The coefficient of variation of GCM precipitation and evaporation increases, which illustrates that, as years go by, the variability in precipitation and evaporation increases more than their corresponding average values. Figure 4-24 and 4-25 illustrate the trend shift in JJA runoff volume and peak flow rate corresponding to the GCM climate change scenarios. The JJA runoff volume is decreased 15.37% and the JJA peak flow rate is decreased 18.01%. Much of these reductions are the result of the decrease of JJA precipitation and the increase of JJA evaporation. The spatial variability of rainfall has already been shown to have an effect on the increase of streamflow (section 4.5.2 and Figure 4-18). Likewise, it should be expected that the temporal variability of rainfall would affect the streamflow pattern. The coefficient of variation of JJA runoff volume increases by 33.8% and that of JJA peak flow by 41.9%. Therefore, peak flow is shown to be more sensitive to the variation of rainfall than the runoff volume.

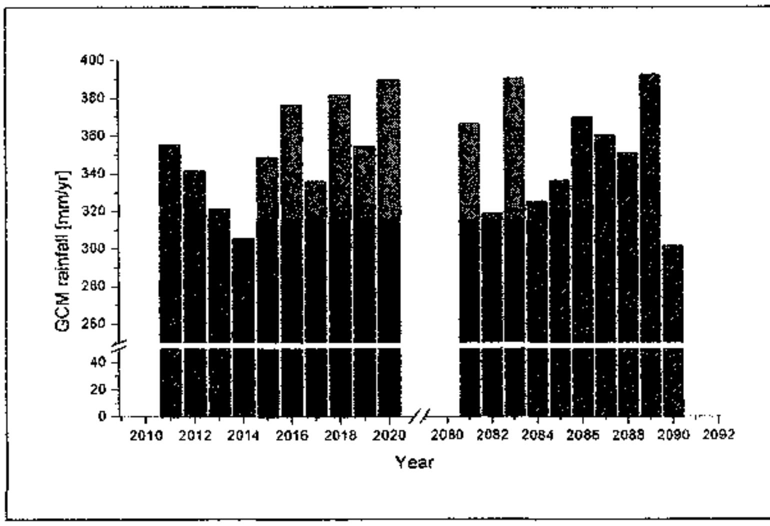

	2011□2020	2081□2090	
Mean	350.9 mm/yr	351.1 mm/yr	0.06% ↑
Standard deviation	26.7 mm/yr	30.4 mm/yr	14.1% ↑
Coeff. of Variation	0.076	0.087	14.5%↑

(a) annual precipitation

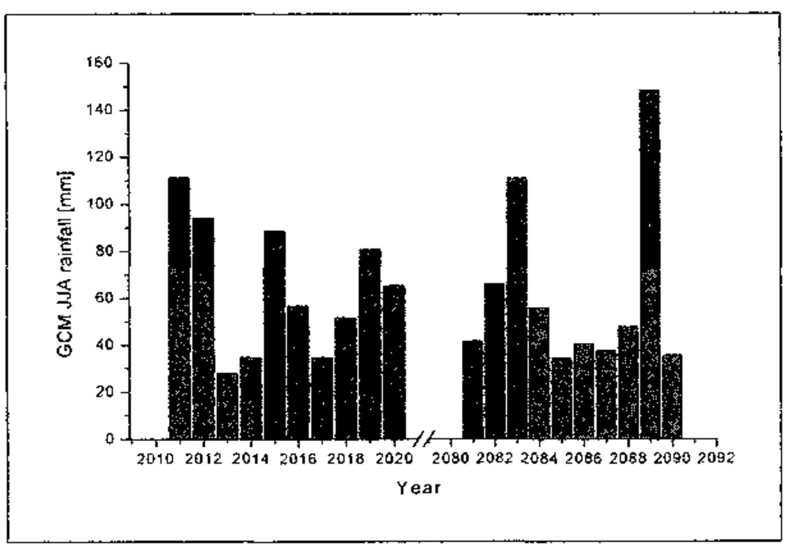

	2011□2020	2081□2090	
Mean	64.4	61.7	4.2% ↓
Standard deviation	28.4	38.1	33.9% ↑
Coeff. of Variation	0.441	0.618	40.0%↑

(b) JJA precipitation

Figure 4-22 The time series of GCM rainfall simulation data set for South Platte Headwaters Basin

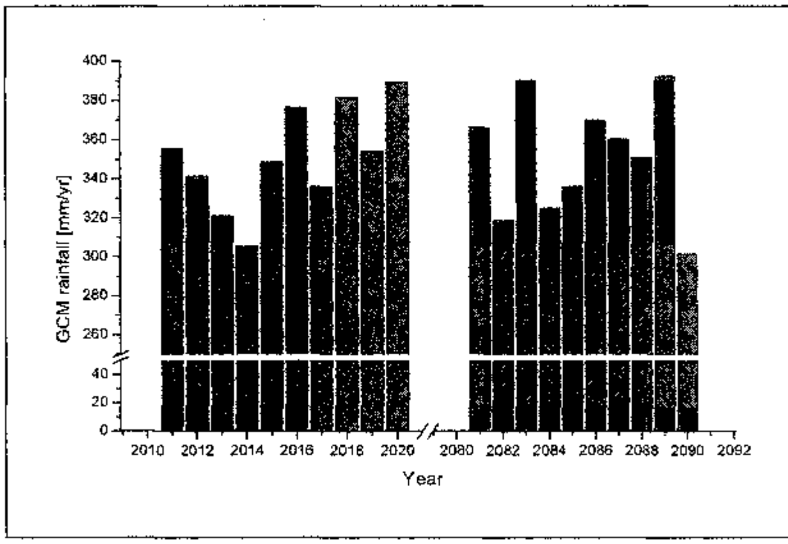

	2011□2020	2081□2090	
Mean	304.3 mm/yr	318.5 mm/yr	4.65% ↑
Standard deviation	13.0 mm/yr	16.7 mm/yr	28.2% ↑
Coeff. of Variation	0.076	0.087	14.5%↑

(a) annual evaporation

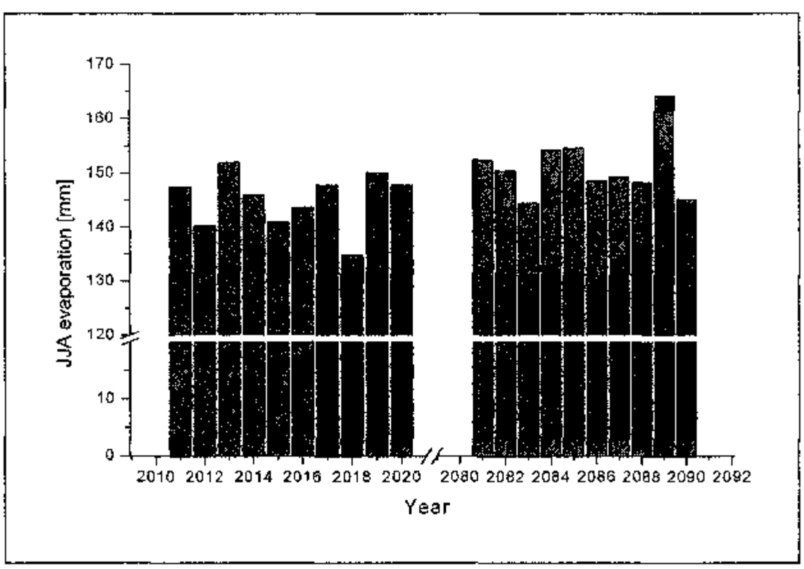

	2011□2020	2081□2090	
Mean	145.0	151.2	4.19% ↑
Standard deviation	5.2	5.7	10.4% ↑
Coeff. of Variation	0.036	0.038	5.56%↑

(b) JJA evaporation

Figure 4-23 The time series of GCM evaporation simulation data set for South Platte Headwaters Basin

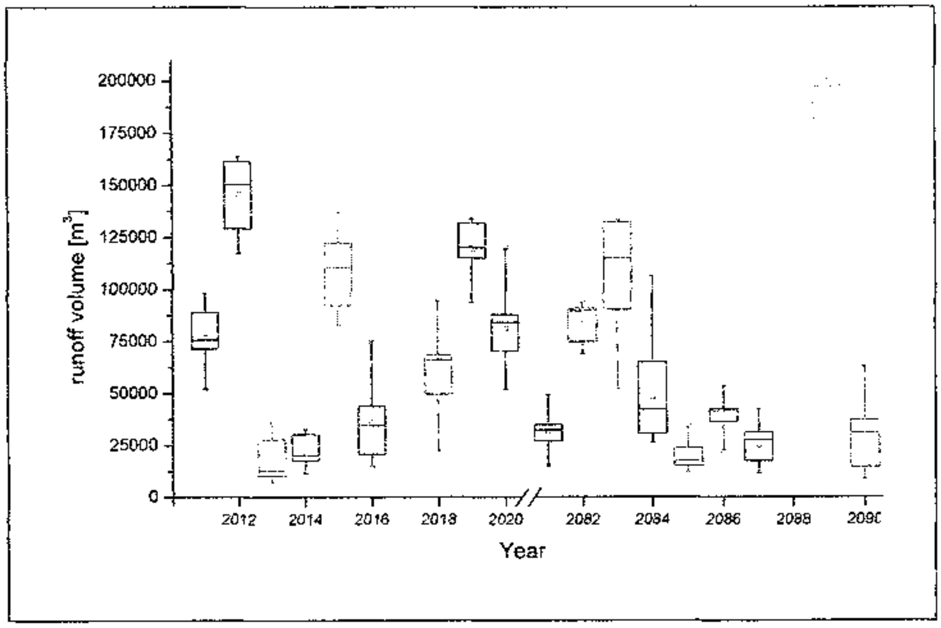

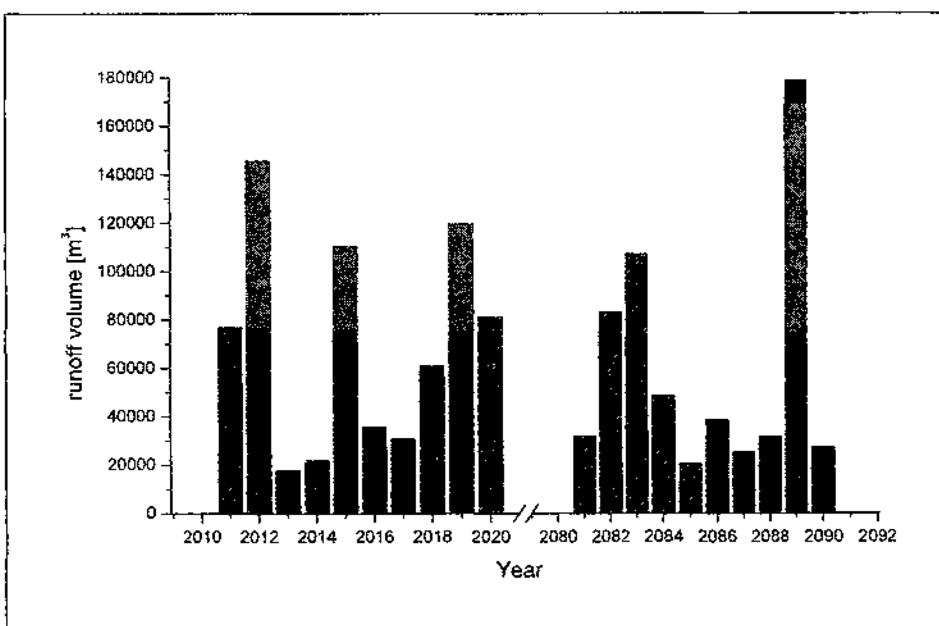

	2011□2020	2081□2090	
Mean	70,092.22□	59,321.01□	15.37% ↓
Standard deviation	44,476.9□	50,391.0□	13.3% ↑
Coeff. of Variation	0.635	0.849	33.7%↑

Figure 4-24 The runoff volume for the GCM rainfall simulation data set

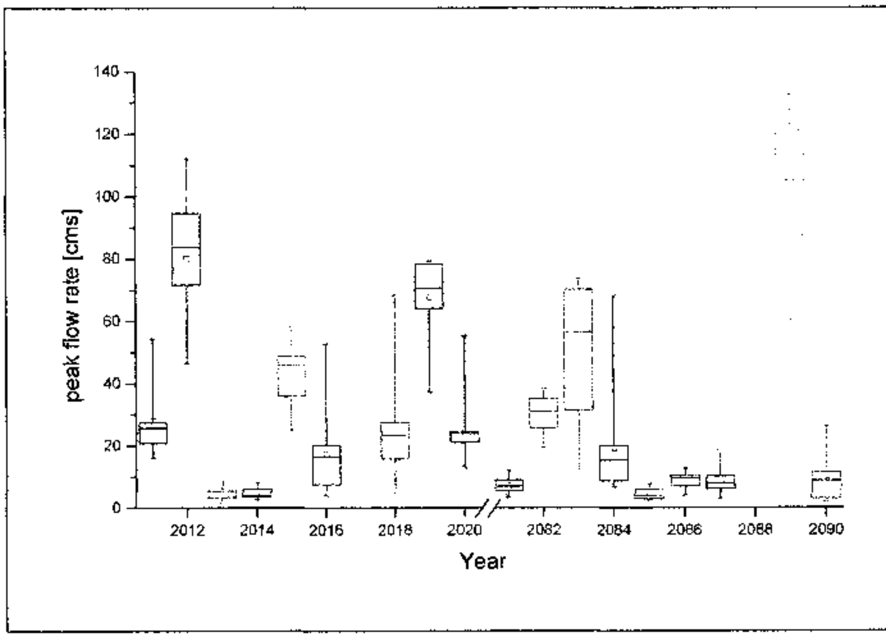

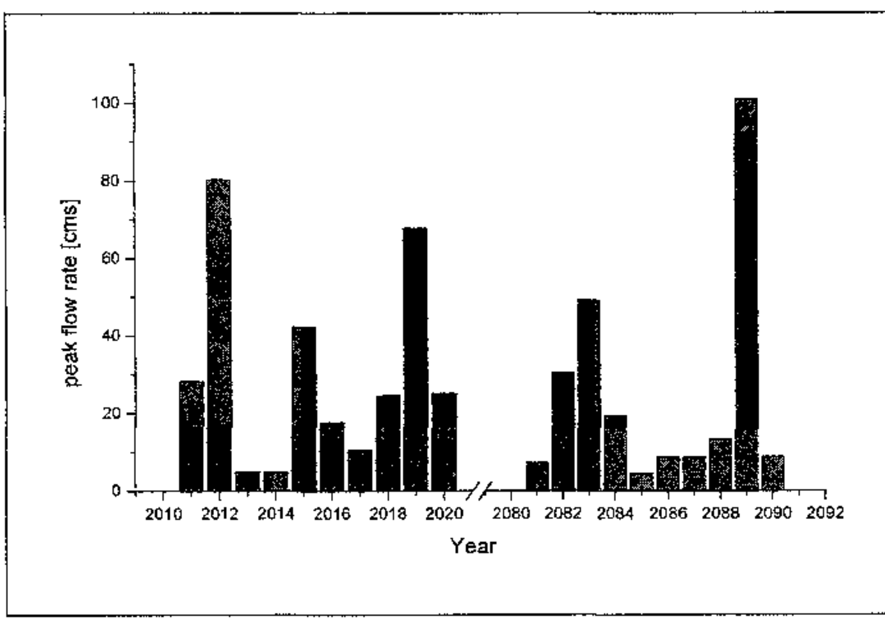

	2011□2020	2081□2090	
Mean	30.53cms	25.03□	18.01% ↓
Standard deviation	25.7□	29.9□	16.3% ↑
Coeff. of Variation	0.842	1.195	41.9%↑

Figure 4-25 The peak flow rate for the GCM rainfall simulation data set

4.5.3. Statistical Tests

The statistical test was made for the null hypothesis of no difference between the means for the first and last ten years. The method of testing the difference between 2 means when the variances are unknown and unequal (Kottegoda and Rosso, 1997) was used because the variance is assumed to vary while climate changes over long periods. When the variances are unequal, the statistic does not have a t-distribution. This is called the Behrens-Fisher problem. In case of observations taken from normal populations with unknown and unequal variances, the statistic

$$T = \frac{(\overline{X}_1 - \overline{X}_2) - (\mu_1 - \mu_2)}{\sqrt{\left(S_1^2 / n_1\right) + \left(S_2^2 / n_2\right)}}$$

has an approximate t distribution with

$$\nu = \frac{\left[\left(\hat{S}_1^2 / n_1\right) + \left(\hat{S}_2^2 / n_2\right)\right]^2}{\left[\left(\hat{S}_1^2 / n_1\right)^2 / (n_1 - 1)\right] + \left[\left(\hat{S}_2^2 / n_2\right)^2 / (n_2 - 1)\right]}$$ degrees of freedom.

Now let's test the null hypothesis for JJA rainfall, runoff volumes, and peak flow rate. The basic statistics for the test are as follows. The test results are shown in Table 4.

	JJA rainfall	Runoff volume	Peak flow rate
ν	17	18	18
T	0.179	0.507	0.440
F at $\alpha = 0.1$	1.333	1.330	1.330
Null hypothesis	Not rejected	Not rejected	Not rejected

Table 4-7 Test of null hypothesis

Table 4-7 tells that the null hypothesis for all variables were not rejected, i.e., the evidence is insufficient to show that there is a difference in means of 2 temporal windows. One of the reason is the absolute value of the standard deviation is relatively high. The other one possibly be the existence of outlier in the year 2089. Then let's do the same test with the outlier being neglected. The basic statistics for the test are as follows.

	2011 ~ 2020	2081 ~ 2090	
Mean	64.4	52.1	- 19.1%
Standard deviation	28.4	24.3	- 14.3%
C.O.V	0.441	0.466	+ 5.36%

Table 4-8. Basic statistics of JJA precipitation without outlier

	2011 ~ 2020	2081 ~ 2090	
Mean	70,092.22 m^3	46,053.13 m^3	- 34.3%
Standard deviation	44,476.9 m^3	29,601.41 m^3	- 33.45%
C.O.V	0.635	0.643	1.24%

Table 4-9 Basic statistics of runoff volumes without outlier

	2011 ~ 2020	2081 ~ 2090	
Mean	30.53cms	16.61 m^3	- 45.61%
Standard deviation	25.7 m^3	14.51 m^3	- 43.65% ↑
C.O.V	0.842	0.874	3.66% ↑

Table 4-10 Basic statistics of peak flow rate without outlier

The test results are shown in Table 4-11.

	JJA rainfall	Runoff volume	Peak flow rate
ν	18	16	14
T	1.038	1.423	1.490
F at $\alpha = 0.1$	1.330	1.330	1.330
Null hypothesis	Not rejected	Rejected	Rejected

Table 4-11. Basic statistics of JJA precipitation without outlier

Table 4-11 shows that the null hypotheses except for JJA rainfall were rejected. So, one can tell the runoff volume and the peak discharge would decrease with level of significance $\alpha = 0.1$. Even though the null hypothesis of JJA rainfall was not rejected when $\alpha = 0.1$, it can be rejected if $\alpha \approx 0.16$.

Even though the null hypotheses of the original case were not rejected, 2 cases above illustrate that runoff volume and peak flow are very sensitive to the rainfall increase or decrease. Climate changes make some region drier or the other wetter. The result of this research shows that decrease of rainfall due to climate change can make the region much drier than the rate of rainfall decrease.

4.6. Summary

This chapter presents a methodology for simulating watershed response using the downscaled precipitation scenarios produced by a GCM. The study area is the South Platte Headwaters Basin ($2{,}465 km^2$) which is located most upstream of the South Platte River and flow is relatively undisturbed. The HEC-HMC model developed by the U.S. Army Corps of Engineers was used for the distributed rainfall-runoff model and the GIS preprocessing was performed using HEC-GeoHMS. The grid (i.e., NEXRAD or GCM) precipitation was used as an input to the HMS. In HMS, the gridded Soil Moisture Accounting scheme (SMA) was selected for calculating sub-basin losses, and the ModClark quasi-distributed linear transform method was applied in combination with the gridded SMA. Baseflow was computed using the exponential recession constant method. Finally, channel routing was performed using the Muskingum method. The 30-arc seconds GTOPO30 DEM data were used for terrain processing. The STATSGO of USDA Natural Resources Conservation Service was used for extracting soil geographic information.

The HMS model was calibrated using the 1997 JJA NEXRAD precipitation. The calibration result shows reasonable fit to observation in amount and timing of the peak flows at the outlet of the Headwaters basin. The only streamflow gage station used for calibration is the South Platte River near Lake George (station ID: 06696000). Therefore, lack of additional streamflow gage stations hinders a more accurate tuning of the sub-basin hydrographs. The sensitivity of streamflow to spatial variability of precipitation demonstrates that a high degree of spatial variability leads to a high amount of excess rainfall and streamflow. For finer scales, the runoff volume is more sensitive to the scale of the rainfall field (therefore, to the variability) than peak flow rate is; whereas, for coarser scales, the peak flow rate is more sensitive to the scale of the rainfall field than the runoff volume.

In this study, the output from the CGCM2 model of the Canadian Climate Center modeling and analysis (CCCma) was used for input to the streamflow prediction model. The climate change scenario corresponds to the IPCC SRES 'B2' scenario, which is a modest scenario based on lower GHG emissions, slower population growth with a more rapidly evolving economy and more emphasis on environmental protection. The GCM rainfall is useful for sensitivity analysis or to assess the likely impacts of scenarios of possible future climates.

The magnitude of the peak flow and the total runoff volume are sensitive to the spatial variability of precipitation. The coefficient of variation of peak flow is higher than those of runoff volumes over most of the years. This illustrates that, for these simulations, the distribution of peak flow rate is more scattered and sensitive to the spatial variability of rainfall than total runoff volume is. The statistics of the simulated GCM precipitation and evaporation for 2 temporal windows of the data set illustrates that the annual evaporation increases by 4.65% due to temperature increases, whereas the average annual precipitation does not change significantly. The JJA evaporation increases by 4.19%, whereas the JJA precipitation decreases by 4.2%, which results in a reduction of stream runoff in the latter 10 years. The coefficient of variation of GCM precipitation and evaporation increases, which illustrates that, as the year goes by, the variability in precipitation and evaporation increases more than their average values. The trend shift in JJA runoff volume and peak flow rate corresponding to the GCM climate change scenarios was also examined. The JJA runoff volume decreases by 15.37% and the JJA peak flow rate decreases by 18.01%. Much of these reductions are the result of the decrease of JJA precipitation and the increase of JJA evaporation. However, the coefficient of variation of JJA runoff volume increases by 33.8% and that of JJA peak flow by 41.9%. Peak flow is shown to be more sensitive to the variation of rainfall than the runoff volume.

The results illustrate that runoff volume and peak flow are very sensitive to the rainfall increase or decrease. The results of this research indicate that decreases of rainfall due to climate change can make the region much drier than the rate of rainfall decrease.

Chapter 5

5. Concluding Remarks

5.1. Summary

Recent improvements in our ability to make meteorological observations and in our ability to forecast weather and climate prompts hydrologists to utilize these achievements to improve hydrologic forecasting. The combined use of meteorological forecasting and hydrologic modeling can enhance the accuracy and reliability of hydrologic forecasting. However, the methodology to combine meteorological forecasting and hydrologic modeling should differ according to the application purposes, forecasting lead time, data availability, required accuracy, etc. The methodology used in this research is based on coupling GCM macro-scale climate prediction as input to a large watershed rainfall-runoff model by means of a new precipitation downscaling algorithm.

The first step of this process is to develop a space-time downscaling model for macro-scale GCM precipitation. The high-resolution ($2 \times 2km$) NEXRAD observation data set was used for extracting the parameters for spatial, temporal distribution, correlation structure, statistical self-similarity, etc. The NEXRAD data set has hierarchical structure according to sampling scales. The temporal and spatial pixel-to-pixel correlation were found to be proportional and inversely proportional to the sampling scale, respectively, and below a certain critical scale the temporal correlation is negligible. Therefore, the space-time stochastic disaggregation model is constructed for the precipitation field above the critical scale and the intermittent random cascade model is applied for the precipitation field below the critical scale. The model was first applied to the resampled $256 \times 256km$-scale 1997 JJA NEXRAD data. The mean and standard deviation are preserved throughout the whole period. Through the self-similarity parameter, β, which indicates the degree of wet portion of underlying field, the wet portion is successfully delineated. From 16*km*- to observation scale (2*km*), the spatial correlation is implicitly preserved in the model. Even though the spatial correlation at 16*km*-scale follows the patterns of the observation, the spatial correlation of precipitation at scales of of 8*km*- or less would be overestimated. The lag-1 (day) temporal correlation as a function of scales is reproduced satisfactorily. Based on the results of this inversion process, GCM precipitation was downscaled to the 2*km*-scale.

The HEC_HMS, which is a semi-distributed grid-based rainfall-runoff modeling system, was applied to South Platte Headwaters basin ($2{,}465km^2$). 30 arc-seconds ($\approx 1km$) GTOPO30 DEM data was used for terrain analysis. Soil properties were estimated from STATSGO data base of the USDA Natural Resources Conservation Service. The gridded Soil Moisture Accounting method was used for partitioning loss from precipitation. The ModClark method, which is technically associated with the gridded SMA, transforms the excess rainfall to direct runoff. The baseflow was assumed to decay exponentially. The Muskingum method was selected for channel routing. The model calibration was performed using the 1997 JJA NEXRAD observation data. The Headwaters basin was chosen as a study area because the virgin flow is not disturbed by man-made hydraulic structures like dams, irrigation networks, urban sewer system, etc. This merit, however, acts as demerit in other aspects because there are not many streamflow gaging stations within the watershed, which hampers an accurate calibration. The entire Headwaters basin was divided into 15 sub-basins. The parameters for 15 sub-basins were calibrated by tuning the runoff simulations to observations only at the outlet of the entire Headwaters basin.

By applying the precipitation of different resampling scales, we found that smoothed spatial variability would lead to the reduction of streamflow estimation. That means that directly applying the GCM precipitation with no downscaling can give rise to underestimated streamflows. The IPCC SRES (Special Report on Emission Scenarios) "B2" scenario, which is based on a mild annual increase (less than 1%) of equivalent CO_2 concentration but envisions slower population growth with a more rapidly evolving economy and more emphasis on environmental protection, was used by CGCM2 (Coupled Global Climate Model 2) of CCCma (Canadian Climate Center for modeling and analysis). The streamflows were predicted for 2 temporal windows (2011-2020 and 2081-2090) of GCM precipitation. 10 hydrographs were simulated for each year using different spatial variabilities. The amounts of peak flow and total runoff volume are sensitive to the spatial variability. Therefore, the average of 10 simulations was used for the statistical comparison of streamflow regime. The results revealed that the runoff volume is decreased 15.37% and the peak flow rate is decreased 18.01%. The decrease of runoff volume and peak flow result from the decrease of absolute rainfall and increase of temporal and spatial rainfall variation.

5.2. Major Contributions

Downscaling methodology for low resolution (macro-scale) precipitation field

- Existing random cascade models (e.g., Over and Gupta 1996) are statistical space-time downscaling models, proven to be useful for reproducing the spatial storm cluster distribution through the self-similarity parameter (β model) and the fluctuation parameter (log-normal model). For example, the model of Over and Gupta (1996) incorporates the temporal evolution of those parameters by relating them to the large scale forcing. Therefore, in that existing model, the precipitation fields are temporally correlated only through the large scale forcing. This research, on the other hand, examines the hierarchical pixel-to-pixel correlation structure in **space** and **time** domain and constructs a stochastic space-time disaggregation model, so that the model can preserve the space-time dependency structure over the full range of scales. This space-time stochastic disaggregation model is then coupled to a random cascade model, so that the combined model possesses not only the ability to reproduce the spatial storm cluster distribution through the self-similarity the fluctuation parameters, but also the space-time dependency structure over the full range of scales.

SensitivityAnalysis to spatial variability of rainfall

- As the wetted fraction becomes smaller, the higher is the precipitation intensity and thus the higher the Horton runoff ratio. In this research, the hierarchical representation for the wetted fraction of the grid-type precipitation along scales through the self-similarity parameter was tested using NEXRAD data. The hydrograph sensitivity to the spatial variability of precipitation fields having different scales was examined. The large-scale precipitation having low spatial variability and high wetted fraction was revealed to yield underestimated runoff.

Coupling of GCM output and hydrologic model

- There have been many studies of the effects of climate changes on water resources environments. Especially, river flow forecasting under global climate change conditions has drawn attention of scientists since '90s. Most of those studies use distributed water-budget or hydrological routing models. However, those models are distributed in the sense that the hydrologic parameters are associated with the distribution of topography, soil type or land use/covers. Even though some of the models use distributed precipitation, they are based on limited number of ground observations. Downscaling of GCM precipitation, if performed, was attained by multi-season, multi-site disaggregation methods based on ground observations (e.g., Epstein and Ramírez 1994; Kite et al. 1994) or multiple regression based on geographical coordinates and elevation (Yao and Terakawa 1999). However, in this research, high-resolution space-time precipitation is obtained through a new downscaling methodology that allows downscaling of macro-scale GCM output using parameters extracted from the remotely sensed NEXRAD data. The streamflow is routed by the distributed GIS-based hydrological model using the downscaled GCM precipitation.

Climate change scenarios

- Generally, GCMs may be good at simulating the global trend of climate change. However, GCMs are unable to predict local variability. In this research, even though the number of GCM (large-scale forcing) realizations was limited to one because of the availability, multiple realizations of local variability having same large-scale forcing were simulated in order to test the sensitivity of the streamflow to local spatial variability of rainfall. The streamflow regimes of projected climate change were compared statistically.

5.3. Recommendations for Future Work

- The statistical space-time downscaling model is computationally efficient. Therefore, the suggested model is useful for coupling macro-scale long-term climate forecasting model and large watershed hydrologic model requiring a large number of simulations for statistical analysis. However, the statistical downscaling model is unable to reproduce the exact location of storm clusters. As it was revealed in section 4.5.2, the streamflow is very sensitive to the spatial variability and/or the location of the center of storm clusters. If the statistical downscaling scheme can be incorporated with a radar image extrapolation scheme and other deterministic physical variables, it may be useful for real-time rainfall-runoff modeling.

- As observed in this study, the critical spatial scale below which the temporal correlation is negligible depends on the time interval which the data is observed over. Therefore, how the critical scale is affected by the combination of spatial and temporal scale needs to be identified by using fine-resolution sets of data in space and time.

- Temporal downscaling into sub-daily scale requires knowledge about diurnal pattern of temporal rainfall distribution, i.e., the number of storms per day, the amount and time of occurrence of each event while maintaining daily statistics. The dependency of those diurnal patterns on storm type (convective, or frontal type) and orographic effect, etc, needs to be examined.

- The GTOPO30 30 arc-second ($\approx 1km$) DEM was used for terrain analysis. Considering the scale of the underlying watershed, the finer resolution DEM data would exponentially decrease the computational efficiency. This could be overcome by using TIN (Triangular Irregular Network) meshes which can adequately represent the hydrologically significant slopes, the stream network and the river floodplain while capturing all watershed areas.

- Due to the limited availability of GCM simulation data, the data of IPCC SRES "B2" scenario, which is the mildest climate change scenario, were used in this study. Because of the steadiness of precipitation over the simulation time span, the effect of trends in precipitation could not be examined. However, datasets corresponding to the other climate change scenario, climate change effects on streamflow regime can be checked over for diverse conditions.

- In continuous streamflow simulation, stream runoff is very sensitive to the state of soil moisture of the ground profile during the dry period. Therefore, utilizing remote sensing of soil moisture will be crucial in distributed watershed modeling and challenging to hydrologists.

6. References

1. Ahrens, S.R., and D.R. Maidment, 1999: Flood Forecasting for the Buffalo Bayou using CRWR-PrePro and HEC-HMS, Center for Research in Water Resources (CRWR) Online Report 99-6, Bureau of Engineering Research, The University of Texas, Austin, TX

2. ASCE, 1999: GIS Modules and Distributed Models of the Watershed, ASCE task committee on GIS Modules and Distributed Models of the Watershed, Reston, VA

3. Ang, Alfredo H-S. and W.H. Tang, 1975; Probability Concepts in Engineering Planning and Design, Volume 1. Basic Principles, pp. 104 – 105, John Wiley & Sons, Inc.

4. Bedient, P.B., and W.C. Huber, 2002: *Hydrology and FloodPlain Analysis*, 3rd edition, Prectice Hall

5. Bellville, J.D., 1999: Recommended Parameter Changes to improve WSR-88D Rainfall Estimates During Cool Season Stratiform Rain Events, from http://www.roc.noaa.gov/ops/z2r_osf5.htm

6. Bennett, T.H., 1993: Development and Application of a Continuous Soil Moisture Accounting Algorithm for the Hydrologic Engineering Center – Hydrologic Modelling System (HEC-HMS), Master's Thesis, The University of California, Davis, CA

7. Carsteanu, A.-A., 1997: Space-Time Rainfall Modeling: Considerations of Scaling and Dynamics, Ph.D. Thesis, The University of Minnesota.

8. Carsteanu, A., E. Foufoula-Georgiou, and V. Venugopal, 1999: Event-specific multiplicative cascades for temporal rainfall, J. Geophys. Res.,Vol. 104(D24), 31,611-622

9. Deidda, R., R. Benzi and F. Siccardi, 1999: Multifractal modeling of anomalous scaling laws

in rainfall, Water Resour. Res, 35(6), 1865-1867

10. Dudhia, J., 1993: A nonhydrostatic version of the Penn State/NCAR mesoscale, model: Validation tests and the simulation of an Atlantic cyclone and cold front. *Mon. Wea. Rev.*, 121, 1493-1513.

11. Dunne, T., 1978: Field Study of Hillslope Flow Processes in Hillslope Hydrology. In Hillslope Hydrology, editted by M.J. Kirkby, pp.227-293, John Wiley, NY

12. Epstein, D., and J. A. Ramírez, 1993: A Statistical Climate Inversion Scheme and its Application in Hydrologic Impact Assessment Studies Associated with Global Climate Variability. *Proceedings Third International Symposium on Engineering Hydrology*. ASCE Conference, San Francisco, C. Y. Kuo Ed., pp. 61-66.

13. Epstein, D., and J. A. Ramírez, 1994: Spatial Disaggregation for Studies of Climatic Hydrologic Sensitivity. *ASCE Journal of the Hydraulics Division* 120(12): 1449-1467.

14. Giorgi, F., 1990: Simulation of Regional Climate Using a Limited Area Model Nested in a General Circulation Model. *Journal of Climate*, 3, 941 - 963.

15. Giorgi, F. and L.O. Mearns. 1991: Approaches to the Simulation of Regional Climate Change: A Review. Reviews of Geophysics. Vol. 29 No. 2: 191-216.

16. Gleick, P.H., D.B. Adams, 2000: Water: The Potential Consequences of Climate Variability and Change for the Water Resources of the United States, *Water Sector Assessment Team of the National Assessment of the Potential Consequences of Climate Variability and Change For the U.S. Global Change Research Program.*

17. Gupta, V.K., and E. Waymire, 1990; Multiscaling Properties of Spatial Rainfall and River Flow Distributions. *Journal of Geophysical Research*, 95(D3): 1999-2009.

18. Gupta, V.K., and E. Waymire, 1993 A Statistical Analysis of Mesoscale Rainfall as a Random Cascade. *Journal of Applied Meteorology*, 12(2): 251-267.

19. Hay, L.E., G.J. McCabe Jr., D.M. Wolock, and M.A. Ayers, 1992 Use of Weather Types to Disaggregate General Circulation Model Predictions, *J. Geophs. Res*, Vol. 97, no. D3, pp 2781-2790.

20. Intergovernmental Panel on Climate Change(IPCC), 1996: Climate Change 1995: Impacts, Adaptations and Mitigation of Climate Change: Scientific-Technical Analysis: Contribution of Working Group II to the Second Assessment Report of the Intergovernmental Panel on Climate Change, Cambridge University Press, New York.

21. Jothiyangkoon, C., M. Sivapalan, and N.R. Viney, 2000: Tests of a space-time model of daily rainfall in southwestern Australia based on nonhomogeneous random cascades, WRR, 36(1), 267-284

22. Kahane, J.-P. and J. Peyriere, 1976: Sur certaines martingales de Benoit Mandelbrot, Adv., Math., 22, 131-145

23. Kang, B. and J. A. Ramirez, 2001: Comparative study of the statistical features of random cascade models for spatial rainfall downscaling. Proceedings AGU Hydrology Days 2001, J. A. Ramirez Ed., Hydrology Days Publications, Fort Collin,s CO. pp 151-164.

24. Karl, T. R., Wang W.-C., Schlesinger, M. E., Knight, R. W., and Portman, D., 1990: A Method of Relating General Circulation Model Simulated Climate to the Observed Local Climate. Part I: Seasonal Statistics. *Journal of Climate*, 3, 1053 - 1079.

25. Kim, J.-W., J.-T. Chang, N. L. Baker, D. S. Wilks, and W. L. Gates, 1984: The Statistical Problem of Climate Inversion: Determination of the Relationship between Local and Large-

Scale Climate. *Monthly Weather Review*, 112, 2069 - 2077.

26. Kolmogorov, A.N., 1962: A refinement of previous hypotheses concerning the local structure of turbulence in a viscous inhomogeneous fluid at high Reynolds number, J. Fluid Mech. 13, 82-5

27. Kottegoda, N.T. and R. Rosso, 1997: Statistics, Probability, and Reliability for Civil and Environmental Engineers, pp. 264, McGraw-Hill

28. Kumar, P. and E. Foufoula-Georgiou, 1993a, A Multicomponent Decomposition of Spatial Rainfall Fields: 1. Segregation of Large- and Small- Scale Features Using Wavelet Transforms, *Water Resources Research*, 29(8), 2515-2532

29. Kumar, P. and E. Foufoula-Georgiou, 1993b, A Multicomponent Decomposition of Spatial Rainfall Fields: 2. Self-Similarity in Fluctuations, *Water Resources Research*, 29(8), 2533-2544

30. Lettenmaier, D. P. and T. Y. Gan, 1990: Hydrologic Sensitivities of the Sacramento-San Joaquin River Basin, California, to Global Warming. *Water Resources Research*, 26(1), 69-86

31. Lovejoy. S., and B.B. Mandelbrot, 1985: Fractal properties of rain and a fractal model. Tellus 37A, 209-32

32. Lovejoy, S. and D. Schertzer, 1992: Multifractals and Rain, in New Uncertainty Concepts in Hydrology and Water Resources, edited by Z. W. Kunzewicz, vol. 235, University Press, Cambridge.

33. Mandelbrot, B.B., 1974: Intermittent turbulence in self-similar cascades: divergence of high moments and dimension of the carrier, J. Fluid Mech., 62(2), pp. 331-358

34. Marshall, J.S., W. Hitschfeld, and K.L.S. Gunn, 1955: Advances in Radar Weather, Adv.

Geophys., 2, 1-56

35. Mejia, J.M. and J. Rousselle, 1976: Disaggregation Models in Hydrology Revisited, WRR, 12(2), 185-186

36. Meng, H., J. A. Ramírez, J.D. Salas, and L. Ahuja, 1996: Scaling Analysis of Infiltration at R-5 Catchment. *Invited Proceedings of the USDA-ARS Workshop on Real World Infiltration,* Pingree Park, CO, July 22-25. CWRRI Information Series No. 86, pp. 239-240

37. Molnár, P., 2000: Precipitation and Erosion Dynamics in the Rio Puerco Basin. Ph.D. Dissertation, Civil Engineering Department, Colorado State University, 200 pp.

38. Molnár, P. and J. A. Ramírez, 1998: Energy Dissipation Theories and Optimal Channel Characteristics of River Networks. Water Resources Research, 34(7), pp. 1809-1818.

39. Muzik, I. 1996: Lumped Modeling and GIS in Flood Prediction, in Geographical Information Systems in Hydrology ed. by V.P. Singh and M. Fiorentino, Kluwer Academic Publishers, 269-301

40. Oboukov, A.M., 1962: Some Specific Features of Atmospheric Turbulence, J. of Fluid Mech., 13, 77-81

41. Ogden, F.L. and P.Y. Julien, 1994: Runoff Model Sensitivity to Radar Rainfall Resolution, J. of Hydrology, 158, 1-18

42. Olsson, J., 1998: Evaluation of a scaling cascade model for temporal rainfall disaggregation, Hydrol. Earth Syst. Sci., 2(1), 19-30

43. Over, T.M., Modeling space-time rainfall at the mesoscale using random cascades, 1995: Ph.D. thesis, Univ. of Colo., Boulder

44. Over, T.M., and V.J. Gupta, 1996: A Space-Time Theory of Mesoscale Rainfall using Random Cascades, J. of Geophy. Res., 101(D21), 26319-26331

45. Perica, S. and E. Foufoula-Georgiou, 1996: Linkage of Scaling and Thermodynamic parameters of Rainfall: Results from midlatitude mesoscale convective systems, J. Geophys. Res., 101(D3), 7431-7448

46. Pielke, R.A. and R. Avissar, 1990: Influence of landscape structure on local and regional climate. Landscape Ecology, 4, 133 - 155.

47. Pielke, R.A., R. Avissar, M. Raupach, H. Dolman, X. Zeng, and S. Denning, 1997: Influence of short- and long-term ecosystem dynamics on weather and climate. Global Change Biology, submitted.

48. Pielke, R.A., W.R. Cotton, R.L. Walko, C.J. Tremback, M.E. Nicholls, M.D. Moran, D.A. Wesley, T.J. Lee, and J.H. Copeland, 1992: A comprehensive meteorological modeling system - RAMS. Meteor. Atmos. Phys., 49, 69-91.

49. Ramírez, J. A. and B. Finnerty, 1996: CO2 and Temperature Effects on Evapotranspiration and Irrigated Agriculture. *ASCE Journal of Irrigation and Drainage Division.* 122(3), 155-163.

50. Ramírez, J. A. and B. Finnerty, 1996: Precipitation and Water Table Effects on Agricultural Production and Economics. *ASCE Journal of Irrigation and Drainage Division.* 122(3), 164-171.

51. Ramírez, J. A. and S. Senarath, 2000: A Statistical-Dynamical Parameterization of Canopy Interception and Land Surface-Atmosphere Interactions. *Journal of Climate.* Vol. 13, 4050-4063.

52. Riedi, R.H., 1998: Multifractals ans wavelets: A potential tool in Geophysics, Technical session on novel transforms, SEG meeting, New Orleans, LA.

53. Rodriguez-Iturbe, I., 1996: Scale of Fluctuation of Rainfall Models, WRR, 22(9), 15S-37S

54. Rodriguez-Iturbe, I., G.K. Vogel, R. Rigon, D. Entekhabi, F. Castelli, and A. Rinaldo, 1995: On the Spatial Organization of Soil Moisture Fields. *Geophysical Research Letters,* 22(20), 2757-2760.

55. Rogriguez-Iturbe, I., V.K. Gupta, and E. Waymire, 1984: Scale considerations in the Modeling of Temporal Rainfall, *Water Resources Research*, 20(11), 1611-1619.

56. Rosenfeld, D., D.B. Wolf, and D. Atlas, 1993: General probability-matched relations between radar reflectivity and rain rate, J. Appl. Meteor., 32, 50-72

57. SCS, 1985: National Engineering Handbook, Section 4: Hydrology, Washington, D.C.

58. Schertzer, D., and S. Lovejoy, 1987: Physical Modeling and analysis of rain and clouds by anisotropic scaling multiplicative processes, J. Geophys. Res., 92(D8), 9693-9714.

59. She, Z.-S. and E.C. Waymire, 1995, Quantized energy cascade and log-Poisson statistics in fully developed turbulence, Phys. Rev. Lett., 74(2)

60. Tessier, Y., S. Lovejoy, and D. Schertzer, 1993. Universal Multifractals: Theory and Observations for Rain and Clouds. *Journal of Applied Meteorology*, 32(2), 223-250.

61. USBR, 1959: Report on the South Platte River Basin, Region 7, Denver, Colorado

62. USDA, 1994: State Soil Geographic (STATSGO) Data Base – Data use information, Natural Resources Conservation Service, National Soil Survey Center, Miscellaneous Publication Number 1492, Fort Worth, TX

63. Vuruputur, V., 1999: Spatio-Temporal Organization and Space-Time Downscaling of Precipitation Fields, Ph.D. Thesis, University of Minnesota

64. Walko, R.L., L. Band, J. Baron, T.G.F. Kittel, R. Lammers, T.J. Lee, D. Ojima, R.A. Pielke Sr.,C. Taylor, C. Tague, C.J. Tremback and P. L. Vidalc, 2000: Coupled Atmosphere-Biophysics-Hydrology Models for Environmental Modeling. Journal of Climate. Vol. 39, 931-944.

65. WSAT , 2000: Water: The potential Consequences of Climate Variability and Change for the Water Resources of the United States, The Report of the Water Sector Assessment Team of the National Assessment of the Potential Consequences, For the U.S. Global Change Research Program.

66. Watson, R.T., M.C.Zinyowera, and R.H.Moss (Ed.), 1997: The Regional Impacts of Climate Change: An Assessment of Vulnerability, A Special Report of IPCC Working group II, Cambridge University Press

67. Wigley, T. M. L., P. D. Jones, K. R. Briffa, and G. Smith, 1990: Obtaining Sub-Grid-Scale Information From Coarse Resolution General Circulation Model Output. *Journal of Geophysical Research.* 95(D2), 1943 - 1953.

68. Wilby, R.L. and T.M.L. Wigley, 1997: Downscaling General Circulation Model output: A review of methods and limitations, Progress in Physical Geography, 21(4), 530-548.

69. Wilks, D. S., 1989: Statistical Specification of Local Surface Weather Elements from Large-Scale Information. *Theoretical and Applied Climatology*, 40, 119 - 134.

70. Woodley, W.L., A.R. Olson, A. Herndon and V. Wiggert, 1975: Comparison of gage and radar methods of convective rain measurement, J. Appl. Meteor., 14, 909-928

Appendix A. NEXRAD Observations and Downscaled Precipitation

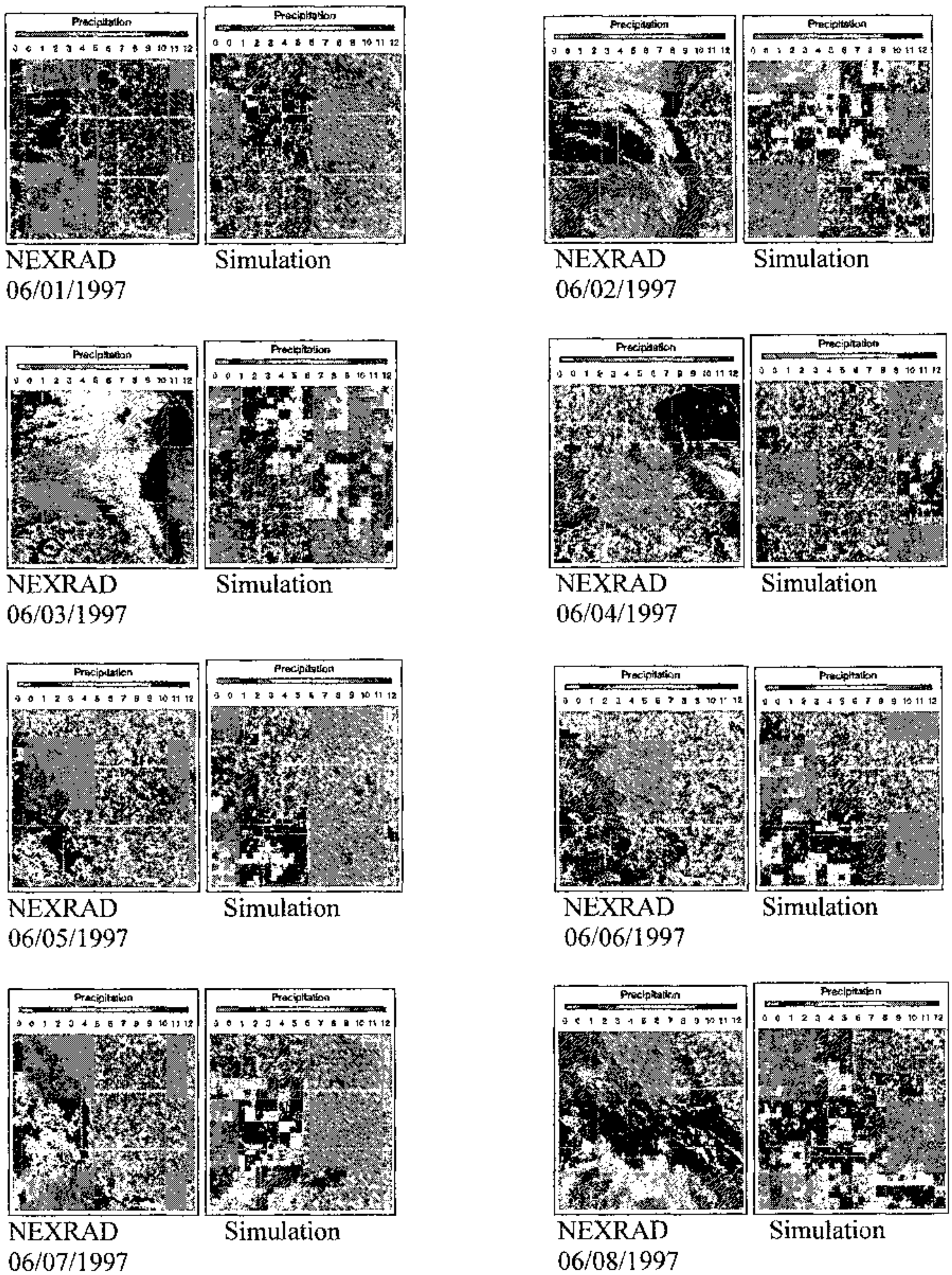

Figure A-A1 NEXRAD observations and corresponding fields simulated using the downscaling model (June 1997)

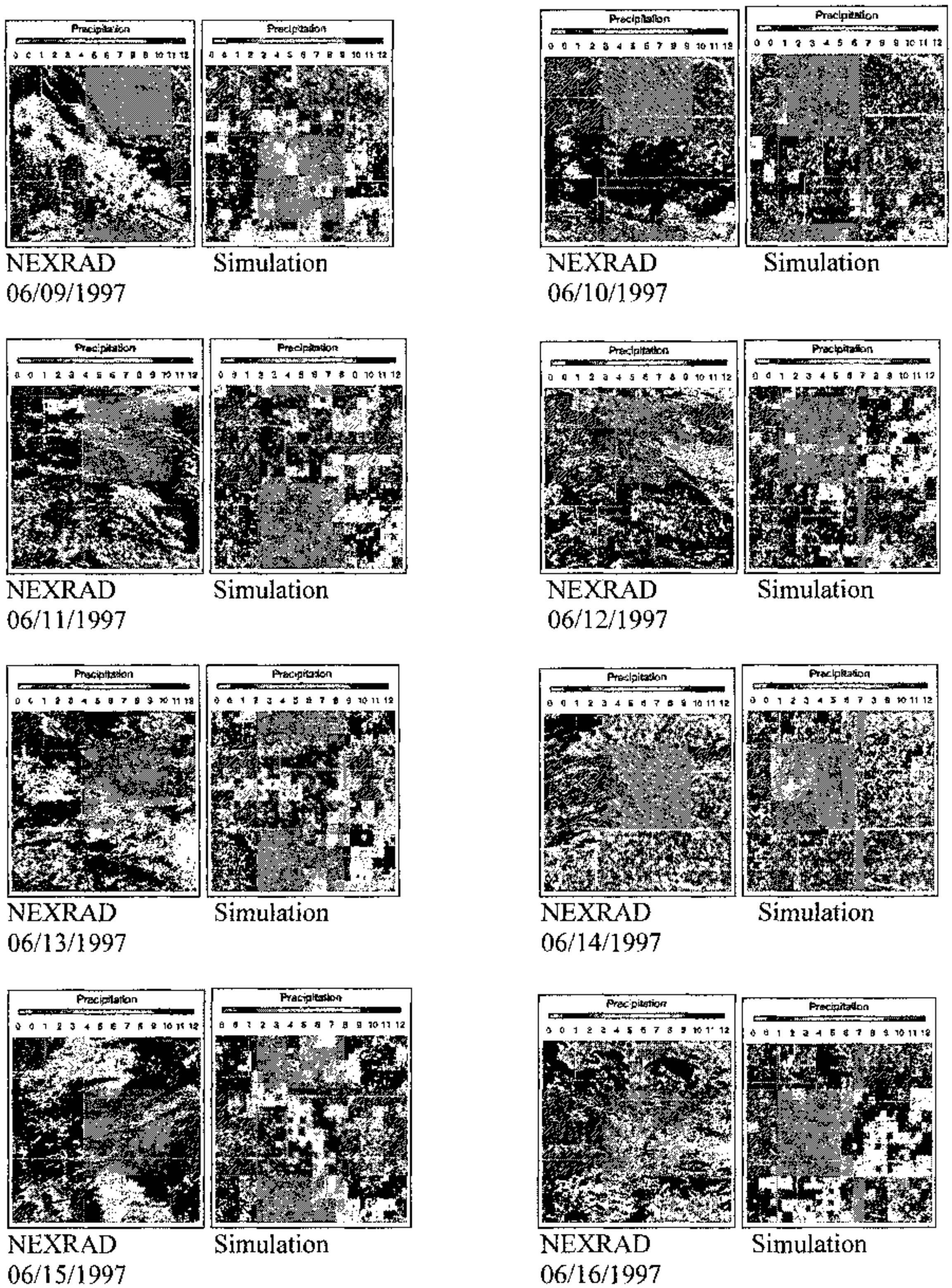

Figure A-A1 NEXRAD observations and corresponding fields simulated using the downscaling model (June 1997) (Continued)

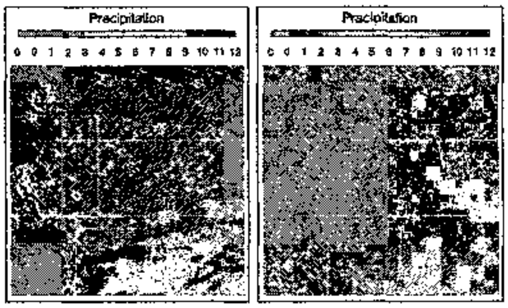

NEXRAD Simulation
06/17/1997

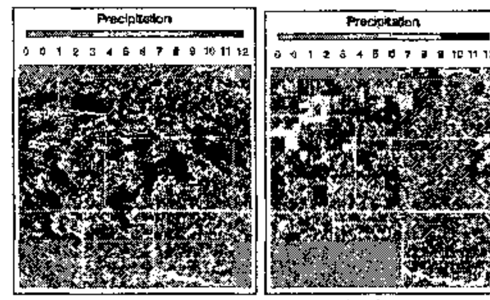

NEXRAD Simulation
06/18/1997

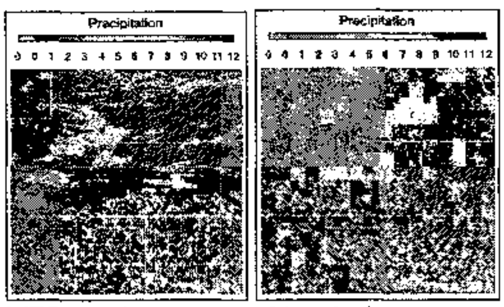

NEXRAD Simulation
06/19/1997

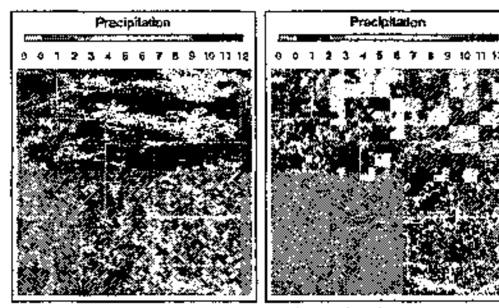

NEXRAD Simulation
06/20/1997

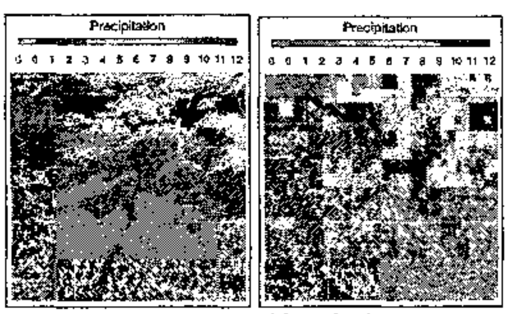

NEXRAD Simulation
06/21/1997

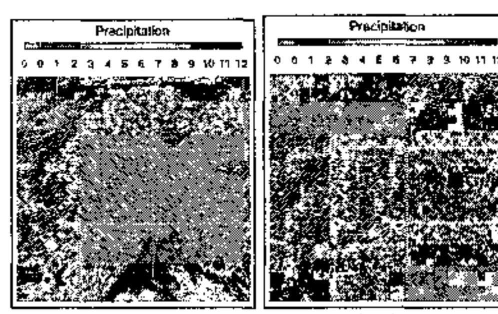

NEXRAD Simulation
06/22/1997

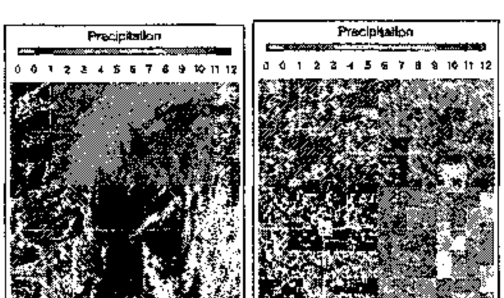

NEXRAD Simulation
06/23/1997

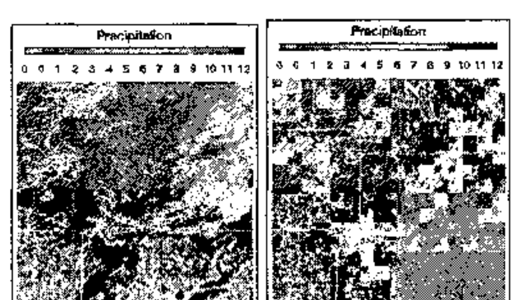

NEXRAD Simulation
06/24/1997

Figure A-A1 NEXRAD observations and corresponding fields simulated using the downscaling model (June 1997) (Continued)

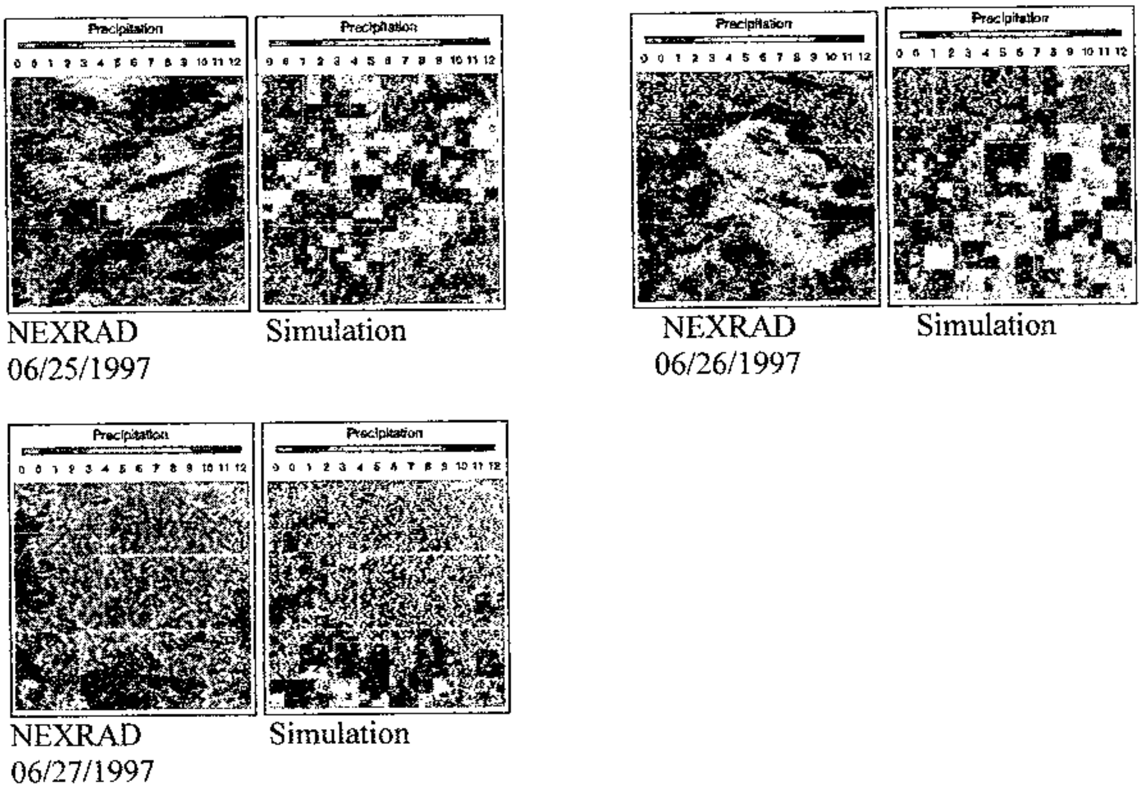

Figure A-A1 NEXRAD observations and corresponding fields simulated using the downscaling model (June 1997) (Continued)

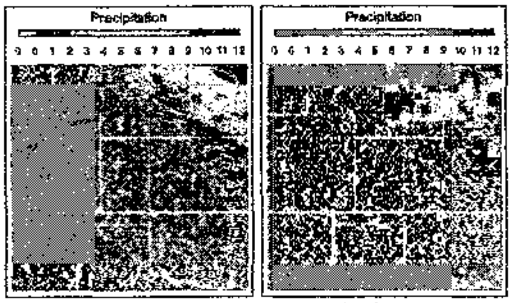

NEXRAD Simulation
07/01/1997

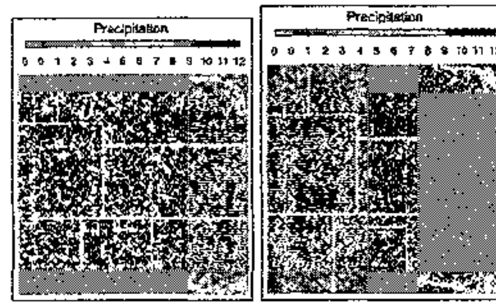

NEXRAD Simulation
07/02/1997

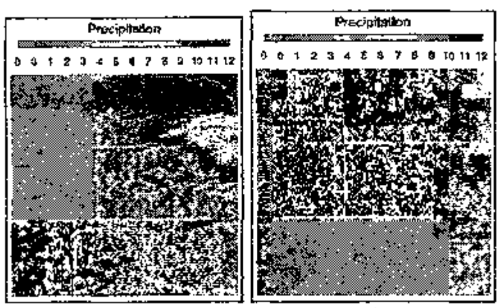

NEXRAD Simulation
07/03/1997

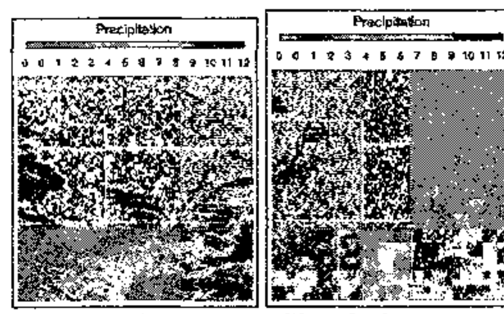

NEXRAD Simulation
07/04/1997

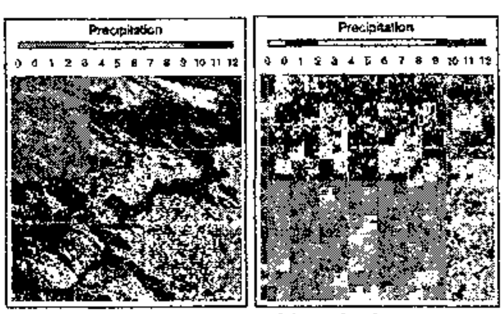

NEXRAD Simulation
07/05/1997

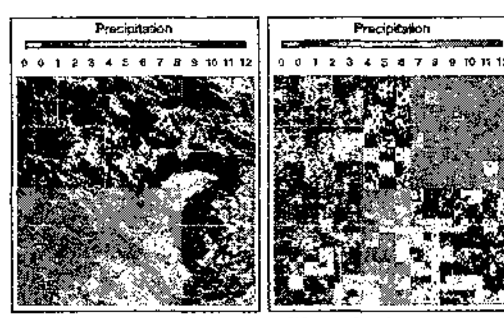

NEXRAD Simulation
07/06/1997

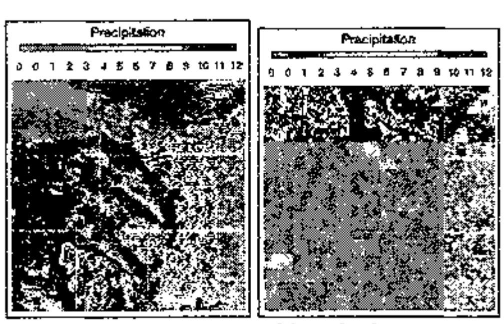

NEXRAD Simulation
07/07/1997

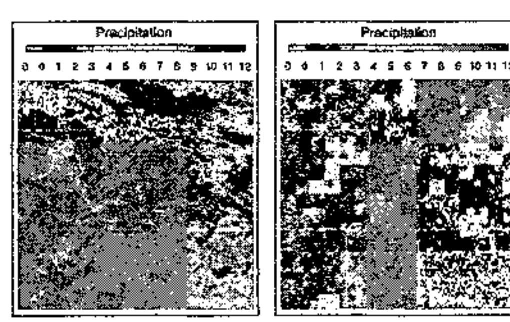

NEXRAD Simulation
07/08/1997

Figure A-A2 NEXRAD observations and corresponding fields simulated using the downscaling model (July 1997)

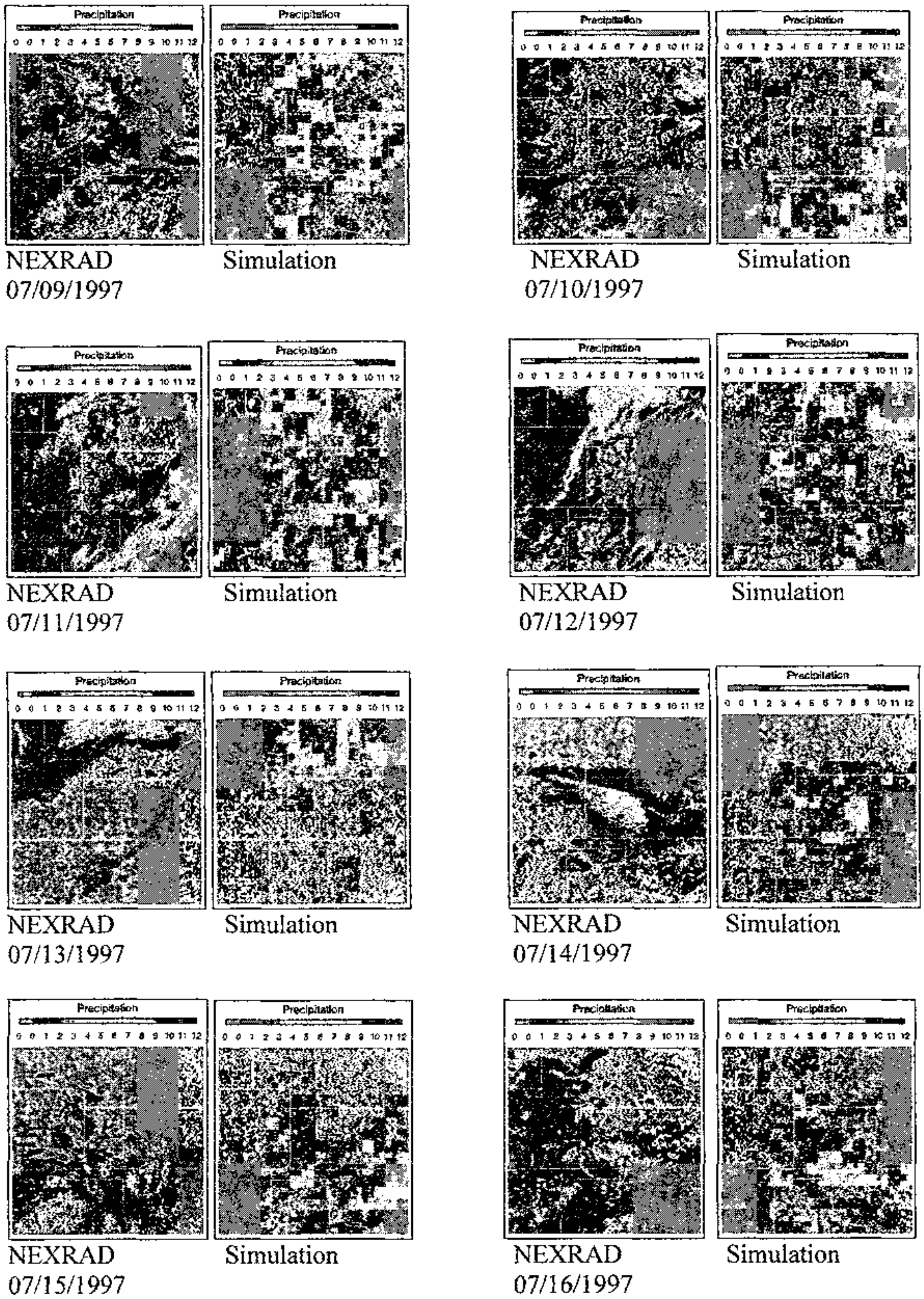

Figure A-A2 NEXRAD observations and corresponding fields simulated using the downscaling model (July 1997) (Continued)

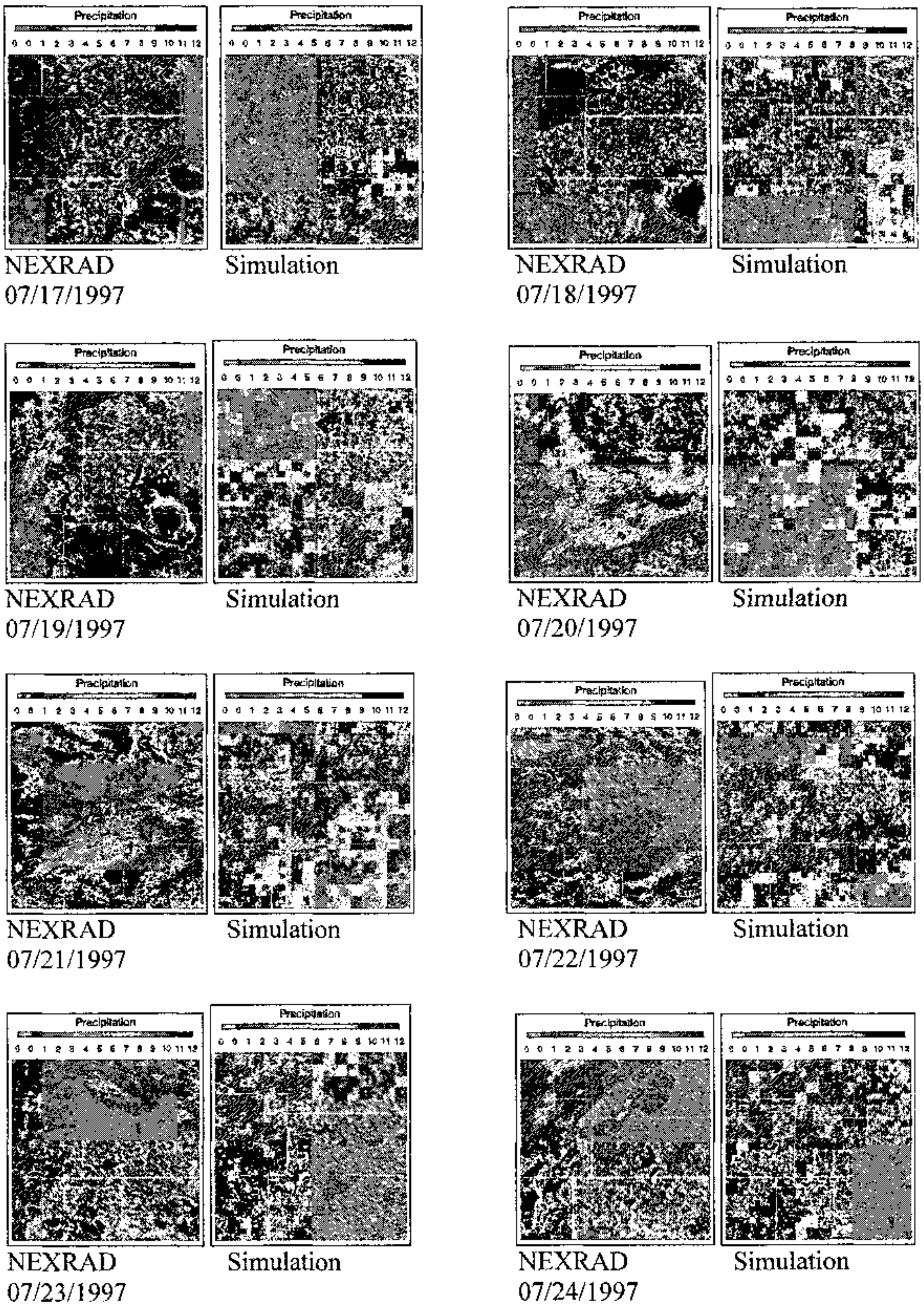

Figure A-A2 NEXRAD observations and corresponding fields simulated using the downscaling model (July 1997) (Continued)

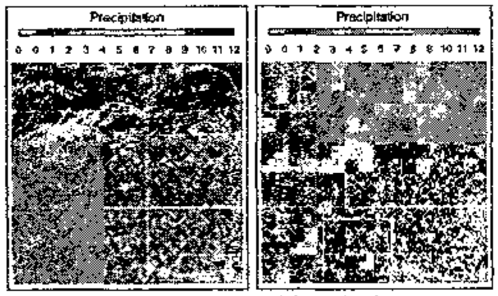

NEXRAD Simulation
07/25/1997

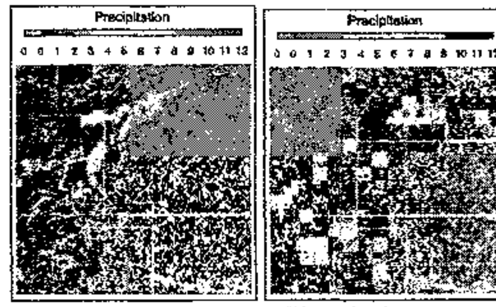

NEXRAD Simulation
07/26/1997

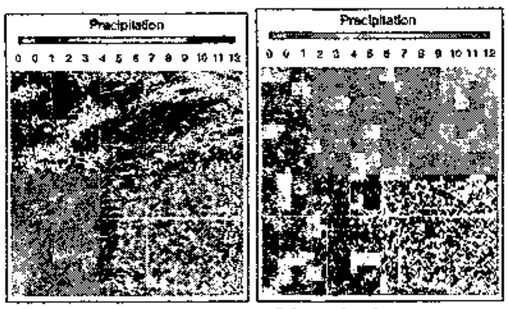

NEXRAD Simulation
07/27/1997

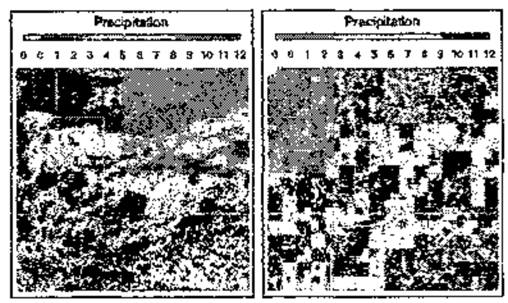

NEXRAD Simulation
07/28/1997

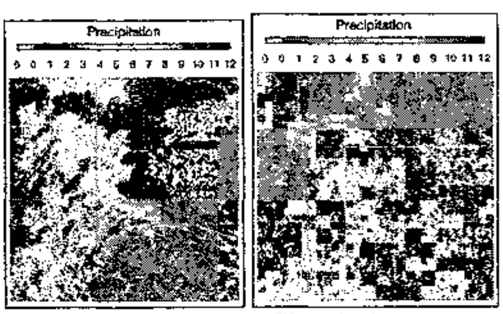

NEXRAD Simulation
07/29/1997

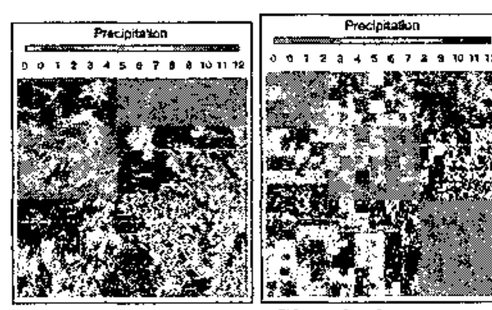

NEXRAD Simulation
07/30/1997

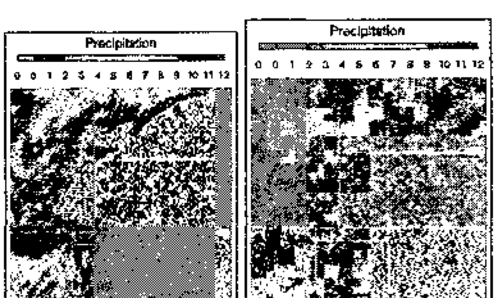

NEXRAD Simulation
07/31/1997

Figure A-A2 NEXRAD observations and corresponding fields simulated using the downscaling model (July 1997) (Continued)

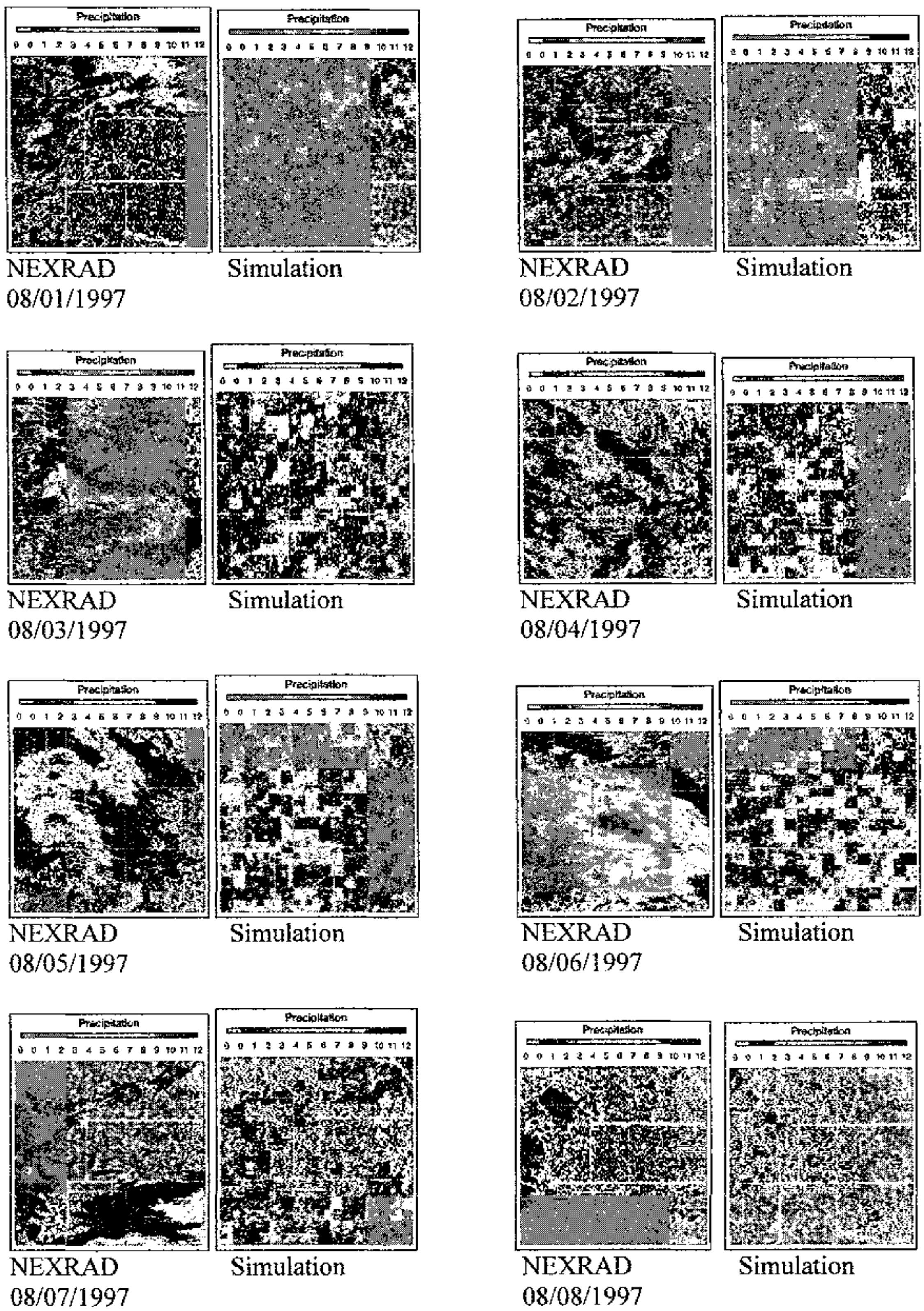

Figure A-A3 NEXRAD observations and corresponding fields simulated using the downscaling model (August 1997)

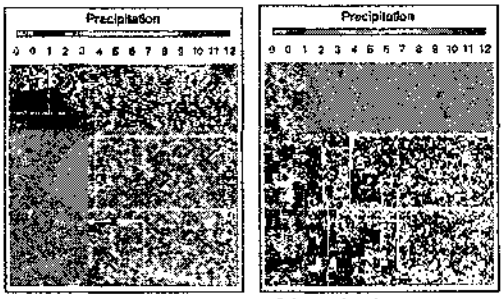

NEXRAD 08/09/1997 Simulation

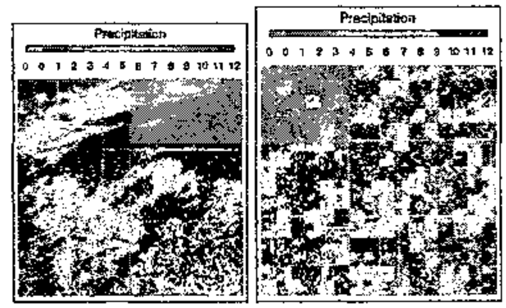

NEXRAD 08/10/1997 Simulation

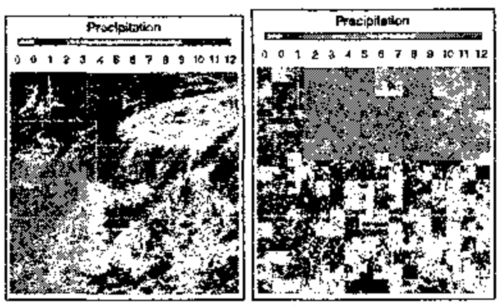

NEXRAD 08/11/1997 Simulation

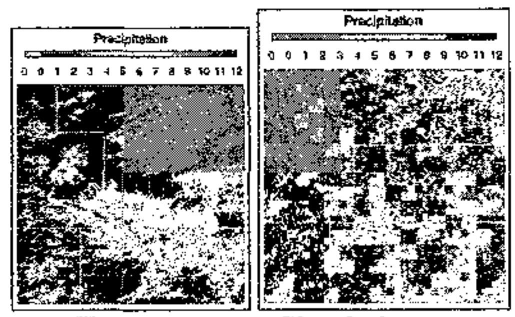

NEXRAD 08/12/1997 Simulation

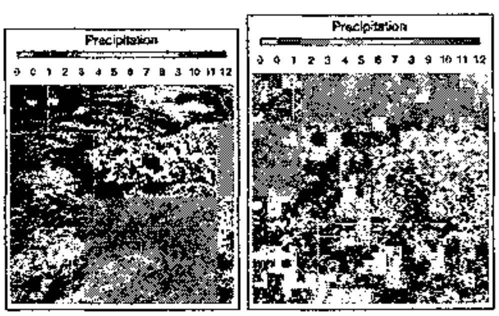

NEXRAD 08/13/1997 Simulation

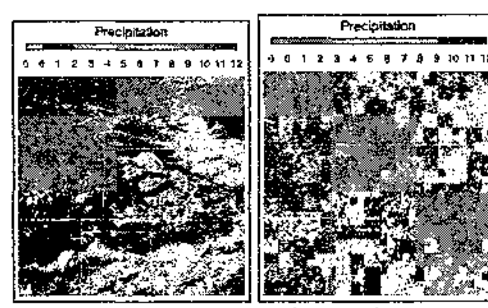

NEXRAD 08/14/1997 Simulation

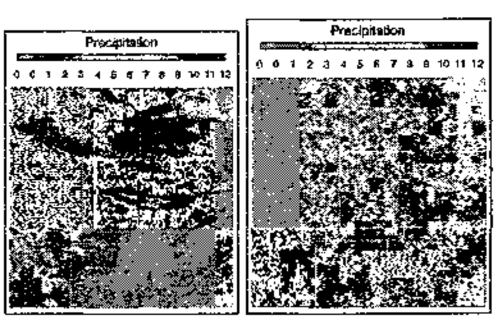

NEXRAD 08/15/1997 Simulation

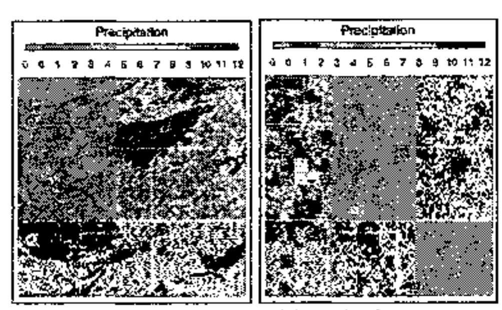

NEXRAD 08/16/1997 Simulation

Figure A-A3 NEXRAD observations and corresponding fields simulated using the downscaling model (August 1997) (continued)

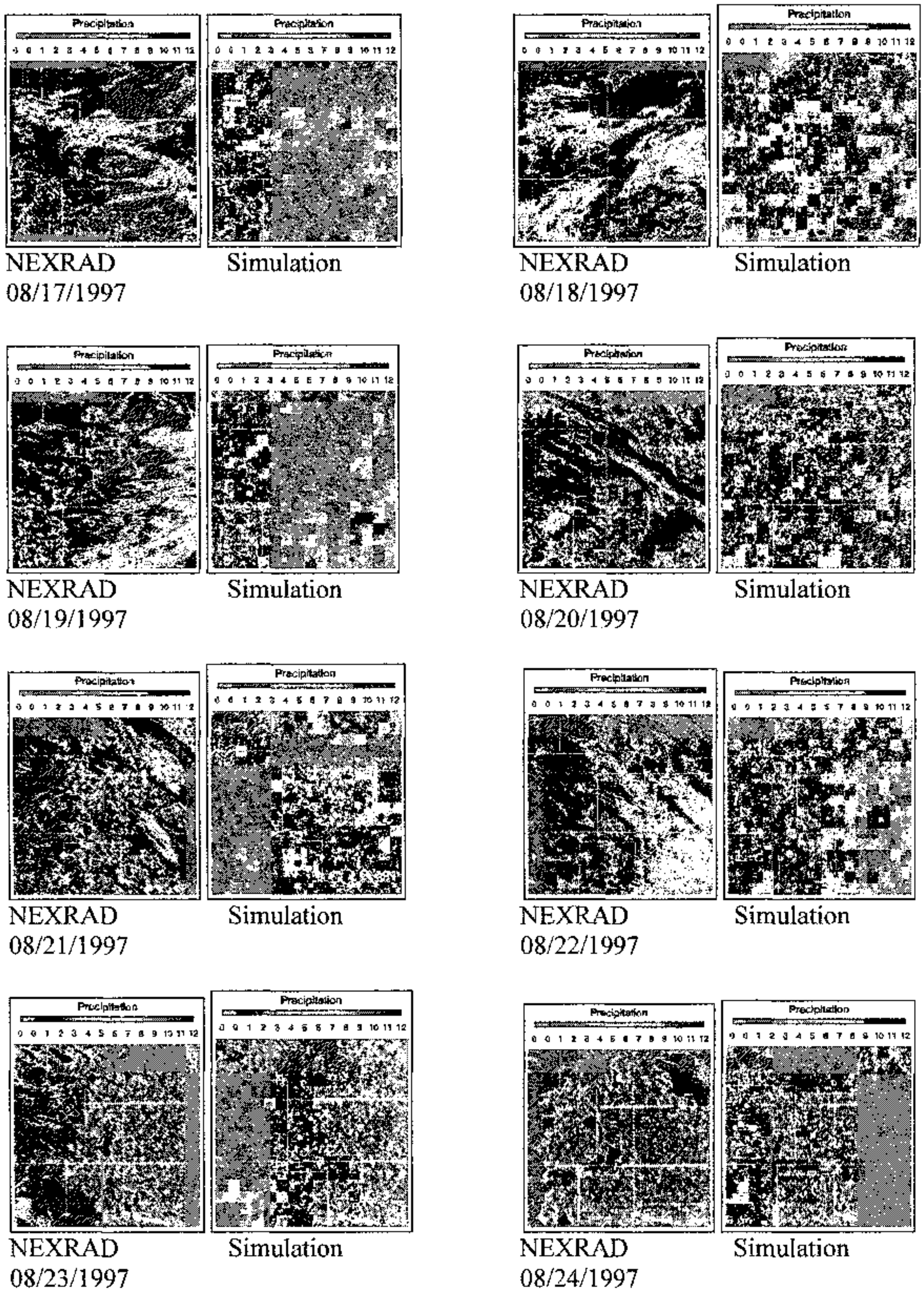

Figure A-A3 NEXRAD observations and corresponding fields simulated using the downscaling model (August 1997) (continued)

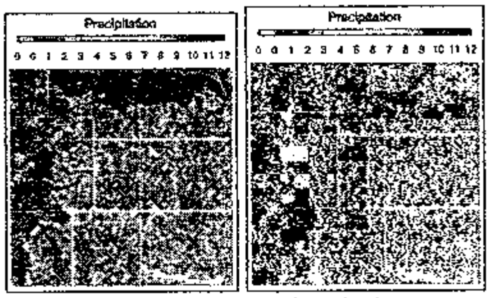

NEXRAD Simulation
08/25/1997

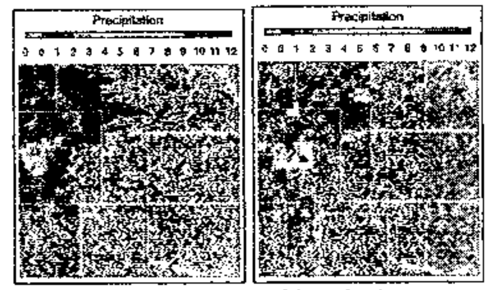

NEXRAD Simulation
08/26/1997

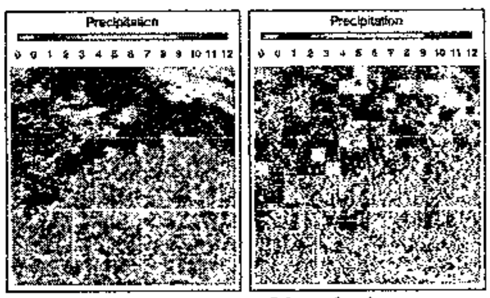

NEXRAD Simulation
08/27/1997

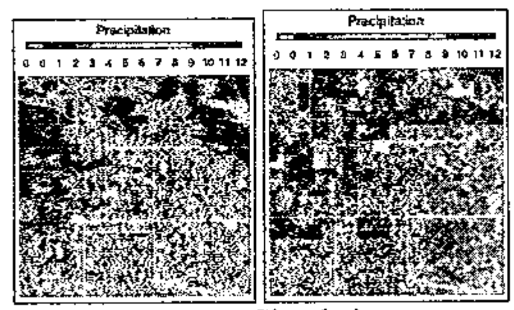

NEXRAD Simulation
08/28/1997

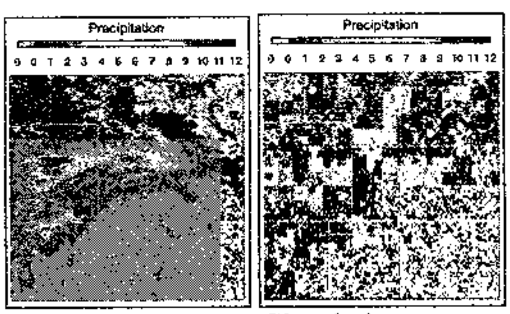

NEXRAD Simulation
08/29/1997

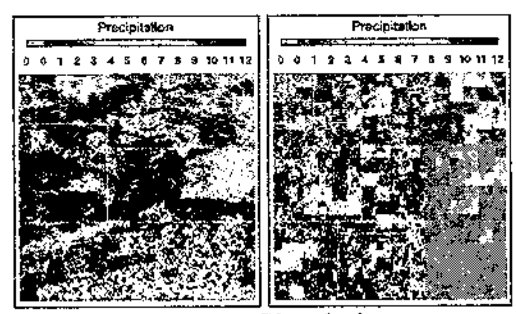

NEXRAD Simulation
08/30/1997

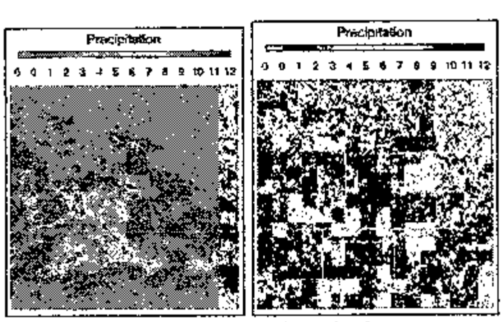

NEXRAD Simulation
08/31/1997

Figure A-A3 NEXRAD observations and corresponding fields simulated using the downscaling model (August 1997) (continued)

Appendix B. Derivation of covariance matrices

$$S_{\mathbf{ZZ}} = E\left[\mathbf{ZZ}^T\right] = Cov\left[\mathbf{Z}, \mathbf{Z}^T\right] = E\left[\begin{bmatrix} \mu_{01}(t) \\ \mu_{02}(t) \\ \mu_{03}(t) \\ \mu_{04}(t) \end{bmatrix} \begin{bmatrix} \mu_{01}(t) & \mu_{02}(t) & \mu_{03}(t) & \mu_{04}(t) \end{bmatrix}\right]$$

$$= \begin{bmatrix} E[\mu_{01}(t)\mu_{01}(t)] & E[\mu_{01}(t)\mu_{02}(t)] & E[\mu_{01}(t)\mu_{03}(t)] & E[\mu_{01}(t)\mu_{04}(t)] \\ E[\mu_{02}(t)\mu_{01}(t)] & E[\mu_{02}(t)\mu_{02}(t)] & E[\mu_{02}(t)\mu_{03}(t)] & E[\mu_{02}(t)\mu_{04}(t)] \\ E[\mu_{03}(t)\mu_{01}(t)] & E[\mu_{03}(t)\mu_{02}(t)] & E[\mu_{03}(t)\mu_{03}(t)] & E[\mu_{03}(t)\mu_{04}(t)] \\ E[\mu_{04}(t)\mu_{01}(t)] & E[\mu_{04}(t)\mu_{01}(t)] & E[\mu_{04}(t)\mu_{03}(t)] & E[\mu_{04}(t)\mu_{04}(t)] \end{bmatrix}$$

$$S_{\mathbf{XX}} = E\left[\mathbf{XX}^T\right] = Cov\left[\mathbf{X}, \mathbf{X}^T\right] = E\left[\begin{bmatrix} \mu_{01}(t-1) \\ \mu_{02}(t-1) \\ \mu_{03}(t-1) \\ \mu_{04}(t-1) \end{bmatrix} \begin{bmatrix} \mu_{01}(t-1) & \mu_{02}(t-1) & \mu_{03}(t-1) & \mu_{04}(t-1) \end{bmatrix}\right]$$

$$= \begin{bmatrix} E[\mu_{01}(t-1)\mu_{01}(t-1)] & E[\mu_{01}(t-1)\mu_{02}(t-1)] & E[\mu_{01}(t-1)\mu_{03}(t-1)] & E[\mu_{01}(t-1)\mu_{04}(t-1)] \\ E[\mu_{02}(t-1)\mu_{01}(t-1)] & E[\mu_{02}(t-1)\mu_{02}(t-1)] & E[\mu_{02}(t-1)\mu_{03}(t-1)] & E[\mu_{02}(t-1)\mu_{04}(t-1)] \\ E[\mu_{03}(t-1)\mu_{01}(t-1)] & E[\mu_{03}(t-1)\mu_{02}(t-1)] & E[\mu_{03}(t-1)\mu_{03}(t-1)] & E[\mu_{03}(t-1)\mu_{04}(t-1)] \\ E[\mu_{04}(t-1)\mu_{01}(t-1)] & E[\mu_{04}(t-1)\mu_{02}(t-1)] & E[\mu_{04}(t-1)\mu_{03}(t-1)] & E[\mu_{04}(t-1)\mu_{04}(t-1)] \end{bmatrix}$$

$$S_{\mathbf{YY}} = E\left[\mathbf{YY}^T\right] = Cov\left[\mathbf{Y}, \mathbf{Y}^T\right] = Var[\mu_0(t)][1]$$

$$S_{\mathbf{ZX}} = E\left[\mathbf{ZX}^T\right] = Cov\left[\mathbf{Z}, \mathbf{X}^T\right] = E\left[\begin{bmatrix} \mu_{01}(t) \\ \mu_{02}(t) \\ \mu_{03}(t) \\ \mu_{04}(t) \end{bmatrix} \begin{bmatrix} \mu_{01}(t-1) & \mu_{02}(t-1) & \mu_{03}(t-1) & \mu_{04}(t-1) \end{bmatrix}\right]$$

$$
= \begin{bmatrix} E[\mu_{01}(t)\mu_{01}(t-1)] & E[\mu_{01}(t)\mu_{02}(t-1)] & E[\mu_{01}(t)\mu_{03}(t-1)] & E[\mu_{01}(t)\mu_{04}(t-1)] \\ E[\mu_{02}(t)\mu_{01}(t-1)] & E[\mu_{02}(t)\mu_{02}(t-1)] & E[\mu_{02}(t)\mu_{03}(t-1)] & E[\mu_{02}(t)\mu_{04}(t-1)] \\ E[\mu_{03}(t)\mu_{01}(t-1)] & E[\mu_{03}(t)\mu_{02}(t-1)] & E[\mu_{03}(t)\mu_{03}(t-1)] & E[\mu_{03}(t)\mu_{04}(t-1)] \\ E[\mu_{04}(t)\mu_{01}(t-1)] & E[\mu_{04}(t)\mu_{02}(t-1)] & E[\mu_{04}(t)\mu_{03}(t-1)] & E[\mu_{04}(t)\mu_{04}(t-1)] \end{bmatrix}
$$

$$
S_{\mathbf{ZY}} = E[\mathbf{ZY}^T] = Cov[\mathbf{Z}, \mathbf{Y}^T] = E\left[\begin{bmatrix} \mu_{01}(t) \\ \mu_{02}(t) \\ \mu_{03}(t) \\ \mu_{04}(t) \end{bmatrix} \mu_0(t)\right] = \begin{bmatrix} E[\mu_{01}(t)\mu_0(t)] \\ E[\mu_{02}(t)\mu_0(t)] \\ E[\mu_{03}(t)\mu_0(t)] \\ E[\mu_{04}(t)\mu_0(t)] \end{bmatrix}
$$

$$
S_{\mathbf{XY}} = E[\mathbf{XY}^T] = Cov[\mathbf{X}, \mathbf{Y}^T] = E\left[\begin{bmatrix} \mu_{01}(t-1) \\ \mu_{02}(t-1) \\ \mu_{03}(t-1) \\ \mu_{04}(t-1) \end{bmatrix} \mu_0(t)\right] = \begin{bmatrix} E[\mu_{01}(t-1)\mu_0(t)] \\ E[\mu_{02}(t-1)\mu_0(t)] \\ E[\mu_{03}(t-1)\mu_0(t)] \\ E[\mu_{04}(t-1)\mu_0(t)] \end{bmatrix}
$$

Appendix C. Derivation of $E[\ln X]$ when X follows $N(1,s^2)$

Let X be a random variable distributed as $N(\mu, s^2)$. The normal distribution has a probability density function given by

$$f_X(x) = \frac{1}{s\sqrt{2\pi}} \exp\left[-\frac{1}{2}\left(\frac{x-\mu}{s}\right)^2\right], \quad -\infty < x < \infty \tag{C-1}$$

Let $Y = \ln X$; then Y will follow log-normal distribution which is $N(\lambda, \zeta^2)$ where λ and ζ are mean and standard deviation of Y, respectively. It follows that $X = e^Y$ and

$$\overline{X} = E(X) = E(e^Y) \tag{C-2}$$

Then:

$$\overline{X} = \frac{1}{\zeta\sqrt{2\pi}} \int_{-\infty}^{\infty} e^y \exp\left[-\frac{1}{2}\left(\frac{y-\lambda}{\zeta}\right)^2\right] dy$$

$$\overline{X} = \frac{1}{\zeta\sqrt{2\pi}} \int_{-\infty}^{\infty} \exp\left[y - \frac{1}{2}\left(\frac{y-\lambda}{\zeta}\right)^2\right] dy \tag{C-3}$$

By completing the square on the exponent, we obtain,

$$\overline{X} = \left[\frac{1}{\zeta\sqrt{2\pi}} \int_{-\infty}^{\infty} \exp\left\{-\frac{1}{2}\left(\frac{y-(\lambda+\zeta^2)}{\zeta}\right)^2 dy\right\}\right] \exp\left(\lambda + \tfrac{1}{2}\zeta^2\right)$$

The quantity within the bracket is the total unit area of the Gaussian density function $N(\lambda+\zeta^2, \zeta)$; hence $\overline{X} = \exp(\lambda + \frac{1}{2}\zeta^2)$. Thus we have $\lambda = \ln\overline{X} - \frac{1}{2}\zeta^2$.

Similarly, we derive the variance of X as follows:

$$E(X^2) = \frac{1}{\zeta\sqrt{2\pi}} \int_{-\infty}^{\infty} e^{2y} \exp\left[-\frac{1}{2}\left(\frac{y-\lambda}{\zeta}\right)^2\right] dy$$

$$E(X^2) = \frac{1}{\zeta\sqrt{2\pi}} \int_{-\infty}^{\infty} \exp\left[-\frac{1}{2\zeta^2}\left\{y^2 - 2(\lambda+2\zeta^2)y + \lambda^2\right\}\right] dy$$

By completing the square on the exponent, the above integral yields,

$$E\left(X^2\right)=\left[\frac{1}{\zeta\sqrt{2\pi}}\int_{-\infty}^{\infty}\exp\left\{-\frac{1}{2}\left(\frac{(y-(\lambda+2\zeta^2))}{\zeta}\right)^2 dy\right\}\right]\exp\left[2\left(\lambda+\zeta^2\right)\right]$$

$$E(X^2)=\exp\left[2\left(\lambda+\zeta^2\right)\right] \tag{C-4}$$

Using $Var(X)=E(X^2)-\overline{X}^2$ and equation (C-1),

$$Var(X)=\exp\left[2\left(\lambda+\zeta^2\right)\right]-\exp\left[2\left(\lambda+\tfrac{1}{2}\zeta^2\right)\right]$$

$$Var(X)=\overline{X}^2\left(e^{\zeta^2}-1\right)$$

From which we obtain

$$\zeta^2=\ln\left(1+\frac{s^2}{\overline{X}^2}\right) \tag{C-5}$$

Therefore,

$$E\left[\ln X\right]=\lambda=\ln\overline{X}-\tfrac{1}{2}\zeta^2=\ln\overline{X}-\tfrac{1}{2}\ln\left(1+\frac{s^2}{\overline{X}^2}\right)$$

In our case, $\overline{X}=1$. So,

$$E\left[\ln X\right]=-\tfrac{1}{2}\ln\left(1+s^2\right) \tag{C-6}$$

If $s/\overline{X}$ is not large, say ≤ 0.30, $\ln\left[1+\left(s^2/\overline{X}^2\right)\right]\cong s^2/\overline{X}^2$. In such cases, the equation (C-5) becomes,

$$\zeta\cong\frac{s}{\overline{X}}$$

Then, the equation (C-6) will be simply

$$E\left[\ln X\right]=-\tfrac{1}{2}s^2$$

Appendix D. Sources of DEM data

Availability of DEM models is improving daily. There are many sources of DEM data files, some for free and some for a nominal cost. A good place to start is at the source of U.S. DEM data: the U.S. Geological Survey (USGS). A few of the many sites offering DEM data are listed below:

- USGS Earth Resources Observation Systems (EROS) Data Center (U.S. Government Site) : http://edc.usgs.gov/products/elevation.html
- USGS 7.5 Minute DEM Data (U.S. Government Site) : http://edcwww.cr.usgs.gov/glis/hyper/guide/7_min_dem
- USGS 1 Degree DEM Data (U.S. Government Site) : http://edcwww.cr.usgs.gov/glis/hyper/guide/1_dgr_dem
- USGS EDC / NASA Distributed Active Archive Center (DAAC) : http://edc.usgs.gov/products/elevation/gtopo30.html
- Micro Map and CAD(Commercial Site) : http://www.micromap.com/micromap/
- Land Info(Commercial Site) : http://www.landinfo.com/
- USGS Geographic Data Download (U.S. Government Site) : http://edc.usgs.gov/doc/edchome/ndcdb/ndcdb.html
- Geography Network (Commercial Site) : http://www.geographynetwork.com/
- GIS Data Depot (Commercial Site) : http://www.gisdatadepot.com/
- GIS.com (Commercial Site) : http://www.gis.com/

Appendix E. GTOPO30 data adjustment and the process of SHG map projection

The data are originally stored in geographic coordinates (latitude/longitude) and are referenced to the World Geodetic Survey (WGS) system of 1984 (WGS84). The basic elevation unit is meters. Neither ArcView nor ArcInfo supports the conversion of signed image data; therefore the negative 16-bit signed values of original GTOPO30 need adjustment after grid conversion (ArcView: Theme-Convert to Grid). The ArcView data adjustment is made on Analysis-Map Calculator using the following syntax:

```
([grdThm]>=32768.AsGrid).Con([grdThm]-65536.AsGrid,[grdThm])
```

The grid-cell parameter file format of HMS is Standard Hydrologic Grid (SHG) or Hydrologic Rainfall Analysis Project (HRAP). The use of SHG can ensure greater alignment and compatibility between grid rainfall, like NEXRAD and a gridded sub-basin. The SHG format uses the Albers Equal Area projection. Therefore the DEM of GTOPO30 must be projected to Albers Equal Area projection using ArcToolbox of ArcGIS. The parameters for the SHG map projection are as follows:

Projection : Albers
Datum : North American Datum of 1983 (NAD83)
Ellipsoid : Geodetic Reference System of 1980 (GRS80)
Map units : meters
Central Meridian : 96^{o}W (-96.00)
Reference Latitude : $23\,^{o}$W (23.00)
Standard Parallel 1: $29\,^{o}30'$N (29.50)
Standard Parallel 2: $45\,^{o}30'$N (45.50)
False Easting : 0.0
False Northing : 0.0

Appendix F. Characteristics of STATSGO soil components

muid	compname	comppct	drainage	surftex	rockdepl	rockdeph	rockhard
COW	WATER	100					
CO023	MIRROR	15	W	STX-SL	51	102	HARD
	MEREDITH	15	W	STX-SL	153	153	
	ROCK OUTCROP	15		UWB	0	0	HARD
	PINKHAM	15	W	ST-FSL	153	153	
	RUBBLE LAND	15	E	FRAG	102	102	HARD
	CRYOFIBRISTS	5	P	FB	153	153	
	VASQUEZ	5	SP,P	ST-L	153	153	
	BROSS	10	W	STX-SL	153	153	
	HAVERLY	5	P,SP	ST-SL	51	102	HARD
CO303	LEADVILLE	25	W	FSL	153	153	
	GRANILE	20	W	GRV-SL	153	153	
	LAKEHELEN	10	W	FSL	51	102	HARD
	SCANDARD	5	W	ST-SL	51	102	HARD
	SEITZ	5	W	GR-FSL	153	153	
	LARAND	5	W	CBV-SL	153	153	
	LEIGHCAN	5	W	STV-SL	153	153	
	LIBEG	3	W	GR-SL	153	153	
	GELKIE	3	W	SL	153	153	
	WOODHALL	3	W	CBV-SL	51	102	HARD
	ESS	3	W	CB-SIL	153	153	
	ENDLICH	2	W	ST-L	51	102	HARD
	BLACKLEED	3	SE	STX-SL	153	153	
	ROCK OUTCROP	3		UWB	0	0	HARD
	ROGERT	3	W	GRV-SL	25	51	HARD
	HIEPRO	1	W	ST-SL	153	153	
	MUGGINS	1	W	ST-SL	153	153	
CO310	ROGERT	42	W	GRV-SL	25	51	HARD
	WOODHALL	13	W	CBV-SL	51	102	HARD
	ROCK OUTCROP	7		UWB	0	0	HARD
	RALEIGH	5	SE	GRV-SL	25	51	SOFT
	RALEIGH	5	SE	GRV-SL	25	51	SOFT
	TROUTDALE	5	W	SL	51	102	SOFT
	PILTZ	5	W	L	51	102	SOFT
	SKUTUM	4	W,MW	FSL	50	153	SOFT
	GUFFEY	4	W	GRV-SL	51	102	SOFT
	ADEL	3	W	L	153	153	
	MONTEZ	3	W	SL	102	153	HARD
	GRANILE	2	W	GRV-SL	153	153	
	LAKEHELEN	1	W	FSL	51	102	HARD
	STECUM	1	W	COSL	51	102	HARD

Table A-F1 Characteristics of STATSGO soil components

muid	compname	comppct	drainage	surftex	rockdepl	rockdeph	rockhard
CO315	GRANILE	30	W	GRV-SL	153	153	
	PEELER	12	W	SL	153	153	
	SEITZ	12	W	GR-FSL	153	153	
	ROGERT	7	W	GRV-SL	25	51	HARD
	LARAND	6	W	GRV-FSL	153	153	
	ROCK OUTCROP	6		UWB	0	0	HARD
	LAKE CREEK	6	W	BYV-SL	51	102	HARD
	LAKE HELEN	6	W	FSL	51	102	HARD
	GUFFEY	5	W	GRV-SL	51	102	SOFT
	WOODHALL	3	W	CBV-SL	51	102	HARD
	NORTHWATER	2	W	STV-L	153	153	
	LAMPHIER	1	W	L	153	153	
	BUNDO	2	W	CBV-SL	153	153	
	CHUBBS	1	W	CL	51	102	SOFT
	HERAKLE	1	W	CNV-L	25	51	HARD
CO318	BUSHVALLEY	25	W	CB-L	18	51	HARD
	ESS	20	W	GRV-L	153	153	
	HOODLE	10	W	L	153	153	
	CRYOBOROLLS	7	W	GRV-L	153	153	
	ADDERTON	6	W	L	153	153	
	YOUGA	5	W	SL	153	153	
	MORSET	4	W	L	153	153	
	SAWFORK	4	W	CBV-L	102	102	HARD
	TELLURA	4	W	GR-CL	153	153	
	COCHETOPA	3	W	CL	153	153	
	ROCK OUTCROP	2		UWB	0	0	SOFT
	HODDEN	2	W	GR-L	153	153	
	CHITTUM	2	W	SL	20	51	HARD
	CUMULIC CRYAQUOLLS	2	VP	CL	153	153	
	SILVERCLIFF	2	W,SE	GR-L	153	153	
	WHITEMANN	1	SE	CB-L	25	51	HARD
	SEITZ	1	W	GR-FSL	153	153	
CO336	BUENA VISTA	25	W	STV-SL	51	102	HARD
	GARO	20	W	CL	25	51	SOFT
	HEATH	15	W	L	153	153	
	TROUT CREEK	14	W	CL	51	102	SOFT
	LAPORTE	7	W	ST-SL	25	51	SOFT
	NATHROP	7	W	L	51	102	HARD
	TRUMP	7	W	L	25	51	HARD
	ROCK OUTCROP	3		UWB	0	0	HARD
	WELLSVILLE	2	W	VF-SL	153	153	

Table A-F1 Characteristics of STATSGO soil components (Cont'd)

muid	compname	comppct	drainage	surftex	rockdepl	rockdeph	rockhard
CO337	BUSHVALLEY	31	W	GRV-L	18	51	HARD
	QUANDER	15	W	CB-SL	153	153	
	HOODLE	15	W	GR-L	153	153	
	FRISCO	10	W	GR-L	153	153	
	ESS	10	W	GR-L	153	153	
	SEITZ	6	W	GRV-L	153	153	
	IRIGUL	5	W	STV-SL	25	51	HARD
	CORPENING	2	W	GR-L	10	51	HARD
	CHITTUM	1	W	SL	20	51	HARD
	ESS	1	W	CB-SIL	153	153	
	SILVERCLIFF	1	W,SE	GR-L	153	153	
	SAWFORK	1	W	CBV-L	102	102	HARD
	LUCKY	1	W	GR-SL	51	102	HARD
	MORSET	1	W	L	153	153	
CO338	HODDEN	40	W	GRV-L	153	153	
	GEBSON	20	W	SL	153	153	
	MORSET	5	W	L	153	153	
	TEMDILLE	5	SE	SL	153	153	
	SPINNEY	5	W	SL	153	153	
	LEVENMILE	3	W	SL	153	153	
	JERRY	2	W	L	153	153	
	POLICH VARIANT	2	W	SIL	102	153	SOFT
	CRYAQUOLLS	2	VP	L	153	153	
	WELLSVILLE	2	W	SL	153	153	
	BUSHVALLEY	2	W	GRV-L	18	51	HARD
	MATHIS	2	SE	STV-LFS	53	104	HARD
	BRINKERT	2	W	L	153	153	
	SILVERCLIFF	2	W,SE	GR-L	153	153	
	LIBEG	2	W	GR-SL	153	153	
	SAWFORK	1	W	CBV-L	102	102	HARD
	THIEL	1	W	CB-L	153	153	
	JODERO VARIANT	1	MW	CL	153	153	
	ROGERT	1	W	GRV-SL	25	51	HARD

Table A-F1 Characteristics of STATSGO soil components (Cont'd)

Element	Long name	Description
COMPNAME	Component Name	The name of the component (series, taxonomic unit, or miscellaneous area) of the map unit
comppct	Component Percent	The percentage of the component of the map unit
drainage	Soil Drainage Class	Code identifying the natural drainage condition of the soil and refers to the frequency and duration of periods when the soil is free of saturation. Example: Well Drained (W); Excessive (E); Moderately Well (MW); Poorly (P); Somewhat Excessively (SE); Somewhat Poorly (SP)
surftex	Surface Soil Texture	Code for the USDA texture for the surface layer or horizon. Example: Loam (L);Sandy loam (SL). Also includes terms used to modify texture and terms used in lieu of texture
rockdepl	Depth to Bedrock	The minimum value for the range in depth to bedrock, expressed in centimeters
rockdeph	Depth to Bedrock	The maximum value for the range in depth to bedrock, expressed in centimeters
rockhard	Bedrock hardness	The degree of hardness of the underlying rock. Rated as: HARD – Excavation requires blasting or special equipment or SOFT – Excavation can be made with trenching machines, backhoes, or small rippers.

Table A-F2 Definition of soil data elements

Appendix G. HEC-HMS data conversion process

Data are stored in blocks, or records, within a file, and each record is identified by a unique name called a "pathname". Each time data are stored or retrieved from the file, a pathname must be given. Along with the data, information about the data (e.g., units) is stored in a "header array". The DSS automatically stores the name of the program writing the data, the number of times the data have been written to, and the last written date and time.

The pathname consists of up to 80 characters and is, by convention, separated into six parts. The parts are referenced by the characters A, B, C, D, E, and F, and are delimited by a slash "/", as follows:

/A/B/C/D/E/F/

A brief description of the pathname for time series data used in this study follows:

PATHNAME PART	*DESCRIPTION*
A	River basin name (SPHead)
B	Data variable (Rainfall)
C	Data source (NEXRAD or GCM)
D	Starting date and time for block of data, such as 01JUN1997:0000
E	Ending date and time for block of data, such as 01JUN1997:2400
F	Year

A typical pathname might be:

/SPHead/Rainfall/NEXRAD/01JUN1997:0000/01JUN1997:2400/D1997/

The original NEXRAD data come in an ascii text file of an array structure consisting of columns and rows of rainfall values and should be converted to grid files which must have a header containing information of number of rows and columns, boundary coordinates in Albers Conic Equal Area Projection, cell size, etc. For example,

NCOLS 64

NROWS 64

XLLCORNER -912967.4104

YLLCORNER 1745819.6320

CELLSIZE 2000

0.000000	0.240450	1.254000	2.640000	0.745637	0.424000	
0.764355	1.345340	0.535520	2.453760	0.035253	0.004640	......

where NCOLS : number of colums, NROWS : number of rows,

XLLCORNER : x coordinate of the lower left corner,

YLLCORNER : y coordinate of the lower left corner.

The grid file must then be converted into DSS format using the "ai2dssGrid" program supplied by Tom Evans of the Hydrologic Engineering Center. The "ai2dssGrid" is a single execution file which runs in the DOS environment. Because the daily NEXRAD or GCM data during June to August covers 92 daily intervals, a batch file with 92 calls of daily run of "ai2dssGrid" was used to create a single DSS file that covers the entire time span of 92 days. With this file completed, one simply needs to appoint the DSS file location for inclusion in a HMS model.

Appendix H. Hydrographs computed using downscaled GCM precipitation

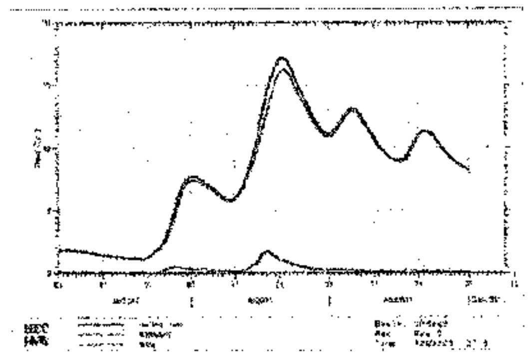

2011 SIMULATION1

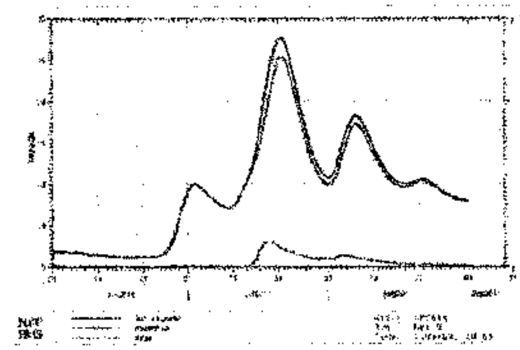

2011 SIMULATION2

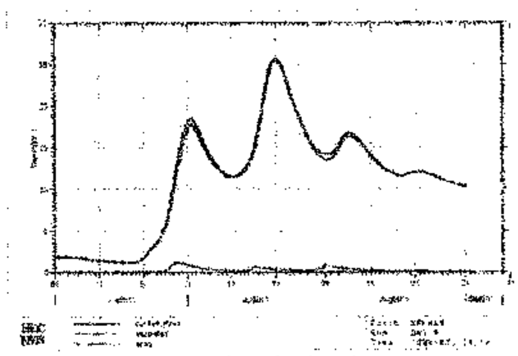

2011 Simulation3

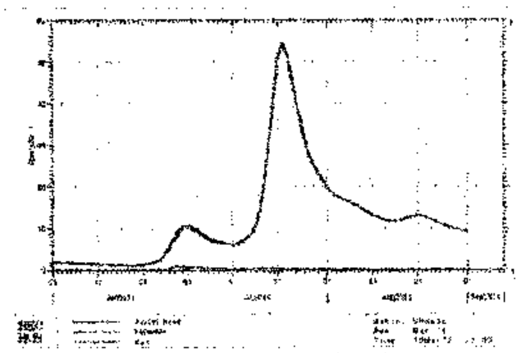

2011 Simulation4

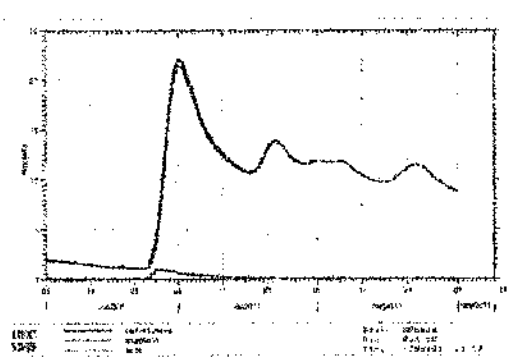

2011 Simulation5

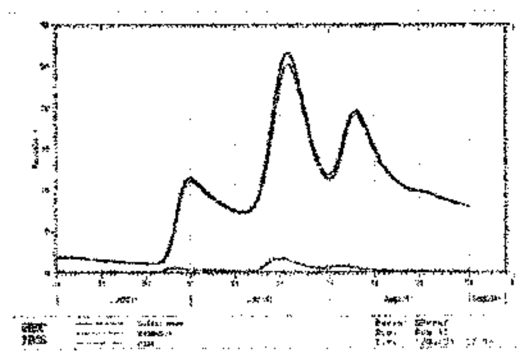

2011 Simulation6

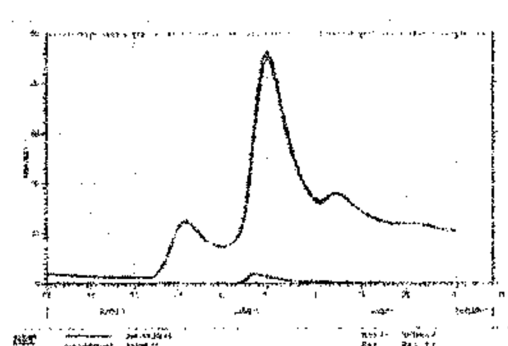

2011 Simulation7

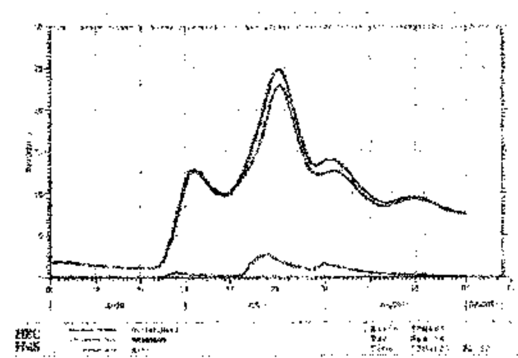

2011 Simulation8

Figure A-H1 The hydrographs using GCM rainfall prediction

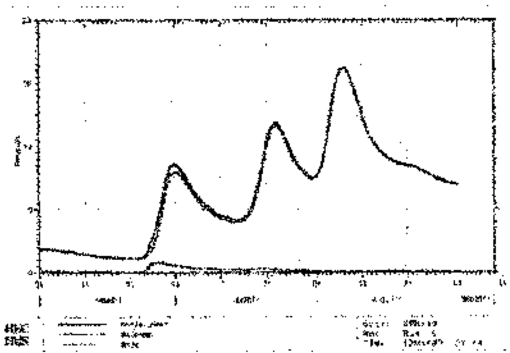

2011 Simulation9

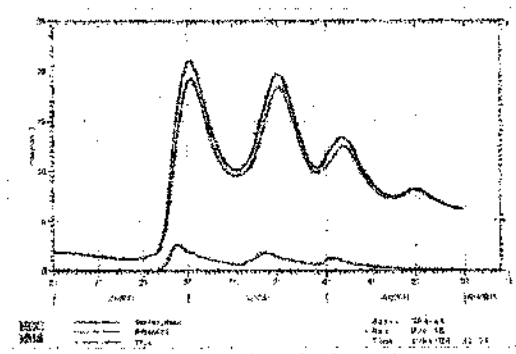

2011 Simulation10

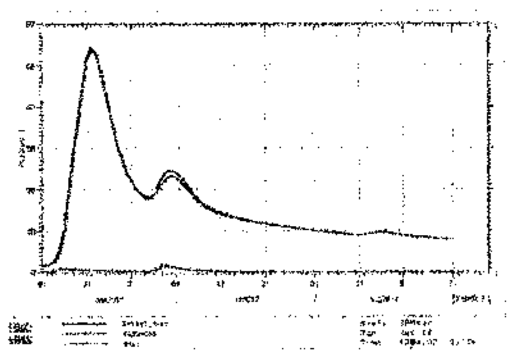

2012 Simulation1

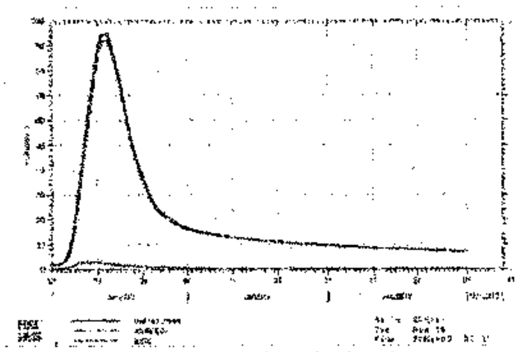

2012 Simulation2

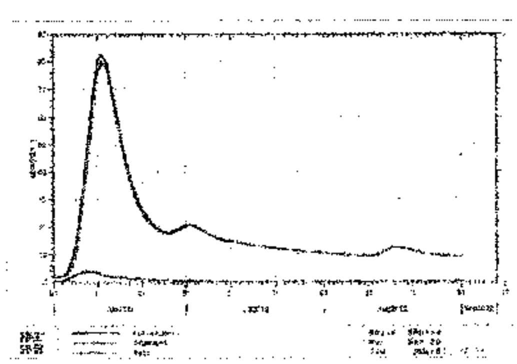

2012 Simulation3

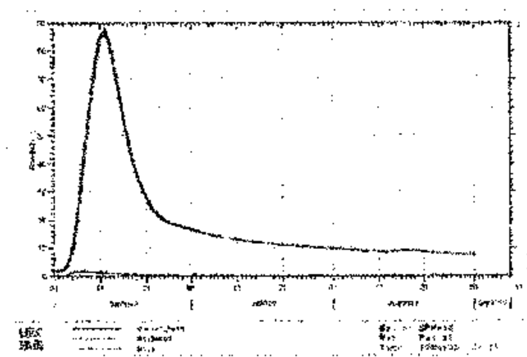

2012 Simulation4

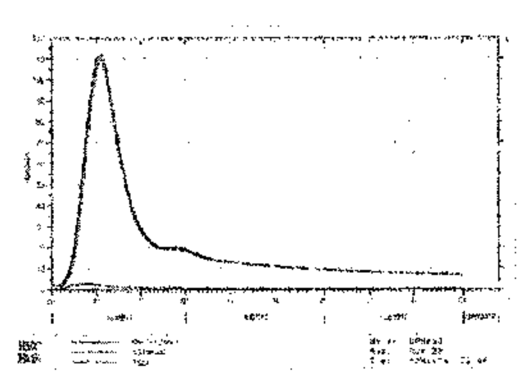

2012 Simulation5

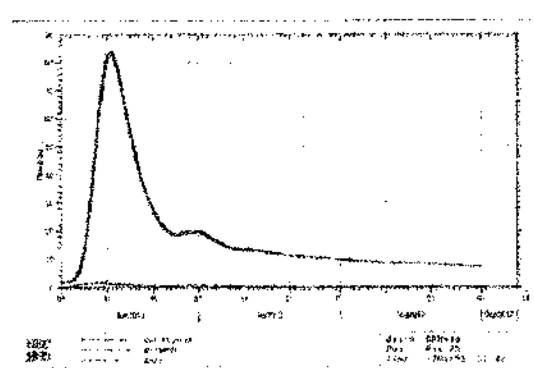

2012 Simulation6

Figure A-H1 The hydrographs using GCM rainfall prediction (cont'd)

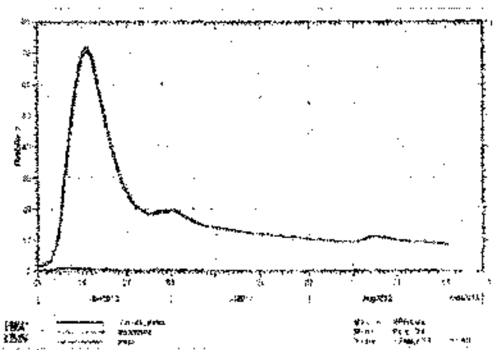
2012 Simulation7

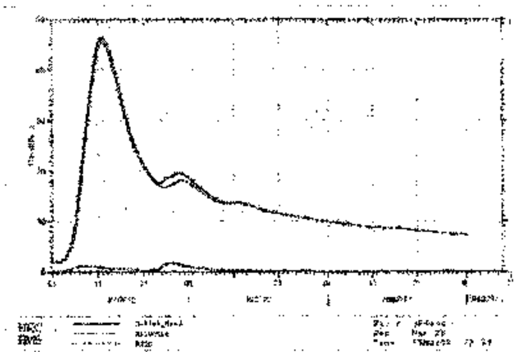
2012 Simulation8

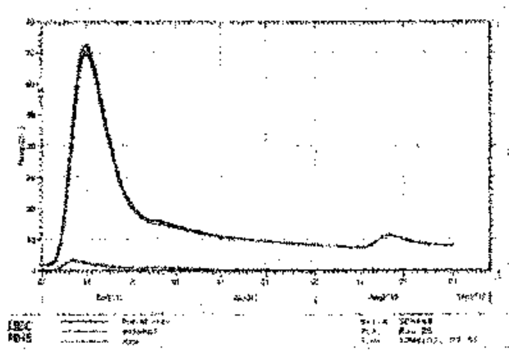
2012 Simulation9

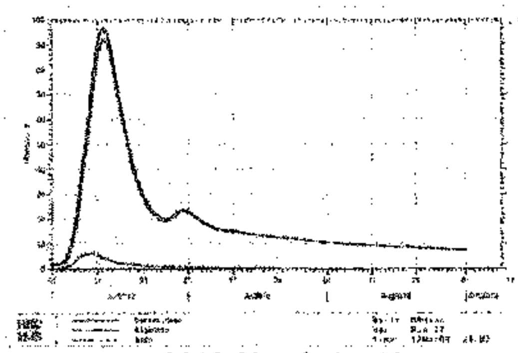
2012 Simulation10

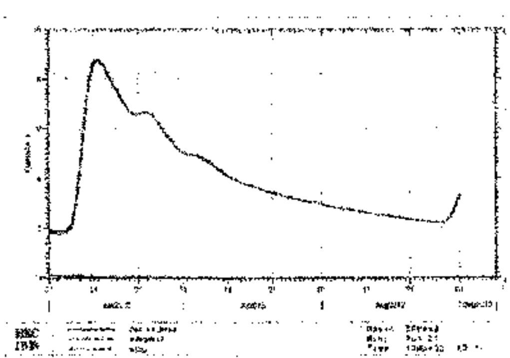
2013 Simulation1

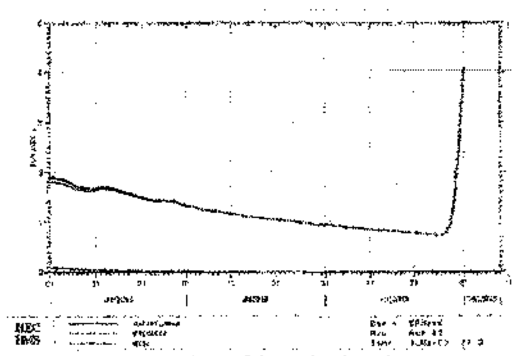
2013 Simulation2

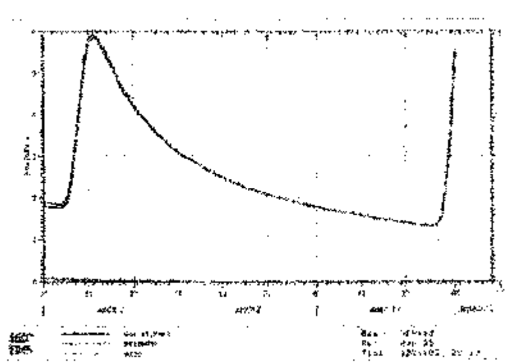
2013 Simulation3

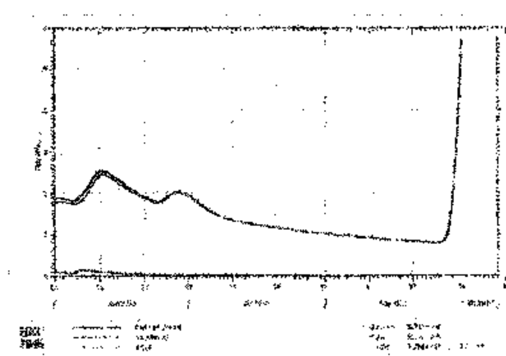
2013 Simulation4

Figure A-H1 The hydrographs using GCM rainfall prediction (cont'd)

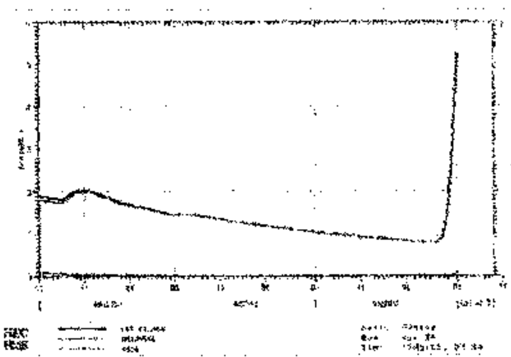

2013 Simulation5

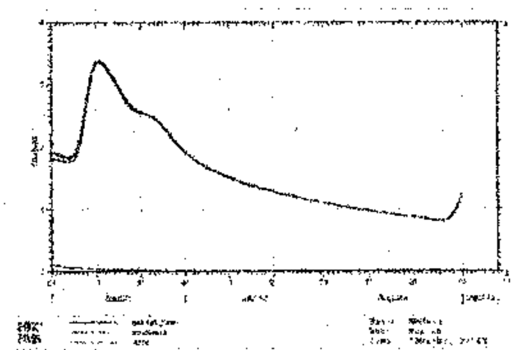

2013 Simulation6

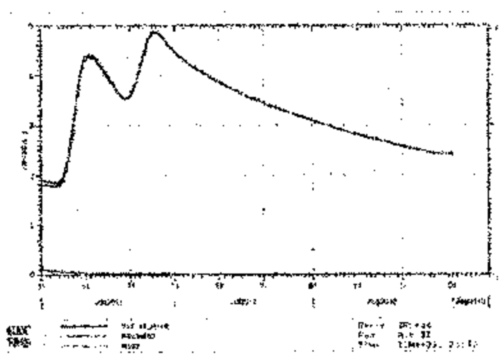

2013 Simulation7

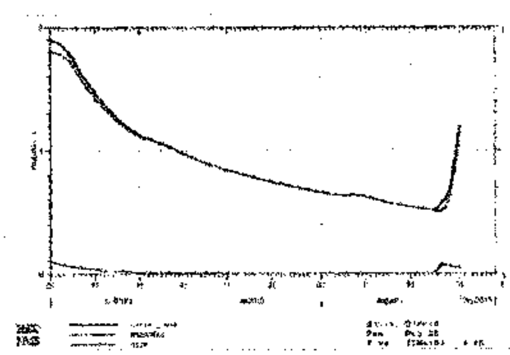

2013 Simulation8

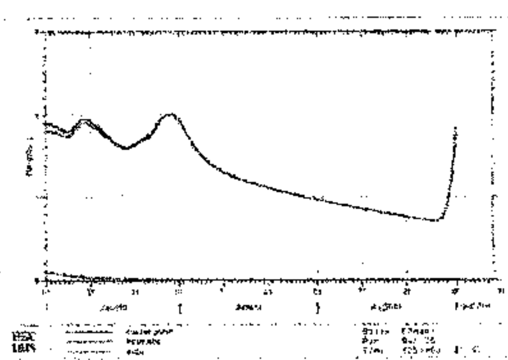

2013 Simulation9

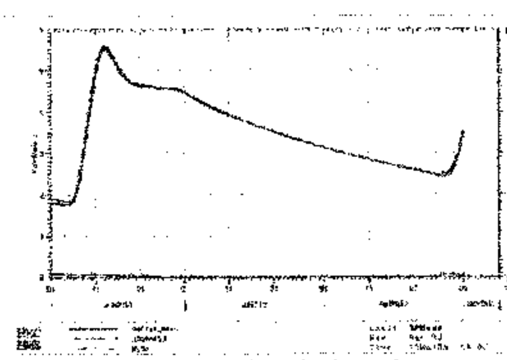

2013 Simulation10

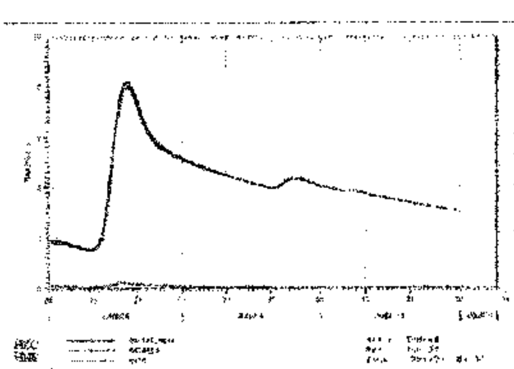

2014 Simulation1

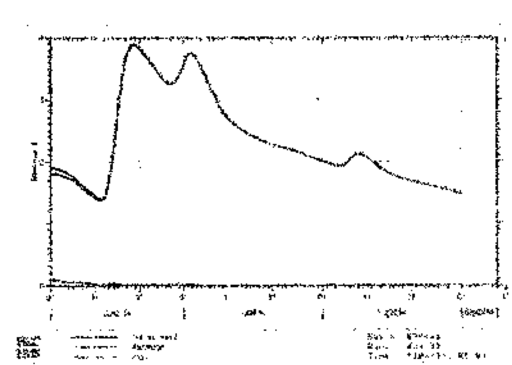

2014 Simulation2

Figure A-H1 The hydrographs using GCM rainfall prediction (cont'd)

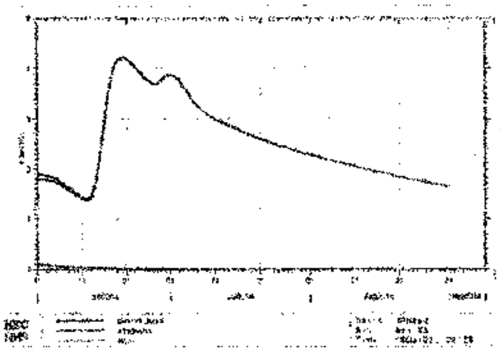

2014 Simulation3

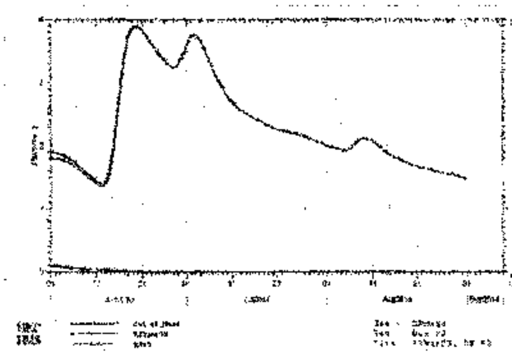

2014 Simulation4

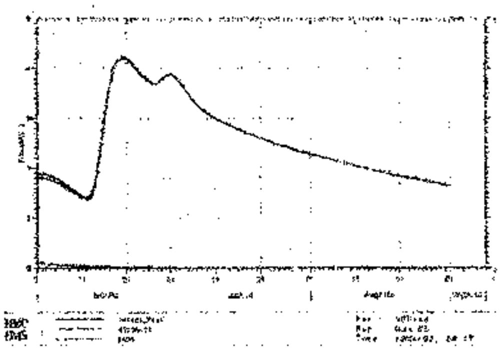

2014 Simulation5

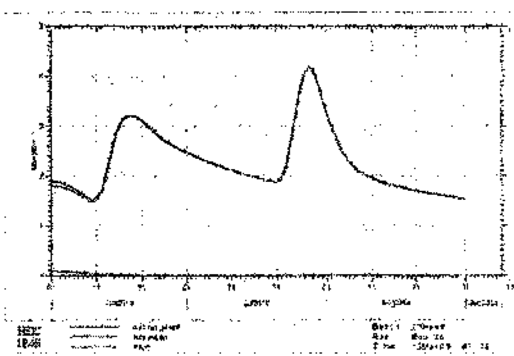

2014 Simulation6

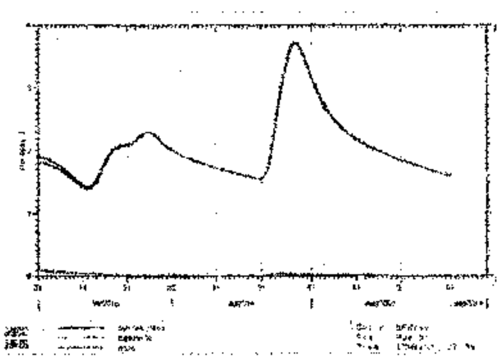

2014 Simulation7

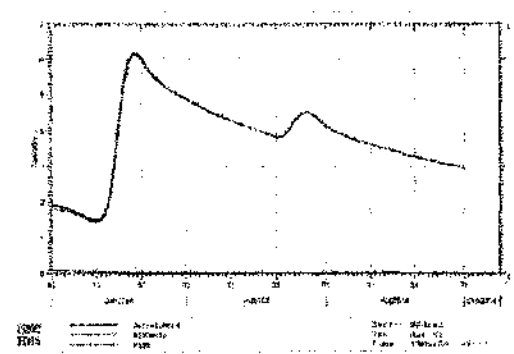

2014 Simulation8

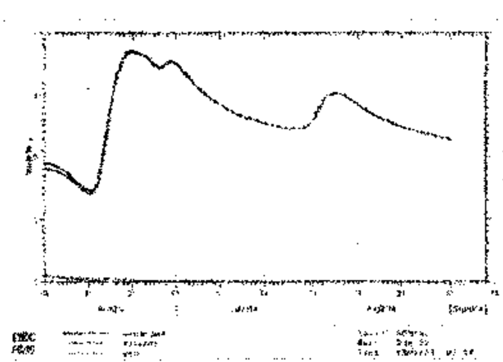

2014 Simulation9

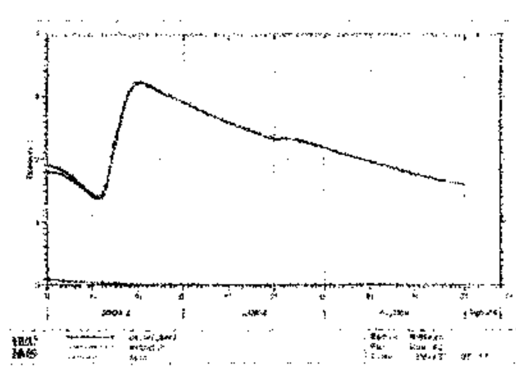

2014 Simulation10

Figure A-H1 The hydrographs using GCM rainfall prediction (cont'd)

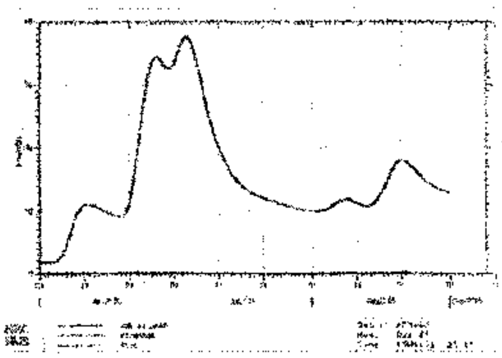

2015 Simulation1

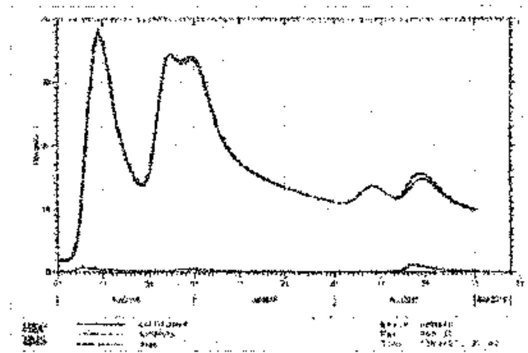

2015 Simulation2

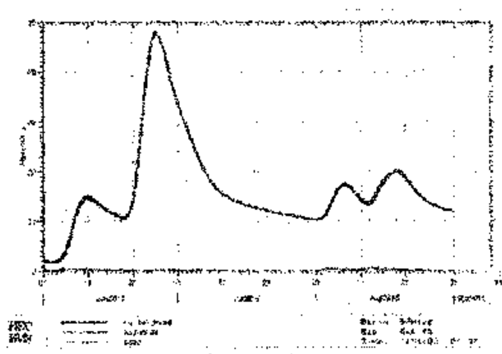

2015 Simulation3

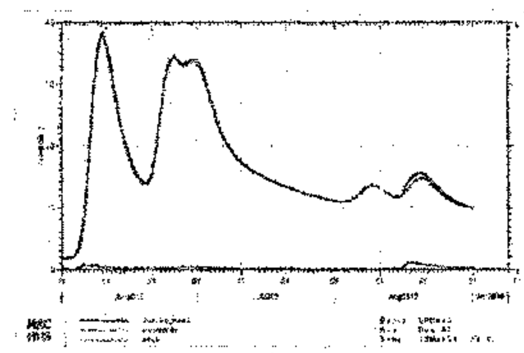

2015 Simulation4

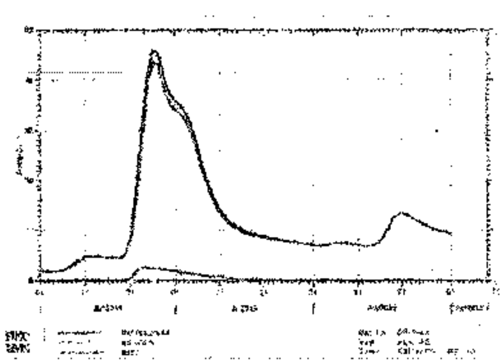

2015 Simulation5

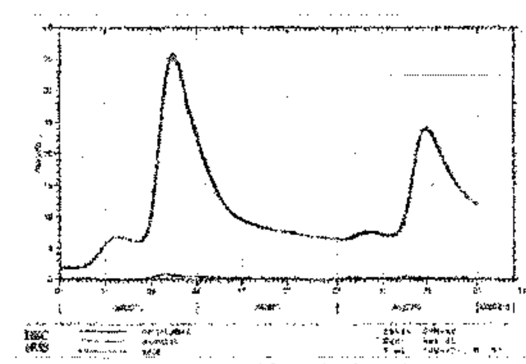

2015 Simulation6

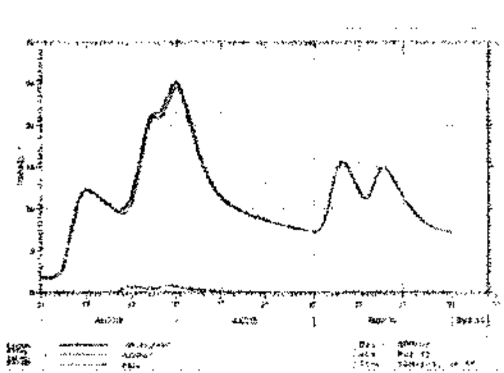

2015 Simulation7

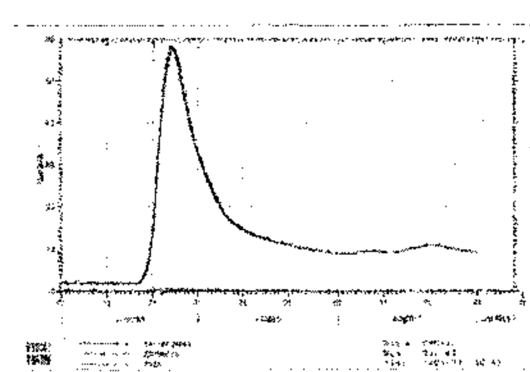

2015 Simulation8

Figure A-H1 The hydrographs using GCM rainfall prediction (cont'd)

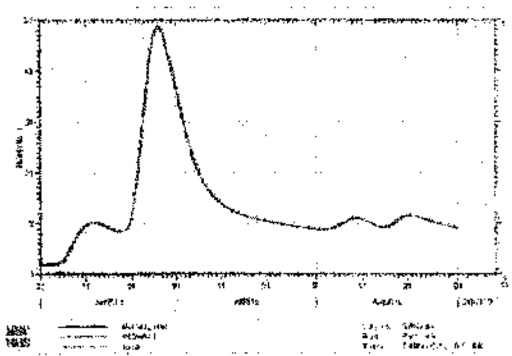

2015 Simulation9

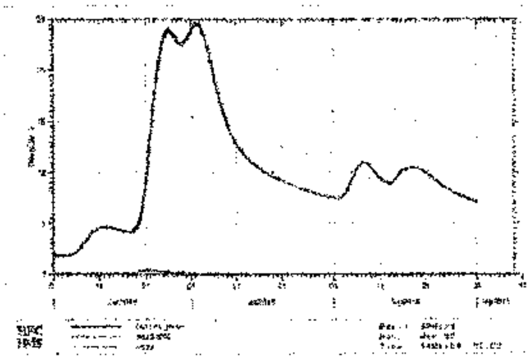

2015 Simulation10

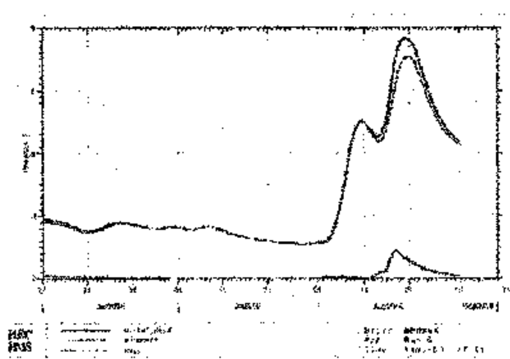

2016 Simulation1

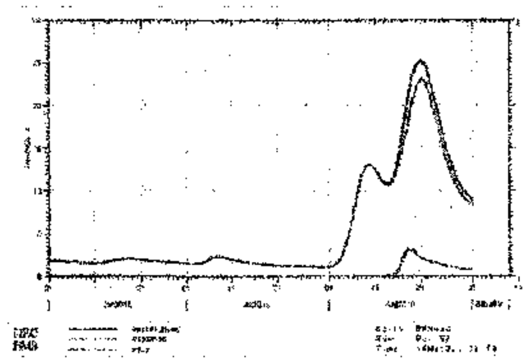

2016 Simulation2

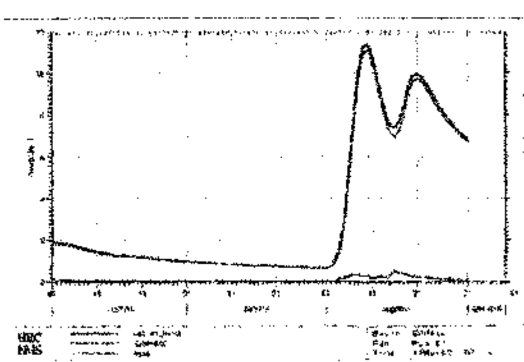

2016 Simulation3

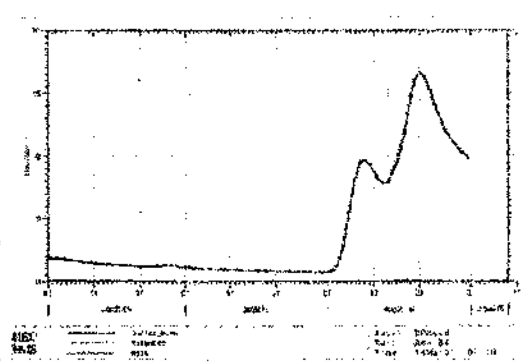

2016 Simulation4

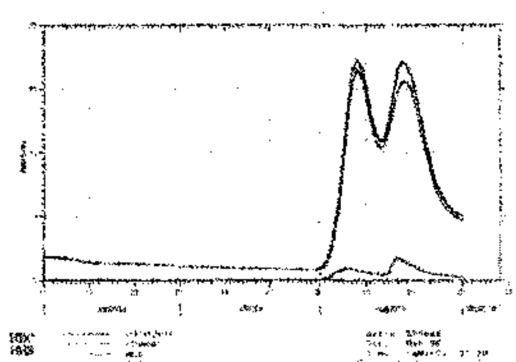

2016 Simulation5

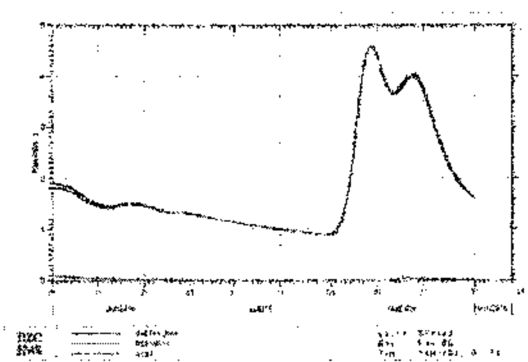

2016 Simulation6

Figure A-H1 The hydrographs using GCM rainfall prediction (cont'd)

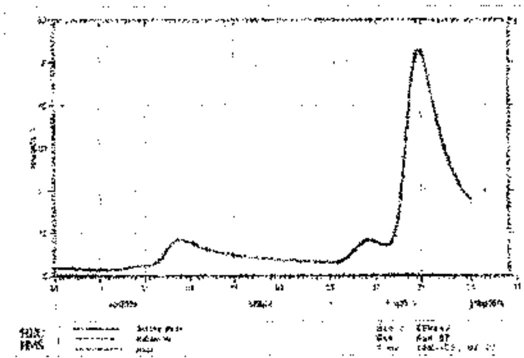
2016 Simulation7

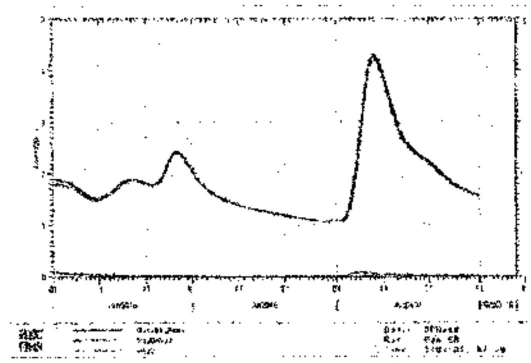
2016 Simulation8

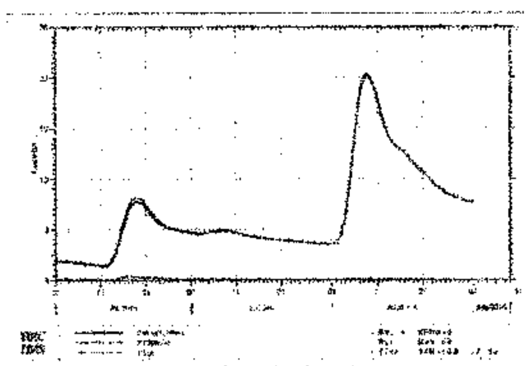
2016 Simulation9

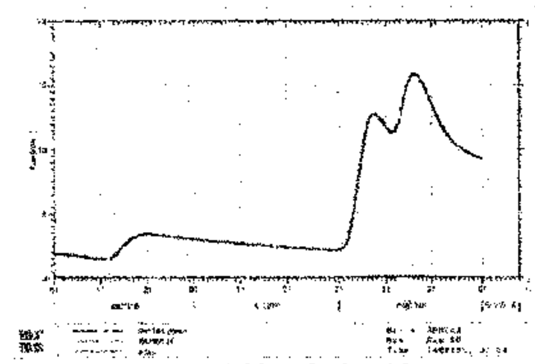
2016 Simulation10

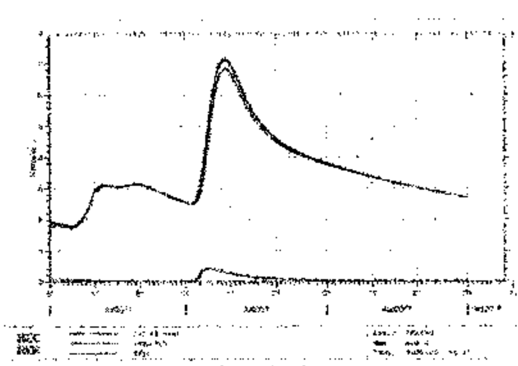
2017 Simulation1

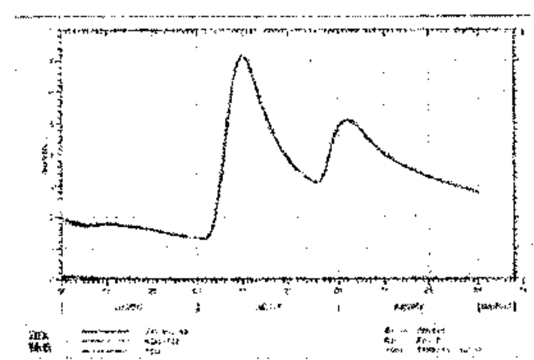
2017 Simulation2

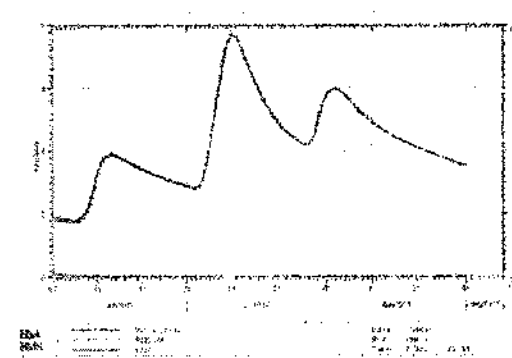
2017 Simulation3

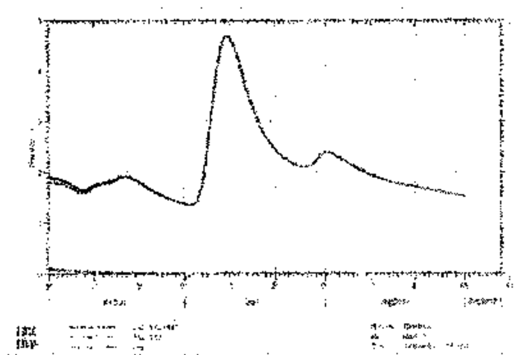
2017 Simulation4

Figure A-H1 The hydrographs using GCM rainfall prediction (cont'd)

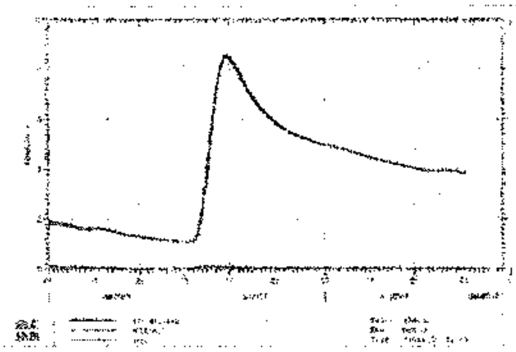

2017 Simulation5

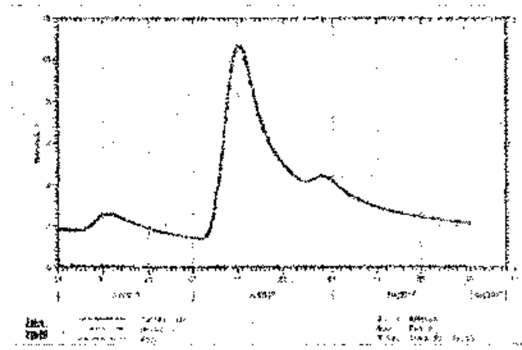

2017 Simulation6

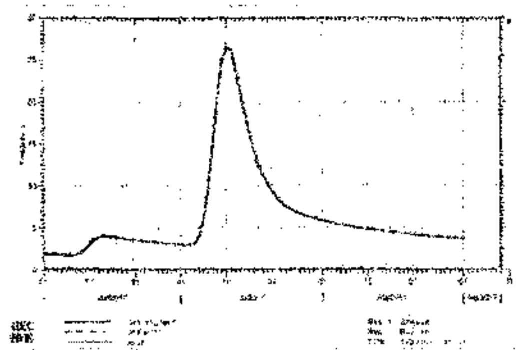

2017 Simulation7

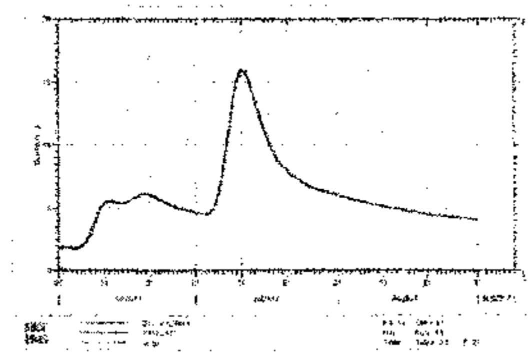

2017 Simulation8

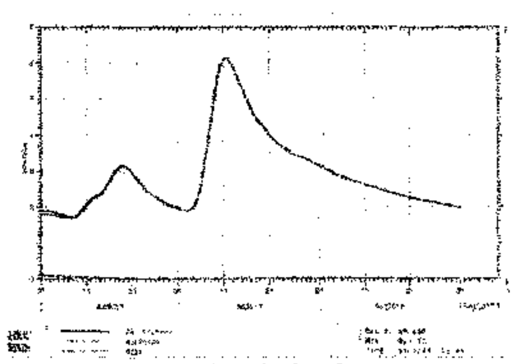

2017 Simulation9

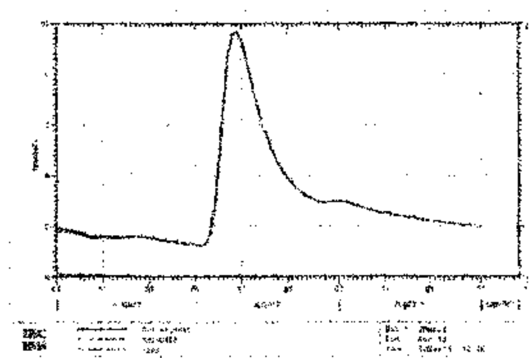

2017 Simulation10

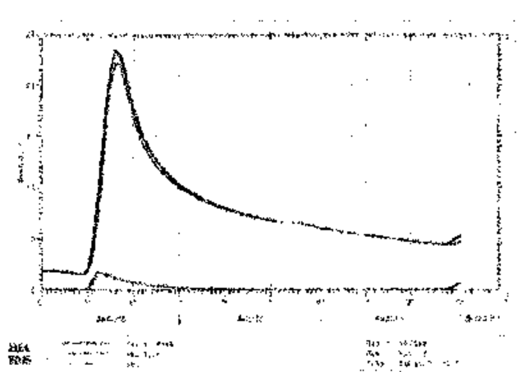

2018 Simulation1

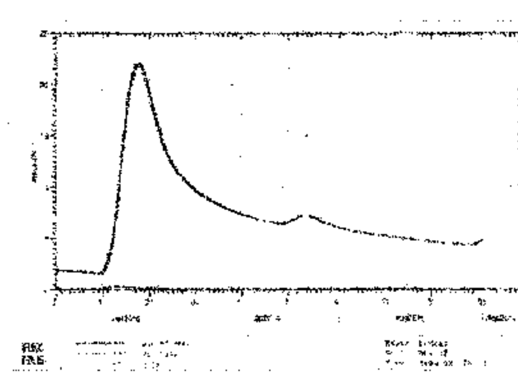

2018 Simulation2

Figure A-H1 The hydrographs using GCM rainfall prediction (cont'd)

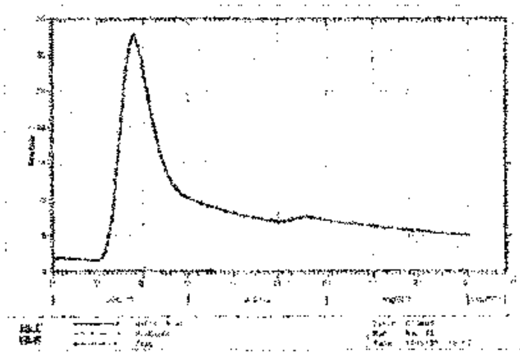

2018 Simulation3

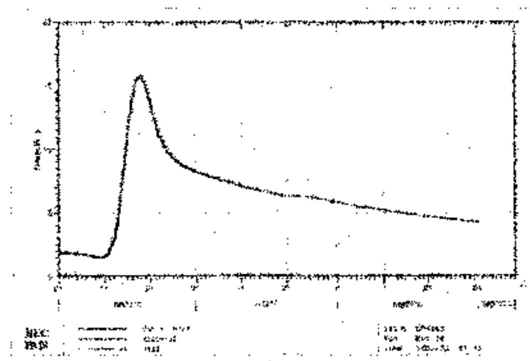

2018 Simulation4

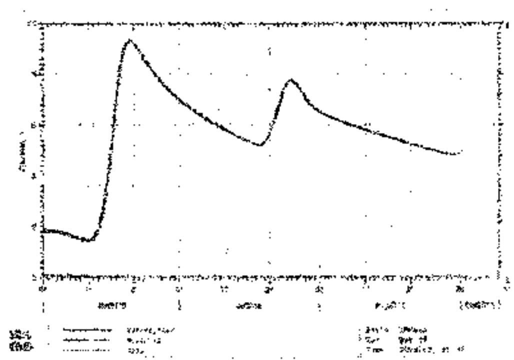

2018 Simulation5

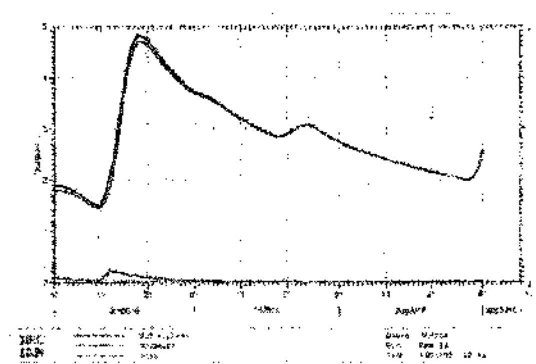

2018 Simulation6

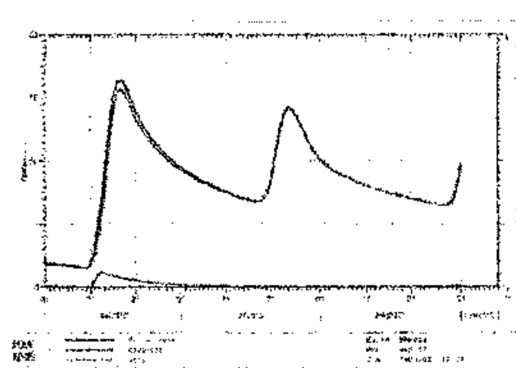

2018 Simulation7

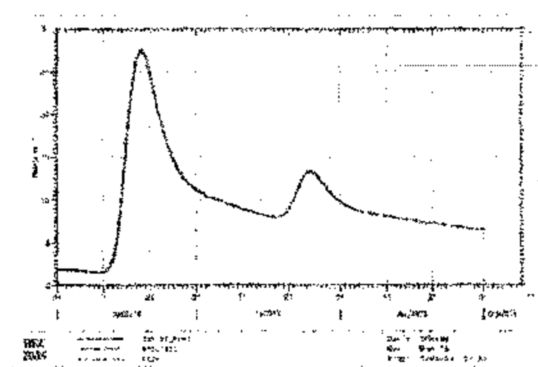

2018 Simulation8

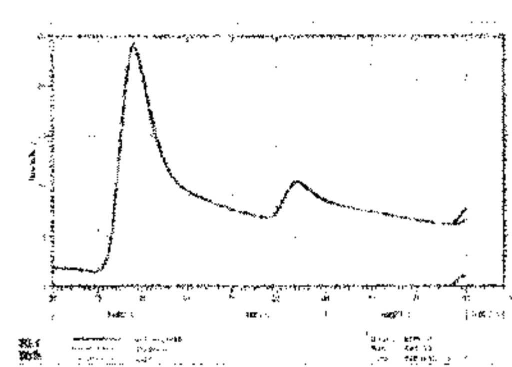

2018 Simulation9

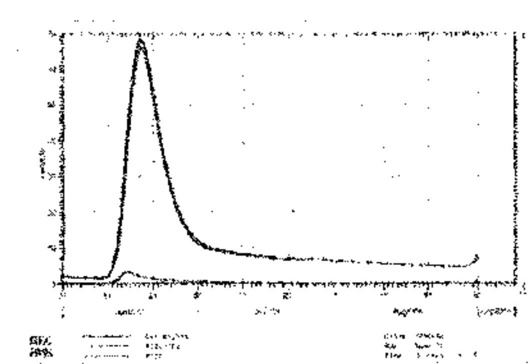

2018 Simulation10

Figure A-H1 The hydrographs using GCM rainfall prediction (cont'd)

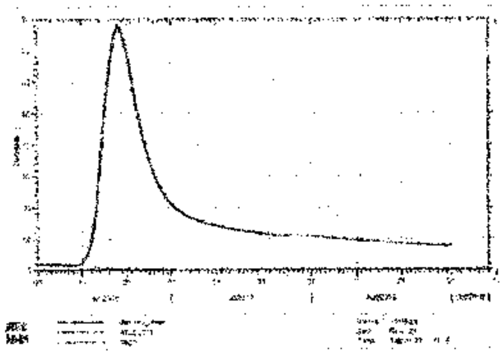

2019 Simulation1

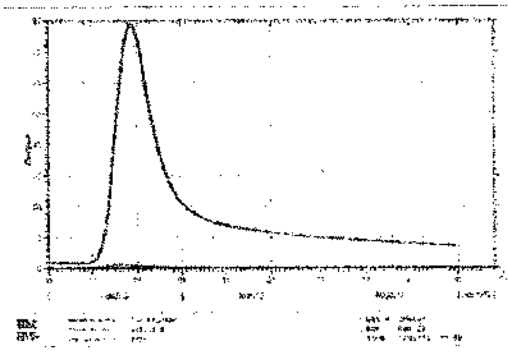

2019 Simulation2

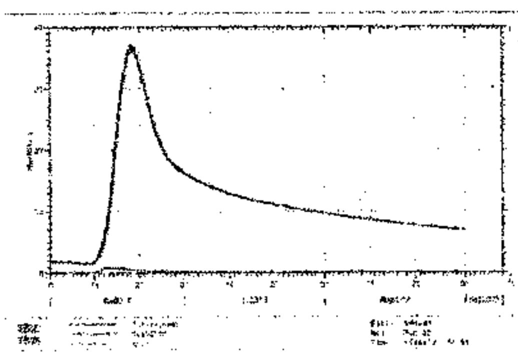

2019 Simulation3

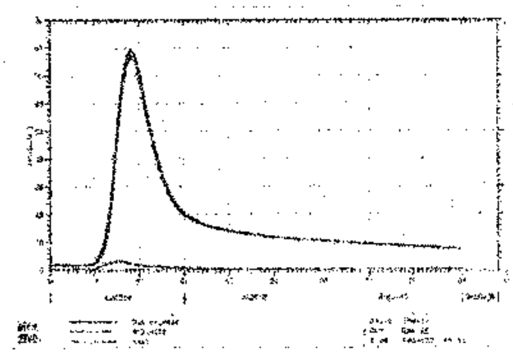

2019 Simulation4

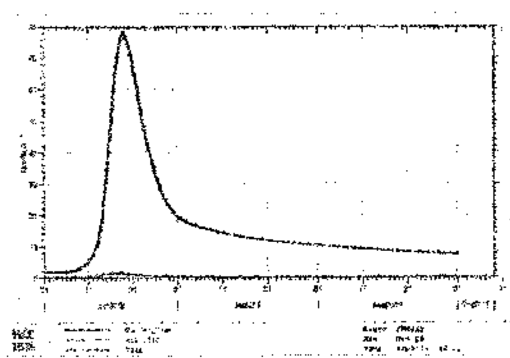

2019 Simulation5

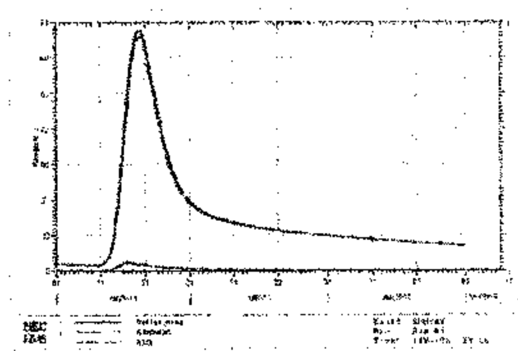

2019 Simulation6

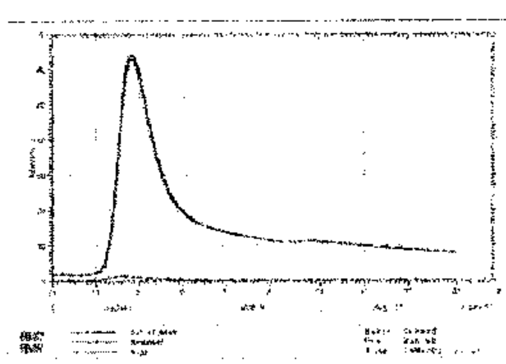

2019 Simulation7

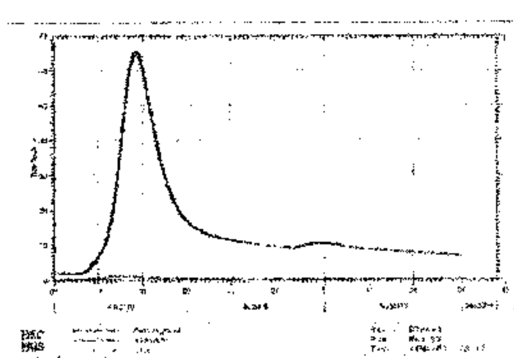

2019 Simulation8

Figure A-H1 The hydrographs using GCM rainfall prediction (cont'd)

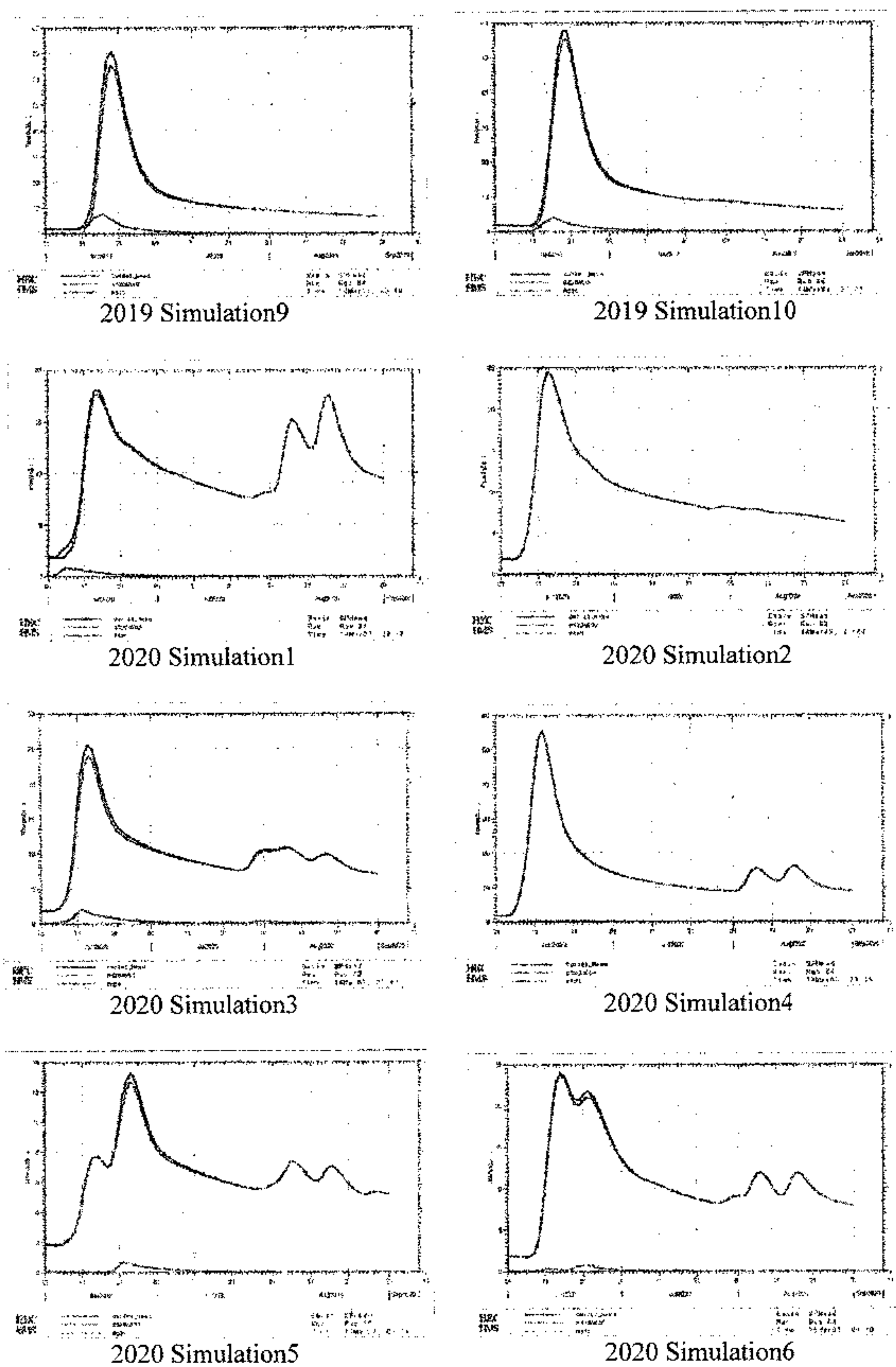

Figure A-H1 The hydrographs using GCM rainfall prediction (cont'd)

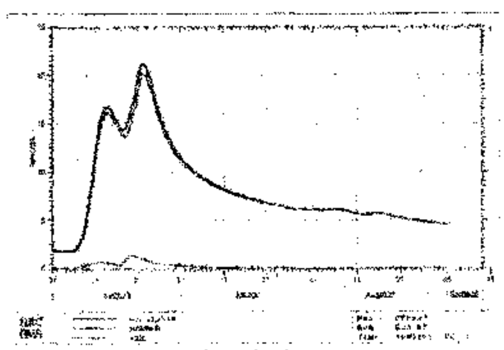

2020 Simulation7

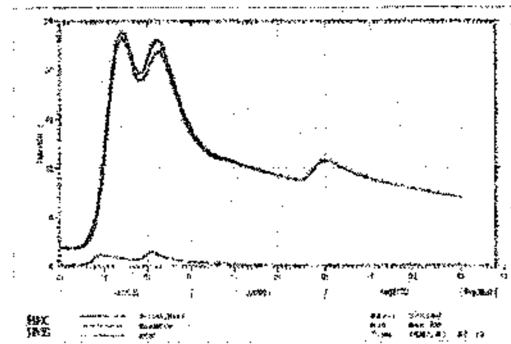

2020 Simulation8

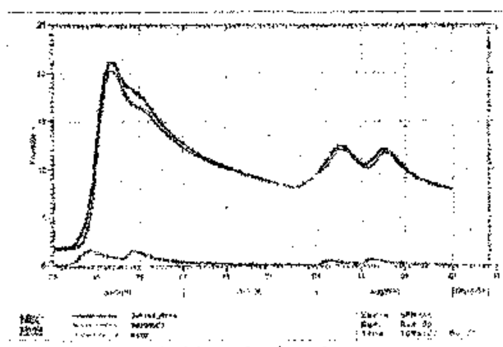

2020 Simulation9

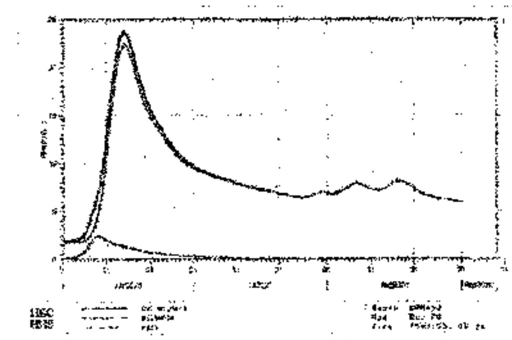

2020 Simulation10

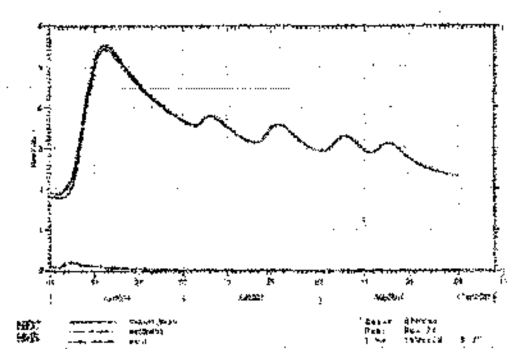

2081 Simulation1

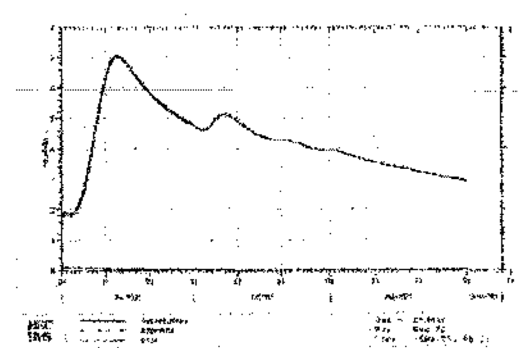

2081 Simulation2

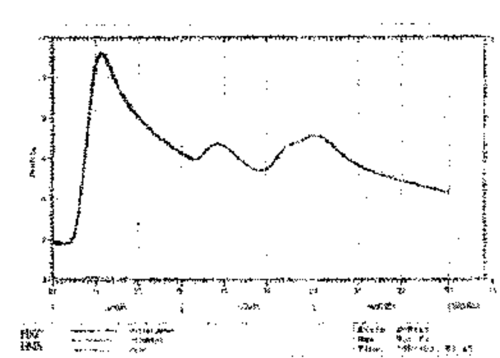

2081 Simulation3

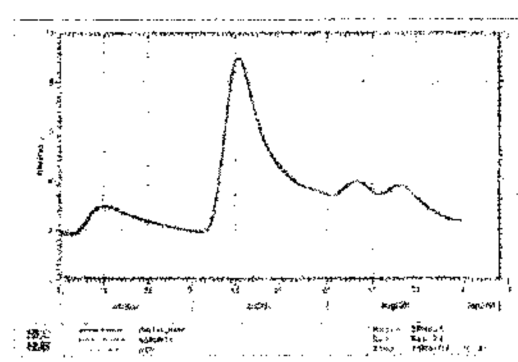

2081 Simulation4

Figure A-H1 The hydrographs using GCM rainfall prediction (cont'd)

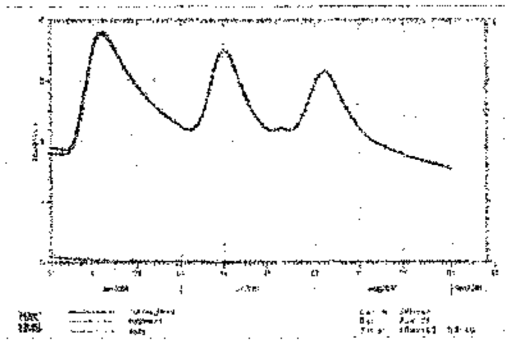

2081 Simulation5

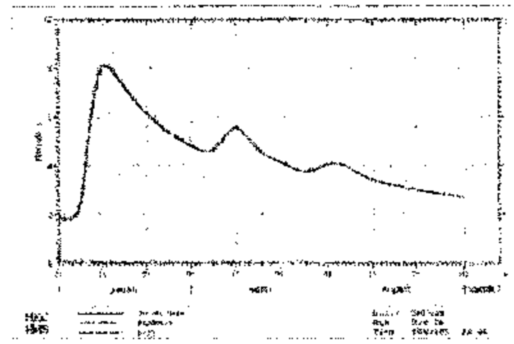

2081 Simulation6

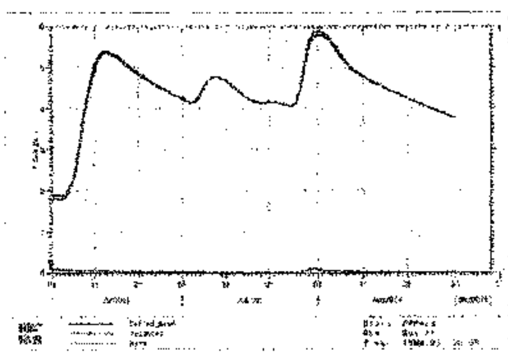

2081 Simulation7

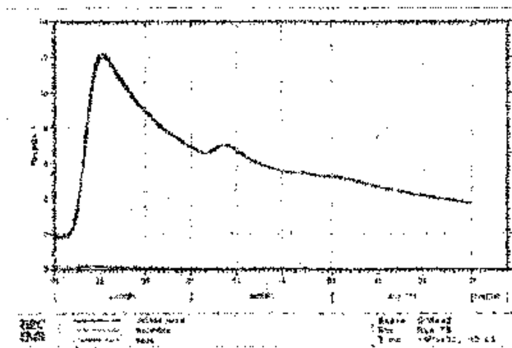

2081 Simulation8

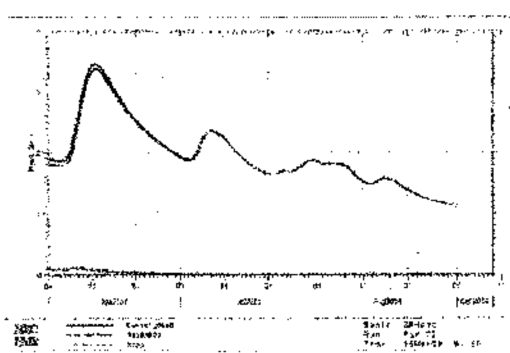

2081 Simulation9

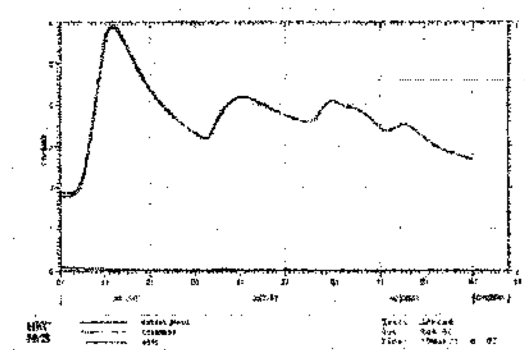

2081 Simulation10

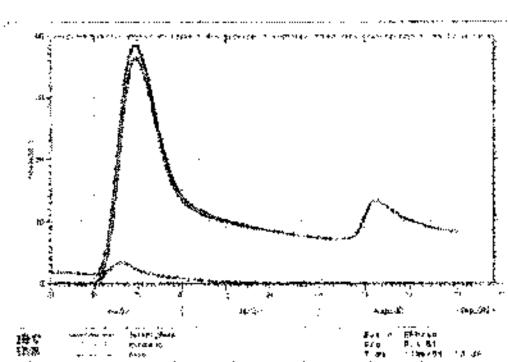

2082 Simulation1

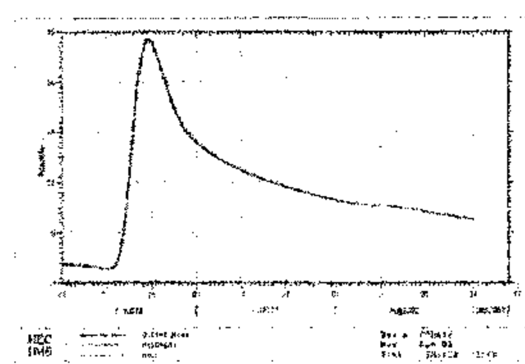

2082 Simulation2

Figure A-H1 The hydrographs using GCM rainfall prediction (cont'd)

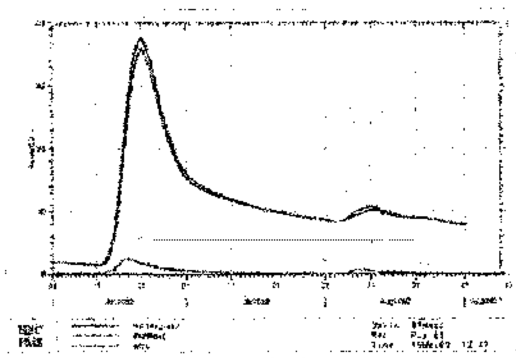

2082 Simulation3

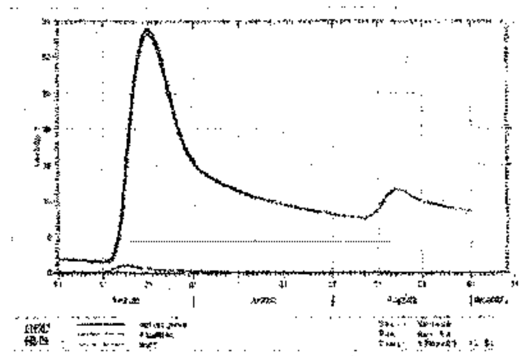

2082 Simulation4

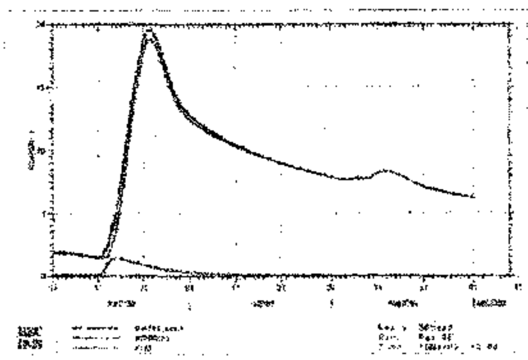

2082 Simulation5

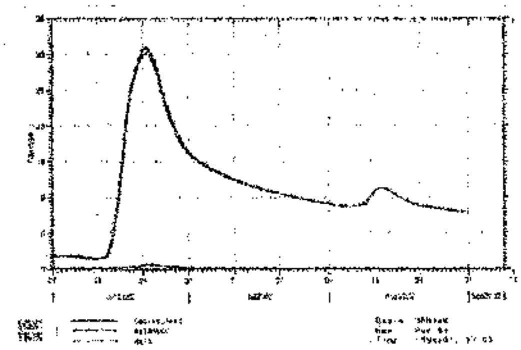

2082 Simulation6

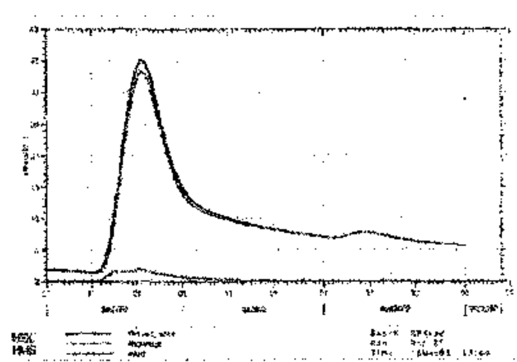

2082 Simulation7

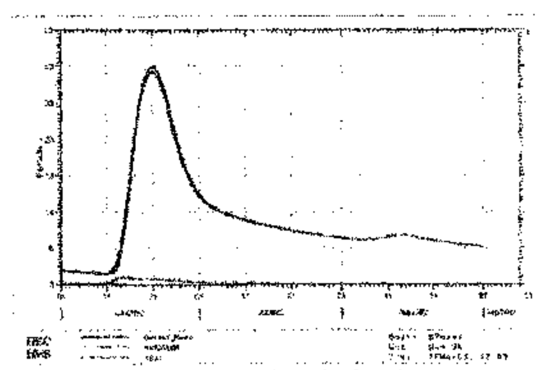

2082 Simulation8

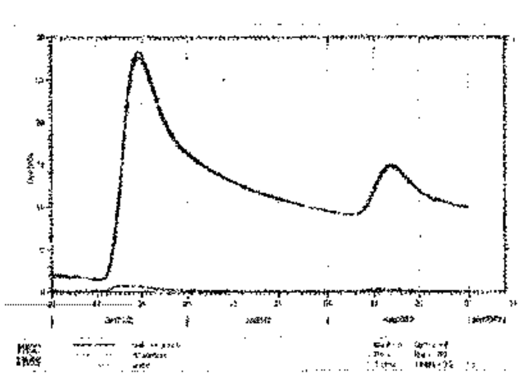

2082 Simulation9

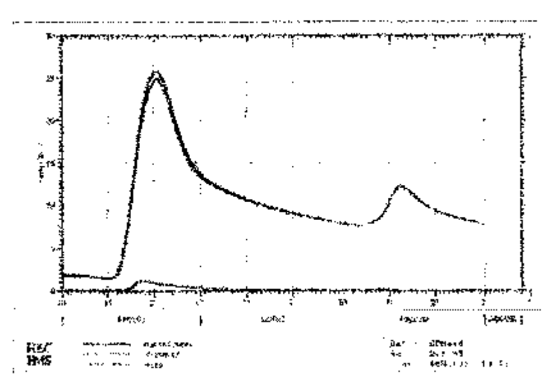

2082 Simulation10

Figure A-H1 The hydrographs using GCM rainfall prediction (cont'd)

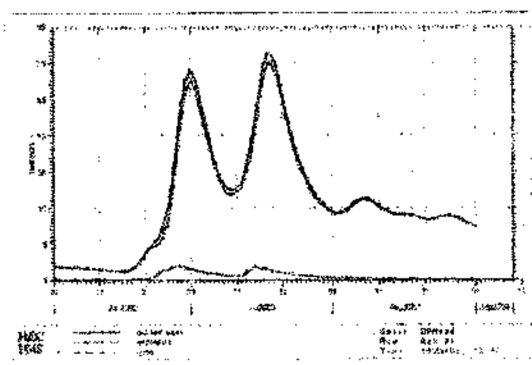

2083 Simulation1

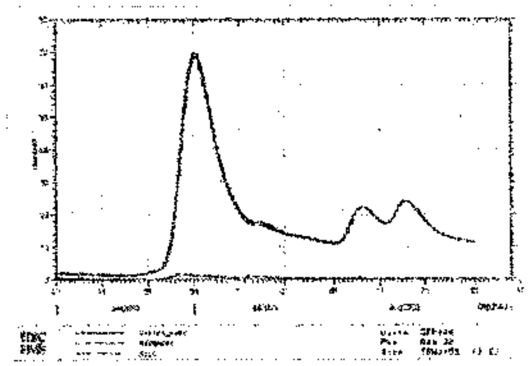

2083 Simulation2

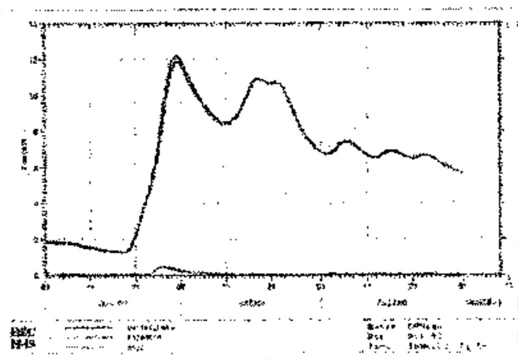

2083 Simulation3

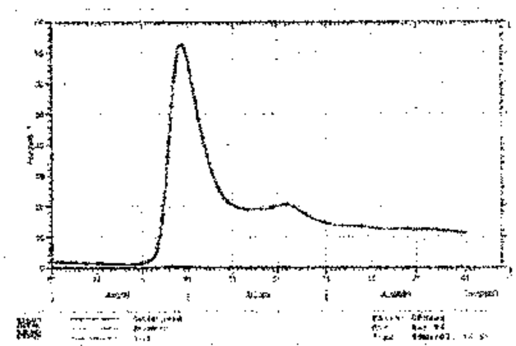

2083 Simulation4

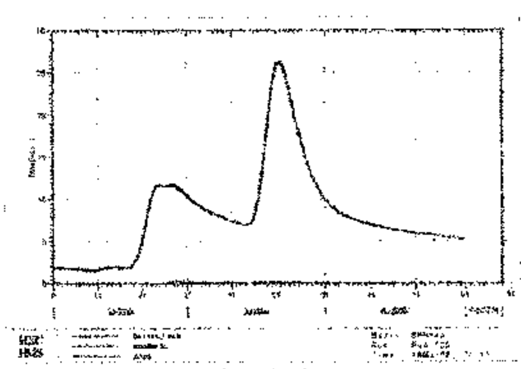

2083 Simulation5

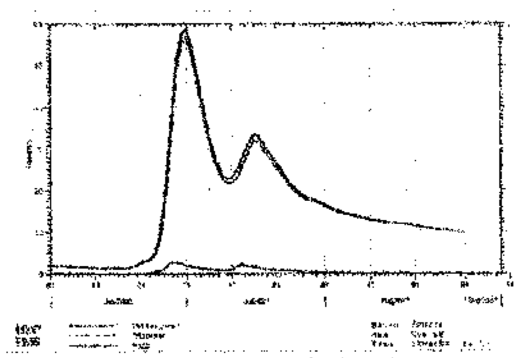

2083 Simulation6

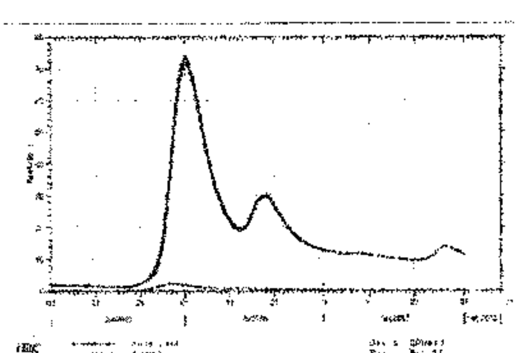

2083 Simulation7

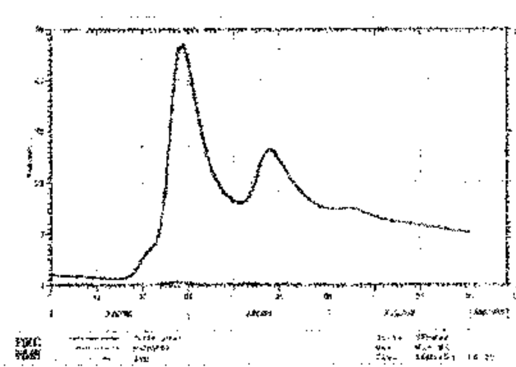

2083 Simulation8

Figure A-H1 The hydrographs using GCM rainfall prediction (cont'd)

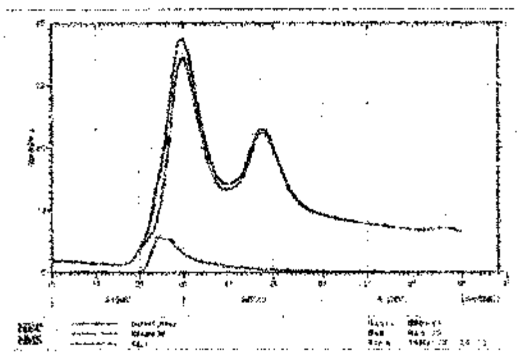

2083 Simulation9

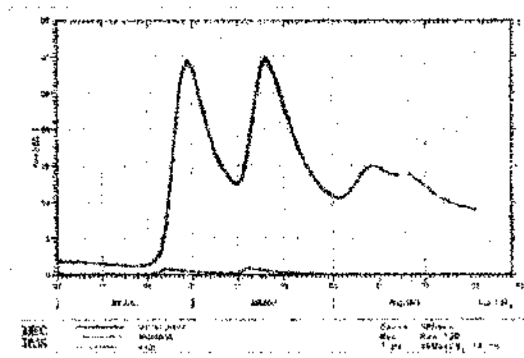

2083 Simulation10

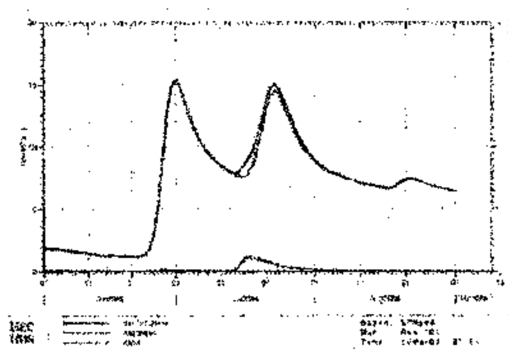

2084 Simulation1

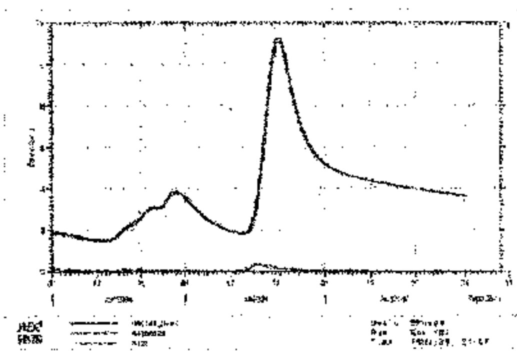

2084 Simulation2

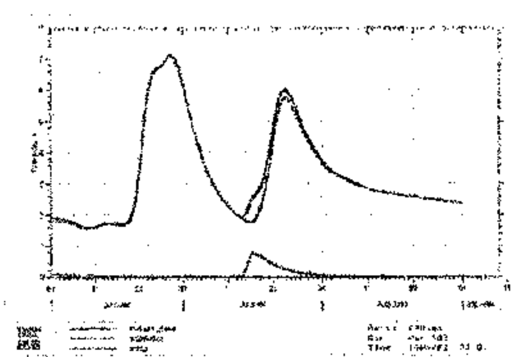

2084 Simulation3

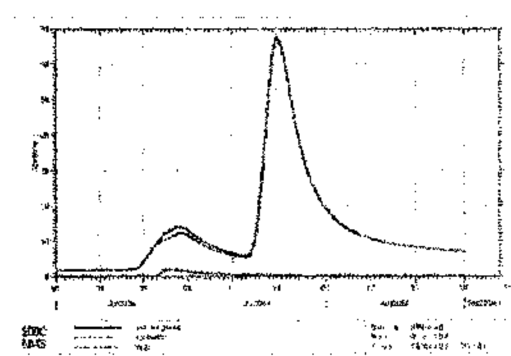

2084 Simulation4

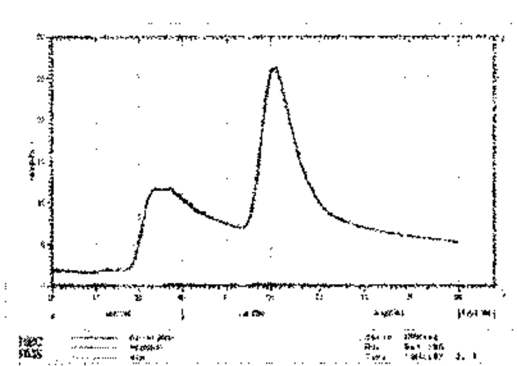

2084 Simulation5

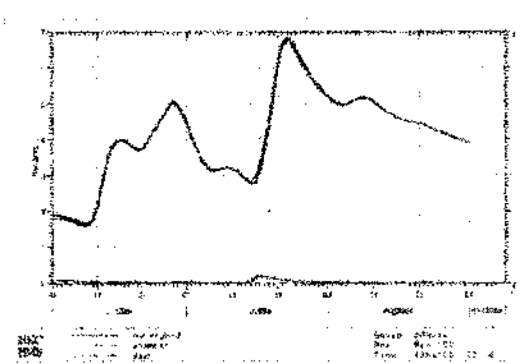

2084 Simulation6

Figure A-H1 The hydrographs using GCM rainfall prediction (cont'd)

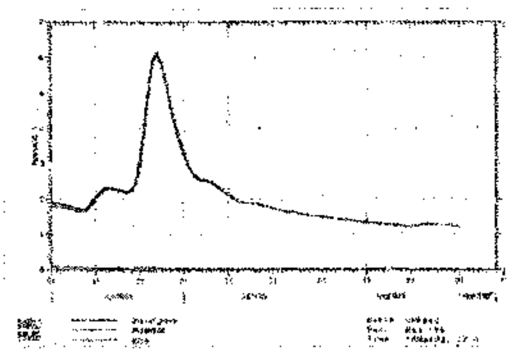

2085 Simulation5

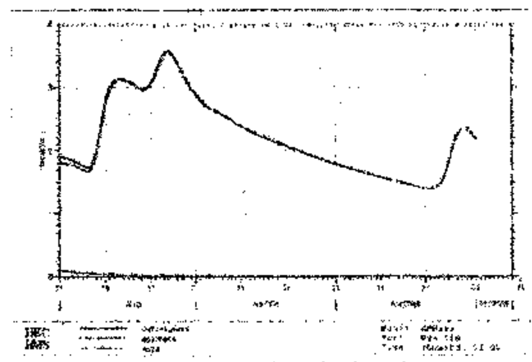

2085 Simulation6

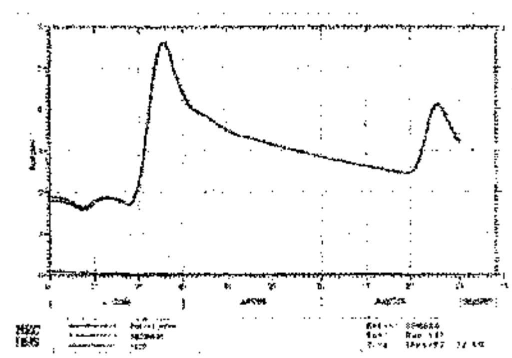

2085 Simulation7

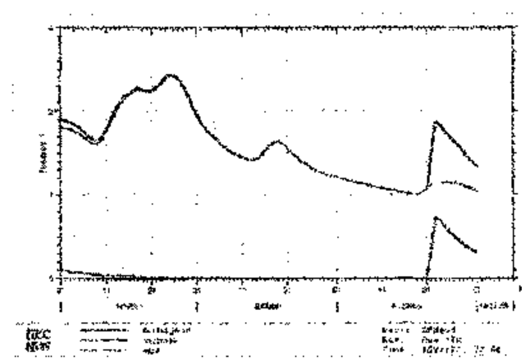

2085 Simulation8

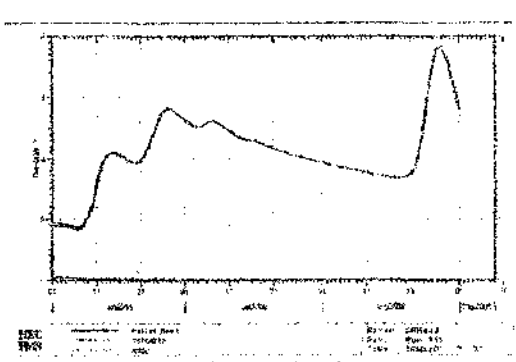

2085 Simulation9

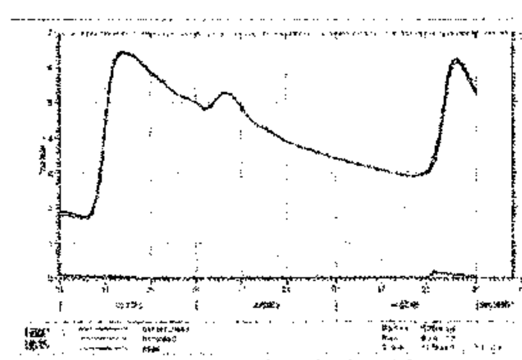

2085 Simulation10

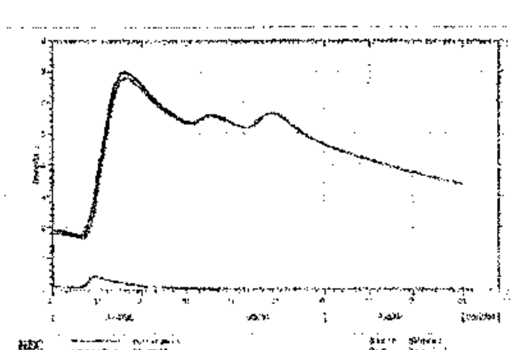

2086 Simulation1

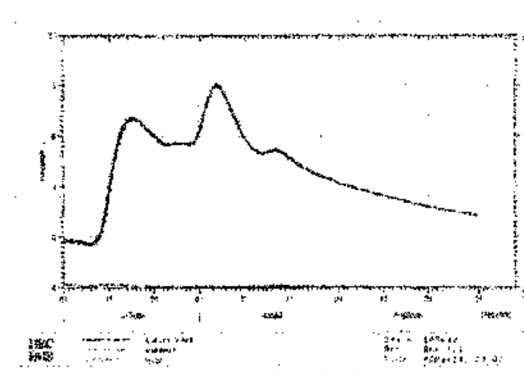

2086 Simulation2

Figure A-H1 The hydrographs using GCM rainfall prediction (cont'd)

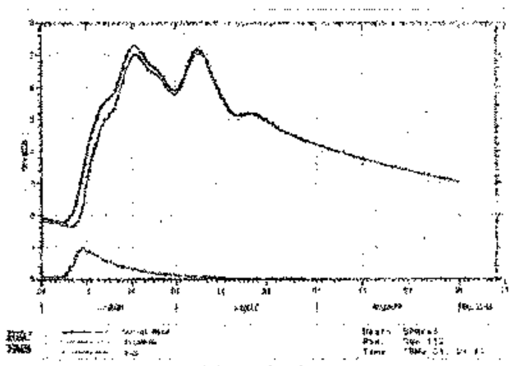

2086 Simulation3

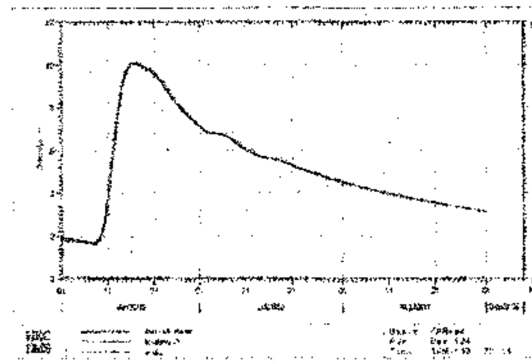

2086 Simulation4

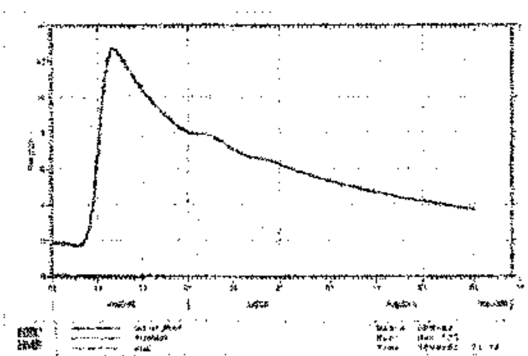

2086 Simulation5

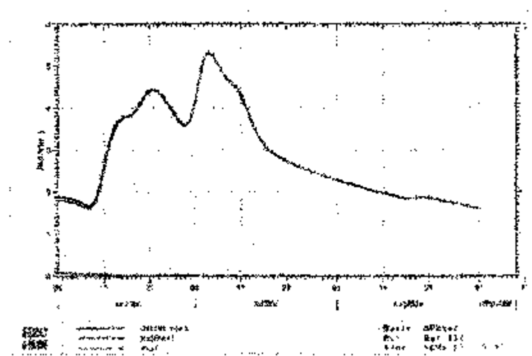

2086 Simulation6

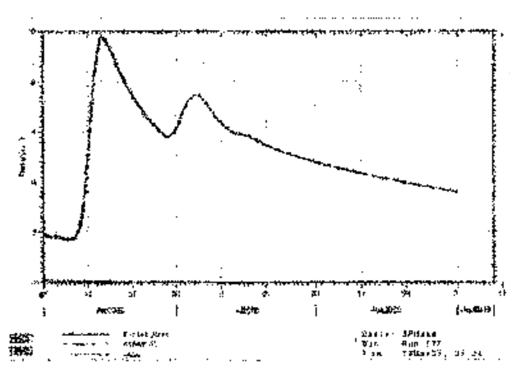

2086 Simulation7

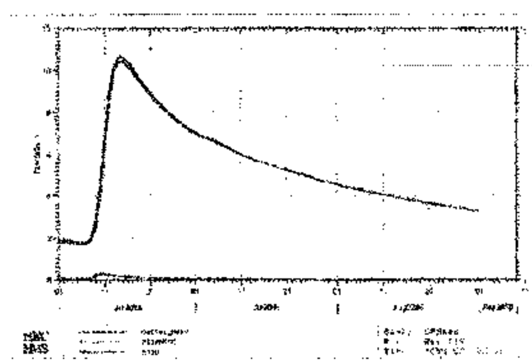

2086 Simulation8

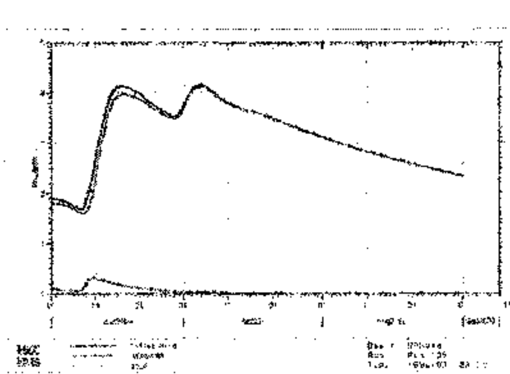

2086 Simulation9

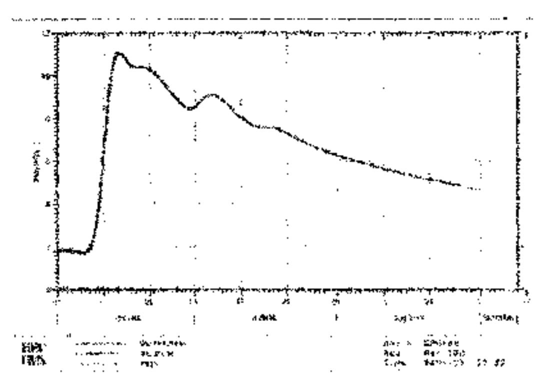

2086 Simulation10

Figure A-H1 The hydrographs using GCM rainfall prediction (cont'd)

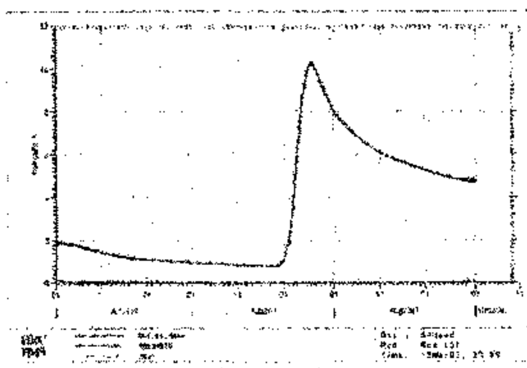

2087 Simulation1

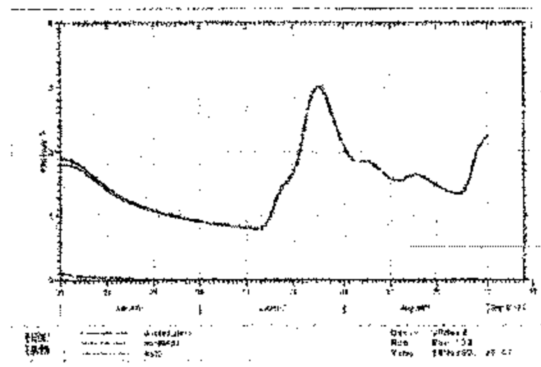

2087 Simulation2

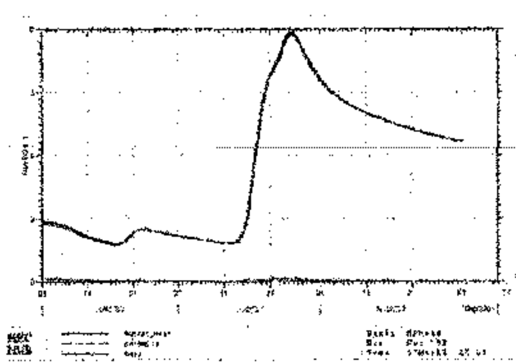

2087 Simulation3

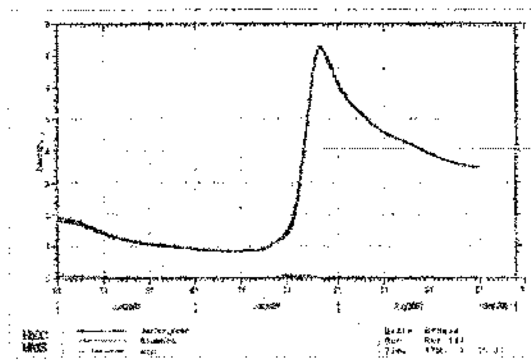

2087 Simulation4

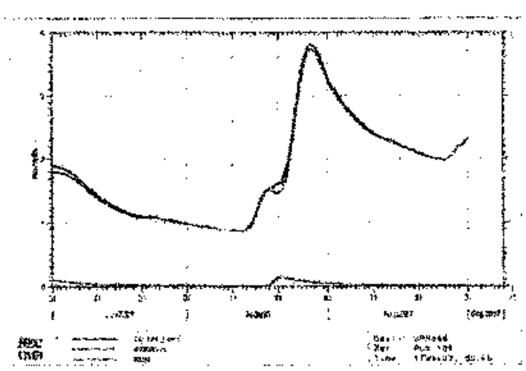

2087 Simulation5

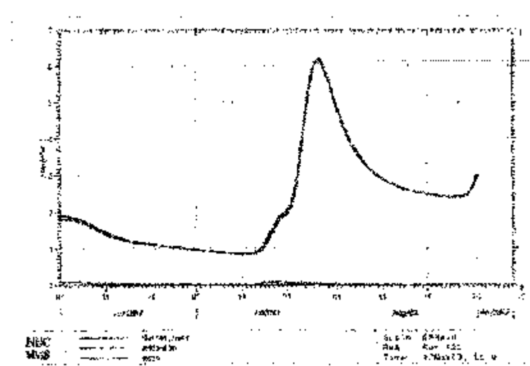

2087 Simulation6

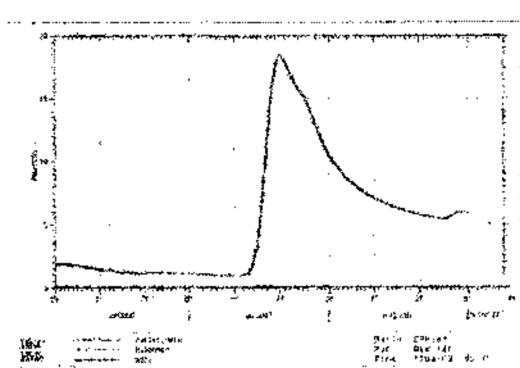

2087 Simulation7

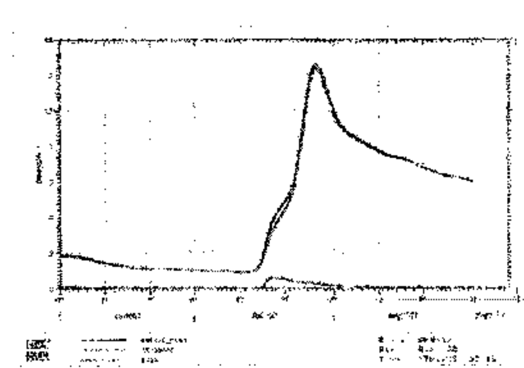

2087 Simulation8

Figure A-H1 The hydrographs using GCM rainfall prediction (cont'd)

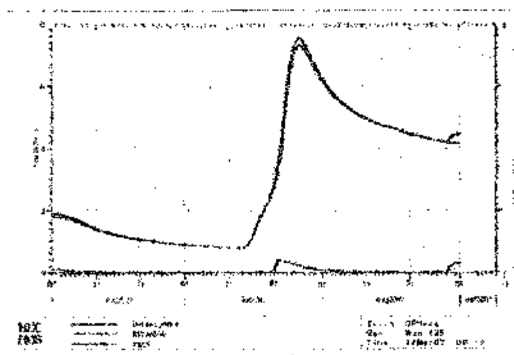

2087 Simulation9

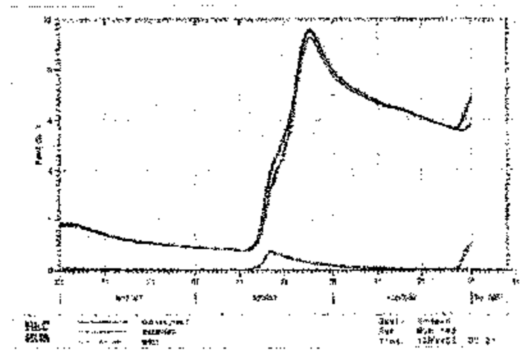

2087 Simulation10

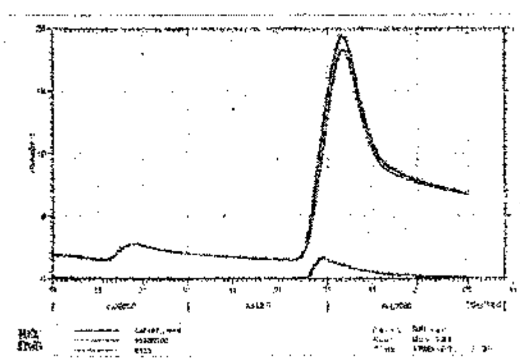

2088 Simulation1

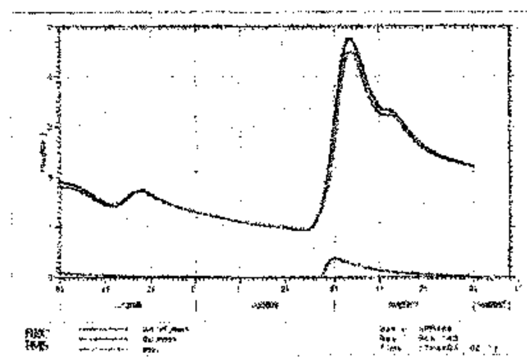

2088 Simulation2

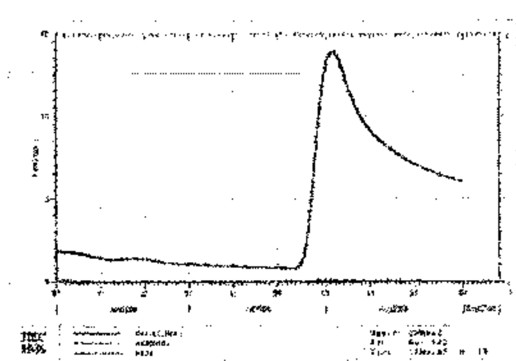

2088 Simulation3

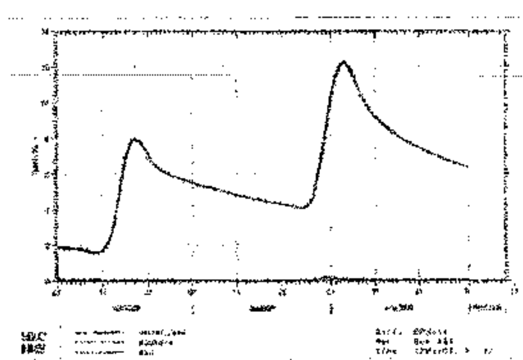

2088 Simulation4

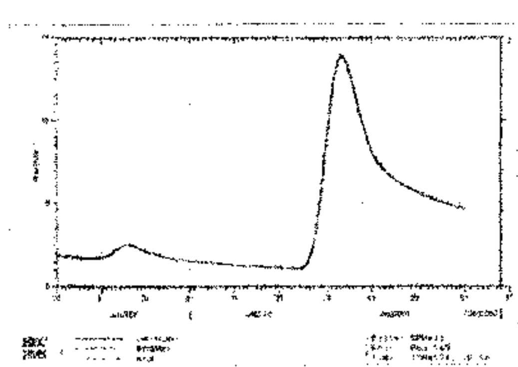

2088 Simulation5

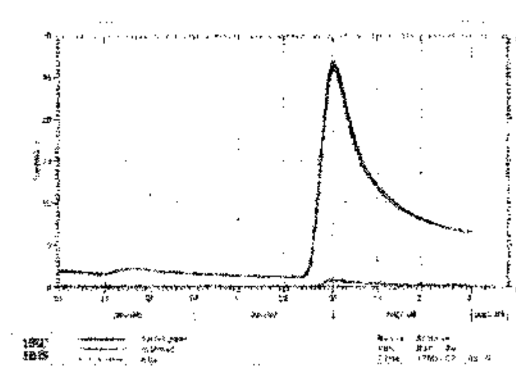

2088 Simulation6

Figure A-H1 The hydrographs using GCM rainfall prediction (cont'd)

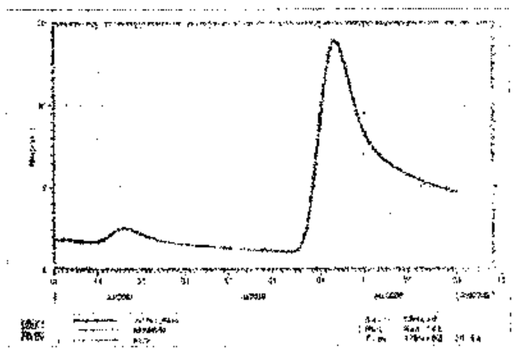

2088 Simulation7

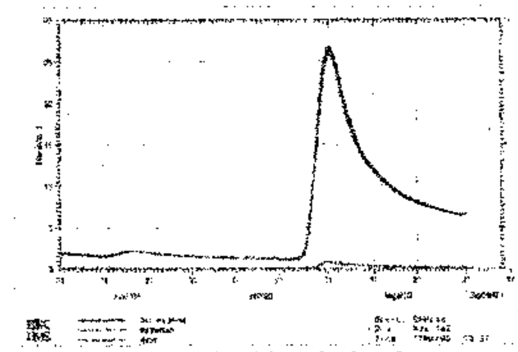

2088 Simulation8

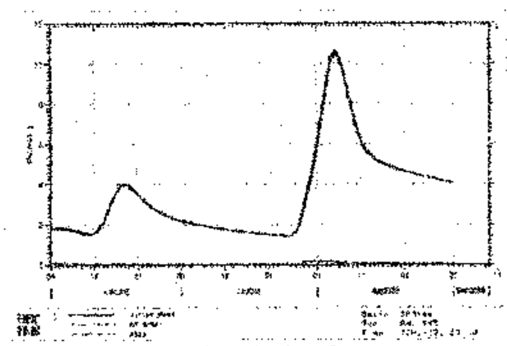

2088 Simulation9

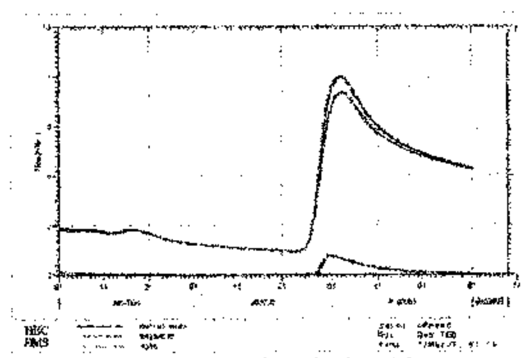

2088 Simulation10

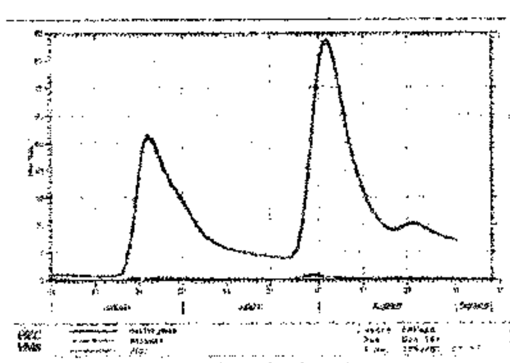

2089 Simulation1

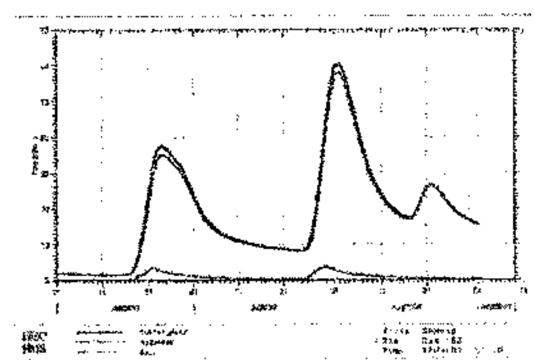

2089 Simulation2

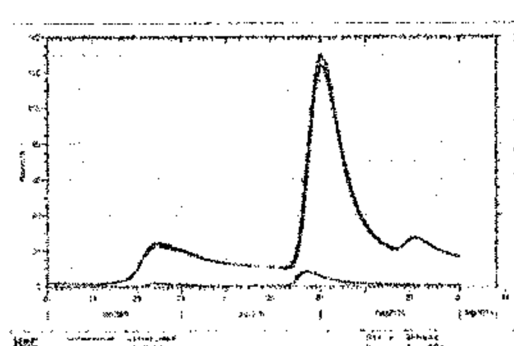

2089 Simulation3

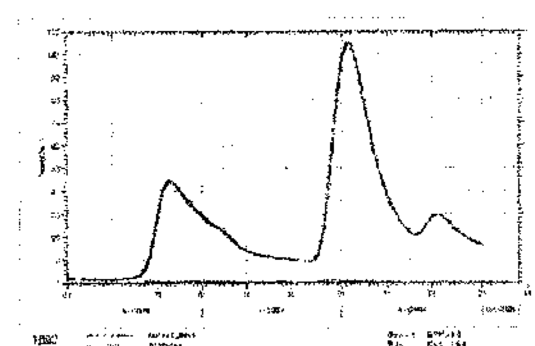

2089 Simulation4

Figure A-H1 The hydrographs using GCM rainfall prediction (cont'd)

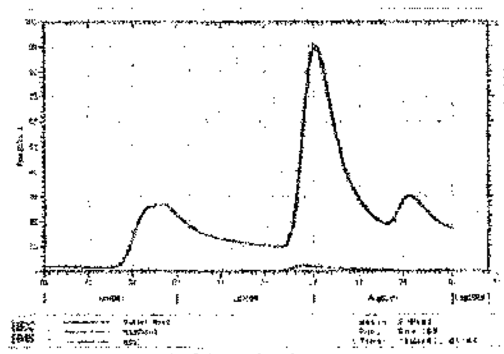

2089 Simulation5

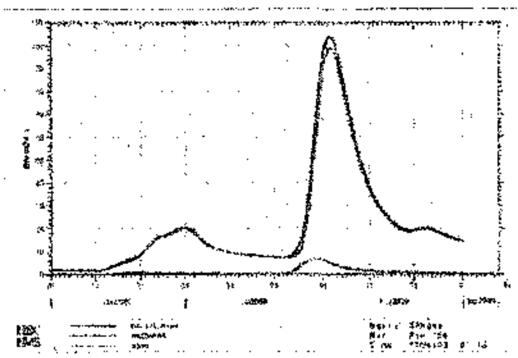

2089 Simulation6

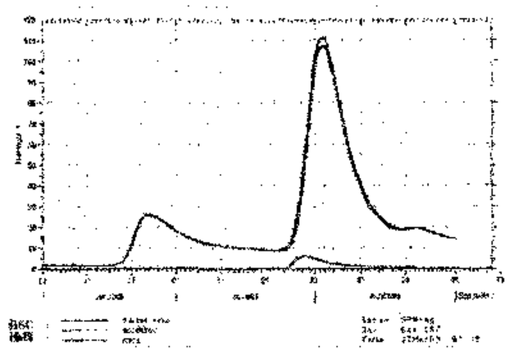

2089 Simulation7

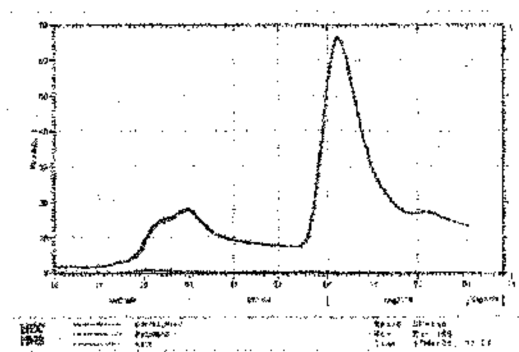

2089 Simulation8

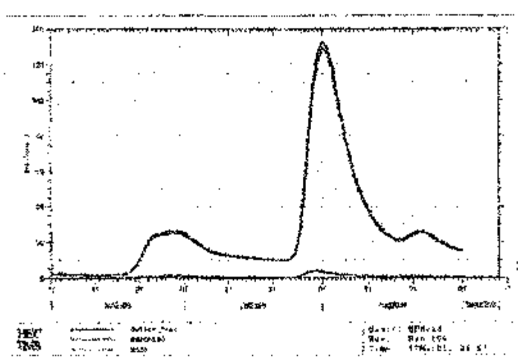

2089 Simulation9

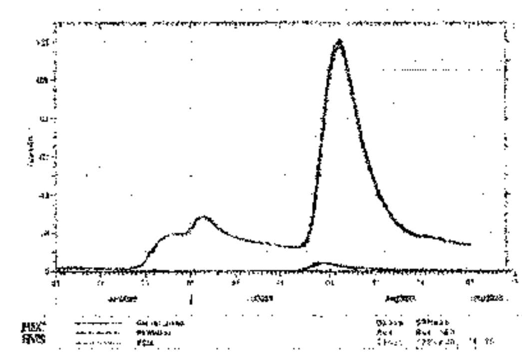

2089 Simulation10

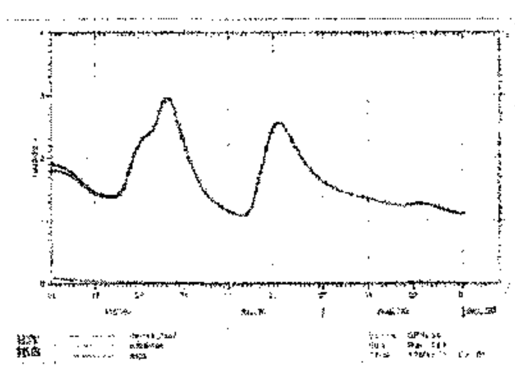

2090 Simulation1

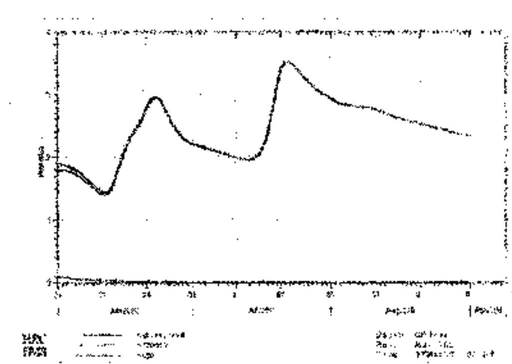

2090 Simulation2

Figure A-H1 The hydrographs using GCM rainfall prediction (cont'd)

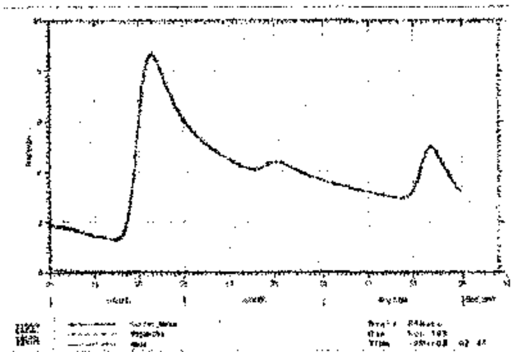

2090 Simulation3

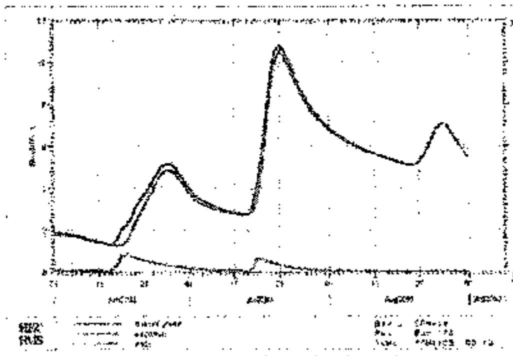

2090 Simulation4

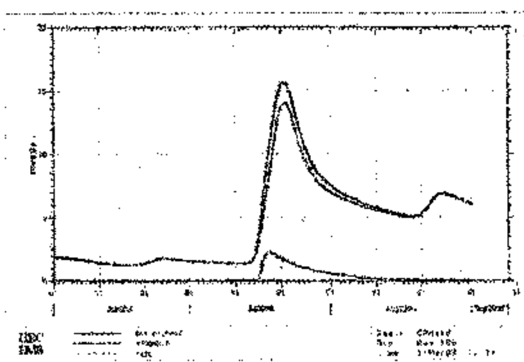

2090 Simulation5

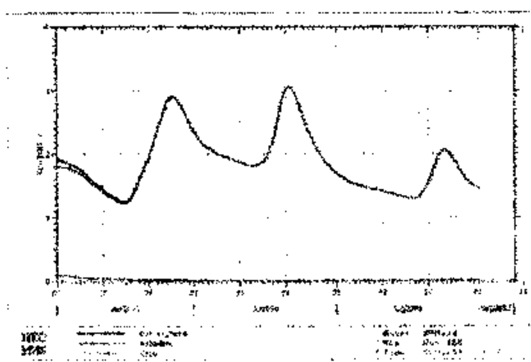

2090 Simulation6

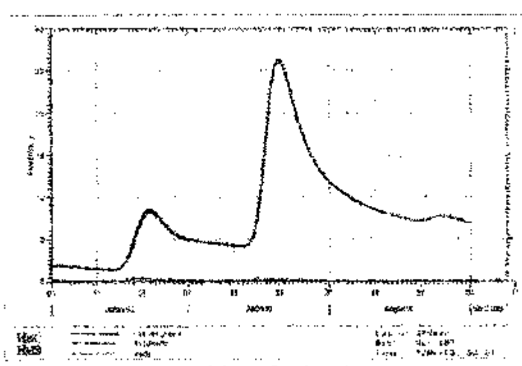

2090 Simulation7

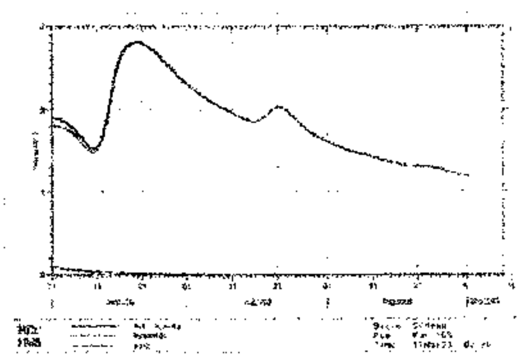

2090 Simulation8

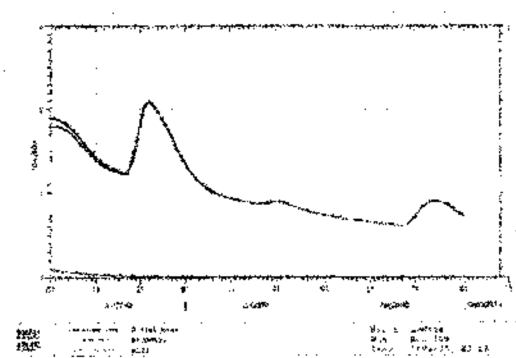

2090 Simulation9

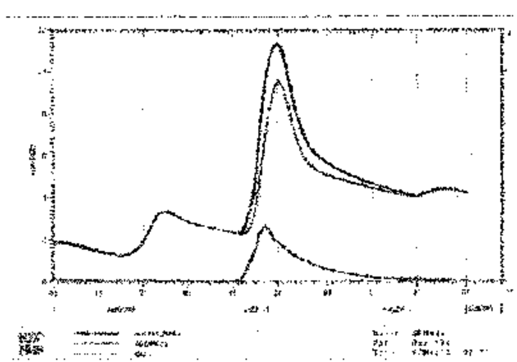

2090 Simulation10

Figure A-H1 The hydrographs using GCM rainfall prediction (cont'd)